Electronic Transport through Systems of Quantum Dots Coupled to a Bosonic Mode

Von der Fakultät für Mathematik, Informatik und Naturwissenschaften der RWTH Aachen University zur Erlangung des akademischen Grades einer Doktorin der Naturwissenschaften genehmigte Dissertation

vorgelegt von

Mara Caltapanides, M. Sc.

aus Bielefeld

Berichter:	Univ.-Prof. Dr. rer. nat. Volker Meden Univ.-Prof. Dr. rer. nat. Dante M. Kennes
Tag der mündlichen Prüfung:	13.12.2024

ABSTRACT

In this thesis, we study the electronic properties of a system of spin-polarized quantum dots coupled to a single mode of a resonator. More specifically, we focus on an open quantum dot system coupled to two leads in both equilibrium and non-equilibrium setups. Our primary method for treating the fermion-boson interaction is the lowest-order perturbation theory. Additionally, we utilize the Lindblad master equation method, exact diagonalization, and the functional renormalization group method in a first-order truncation scheme to complement our analysis.

We consider two different types of coupling to the resonator. First, we analyze a linear chain of dots coupled to the light field of a microcavity. We extend the widely used Peierls substitution in Coulomb gauge, which is usually applied on homogenous lattices, to systems where light couples to only a finite part of the lattice. Subsequently, we investigate the effects of considering only the lowest order in the vector potential of the exponential function containing the Peierls phase. We further extend the formalism to include second-order contributions at the mean-field level when utilizing lowest-order perturbation theory. This formalism is then used to study interference effects in the linear conductance of a quantum dot chain consisting of three dots, as well as boson-assisted tunneling in non-equilibrium systems with a finite voltage bias applied across a double quantum dot setup. Additionally, we study the light-matter coupling in the dipole gauge, focusing again on systems where light couples only to a finite section of the lattice.

As the second model, we explore the coupling to the vibrational degrees of freedom of the quantum dot system, which is analogous to an *LC* resonator in electronic circuits and modeled by a capacitive coupling between the fermionic and bosonic degrees of freedom. We investigate the low-energy scale induced by the fermion-boson coupling and its impact on the electric transport properties of the system. This includes, in particular, interference effects in the linear conductance of a triple-dot chain resulting from the coupling. Additionally, for capacitive coupling, we also study boson-assisted tunneling and the related energy transfer between the quantum dot system and the resonator. More specifically, we consider a triple dot system with next-nearest neighbor hopping in a triangular configuration and compare its electronic properties to a linear configuration. Finally, besides the capacitive fermion-boson coupling, we incorporate a nearest-neighbor Coulomb interaction in lowest-order perturbation theory, which represents a combined system of the spinless Anderson-Holstein model and the interacting resonant level model. In this analysis, we focus on the particle current and differential transport coefficients in the presence of the two interactions. In particular, we study how the fermion-boson and fermion-fermion interaction influence each other.

ZUSAMMENFASSUNG

In dieser Dissertation untersuchen wir die elektronischen Eigenschaften eines Systems von spinpolarisierten Quantenpunkten, die an eine einzelne Resonatormode gekoppelt sind. Genauer gesagt betrachten wir ein offenes Quantenpunktsystem, das an zwei Elektroden gekoppelt ist sowohl im Gleichgewicht als auch im Nichtgleichgewicht. Wir verwenden hauptsächlich Störungstheorie in niedrigster Ordnung um die Fermion-Boson-Wechselwirkung zu behandeln. Zusätzlich verwenden wir die Lindblad-Mastergleichung, exakte Diagonalisierung und die Methode der Funktionalen Renormierungsgruppe für die Selbstenergie, um unsere Analyse zu ergänzen.

Wir betrachten zwei verschiedene Kopplungsarten zwischen den Quantenpunktsystem und dem Resonator. Als erstes analysieren wir eine lineare Kette von Quantenpunkten, die an das elektro-magnetisches Feld eines optischen Resonators gekoppelt ist. Wir erweitern die weit verbreitete Peierls-Substitution in der Coulomb-Eichung, die üblicherweise für unendliche Gitter verwendet wird, auf Systeme bei denen Licht nur an einen endlichen Teil des Festkörpers koppelt. Anschließend untersuchen wir die Auswirkungen wenn nur die lineare Ordnung im Vektorpotential der Exponentialfunktion, die die Peierls-Phase enthält, berücksichtigt wird. Wir erweitern die Störungstheorie erster Ordnung um Beiträge zweiter Ordung der Exponentialfunktion in der Mean-Field-Nährung zu berücksichtigen. Diese Formalismus wird dann verwendet, um Interferenzeffekte in der linearen Leitfähigkeit einer Quantenpunktkette, die aus drei Punkten besteht, sowie bosonisch unterstütztes Tunneln in Nichtgleichgewichtssystemen mit einer angelegten endlichen Spannung über ein Doppel-Quantenpunkt-Konfiguration zu untersuchen. Darüber hinaus untersuchen wir die Licht-Materie-Kopplung in der Dipol-Eichung und betracten sie für Systeme, bei denen Licht nur an einen endlichen Abschnitt des Festkörpers koppelt.

Als zweites erforschen wir die Kopplung an die Schwingungsfreiheitsgrade des Quantenpunktsystems, die analog zu der Kopplung an einen *LC*-Resonator in einem elektronischen Schaltkreis ist. Sie wird durch eine kapazitive Kopplung zwischen den fermionischen und bosonischen Freiheitsgraden modelliert. Wir untersuchen die Auswirkungen der Fermion-Boson-Kopplung auf die elektrischen Transporteigenschaften des Systems. Dies umfasst insbesondere Interferenzeffekte in der linearen Leitfähigkeit einer Drei-Quantenpunkt-Kette, die aus der Kopplung resultieren. Darüber hinaus untersuchen wir bei kapazitiver Kopplung auch bosonisch unterstütztes Tunneln und dem damit verbundenen Energieaustausch zwischen dem Quantenpunktsystem und dem Resonator. Genauer gesagt betrachten wir ein Drei-Quantenpunkt-System in einer dreieckigen Konfiguration, wo ein Tunneln zwischen dem nächsten und übernächsten Nachbarn möglich ist. Wir vergleichen dessen elektronische Eigenschaften mit einer linearen Konfiguration. Schließlich betrachten wir zusätzlich zu der kapazitiven Fermion-Boson-Kopplung auch eine Coulomb-Wechselwirkung zwischen Elektronen auf benachbarten Quantenpunkten in der Störungstheorie erster Ordnung. Dies stellt ein kombiniertes System des "spinless Anderson-Holstein models" und des "interacting resonant level models" dar. In dieser Analyse konzentrieren wir uns auf den Teilchenstrom und die differentiellen Transportkoeffizienten in Anwesenheit der beiden Wechselwirkungen. Insbesondere untersuchen wir, wie sich Fermion-Boson- und Fermion-Fermion-Wechselwirkungen gegenseitig beeinflussen.

CONTENTS

Part I.

Introduction

In the beginning, we provide the motivation behind the study of the systems under consideration in Chapter 1. Subsequently, in Chapter 2, we introduce a generalized physical model, which is able to describe the systems introduced before and discuss the approximations used to simplify the overall description. The model incorporates fermionic degrees of freedom, representing a quantum dot system, coupled to two non-interacting leads. The fermions on the quantum dot system can further interact via a repulsive Coulomb interaction. Additionally, bosonic degrees of freedom are introduced and modeled by a harmonic oscillator. We distinguish the generalized model between two cases, with different coupling of the fermionic and bosonic degrees of freedom. This distinction is conducted on the basis of the two physical systems discussed in the aforementioned Chapter 1.

1. Motivation

1.1. Low-dimensional correlated quantum systems

The rapid advances in nanotechnology and the emergence of promising applications, such as next-generation transistors [1, 2], in quantum technology [3–6] or in medicine [7, 8], have generated the growing need to experimentally as well as theoretically study electron systems on the nanoscale. In these systems, the quantization of energy levels becomes relevant, and quantum mechanical effects play a dominant role. These effects are especially intriguing for strongly correlated many-body systems, where interactions between electrons give rise to collective behavior. These fermionic interactions include for example Coulomb interaction or can be mediated by electron-phonon interaction. The correlations can lead to fascinating emergent phenomena, including superconductivity, Mott insulators, and many more [9–11]. The theoretical study of these systems is crucial for understanding ongoing experimental efforts and enabling future developments.

In the present thesis, we focus on correlation effects introduced by coupling the fermionic degrees of a finite part of the system to the bosonic degrees of freedom of a single-mode resonator, where only the dominant resonator mode is taken into account. This coupling leads to effective long-range interaction between the fermionic degrees of freedom, changing the electronic properties. Two possible couplings to the resonator and the experimental platforms on which they are realized are described in the following two Sects. 1.2 and 1.3. They will be studied in Parts III and IV of this thesis.

Strongly correlated impurity models

In the present thesis, we focus on low-dimensional electronic systems, meaning dot-like systems and linear chains. In this context, quantum dot systems offer a tunable and controllable setting for the experimental and theoretical study of low-dimensional, as well as strongly correlated electronic systems. We are primarily interested in the transport phenomena of open quantum dot systems. Thus, we focus on impurity models, which describe systems where only a part of the full electronic system experiences interactions, referred to as the impurity or impurity region. The remainder of the electronic system consists of non-interacting leads, which are coupled to the impurity region. These leads generally introduce dissipative effects in the impurity region but also allow for the study of the impurity in non-equilibrium setups, such as when a finite bias voltage is applied between different leads. Thus, they serve as natural test benches for quantum platforms with local correlations in non-equilibrium regimes that have, for instance, been investigated in [12–16].

Quantum dots can be realized experimentally through various means [17], such as semiconductor heterostructures and carbon nanotube molecular wires [18–22]. One example is described in [19] and the references therein, where metal nanotubes are incorporated into complex circuits, facilitating the study of open quantum dot systems.

The properties of these systems depend on the ratios of their bare energy scales, with new effective energy scales emerging due to interactions. A prominent example of how correlations change the equilibrium and non-equilibrium properties is the Kondo model [23], where on-site Coulomb interactions on a quantum dot coupled to two leads induce correlations in the system and give rise to the so-called Kondo temperature T_K as an effective energy scale [24, 25]. At temperatures above this scale, the system exhibits suppressed conductance due to the Coulomb blockade. When lowering the temperature of the system below T_K against the naive expectation, the so-called Kondo resonance leads to an increase in the conductance through the impurity [26, 27]. This occurs because the conduction electrons screen the impurity's spin, suppressing spin-flip scattering, which is responsible for the higher resistance at temperatures above the Kondo temperature. One approach to correctly calculate such effective energy scales is renormalization group methods, which will be discussed in Sect. 5 and applied in Sect. 12.

In general, Coulomb interactions are important in small quantum dot systems, where the kinetic energy is limited and the interaction strength becomes dominant. Besides the Kondo model, another model in which Coulomb interaction leads to interesting correlation effects is the interacting resonant level model (IRLM). It consists of a spin-polarized quantum dot coupled to two spin-polarized leads. The fermions on the quantum dot interact with a nearest-neighbor Coulomb interaction with fermions in the leads. At low temperatures, and therefore at low energy scales, correlated charge fluctuations dominate the behavior of this system. The IRLM has been extensively studied using various methods, both in and out of equilibrium [13, 28–32]. In the presence of finite bias and finite Coulomb interaction, intriguing phenomena were found in the electronic transport, such as negative differential conductance and a power-law suppression of the particle current at large voltages [13, 28, 31, 32]. These power-law behaviors are characterized by exponents that depend directly on the interaction strength [28, 30, 32, 33], and the effective hopping from the leads onto the impurity site was identified as the new effective energy scale [13, 34]. This energy scale will also be discussed in Sect. 12.

Artificial molecules

Quantum dots, with their highly tunable properties, have already been employed as analog simulators for various electronic many-body systems, where the complexity of the system is beyond the scope of current theoretical methods. For instance, they have been used to simulate systems which show indications of Nagaoka ferromagnetism [35], Mott insulator instabilities [36], and the formation of resonating valence bonds [37]. These experiments often utilize quantum dot arrays based on GaAs/AlGaAs substrates. Additionally, quantum dot systems can be used to simulate artificial molecules [17], such as cyclobutadiene molecules consisting of four carbon atoms and which exhibit the Jahn-Teller effect [38]. The same holds for qubits [39]. For example, transmons can be used to simulate molecules in electrical circuit setups. By replacing the geometric conductance in an *LC* oscillator with a Josephson junction, the superconducting part introduces non-linearity into the system, resulting in non-equidistant energy levels, forming an artificial atom.

While simple setups of these quantum dot arrays contain a single quantum dot or a linear chain of quantum dots, realistic molecules have a more intricate internal structure [40]. When the circuit dimensions are comparable to the electronic phase coherence length, quantum interference effects, akin to the Aharonov-Bohm effect [41], become critical [42]. Thus, transport through even single molecules can exhibit interference effects such as Fano anti-resonances in the conductance or the particle current. These have been reported in experimental setups for real molecules [43, 44]. Whether the interferences occur and are constructive or destructive depends strongly on the symmetry of the system. By increasing the spatial complexity of quantum dot systems, e.g. introducing long-range interaction or hoppings, these interference effects can also be simulated and the artificial molecules become more realistic. Also in quantum dot systems, interference in the transmission has already been reported in experimental setups [45, 46] and studied theoretically [47–50]. In Sect. 11, we will pursue the idea of including spatial structure into a quantum dot system to make it a more realistic analog simulator for molecules.

1.2. Coupling matter to quantum light in cavity quantum electrodynamics

The possibility of controlling matter with light sparked new research interest in the condensed matter community in recent years [51–54]. As light is very well controllable in state-of-the-art experimental setups, see e.g. [55] and references therein, it is found to be a very versatile tool to tune the properties of matter. Also in the field of quantum information, light control is seen as a promising pathway for precise qubit manipulation [56]. Previous studies have explored the use of short, intense laser pulses, where the high intensity of the light source results in strong light-matter coupling. A notable example is the induction of superconducting-like states via infrared laser pulses, which occur at relatively high critical temperatures compared to equilibrium expectations [57]. This was for example archieved in cuprates [58] or in molecular compounds [59, 60]. One can find a comprehensive review on matter control through fast laser pulses in e.g. [53].

Effects of the light-electron coupling

Energy deposition from the laser can lead to significant heating effects in the sample [61, 62], which may not only alter the experimental conditions but also potentially damage or destroy the sample. To address the issue of short sample lifetimes, one straightforward approach to mitigate it is the reduction of the light fluence. However, this also reduces the effective light-matter coupling. Another novel approach involves placing the material inside a vacuum or 'dark' cavity to minimize unwanted heating effects. In this setup, light-matter coupling is enhanced through confinement, rather than by using a large number of photons interacting with the electronic system. This allows fewer photons to influence the matter states, thereby minimizing the energy deposited by the light. This field of research is called cavity quantum electrodymanics (cavity QED) and studies the coherent interaction between electronic degrees of freedom in matter or of individual emitters and quantum radiation fields [52, 63]. Multiple effects are even mediated by the fluctuations of the vacuum light field without cavity are long and widely known such as the Lamb shift [64, 65], the Casimir force [66], the Purcell effect [67] or van der Waals force [68]. The inclusion of a cavity can strengthen those effects [54].

As stated above, the main idea of cavity QED is to increase the interaction strength g between atoms and photons by increasing the confinement of the radiation field. Current experimental setups can achieve a broad range of interaction strengths, allowing the field to distinguish between various coupling regimes [52, 63]. Weak coupling is defined by the coupling strength g being smaller than the loss rate of the cavity κ and the emitter γ, $g \ll \kappa, \gamma$. For these couplings, the emission properties of individual atoms are merely renormalized by the cavity, without any coherent effects being present, cf. [52, 69] and references therein, such as observed in the Purcell effect. In this regime, single atoms interact independently with the radiation field and no collective behavior can be observed. In the strong coupling regime, where losses are smaller than the coupling strength, $g \gtrsim \kappa, \gamma$, coherent energy transfer between the light and matter systems can occur before energy is dissipated through other channels. Here, emitter states and the cavity mode hybridize to so-called polaritons [70], which inherit properties of both the light and matter degrees of freedom. This is the regime, of interest to us, as it offers the potential to control the emergent properties of matter through the cavity. Additionally, the strong coupling regime is distinguished from the ultrastrong coupling regime with $g \lesssim \omega_0$, where the strength of the coupling is comparable to the frequency of the photon modes ω_0. Here, counter-rotating terms become relevant and contribute significantly to the dynamics of the system. Thus, the often applied rotating-wave approximation [71] breaks down. Moreover, the photon-electron coupling alters the energy space of both constituents, also affecting the ground state of the coupled systems, which contains photon-electron correlations. Finally, state-of-the-art experimental setups are able to reach the so-called deep-strong regime, where the coupling strength exceeds the photon frequency, $g > \omega_0$, and where coherent coupling is dominant.

First experiments realizing cavity QED placed Rydberg atoms into microwave or optical cavities, see [54] and references therein. Even though the strong coupling regime is hard to achieve experimentally, in recent years, multiple platforms have been developed to do so. These include e.g. microcavities, semiconductor cavities, plasmon polariton coupling, and Fabry-Perot cavities. For a more thorough reading, we refer to [52, 55] and references therein. In these setups, a wide range of matter control was already achieved. It was shown that the presence of these cavities can strongly influence, for example, chemical reactions [54], especially in organic molecules. This field is known as cavity-modified chemistry and is hoped to have a wide range of applications also in the chemical industry. Also, the particle and energy transport across molecules or other electronic systems was found to change in the presence of a cavity [72–75]. For example, the so-called Föster resonance energy transfer describes that in those organic materials, energy transfer occurs due to short-range dipole-dipole interactions. They are largely affected by dissipation and dephasing when considering large distances. Due to the delocalization of the matter states induced by the hybridization of light and matter states, the inclusion of the cavity was found to be able to increase the spatial range of the transport [75]. Another example of matter control through a light cavity is the metal-to-insulator transition observed in a transition metal dichalcogenide placed in a low-energy cavity in Ref. [76]. The authors hypothesize that the transition occurs due to an effective lowering of the free energy of the metallic phase, which they achieved by adjusting the cavity volume. Recent experiments demonstrating light-induced superconducting states via laser driving, as mentioned above, have also inspired the concept of cavity-induced superconductivity. However, for this highly sought-after objective, only theoretical proposals exist at present, see [52] and references therein. For example, Refs. [52, 54] give a more in-depth overview of the effects in cavity QED. In the present thesis, we are mostly interested in the influence of the light degrees of freedom on electronic properties. A special focus will be set on the theoretical study of the electronic transport properties influenced by a cavity, stemming from energy transfer between the two systems. This will be discussed in Sects. 8 and 9.

Modeling the light-matter coupling

Due to the recent experimental advances, the necessity of a comprehensive theoretical description of the light-matter coupling is evident. Some effects mentioned above are well described with the Dicke model [77–79], where isolated atoms are coupled to the radiation field. The model, where only one atom interacts with the radiation field is called the Jaynes-Cummings model [80]. It captures the hybridization of the two constituents, leading to the so-called polaronic states differing in energy by the Rabi-splitting $\Omega_\mathrm{R} = \sqrt{4g^2 - (\kappa - \gamma)^2}$ [54]. Dicke also discovered that when an excited atom is placed near another atom, the relaxation process occurs much more rapidly due to their mutual interaction with the surrounding radiation field. Considering many emitters, this enhancement of radiation is called superradiance [77].

On the other hand, when considering a condensed matter lattice inside of a cavity instead of individual atoms, the coupling is often described by an extension of the Bloch theorem which is called Peierls substitution. It modifies the lattice hopping by entering a phase factor, which depends on the vector potential ($\vec{A}$) [81–83].

This description has been the subject of much discussion in recent years [83–86]. In the strong coupling regime, photonic and atomic states build a strongly hybridized state that exhibits light as well as matter characteristics. Because this is a highly quantum mechanical process, we need to describe matter and light quantum mechanically. The Peierls substitution has originally been derived for classical light but can be extended to a quantum mechanical description by quantizing the transverse vector potential in the Coulomb gauge. This leads to a phase of the form $e^{\mathrm{i}\, g(a+a^\dagger)}$, where the coupling g depends on the vector potential $\vec{A}$. Here, a and $a^\dagger$ represent the annihilation and creation operators for photons in a single cavity mode. When assuming a weak vector potential, and therefore a small coupling, an intuitive ansatz is the expansion of the exponential function in the Peierls substitution to low orders of g. However, it has been shown that the expansion can lead to unphysical behavior. Neglecting orders of g^2, for example, leads to the wrong predictions of a superradiance phase [84, 87], similar to the Dicke model in equilibrium for individual atoms. In this model also higher-order effects in the vector potential are neglected and a false superradiant phase is obtained [77–79, 88, 89]. The truncation of the expansion was also shown to break gauge invariance, which leads not only to unphysical behavior but also to the question, of which gauge is best to work in. On a similar footing, it was also found, that the few band approximation for the lattice provides different results in different gauges. The number of bands that are necessary to consider depends on the choice of the gauge [83].

This motivates the necessity to further work on the theoretical description of cavity QED. In the present thesis, we aim to contribute to extending the theory, especially focusing on a light field coupling only on a finite part of the lattice. Further, we will discuss how the second-order in the vector potential can be included consistently in the perturbative treatment of such a system. These discussions can be found in Sect. 7.

The coupling to a light cavity will be discussed in Part III.

1.3. Coupling matter to vibrations and circuit quantum electrodynamics

When studying transport through molecules or extended systems rather than quantum dots, vibrational effects can significantly influence the physics of the system. In these cases, the vibrational mode is displaced when the molecule or quantum dot is charged, leading to phonon-matter coupling. The phonon mode represents the dominant vibrational mode of the electronic system [15, 90–92]. These vibrations can lead to both decreases and increases in current, along with changes in conductance due to the vibrational degrees of freedom.

Effects of the vibrations

Experimentally, [93] showed that a C_{60} transistor coupled to gold leads exhibits features in the electronic transport that are consistent with the vibrations of the center of mass of the C_{60} molecule. This includes conductance side bands and step-like features in the current. Similarly, coupling to vibrational modes has been observed in suspended nanotubes [21, 22] or other nanoscale systems, see [42, 94] and references therein. Another prominent effect observed in these systems is the Franck-Condon blockade, which was experimentally found in e.g. suspended nanotubes in [21, 22]. This blockade manifests as a suppression of current at low bias voltages. For the bosonic system, the coupling to a quantum dot system in non-equilibrium can lead to driving or damping effects [20], and in some cases, even vibrational instabilities [42, 95].

A simple theoretical model used to study the effects of vibrational excitations is the spinless Anderson-Holstein model (SAHM). It is an impurity model consisting of one central quantum dot coupled to two non-interacting leads and, further, a single-mode harmonic oscillator. In this system, the effective hopping onto the impurity becomes a significant low-energy scale [34, 96, 97]. We will also broach the issue of the effective energy scale arising due to the phonon-coupling in Sect. 12. The SAHM has been explored both in and out of equilibrium. For example, in nonequilibrium systems, the Franck-Condon blockade was analyzed theoretically [90, 96, 98]. Further, sidebands in the spectral function for the SAHM were shown to result in resonance peaks in conductance and shoulder-like features in the current [99–101]. Other theoretical work in Ref. [87] explored single- and multi-atom systems coupled to vibrational modes using first-order perturbation theory. They found that vibrational instabilities occur when the imaginary part of the bosonic self-energy becomes negative, signaling a breakdown of perturbation theory.

Artificial Molecules with vibrational degrees of freedom in circuit quantum electrodynamics

Returning to the concept of using quantum dot systems as artificial molecules, these simulators should also be capable of representing the vibrational modes of the nuclear degrees of freedom found in real molecules. One prominent platform that combines electronic systems at the nanoscale with resonators is circuit quantum electrodynamics (circuit QED) [39], where both systems couple capacitively [102]. The coupling was shown experimentally in e.g. Ref. [103]. As an example, nonlinear superconducting circuits can act as artificial atoms in such setups [39]. Examples of resonators in this context include microwave photons in open 3D cavities, discrete LC oscillators, large Josephson junctions, or 2D planar structures, where confinement leads to the discretization of the electromagnetic field [104]. A notable example is the coplanar waveguide resonator, as demonstrated in [105], where the amplitude of the mode scales with $1/\sqrt{d}$, with d being the length of the waveguide. The above-discussed transmon artificial atoms can be capacitively coupled to those microwave resonators. If we downscale all energy scales of the circuit QED system by a factor of 10^4, this system's energy scales become comparable to the ones of molecules at room temperature [18, 22, 106–108]. Because the physics of the system only depends on the ratio of the energy scales, this system provides a feasible platform to simulate molecules.

One goal of the present thesis is to extend the study of the transport properties of the electronic system and the influence of the vibrational degrees of freedom on them. These effects are strongly characterized by the energy transfer between the two systems, which we will analyze in depth in Sect. 11. Additionally, we aim to bring out a clear set of predictors and distinct points, which could be recognized in experiments to checkmark analog simulators.

Since nonlinear superconducting circuits can also function as qubits, these platforms are of significant interest in quantum information processing as well. Coupling to the resonator can be used to control the qubits. An overcoupled resonator, where losses due to input and output ports are smaller than internal losses (quality factors $Q_{\text{ext}} \ll Q_{\text{int}}$), can be utilized for fast qubit measurements [39]. Conversely, undercoupled resonators ($Q_{\text{ext}} \gg Q_{\text{int}}$) are more suitable for quantum memory applications.

The coupling to a vibrational mode will be discussed in Part IV.

2. Model

In the present thesis, we aim to study electric and energy transport through a fermionic low-dimensional system of quantum dots in the steady-state limit and in the linear-response regime as well as for finite bias applied across the system. In particular, we are interested in how the transport properties change when the fermionic system is coupled to a bosonic degree of freedom, approximated by a single-mode harmonic oscillator. In the following studies, these degrees of freedom will often model a resonator. That is why, we will use the expressions resonator and bosonic degree of freedom interchangeably. The general setup is described in the following chapter and is illustrated in Fig. 2.1. The full Hamiltonian consists of a fermionic part (f), a bosonic part (b), and a coupling between the two (fb) and is described by the Hamiltonian

$$H = H_\mathrm{f} + H_\mathrm{b} + H_\mathrm{fb}. \tag{2.1}$$

In the present thesis, we will use units where the elementary charge $|e|$, Planck's constant $\hbar$, the Boltzmann constant k_B and the speed of light c are set to one, $-e = \hbar = k_\mathrm{B} = c = 1$.

2.1. Fermionic system

First, let us consider the fermionic system, in which the electrons are assumed to be spin-polarized. It consists of four different parts and is described by the Hamiltonian

$$H_\mathrm{f} = H_\mathrm{1D} + H_\mathrm{res} + H_\mathrm{coup,res} + H_U. \tag{2.2}$$

The central region of the fermionic system consists of M single-level quantum dots on a linear chain and is modeled by

$$H_\mathrm{1D} = \sum_{j=1}^{M} \varepsilon_j c_j^\dagger c_j + \sum_{i\neq j=1}^{M} \left[t_{ij} c_i^\dagger c_j + \mathrm{h.c.} \right]. \tag{2.3}$$

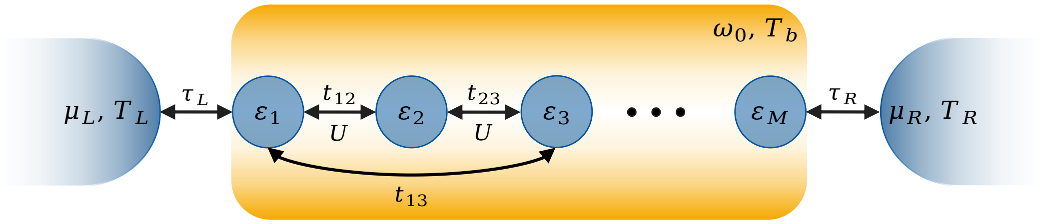

Figure 2.1.: Sketch of the general model. M quantum dots with on-site energies ε_i and connected by hopping amplitudes t_{ij}, $i, j = 1, 2, .., M$, are coupled to two conducting, non-interacting leads via the hopping parameters $\tau_{L/R}$. The hoppings t_{12}, t_{23}, and t_{13} are provided as examples. The leads are characterized by their chemical potential $\mu_{L/R}$ and temperature $T_{L/R}$. The central M quantum dots, which will be referred to as the impurity or the quantum dot region, are coupled to a bosonic reservoir with a single-mode frequency ω_0 at temperature T_b. The nature of this coupling is further detailed in the main text. Additionally, a nearest-neighbor Coulomb interaction U is considered between the quantum dots.

Here, $c_j^\dagger$ and c_j are fermionic operators that create or annihilate a particle on the j^{th} quantum dot. The quantum dots are assumed to contain only one state with an on-site energy ε_j. The hopping between the dots, t_{ij}, is generally assumed to be of nearest-neighbor type: $t_{ij} = t(\delta_{i,j+1} + \delta_{i,j-1})$. If a different hopping configuration is considered, it will be explicitly stated. In general, Equ. (2.3) also describes a 1D tight-binding chain [109, 110], where each quantum dot represents a lattice site in a solid when considering only one orbital per site. The part of the system described by H_{1D} will be referred to as the impurity or quantum dot region in the following.

Two non-interacting leads are coupled to the outer sites of the quantum dot region, allowing a bias voltage or a temperature gradient to be applied across the quantum dot system. Thus, the impurity can be studied under both equilibrium and non-equilibrium conditions. The leads are generally described by the diagonalized Hamiltonian

$$H_{\text{res}} = \sum_{l=L,R} \sum_{k_l} \varepsilon_{k_l} c_{k_l}^\dagger c_{k_l}, \tag{2.4}$$

where $c_{k_l}^\dagger$ and c_{k_l} create or annihilate fermions in the left ($l = L$) or right ($l = R$) lead in the state with energy ε_{k_l}.

The leads are coupled to the left and right outermost sites of the impurity via

$$H_{\text{coup,res}} = \sum_{k_L,k_R} \left[\frac{\tau_L}{\sqrt{N}} c_1^\dagger c_{k_L} + \frac{\tau_R}{\sqrt{N}} c_M^\dagger c_{k_R} + \text{h.c.} \right]. \tag{2.5}$$

The coupling to the leads is given by τ_l, where $l \in \{L, R\}$, and it scales with the size of the reservoirs N, which is the total number of states in the reservoir. When modeling the leads by tight-binding chains, N is the number of lattice sites.

Finally, for the spinless fermions, we include a nearest-neighbor Coulomb interaction in the impurity region

$$H_U = U \sum_{j=1}^{M-1} c_j^\dagger c_j c_{j+1}^\dagger c_{j+1}. \tag{2.6}$$

This interaction will be included in some of the analyses and serves as a competing effect to the bosonic coupling, which will be introduced below.

2.1.1. Particle-hole symmetry

As the name suggests, particle hole symmetry (PHS) is the invariance of the Hamiltonian under the exchange of particles with holes and vice versa. Accordingly, the particle-hole symmetric point is the point in parameter space, where the Hamiltonian is particle-hole symmetric. For our model, the point is defined by the on-site energies ε_j. The transformation is defined by the unitary operator K, which transforms the creation operator as $Kc_j^\dagger = \tilde{c}_j$. Assuming the transformation leaves the Hamiltonian invariant at on-site energies $\vec{\varepsilon}_{\text{PHS}} := \left(\varepsilon_{1,\text{PHS}}, \varepsilon_{2,\text{PHS}}, ..., \varepsilon_{M,\text{PHS}}\right)$, i.e., $H(\vec{\varepsilon}_{\text{PHS}}) = \tilde{H}(\vec{\varepsilon}_{\text{PHS}})$, the expectation value of the occupation operator transforms as

$$\begin{aligned} N(\vec{\varepsilon}_{\text{PHS}}) &= \sum_j \left\langle c_j^\dagger c_j \right\rangle_{H(\vec{\varepsilon}_{\text{PHS}})} = \sum_j \left(1 - \left\langle \tilde{c}_j^\dagger \tilde{c}_j \right\rangle_{H(\vec{\varepsilon}_{\text{PHS}})} \right) = \sum_j \left(1 - \left\langle \tilde{c}_j^\dagger \tilde{c}_j \right\rangle_{\tilde{H}(\vec{\varepsilon}_{\text{PHS}})} \right) = \sum_j \left(1 - \tilde{n}(\vec{\varepsilon}_{\text{PHS}})\right) \\ &= M - \sum_j n(\vec{\varepsilon}_{\text{PHS}}) = M - N(\vec{\varepsilon}_{\text{PHS}}). \end{aligned} \tag{2.7}$$

This shows that the mean number of particles equals the mean number of holes.

To study PHS for the impurity with Coulomb interaction, $H_{1\mathrm{D}} + H_U$, the lattice is divided into two sublattices, A and B, such that neighboring sites belong to different sublattices. The transformation is then chosen as follows [111]:

$$c_j \to \tilde{c}_j = \begin{cases} -c_j^\dagger & \text{for } j \in \mathrm{A} \\ c_j^\dagger & \text{for } j \in \mathrm{B}. \end{cases} \tag{2.8}$$

The Hamiltonian reads

$$\tilde{H}_{1\mathrm{D}} + \tilde{H}_U = -\sum_{j=1}^{M} \varepsilon_j c_j^\dagger c_j - U \sum_{j=1}^{M-1} \left[c_j^\dagger c_j + c_{j+1}^\dagger c_{j+1} \right] + t \sum_{j=1}^{M-1} \left[c_j^\dagger c_{j+1} + c_{j+1}^\dagger c_j \right] + U \sum_{j=1}^{M-1} c_j^\dagger c_j c_{j+1}^\dagger c_{j+1}, \tag{2.9}$$

where we have neglected all emerging constant terms. Therefore, the Hamiltonian is particle-hole symmetric at the on-site energies $\vec{\varepsilon}_{\mathrm{PHS}} = (-U/2, -U, \dots, -U/2)$. By redefining the on-site energy space $(\varepsilon_1, \varepsilon_2, \dots, \varepsilon_M) \to (\varepsilon_1 + U/2, \varepsilon_2 + U, \dots, \varepsilon_M + U/2)$, we can shift this point to $\vec{\varepsilon}_{\mathrm{PHS}} = (0, 0, \dots, 0)$. This is equivalent to redefining the Coulomb part of the Hamiltonian by

$$H_U = U \sum_{j=1}^{M-1} \left(c_j^\dagger c_j - \frac{1}{2} \right) \left(c_{j+1}^\dagger c_{j+1} - \frac{1}{2} \right). \tag{2.10}$$

We further assume that the leads are particle-hole symmetric, such that for every k_l there exists a k_l' with $\varepsilon_{k_l'} = -\varepsilon_{k_l}$. With the additional transformation $c_{k_l} \to \tilde{c}_{k_l} = -c_{k_l'}^\dagger$, the lead contribution Equ. (2.4) of the Hamiltonian remains invariant, making the entire fermionic Hamiltonian H_{f} particle-hole symmetric at $\vec{\varepsilon}_{\mathrm{PHS}} = (0, 0, \dots, 0)$.

2.1.2. Tight-binding Hamiltonian

As described above, the quantum dot region is modeled by a tight-binding Hamiltonian, so it is worth recapping some basic properties of this model. The tight-binding approximation assumes that the electrons are strongly localized around the lattice sites, allowing the wave function to be expanded in localized orbitals. In theoretical studies, it is often elaborate or impossible to deal with all electronic states. Therefore, the fermionic Hilbert space is truncated by considering only a few orbitals per site, mostly those close to the Fermi surface, and projecting the Hamiltonian onto these. For this approximation to hold, the energy states under consideration must be well separated from the neglected ones. In the case of the Hamiltonian Equ. (2.3), we consider one orbital per site. We will briefly discuss later in Sect. 7.4 how incautious truncation can lead to unphysical behavior.

First, we discuss the tight-binding formulation in a three-dimensional solid. A more thorough introduction can be found in e.g. [109, 110]. The single-particle Hamiltonian describing a fermion with momentum $\vec{p}$ and mass m in a periodic lattice potential $V(\vec{r})$, reads

$$H = \frac{\vec{p}^2}{2m} + V(\vec{r}). \tag{2.11}$$

Here, $\vec{p}$ and $\vec{r}$ are the canonical momentum and position operators. When assuming that the fermions are mostly localized around the lattice sites, the wave functions Ψ, solving the Schrödinger equation, can be expanded in the Wannier basis $\{a_m(\vec{r})\} = \{a(\vec{r} - \vec{R}_m)\}$, with $a(\vec{r})$ being a function localized around $\vec{r} = 0$. The basis describes localized orbitals around the lattice sites $\vec{R}_m$. Here, we only take into account one orbital per lattice site, which is called the one-orbital approximation. This is a valid assumption when the inter-orbital contributions can be neglected and only one set of orbitals is energetically close to the Fermi surface The wave function expressed in the Wannier basis reads

$$\Psi(\vec{r}) = \sum_m \psi_m a_m(\vec{r}). \tag{2.12}$$

The on-site energies and hopping parameters are given by the diagonal and off-diagonal matrix elements of the Hamiltonian respectively

$$\varepsilon_{mm} = -\int \mathrm{d}\vec{r}\, a_m^*(\vec{r}) H a_m(\vec{r}), \qquad t_{mm'} = -\int \mathrm{d}\vec{r}\, a_m^*(\vec{r}) H a_{m'}(\vec{r}) \text{ , for } m \neq m'. \tag{2.13}$$

When the M lattice sites are connected in a linear chain oriented in x-direction, without loss of generality, the y and z direction can be integrated out leading to an effective x-integral in Equ. (2.13). This defines the energies ε_j and hopping parameters t_{ij} for lattice sites at R_i and R_j and results in the tight-binding Hamiltonian H_{1D} in Equ. (2.3).

Neglecting the fermionic reservoirs initially, the impurity H_{1D} is modeled as an open tight-binding chain. For a homogeneous system where $\varepsilon_j = \varepsilon$ for all sites $j \in [1, M]$, the Hamiltonian is known to have eigenenergies (see, e.g., [112])

$$\varepsilon_{k_n} = \varepsilon + 2t\cos(k_n), \qquad \text{with } k_n = \frac{\pi}{M+1}n,\ n \in \{1, 2, \ldots, M\} \tag{2.14}$$

and eigenfunctions

$$\langle j|\psi_{k_n}\rangle = \sqrt{\frac{2}{M+1}}\sin(k_n j). \tag{2.15}$$

Furthermore, we will also consider the reservoirs to be modeled by half-infinite tight-binding chains in the so-called wide-band limit, which will be discussed in Sect. 3.3.1.

2.2. Bosonic system

The fermionic system with the presented structure has been studied under a multitude of aspects, such as e.g. studying transport properties, including interactions, adaptable chain lengths, or disorder in spatial expansion of the orbitals, see [13, 97, 113–116] and many more. In the present thesis, we couple the fermions in the impurity to a single-mode resonator of two different kinds. The bosonic model is described by the free harmonic oscillator

$$H_{\mathrm{b}} = \omega_0 a^\dagger a, \tag{2.16}$$

with the bosonic creation and annihilation operators $a^\dagger$ and a, and the mode frequency ω_0.

Additionally, we consider dissipative processes by coupling the resonator to a bosonic bath consisting of auxiliary harmonic oscillators

$$H_{\mathrm{bath}} = \sum_\alpha \omega_\alpha a_\alpha^\dagger a_\alpha + \sum_\alpha g_\alpha \left(a^\dagger a_\alpha + a_\alpha^\dagger a\right). \tag{2.17}$$

Bosons in the mode with frequency ω_α are generated or annihilated by $a_\alpha^\dagger$ and a_α, respectively, and are coupled to the resonator by individual coupling strengths g_α. The bosonic baths are then integrated out, leading to the hybridization κ. This is analog to the integrating out of the fermionic leads, which will be discussed in Sect. 3.3.1. At this point, it is only important to know that κ measures the bosonic dissipation from the resonator into the bosonic bath. Note that the physical coupling of the bosonic bath to the resonator is rather described by a coupling of the form $\sim \left(a + a^{\dagger}\right)\left(a_s + a_s^{\dagger}\right)$ [117]. For the small κ-limit, where the dissipation is smaller than any other energy scale in the system and which we will consider in the following, how exactly the bosonic bath is coupled to the resonator has a negligible effect on the fermionic degrees of freedom. We therefore choose a coupling, which is of a similar form to the coupling of the quantum dot system to the fermionic reservoirs in Equ. (2.5) and do not discuss this topic further.

The resonator can be coupled to the fermionic system in different ways. As described in the introduction, Sect. 1, the present thesis focuses on coupling the quantum dot region to a bosonic resonator in two different ways: (i) via Peierls substitution and (ii) capacitively to the local fermionic occupation. Under certain approximations, these couplings can be treated mathematically on the same footing and show certain similarities, but they can also exhibit physically very distinct behavior.

2.2.1. Peierls coupling

It has been shown that the coupling of light and matter can be described by the so-called Peierls substitution in the tight-binding formulation; see, e.g., [81, 83, 85]. We will take a closer look at the derivation of the substitution in Sect. 7.1.1. In general, the coupling to a light cavity is included by the renormalization of the hopping in Equ. (2.3)

$$H_{\mathrm{f}} \to \sum_j \varepsilon_j c_j^{\dagger} c_j + t \sum_{j=1}^{M-1} \left[e^{\mathrm{i}\, g_{j(j+1)}\left(a+a^{\dagger}\right)} c_{j+1}^{\dagger} c_j + \mathrm{h.c.} \right], \tag{2.18}$$

with the coupling strength $g_{j(j+1)} = g_{(j+1)j}$. We call the exponential function containing the coupling, the Peierls factor in the present thesis. By expanding the phase for small coupling to first order in g, we obtain

$$H_{\mathrm{f}} + H_{\mathrm{fb}} := \sum_j \varepsilon_j c_j^{\dagger} c_j + t \sum_{j=1}^{M-1} \left[\left(1 + \mathrm{i}\, g_{j(j+1)} \left(a + a^{\dagger}\right)\right) c_{j+1}^{\dagger} c_j + \mathrm{h.c.} \right] + \mathcal{O}(g^2). \tag{2.19}$$

The first term of the expansion provides the initial hopping of the tight-binding chain in Equ. (2.3). The implications of this expansion will be further discussed in Sect. 7.3.

2.2.2. Capacitive coupling

When placing a quantum dot close to a superconducting transmission line, the fermionic charge couples capacitively to the excitons of the transmission line [39]. A transmission line is defined by its length l and capacitance per unit length c_0, which is assumed to be constant here. The allowed resonator frequencies are given by $\omega_n = \frac{(n+1)\pi}{l c_0 Z_0}$, with characteristic impedance Z_0. The resonator can be modeled by the harmonic oscillator in Equ. (2.16). In the present thesis, we will assume that only one mode, with frequency ω_0, couples to the fermionic degrees of freedom, and neglect the remaining modes. The capacitive coupling is then given by the electrostatic potential energy $H_{\mathrm{fb}} = V \sum_j n_j \alpha_j$ [102]. Here, V is the homogeneous electrostatic potential, n_j the occupation of site j, and $\alpha_j = \frac{C_{\mathrm{t}}^j}{C_{\mathrm{t}}^j + C_{\mathrm{g}}^j}$ is given by C_{t}^j, the capacitance between site j and the transmission line, and C_{g}^j, the capacitance between site j and the ground. By quantizing the system, $V = \sqrt{\frac{\omega_0}{l c_0}} \left(a^{\dagger} + a\right)$ and $n_j = c_j^{\dagger} c_j$, the coupling of M quantum dots with one resonator mode ω_0 is described by

$$H_{\mathrm{fb}} = \sum_j \lambda_j c_j^\dagger c_j \left(a + a^\dagger\right), \tag{2.20}$$

with $\lambda_j = \alpha_j \sqrt{\frac{\omega_0}{l c_0}}$.

2.2.3. Generalized coupling

Both couplings we are interested in are of the generalized form

$$H_{\mathrm{fb}} = a^\dagger \sum_{i,j=1}^{M} A_{ij} c_i^\dagger c_j + \text{h.c.}, \tag{2.21}$$

where $A_{ij} \in \mathbb{C}$ gives the structure of the respective coupling. For the Peierls coupling Equ. (2.19), we find $A_{ij} = \mathrm{i}\, gt \left(\delta_{i,j+1} - \delta_{i,j-1}\right)$ when neglecting contributions of $\mathcal{O}(g^2)$, and for the capacitive coupling Equ. (2.20) $A_{ij} = \lambda_j \delta_{i,j}$.

Part II.

Methods, Formalisms and Implementations

In this part, we present the theoretical methods and formalisms employed throughout this thesis. In Chapter 3, we introduce the Green function formalism. This includes the Matsubara formulation for studying equilibrium systems, as well as the Green functions on the Keldysh contour, used to address non-equilibrium problems. Subsequently, we demonstrate how Green functions can be utilized to approximate two-particle interactions in the study of many-body systems. We introduce first-order perturbation theory in Chapter 4 and functional renormalization group theory (FRG) with a first-order truncation in Chapter 5. Furthermore, we illustrate how these methods can be applied to the specific system considered in this thesis. Finally, we introduce two complementary methods in Chapter 6: exact diagonalization and the Lindblad master equation.

3. Green Functions

In this chapter, we explore the Green function formalism, a fundamental tool in many-particle physics for analyzing a variety of systems. Green functions allow us to calculate numerous physical quantities and serve as the foundational elements of diagrammatic techniques such as perturbation theory or the functional renormalization theory group method, which are used in the present thesis. We will provide only a brief overview of the Green function formalism, which is based on my master's thesis [118]. The interested reader is referred to a wide range of literature, such as [119], focusing on the equilibrium setup, [120], discussing the Kelysh formalism, and [121–123], giving a broader overview of non-equilibrium many-body physics.

As a starting point, we consider a general time-independent Hamiltonian with a two-particle interaction

$$H = H_0 + V = \sum_{v,v'} \varepsilon_{v'v} c^\dagger_{v'} c_v + \frac{1}{4} \sum_{v_1',v_2',v_1,v_2} \bar{v}_{v_1'v_2'|v_1v_2} c^\dagger_{v_1'} c^\dagger_{v_2'} c_{v_2} c_{v_1}. \tag{3.1}$$

In this chapter, $c^\dagger_v$ and c_v are general creation and annihilation operators of particles with a set of arbitrary quantum numbers v, which fulfill the standard (anti-)commutation relations

$$\left[c_v, c^\dagger_{v'}\right]_{-\zeta} = \delta_{v,v'}, \qquad \left[c_v, c_{v'}\right]_{-\zeta} = \left[c^\dagger_v, c^\dagger_{v'}\right]_{-\zeta} = 0, \tag{3.2}$$

where $\zeta = 1$ for bosons and $\zeta = -1$ for fermions. The corresponding one-particle and two-particle matrix elements are given by $\varepsilon_{v'v}$ and $\bar{v}_{v_1'v_2'v_1v_2}$, where the latter is symmetrized in the case of bosons and anti-symmetrized in the case of fermions. We are generally interested in studying correlation functions and expectation values of observables for times $t > t_0$. Here, t_0 defines the time when the system is assumed to be prepared in an equilibrium system without any interactions and can therefore be described by an uncorrelated density operator [124]. Then, the interactions are adiabatically switched on and we study the system at times $t > t_0$, when the interaction has reached its full strength [122].

The time-dependent n-particle Green function is then defined as

$$G_n(x_1, \dots, x_n | x_1', \dots, x_n') = (-\mathrm{i})^n \left\langle \mathcal{T} c_{v_1}(t_1) \dots c_{v_n}(t_n) c_{v_n'}{}^\dagger(t_n') \dots c_{v_1'}{}^\dagger(t_1') \right\rangle, \tag{3.3}$$

with the multi-indices x_i, x_i' containing time (or later frequency), and all quantum numbers v. Here, $\langle \cdot \rangle$ denotes the average with respect to the density matrix ρ. The time-ordering operator $\mathcal{T}$ orders the operators chronologically with time, so that the latest time is on the left and the earliest on the right. Analogously, the anti-time-ordering operator $\bar{\mathcal{T}}$ orders the operators the other way around. The annihilation and creation operators are in the Heisenberg picture:

$$c^{(\dagger)}(t) = U(t_0, t) c^{(\dagger)} U(t, t_0), \tag{3.4}$$

with respect to the time-evolution operator

$$U(t, t') = \mathcal{T} e^{\mathrm{i} \int_{t'}^{t} \mathrm{d}\tilde{t}\, H} = e^{-\mathrm{i}\, H(t-t')}, \tag{3.5}$$

where we used that the Hamiltonian is time-independent in the last equality. Later, we will also require the interaction picture, which is given by the time-evolution operator with respect to the free Hamiltonian $U_0(t,t') = e^{-\mathrm{i}\,H_0(t-t')}$, and given as

$$c_{\mathrm{I}}^{(\dagger)}(t) = U_0(t_0,t)c^{(\dagger)}U_0(t,t_0). \tag{3.6}$$

In the following, we will utilize the single-particle Green function $n = 1$, thus, we will concentrate on this case. To obtain the expectation value of observables, it is useful to define the greater, lesser, causal, and anti-causal Green functions, depending on the ordering of the operators in time:

$$\begin{aligned} G^{>}(x|x') &= -\mathrm{i}\left\langle c_v(t)c_{v'}^{\dagger}(t')\right\rangle & G^{<}(x|x') &= -\mathrm{i}\,\zeta\left\langle c_{v'}^{\dagger}(t')c_v(t)\right\rangle \\ G^{c}(x|x') &= -\mathrm{i}\left\langle \mathcal{T}c_v(t)c_{v'}^{\dagger}(t')\right\rangle & G^{\bar{c}}(x|x') &= -\mathrm{i}\left\langle \bar{\mathcal{T}}c_v(t)c_{v'}^{\dagger}(t')\right\rangle . \end{aligned} \tag{3.7}$$

These Green functions are not independent of each other in all cases and not all have a direct physical meaning, but we will revisit this point later in this chapter.

The present thesis focuses on the steady-state limit for $t, t' \gg t_0$, after a sufficiently long time has passed since the interaction of the system was switched on, where the system relaxes to a stationary state. In this case, the system is time-translation invariant, and the Green function obeys $G^a_{v|v'}(t_1|t_1') = G^a_{v|v'}(t_1 - t_1' = t|0)$, for $a \in \{>, <, c, \bar{c}\}$. Given this assumption, working in frequency space is beneficial:

$$G^a_{v|v'}(\omega) = G^a_{v|v'}(\omega|t' = 0) = \lim_{\eta\to 0^+}\frac{1}{2\pi}\int_{-\infty}^{\infty}\mathrm{d}\,t e^{-\eta|t|}e^{\mathrm{i}\,\omega t}G^a_{v|v'}(t), \tag{3.8}$$

where the convergence factor η was introduced. In the steady-state limit, also the assumption of the initial density at $t > t_0$ to be uncorrelated can be softened. One can show that initial correlations decay exponentially with time and thus, the system becomes independent from initial correlations after enough time has passed [124, 125].

3.1. Equilibrium - the Matsubara formalism

In equilibrium, the ensemble average is taken with respect to the grand canonical density operator

$$\rho_{\mathrm{E}} = \frac{e^{-\beta(H-\mu N)}}{\mathrm{Tr}\, e^{-\beta(H-\mu N)}}, \tag{3.9}$$

with the inverse temperature $\beta = 1/T$, the chemical potential μ and the particle number operator $N = \sum_v c_v^{\dagger} c_v$. So, the density operator and the time evolution operator Equ. (3.5) can be treated on the same footing, when introducing the imaginary time $t \to \mathrm{i}\,\tau$, where the Heisenberg picture is simply given by $c^{(\dagger)}(\tau) = e^{(H-\mu N)(\tau-\tau_0)}c^{(\dagger)}e^{-(H-\mu N)(\tau-\tau_0)}$

We introduce an abbreviated form, to write the single-particle Green function in the form

$$G_{vv'}(\tau) := G_{1,v_1|v_1'}(\tau_1|\tau_1') = -\left\langle \mathcal{T}_\tau c_v[\tau_1 - \tau_1']c_{v'}^{\dagger}\right\rangle_{\mathrm{E}} . \tag{3.10}$$

$\mathcal{T}_\tau$ is the imaginary time order operator and orders the imaginary time in the same way as the time ordering operator orders in real time. The ensemble average $\langle\cdot\rangle_{\mathrm{E}}$ is taken with respect to the equilibrium density Equ. (3.9). The equal time Green function can be chosen as $G_{vv'}(0) := -\lim_{\eta\to 0^+}\langle \mathcal{T}_\tau c_v[-\eta]c_{v'}^{\dagger}\rangle_{\mathrm{E}}$. In equilibrium, $[H, \rho_{\mathrm{E}}] = 0$ holds, so that the Green function is time-translational invariant and only depends on $\tau = \tau_1 - \tau_1'$. This can be seen when additionally using the invariance under cyclic permutation of the trace in Equ. (3.10). Furthermore, this leads to a β-(anti)periodicity in the single-particle Green function

$$G_{\nu\nu'}(\tau + \beta) = \zeta G_{\nu\nu'}(\tau). \tag{3.11}$$

Thus, one can define the discrete Fourier series

$$G_{\nu\nu'}(\tau) = \frac{1}{\beta} \sum_{n=-\infty}^{\infty} e^{-\mathrm{i}\,\omega_n \tau} G_{\nu\nu'}(\mathrm{i}\,\omega_n), \qquad G_{\nu\nu'}(\mathrm{i}\,\omega_n) = \int_0^\beta \mathrm{d}\,\tau e^{\mathrm{i}\,\omega_n \tau} G_{\nu\nu'}(\tau). \tag{3.12}$$

The so-called Matsubara frequencies are given by

$$\omega_n = \begin{cases} \frac{2n+1}{\beta}\pi & \text{, for fermions} \\ \frac{2n}{\beta}\pi & \text{, for bosons.} \end{cases}, \qquad \text{for } n \in \mathbb{Z}. \tag{3.13}$$

In the present thesis, we will always assume the zero-temperature limit when considering a system in equilibrium, where the Matsubara frequencies become continuous.

3.2. Non-equilibrium - the Keldysh formalism

In the following studies, we are particularly interested in systems that, in addition to experiencing interaction, are also driven out of equilibrium. In our model, this non-equilibrium condition arises from the influence of the leads, as described in Equ. (2.4). Since we are ultimately interested in the steady-state limit as $t_0 \to -\infty$, how exactly the coupling to the lead is introduced is not essential. As the dependence on the initial preparation decays exponentially, it does not influence the system in this limit. After a transient period, the system adjusts to a steady-state current. In the limit of infinitely large leads, this current persists indefinitely, and equilibrium is never achieved [124]. As noted above, the only important assumption is that the initial density operator for $t < t_0$ is uncorrelated.

In a non-equilibrium situation the density operator can no longer be written down directly as in Equ. (3.9) and it is convenient to introduce the so-called Keldysh contour, which distinguishes the evolution forward (f) in time from the one backward (b) in time and will be indicated by the index ν [122, 126, 127]. The expectation value of an arbitrary operator A at time t is given by the general expectation value in equilibrium and the time evolution operator $U_\mathrm{I}(t, t')$ in the interaction picture, cf. Equ. (3.6),

$$\langle A \rangle_{\rho(t)} = \langle A(t) \rangle_\mathrm{E} = \langle U_\mathrm{I}(t_0, t) A_\mathrm{I}(t) U_\mathrm{I}(t, t_0) \rangle_\mathrm{E}\,. \tag{3.14}$$

The time evolution takes a different form depending on whether the evolution is forward or backward in time and is given as

$$U_\mathrm{I}(t, t') = \begin{cases} \mathcal{T} e^{-\mathrm{i} \int_{t'}^{t} \mathrm{d}t'' V_\mathrm{I}(t'')}, & t > t' \\ \bar{\mathcal{T}} e^{-\mathrm{i} \int_{t'}^{t} \mathrm{d}t'' V_\mathrm{I}(t'')}, & t < t', \end{cases} \tag{3.15}$$

for $t > t_0$. Considering this now on the described forward-backward contour, the average can be written as

$$\langle A \rangle_{\rho(t)} = \left\langle \mathcal{T}_c e^{-\mathrm{i} \int_{t_0}^{\infty} \mathrm{d}t' \left(V_\mathrm{I}^f(t') - V_\mathrm{I}^b(t') \right)} A_\mathrm{I}^f(t) \right\rangle_\mathrm{E}, \tag{3.16}$$

where the combined contour-ordering operator $\mathcal{T}_c$ orders operators on the forward branch as $\mathcal{T}$ and on the backward branch as $\bar{\mathcal{T}}$, while ordering all b-operators to the left of all f-operators. The contour index can be treated as an additional quantum number so that the annihilation and creation operators obey the (anti-)commutation relations:

$$\left[c_v^{\nu}, c_{v'}^{\nu'\dagger}\right]_{-\zeta} = \delta_{v,v'}\delta_{\nu,\nu'}, \qquad \left[c_v^{\nu}, c_{v'}^{\nu'}\right]_{-\zeta} = \left[c_v^{\nu\dagger}, c_{v'}^{\nu'\dagger}\right]_{-\zeta} = 0. \tag{3.17}$$

Hereafter, the contour index will be included in the multi-index x when considering the Keldysh formalism.

The interaction with respect to the contour index is defined as

$$\bar{v}^{\nu_1',\nu_2'|\nu_1,\nu_2}_{v_1',v_2'|v_1,v_2} = \mathrm{sign}(\nu_1)\bar{v}_{v_1',v_2'|v_1,v_2}\delta_{\nu_1,\nu_1'}\delta_{\nu_1,\nu_2'}\delta_{\nu_1,\nu_2}, \qquad \mathrm{sign}(\nu) = \delta_{\nu f} - \delta_{\nu b}, \tag{3.18}$$

For the single-particle Green function, one distinguishes four cases, which are equivalent to the lesser, greater, chronological, and anti-chronological Green functions introduced in Equ. (3.7),

$$\begin{aligned} G^{f|b}_{v|v'}(t|t') &= G^{<}_{v|v'}(t|t') \\ G^{b|f}_{v|v'}(t|t') &= G^{>}_{v|v'}(t|t') \\ G^{f|f}_{v|v'}(t|t') &= G^{c}_{v|v'}(t|t') = \begin{cases} G^{f|b}_{v|v'}(t|t'), & t \le t' \\ G^{b|f}_{v|v'}(t|t'), & t > t' \end{cases} \\ G^{b|b}_{v|v'}(t|t') &= G^{\bar{c}}_{v|v'}(t|t') = \begin{cases} G^{b|f}_{v|v'}(t|t'), & t < t' \\ G^{f|b}_{v|v'}(t|t'), & t \ge t' \end{cases} \end{aligned} \tag{3.19}$$

As we stated above, these Green functions are not independent. Instead, the causality relation

$$G^{f|f}_{v|v'}(t|t') + G^{b|b}_{v|v'}(t|t') = G^{b|f}_{v|v'}(t|t') + G^{f|b}_{v|v'}(t|t') \tag{3.20}$$

holds for $t \neq t'$. Therefore, a change in basis can be advantageous. Using the rotation matrix

$$R_A = R_A^{-1} = \frac{1}{\sqrt{2}}\begin{pmatrix} 1 & 1 \\ 1 & -1 \end{pmatrix}, \qquad R_B = R_B^{-1,T} = \frac{1}{\sqrt{2}}\begin{pmatrix} 1 & -1 \\ 1 & 1 \end{pmatrix}, \tag{3.21}$$

we change from the contour basis to the Keldysh basis:

$$\begin{pmatrix} G^{\mathrm{R}} & G^{\mathrm{K}} + G^{\mathrm{P}} \\ G^{\mathrm{P}} & G^{\mathrm{A}} \end{pmatrix} = R_A \begin{pmatrix} G^{f|f} & G^{f|b} \\ G^{b|f} & G^{b|b} \end{pmatrix} R_B, \tag{3.22}$$

where the matrix notation $[G^{\mathrm{R/A/K/P}}]_{i,j} = G^{\mathrm{R/A/K/P}}_{v_i,v_j}(t_i, t_j)$ was used. Here, the patch component $G^{\mathrm{P}}(t, t')$ vanishes for all $t \neq t'$ and therefore only gives a contribution of measure zero in all diagrams in frequency space and can be neglected in our calculations. The other components are the retarded (R), advanced (A), and Keldysh (K) components, given by

$$G^{\mathrm{R}}_{v|v'}(t|t') = -\mathrm{i}\,\theta(t - t')\left\langle \left[c_v(t), c_{v'}^{\dagger}(t')\right]_{-\zeta} \right\rangle, \tag{3.23}$$

$$G^{\mathrm{A}}_{v|v'}(t|t') = \mathrm{i}\,\theta(t' - t)\left\langle \left[c_v(t), c_{v'}^{\dagger}(t')\right]_{-\zeta} \right\rangle, \tag{3.24}$$

$$G^{\mathrm{K}}_{v|v'}(t|t') = -\mathrm{i}\left\langle \left[c_v(t), c_{v'}^{\dagger}(t')\right]_{\zeta} \right\rangle. \tag{3.25}$$

Here, we see why the retarded Green function is also called the response function: it only depends on positive times.

A two-particle interaction vertex, as a tensor, transforms as

$$\hat{\bar{v}}^{\alpha_1'\alpha_2'|\alpha_1\alpha_2}_{\upsilon_1',\upsilon_2'|\upsilon_1,\upsilon_2}(\omega_1',\omega_2'|\omega_1,\omega_2) = (R_B^{-1})_{\alpha_1'\nu_1'}(R_B^{-1})_{\alpha_2'\nu_2'}\bar{v}^{\nu_1'\nu_2'|\nu_1\nu_2}_{\upsilon_1',\upsilon_2'|\upsilon_1,\upsilon_2}(\omega_1',\omega_2'|\omega_1,\omega_2)(R_A^{-1})_{\nu_2\alpha_2}(R_A^{-1})_{\nu_1\alpha_1}, \tag{3.26}$$

where $\nu = f, b$ are the contour indices and $\alpha = 1, 2$ the Keldysh indices, considering the matrix structure introduced above. In the special case $\bar{v}(x_1', x_2'|x_1, x_2) \sim \delta_{\nu_1'=\nu_2'=\nu_1=\nu_2}\operatorname{sgn}(\nu)$, from Equ. (3.18), this takes the simple form:

$$\hat{\bar{v}}^{\alpha_1'\alpha_2'|\alpha_1\alpha_2}_{\upsilon_1',\upsilon_2'|\upsilon_1,\upsilon_2}(\omega_1',\omega_2'|\omega_1,\omega_2) = \begin{cases} \frac{1}{2}\bar{v}_{\upsilon_1',\upsilon_2'|\upsilon_1,\upsilon_2}\delta(\omega_1'+\omega_2'-\omega_1-\omega_2) & \alpha_1'+\alpha_2'+\alpha_1+\alpha_2 \text{ odd,} \\ 0 & \text{else.} \end{cases} \tag{3.27}$$

Under the steady-state assumption, the system is time-translation invariant, and it is advantageous to work in frequency space:

$$G^x_{\upsilon\upsilon'}(\omega) := G^x_{\upsilon|\upsilon'}(\omega|t=0) = \int_{-\infty}^{\infty} \mathrm{d}t' e^{-\eta|t'|} e^{\mathrm{i}\,\omega t'} G^x_{\upsilon|\upsilon'}(t'|t=0), \qquad x \in \text{R,A,K}. \tag{3.28}$$

Because the rotation and the Fourier transformation are linear operations, the transformation has the same form as Equ. (3.8) with $a \to x$. Only positive times contribute to the integral for the retarded Green function, while only negative times contribute to the advanced one. Therefore, $G^{\mathrm{R}}_{\upsilon\upsilon'}(\omega)$ is analytic in the upper half of the complex plane, and $G^{\mathrm{A}}_{\upsilon\upsilon'}(\omega)$ in the lower half.

In the equilibrium limit, one can show, that also the Green functions in the Keldysh basis are not independent. Instead, they follow the dissipation-fluctuation theorem

$$G^{\mathrm{K}}_{\upsilon|\upsilon'}(\omega) = \left[1 - 2n_\zeta(\omega)\right]\left[G^{\mathrm{R}}_{\upsilon|\upsilon'}(\omega) - G^{\mathrm{A}}_{\upsilon|\upsilon'}(\omega)\right], \tag{3.29}$$

with the Fermi-Dirac $n_-(\omega) = f(\omega)$ and Bose-Einstein $n_+(\omega) = b(\omega)$ distribution

$$n_\zeta(\omega) = \frac{1}{e^{\beta(\omega-\mu)} - \zeta}. \tag{3.30}$$

Further, one can show that by analytic continuation of the Matsubara Green function in energy space onto the real axis, one recovers the retarded and advanced Green function, see e.g. [119],

$$G^{\mathrm{R/A}}_{\upsilon\upsilon'}(\omega) = G_{\upsilon\upsilon'}(i\omega_n \to \omega \pm \mathrm{i}\,\eta) \tag{3.31}$$

for $\eta \to 0^+$. The Keldysh component is then obtained via Equ. (3.29). In practice, the Matsubara Green function is mostly obtained numerically, as we will see in the following studies. Thus, the analytic continuation has to be conducted numerically as well, which is a highly non-trivial task [127]. In the present thesis, we are able to calculate all observables of interest to us directly with the Matsubara Green function and if not, we can directly calculate the Green functions on the Keldysh contour. So we do not have to consider this subject further.

3.3. Dyson equation

Interaction effects inside the impurity region, as well as the influence of the leads, can be included by considering the so-called self-energies. These are given by the one-particle irreducible diagrams. We will not introduce diagrammatics in detail; the reader is therefore referred to, e.g., [119, 128]. When the free propagator $G_0(x|x')$ and the self-energy $\Sigma(x|x')$ are known, the full Green function is given by the self-consistent equation

$$G(x|x') = G_0(x|x') + \sum_{x_1 x_1'} G_0(x|x_1')\Sigma(x_1'|x_1)G(x_1|x'), \tag{3.32}$$

where x is again the multi-index, now including all quantum numbers (υ), the time (τ or t) or frequency ($\mathrm{i}\,\omega$ or ω), and the contour index (ν) for the Keldysh formalism. Evaluating this self-consistent equation provides the so-called Dyson equation.

For the Matsubara Green function, it reads

$$G = \left[[G_0]^{-1} - \Sigma\right]^{-1}, \tag{3.33}$$

where the matrix notation $[G]_{ij} = G_{\upsilon_i\upsilon_j}(\mathrm{i}\,\omega)$, and analogously for the self-energy, was introduced. The free propagator in steady-state for an interaction free system $V = 0$ can easily be calculated by Fourier transforming Equ. (3.10), leading to [128]

$$G_{0,\upsilon\upsilon'}(\mathrm{i}\,\omega) = \left[\frac{1}{\mathrm{i}\,\omega - h_0}\right]_{\upsilon\upsilon'}, \tag{3.34}$$

where the matrix h_0 is the single-particle Hamiltonian of H_0 in υ-space.

In the Keldysh formalism, the self-energy takes the form

$$\Sigma = \begin{pmatrix} \Sigma^{\mathrm{R}} & \Sigma^{\mathrm{K}} \\ 0 & \Sigma^{\mathrm{A}} \end{pmatrix} \tag{3.35}$$

in the matrix notation introduced in Equ. (3.22). The Dyson equation gives the full Green function components as

$$G^{\mathrm{R/A}} = \left[[G_0^{\mathrm{R/A}}]^{-1} - \Sigma^{\mathrm{R/A}}\right]^{-1}, \qquad G^{\mathrm{K}} = G^{\mathrm{R}}\left[\left[G_0^{\mathrm{R}}\right]^{-1} G_0^{\mathrm{K}} \left[G_0^{\mathrm{R}}\right]^{-1} + \Sigma^{\mathrm{K}}\right] G^{\mathrm{A}} = G^{\mathrm{R}}\Sigma^{\mathrm{K}}G^{\mathrm{A}}, \tag{3.36}$$

where the last equality for the Keldysh component holds when $G^{\mathrm{R/A}}$ have a finite imaginary part. The free Green functions G_0 in frequency space is given by [123]

$$G_{0,\upsilon\upsilon'}^{\mathrm{R/A}}(\omega) = \left[\frac{1}{\omega - h_0 \pm \mathrm{i}\,\eta}\right]_{\upsilon\upsilon'} \tag{3.37}$$

and the Keldysh component can be calculated with the dissipation-fluctuation theorem Equ. (3.29).

3.3.1. Integrating out the reservoir degrees of freedom

In the system considered in the present thesis, the leads Equ. (2.4) are assumed to be non-interacting, and therefore, the reservoir degrees of freedom can be integrated out. The effects of the reservoirs can then be incorporated via a self-energy contribution, which is included in the Green function of the quantum dot region through the Dyson equation. Including the leads in this way is an exact approach. The self-energy contributions can be derived through a projection scheme [127, 129] or from diagrammatic arguments [124]. In the steady-state limit, they are given by

$$\Sigma_{\mathrm{res},jj'}(\mathrm{i}\,\omega) = \sum_{l} \frac{\tau_l^2}{N} \left(G_{0,\mathrm{res}}(\mathrm{i}\,\omega)\right)_l \left(\delta_{i=i'=1}\delta_{l,L} + \delta_{i=i'=M}\delta_{l,R}\right) \tag{3.38}$$

in the so-called Matsubara formalism, discussed in Sect. 3.1, and

$$\begin{pmatrix} \mathit{\Sigma}^{\mathrm{R}}_{\mathrm{res},ii'}(\omega) & \mathit{\Sigma}^{\mathrm{A}}_{\mathrm{res},ii'}(\omega) \\ 0 & \mathit{\Sigma}^{\mathrm{K}}_{\mathrm{res},ii'}(\omega) \end{pmatrix} = \sum_l \frac{\tau_s^2}{N} \begin{pmatrix} G^{\mathrm{R}}_{0,\mathrm{res}}(\omega) & G^{\mathrm{A}}_{0,\mathrm{res}}(\omega) \\ 0 & G^{\mathrm{K}}_{0,\mathrm{res}}(\omega) \end{pmatrix}_l \left(\delta_{i=i'=1}\delta_{l,L} + \delta_{i=i'=M}\delta_{l,R}\right) \tag{3.39}$$

on the Keldysh contour, introduced in Sect. 3.2. Here, G_0 is the local Green function of the isolated leads.

In the following evaluations, we will include the reservoir self-energies directly into the free propagator for $\mathit{\Gamma} \neq 0$:

$$\left[[G_0]^{-1} - \mathit{\Sigma}_{\mathrm{res}}\right]^{-1} \to G_0 \tag{3.40}$$

for the Matsubara Green function, and

$$\left[[G_0^{\mathrm{R/A}}]^{-1} - \mathit{\Sigma}^{\mathrm{R/A}}_{\mathrm{res}}\right]^{-1} \to G_0^{\mathrm{R/A}}, \qquad G_0^{\mathrm{R}}\mathit{\Sigma}^{\mathrm{K}}_{\mathrm{res}}G_0^{\mathrm{A}} \to G_0^{\mathrm{K}} \tag{3.41}$$

for the retarded, advanced, and Keldysh Green functions. The self-energy contributions due to the interaction will then be included within the Dyson equation Equs. (3.33) and (3.36).

Wide-band limit

As we are not interested in the effects of the specific band structure of the reservoirs, we can assume wide and uniform reservoir bands, which are characterized by a linear dispersion or equivalent by a constant density of states $\rho_{\mathrm{res}}(\omega) \approx \rho_{\mathrm{res}}(0)$. This is called the wide-band limit. Then, one can define a constant hybridization [122, 123, 127]

$$\mathit{\Gamma}_l := \pi \rho^l_{\mathrm{res}}(0)\, |\tau_l|^2 , \tag{3.42}$$

leading to self-energy contributions

$$\mathit{\Sigma}_{\mathrm{res}}(\mathrm{i}\,\omega) = -\,\mathrm{i}\,\mathrm{sign}(\omega) \begin{pmatrix} \mathit{\Gamma}_L & 0 & \dots & 0 \\ 0 & 0 & \dots & 0 \\ \dots & & & \dots \\ 0 & 0 & \dots & \mathit{\Gamma}_R \end{pmatrix} \tag{3.43}$$

and

$$\mathit{\Sigma}^{\mathrm{R/A}}_{\mathrm{res}}(\omega) = \pm\,\mathrm{i} \begin{pmatrix} \mathit{\Gamma}_L & 0 & \dots & 0 \\ 0 & 0 & \dots & 0 \\ \dots & & & \dots \\ 0 & 0 & \dots & \mathit{\Gamma}_R \end{pmatrix}, \qquad \mathit{\Sigma}^{\mathrm{K}}_{\mathrm{res}}(\omega) = -2\,\mathrm{i} \begin{pmatrix} \mathit{\Gamma}_L(1-2f_L(\omega)) & 0 & \dots & 0 \\ 0 & 0 & \dots & 0 \\ \dots & & & \dots \\ 0 & 0 & \dots & \mathit{\Gamma}_R(1-2f_R(\omega)) \end{pmatrix}, \tag{3.44}$$

with $f_l(\omega)$ being the Fermi function for lead $l = L, R$ with chemical potential μ_l and temperature T_l. So, the influence of the leads on the impurity does not depend on their energetic structure. For simplicity, to reduce the parameter space under consideration, we will consider symmetric couplings in the following calculations, $\mathit{\Gamma}_L = \mathit{\Gamma}_R = \mathit{\Gamma}$. Asymmetric coupling, which is relevant for experimental setups, where fine-tuning is only hardly reached, was e.g. studied in [29]. Further, we will assume a symmetrically applied voltage-bias $\mu_L = -\mu_R = V/2$ and, if not stated otherwise, no temperature gradient $T_L = T_R = T$.

To provide a more detailed example of how the wide-band limit is applied, we assume the reservoirs are modeled by tight-binding chains with on-site energy ε_l and hopping t'_l. In this case, one can show that the local density of states at the impurity-adjacent site takes the form [124, 127]

$$\rho^l_{\text{res}}(\omega) = \frac{1}{2\pi t'_l}\sqrt{4t'^2_l - \omega^2}\theta\big(2t'_l - |\omega|\big)\,. \tag{3.45}$$

From this expression, it becomes clearer how the wide-band limit must be taken in the case of tight-binding leads. While the band is supposed to become wide and structureless in the limit $t'_l \to \infty$, the hybridization must not diverge but remain constant. Therefore, $\tau_l \to \infty$ must scale to counterbalance the divergence caused by t'_l. By introducing $a \to \infty$ and scaling $\tau = \sqrt{a}\tau_{l,0}$ and $t'_l = at'_{l,0}$, we obtain the hybridization

$$\Gamma \to \frac{\tau^2_{l,0}}{t'_{l,0}}, \tag{3.46}$$

if $at'_{l,0} \gg \omega$ for all ω of interest.

3.4. Symmetries

Considering the definition of the one-particle Matsubara Green function Equ. (3.10), we conclude that

$$[G(\tau|\tau')]^\dagger = G(\tau|\tau'), \tag{3.47}$$

and therefore, in frequency space, it holds that

$$G(\mathrm{i}\,\omega_n)^\dagger = G(-\mathrm{i}\,\omega_n), \qquad \Sigma(\mathrm{i}\,\omega_n)^\dagger = \Sigma(-\mathrm{i}\,\omega_n), \tag{3.48}$$

where we used the Dyson equation Equ. (3.33) to deduce the symmetry of the self-energy.

From the definitions of the Keldysh Green functions Equs. (3.23), (3.24) and (3.25) the symmetries

$$\left[G^{\mathrm{R}}_{v|v'}(t|t')\right]^* = G^{\mathrm{A}}_{v'|v}(t'|t), \qquad \left[G^{\mathrm{K}}_{v|v'}(t|t')\right]^* = -G^{\mathrm{K}}_{v'|v}(t'|t) \tag{3.49}$$

follow directly. In the matrix notation, this gives in frequency space

$$\left[G^{\mathrm{R}}\right]^\dagger(\omega) = G^{\mathrm{A}}(\omega), \qquad \left[G^{\mathrm{K}}\right]^\dagger(\omega) = -G^{\mathrm{K}}(\omega). \tag{3.50}$$

The symmetries of the self-energies then read:

$$\left[\Sigma^{\mathrm{R}}\right]^\dagger(\omega) = \Sigma^{\mathrm{A}}(\omega), \qquad \left[\Sigma^{\mathrm{K}}\right]^\dagger(\omega) = -\Sigma^{\mathrm{K}}(-\omega). \tag{3.51}$$

3.5. Calculate observables with Green functions

The Green functions provide direct access to multiple observables. Besides the quantum dot occupation, we are primarily interested in the transport properties of the system. In this section, we demonstrate how to obtain these observables from the Matsubara Green function for the equilibrium cases and from the Keldysh Green functions for the non-equilibrium ones, respectively. Ultimately, we are interested in the properties of the fermions in the impurity region (see Sect. 2.1) and will therefore consider fermionic operators c_i and set $\zeta = -1$. Similar expressions for the observables of bosonic particles can be found in [118] or in alternative sources, such as [127, 130].

Average Occupation

The average occupation of a quantum dot state i can be written in Matsubara formalism as

$$n_i(\tau) = \left\langle c_i^\dagger c_i \right\rangle = \lim_{\eta\to 0^+} \left\langle c_i^\dagger c_i(-\eta) \right\rangle = - \lim_{\eta\to 0^+} \left\langle T c_i(-\eta) c_i^\dagger \right\rangle = \frac{1}{\beta} \sum_n e^{-\mathrm{i}\,\omega_n(-\eta)} G_{ii}(\mathrm{i}\,\omega_n) \tag{3.52}$$

$$\xrightarrow{T\to 0} \frac{1}{2\pi} \int \mathrm{d}\,\omega\, e^{\mathrm{i}\,\omega\eta} G_{ii}(\mathrm{i}\,\omega), \tag{3.53}$$

where the zero-temperature limit was assumed in the last step.

In a non-equilibrium scenario, the occupation can be calculated via the Keldysh component of the Green function:

$$n_i(t,t) = \left\langle d_i^\dagger(t) d_i(t) \right\rangle = \frac{1}{2} \left\langle [d_i^\dagger(t), d_i(t)]_- + [d_i^\dagger(t), d_i(t)]_+ \right\rangle = -\frac{1}{2} \left[G_{ii}^{\mathrm{K}}(t,t) - 1 \right]. \tag{3.54}$$

Assuming the steady-state limit, this can be reexpressed involving the frequency space Green function

$$n_i(t=0) = \frac{1}{2} \left[1 + \frac{1}{2\pi} \int_{-\infty}^{\infty} \mathrm{d}\,\omega\, G_{ii}^{\mathrm{K}}(\omega) \right]. \tag{3.55}$$

After introducing the spectral function

$$A_{ii}(\omega) = -\frac{1}{\pi} \operatorname{Im} G_{ii}^{R}(\omega), \tag{3.56}$$

one can further define a non-equilibrium distribution function

$$f_i^{\mathrm{NE}}(\omega) = -\frac{\operatorname{Im} G_{ii}^{\mathrm{K}}(\omega) - 2 \operatorname{Im} G_{ii}^{\mathrm{R}}(\omega)}{4 \operatorname{Im} G_{ii}^{\mathrm{R}}(\omega)} \tag{3.57}$$

to find an expression for the occupation number:

$$n_i(t=0) = \int_{-\infty}^{\infty} \mathrm{d}\,\omega\, A_{ii}(\omega) f_i^{\mathrm{NE}}(\omega). \tag{3.58}$$

This also directly defines the spectral weight

$$n_i^A(\omega) = A_{ii}(\omega) f_i^{\mathrm{NE}}(\omega) = -\frac{\mathrm{i}}{2\pi} G^<(\omega) \tag{3.59}$$

In equilibrium, where we can apply the dissipation-fluctuation theorem Equ. (3.29), $f_i^{\mathrm{NE}}(\omega)$ in Equ. (3.57) becomes the Fermi-Dirac distribution $n_{\zeta=-}(\omega) = f(\omega)$ in Equ. (3.30).

3.5.1. Particle current

An important non-equilibrium observable is the particle current, which assesses the number of particles per time traveling through the quantum dot region from one lead to the other. We focus on the case considered in Sect. 2.1, where two leads ($l = L, R$) with different chemical potentials $\mu_{L/R}$ are attached to either side of an impurity region. The current can then be defined by the change in the number of particles $N_l = \sum_{k_l} c_{k_l}^\dagger c_{k_l}$ in the left or right lead [131, 132], where we distinguish between the left current

I_L^N leaving the left lead into site $i = 1$ of the impurity and the right current I_R^N, respectively defined on the right side of the impurity:

$$I_l^N(t,t) = -\left\langle \frac{\mathrm{d}}{\mathrm{d}t} N_l(t) \right\rangle = -\mathrm{i}\left\langle [H, N_l(t)]_+ \right\rangle . \tag{3.60}$$

Considering a Hamiltonian of the form introduced in Sect. 2, $N_l(t)$ commutes with all parts of the Hamiltonian except with the coupling terms between the quantum dot region and the leads of Equ. (2.5), and the current can then be evaluated as [127]

$$I_l^N(t,t) = -\frac{\tau_l}{\sqrt{N}} \sum_{i,k_l} \mathrm{Re}\left[G^{\mathrm{K}}_{i|k_l}(t|t) \right] (\delta_{l,L}\delta_{i,1} + \delta_{l,R}\delta_{i,M}). \tag{3.61}$$

The Keldysh Green function here is the propagator between a lead state k_l and a quantum dot state i and can be calculated as

$$G^{\mathrm{K}}_{i|k_l} = \sum_{i'} \int_{t_0}^{t} \mathrm{d}t' \left[G^{\mathrm{R}}_{i|i'}(t|t') \frac{\tau_l}{\sqrt{N}} \delta_{i',i} G^{\mathrm{K}}_{0,k_l' k_l}(t'|t) + G^{\mathrm{K}}_{i|i'}(t|t') \frac{\tau_l}{\sqrt{N}} \delta_{i',i} G^{\mathrm{A}}_{0,k_l' k_l}(t'|t) \right]. \tag{3.62}$$

As we are considering non-interacting leads in the eigenbasis k_l, the lead Green functions are diagonal and given by Equ. (3.37). Within the steady-state limit $t_0 \to -\infty$, the particle current takes the final form

$$\begin{aligned} I_l^N &= -\Gamma_l \int \frac{\mathrm{d}\omega}{2\pi} \, \mathrm{Im}\left[G^K_{ii}(\omega) - 2(1 - 2f_i(\omega)) G^R_{ii}(\omega) \right] (\delta_{l,L}\delta_{i,1} + \delta_{l,R}\delta_{i,M}) \\ &= 4\pi\Gamma_l \int \frac{\mathrm{d}\omega}{2\pi} \left[f_i^{NE}(\omega) - f_i(\omega) \right] A_{ii}(\omega)(\delta_{l,L}\delta_{i,1} + \delta_{l,R}\delta_{i,M}). \end{aligned} \tag{3.63}$$

The second line shows that the current depends on how the non-equilibrium distribution function of the leads changes with respect to the equilibrium one. Therefore, in equilibrium, the integrand vanishes, and, on average, no particles cross the impurity.

The full system under consideration, as presented in Sect. 2, is generally particle-conserving $I_L^N = -I_R^N$. Thus, one can define the symmetrized particle current

$$I^N = \frac{I_L^N - I_R^N}{2}, \tag{3.64}$$

which, in the conserving case, is equal to the left and right current, respectively. However, by approximations of the Green function, such as when, e.g., treating the interaction perturbatively, this symmetry can be broken. Then, one can observe a finite difference in the number of particles leaving the left lead and entering the right one, quantified by

$$\Delta I^N = \left| I_L^N + I_R^N \right|, \tag{3.65}$$

which gives the magnitude of the possible violation of particle conservation.

3.5.2. Heat and energy current

In addition to the particle current, we can analyze the energy transported through the quantum dot system by considering the change of energy in the leads:

$$I_l^E(t) = -\left\langle \frac{\mathrm{d}}{\mathrm{d}t} H_{\mathrm{res},l}(t) \right\rangle = -\mathrm{i}\left\langle \left[H, H_{\mathrm{res},l}(t) \right]_+ \right\rangle . \tag{3.66}$$

Following [133], the commutator can be evaluated similarly to the one for the particle current to obtain

$$\begin{aligned} I_l^E(t=0) &= -\Gamma_l \int_{-\infty}^{\infty} \mathrm{d}\,\omega\, \omega \,\mathrm{Im}\left[G_{ii}^{\mathrm{K}}(\omega) - 2\left[1-2f_s(\omega)\right] G_{ii}^{\mathrm{R}}(\omega)\right] (\delta_{l,L}\delta_{i,1} + \delta_{l,R}\delta_{i,M}) \\ &= 4\pi\Gamma_l \int \mathrm{d}\,\omega\, \omega \left[f_i^{NE}(\omega) - f_L(\omega)\right] A_{ii}(\omega)(\delta_{l,L}\delta_{i,1} + \delta_{l,R}\delta_{i,M}). \end{aligned} \tag{3.67}$$

Contrary to the particle number, when coupling to a bosonic system as described in Sect. 2.2, the energy going through the impurity region is not conserved, as absorption or emission into the bosonic system can lead to energy gains or losses. Therefore, we quantify the energy transported from the fermionic to the bosonic system as the energy dissipation of the quantum dot region:

$$\varDelta I^E = I_L^E + I_R^E. \tag{3.68}$$

Lastly, we introduce the heat current as the difference between the total energy current and the energy current due to the particle flow:

$$I_l^Q = I_l^E - \mu_l I_l^N. \tag{3.69}$$

3.5.3. Transport coefficients

In the scope of the present thesis, a non-equilibrium configuration can be achieved in two different ways: by applying a symmetric bias voltage $\mu_L = -\mu_R = V/2$ or a finite temperature gradient $\varDelta T = T_R - T_L$ across the impurity. To study the transport properties beyond the currents, the generalized transport coefficients are considered [134]:

$$G = \partial_V I^{\mathrm{N}}\big|_{\varDelta T}, \tag{3.70}$$

$$S = -\frac{\partial_{\varDelta T} I^{\,\mathrm{N}}\big|_V}{\partial_V I^{\,\mathrm{N}}\big|_{\varDelta T}}, \tag{3.71}$$

$$\kappa_{\,\mathrm{e}} = \partial_{\varDelta T} I_R^{\mathrm{Q}}\big|_V - \partial_{\varDelta T} I_R^{\mathrm{Q}}\big|_V \frac{\partial_{\varDelta T} I^{\,\mathrm{N}}\big|_V}{\partial_V I^{\mathrm{N}}\big|_{\varDelta T}}. \tag{3.72}$$

This includes the conductance G, the Seebeck coefficient S, and the electron contribution to the thermal conductance κ_{e}, see e.g. [92, 135].

When considering the equilibrium limit, with $\mu_L = \mu_R$, and simultaneously the zero-temperature limit, $T_L = T_R = 0$, the linear conductance can be simplified to [136]

$$\frac{G}{G_0} = \partial_V I^{\mathrm{N}}\big|_{V=0,T=0} = 4\Gamma \left|G_{1M}^{\mathrm{R}}(\omega=0)\right|^2 := 4\Gamma T_{1M}(0), \tag{3.73}$$

with the transmission function $T_{1M}(\omega) = \left|G_{1M}^{\mathrm{R}}(\omega)\right|^2$ [137].

3.5.4. Effective energy spectrum

The effective energy spectrum is not directly a physical observable, but we will see that a wide range of effects seen in observables can be explained with the help of the spectrum of the quantum dot region. We define the spectrum as the eigenenergies of the static effective Hamiltonian of the impurity, given by $H_{\mathrm{eff}} = -\left[G^{\mathrm{R}}(\omega=0)\right]^{-1} = -\left[G(\mathrm{i}\,\omega = \mathrm{i}\,0^+)\right]^{-1}$. Via the Dyson equation Equs. (3.33) and (3.36), the

Green function contains self-energy contributions from the leads as well as from the interactions, which affect the spectrum of the quantum dot region. We will denote the eigenenergies of the non-Hermitian H_{eff} as $E_{\text{eff}} = \varepsilon_{\text{eff}} + \mathrm{i}\,\Gamma_{\text{eff}}$, which can, in general, be complex. The spectrum for the non-interacting system with only the lead contributions included will be indicated by an additional zero: $E^0_{\text{eff}} = \varepsilon^0_{\text{eff}} + \mathrm{i}\,\Gamma^0_{\text{eff}}$.

3.6. Functional integrals

For completeness, we briefly introduce the functional integral representation. A more thorough introduction to this formalism can be found in a wide range of literature, e.g. [119, 121, 122]. It differs from the conventional Schrödinger or Heisenberg formulations in that it represents the evolution of a quantum system as a sum over all possible paths that a particle could take between two points, rather than a single trajectory or a state vector evolving in time. Path integrals are particularly useful in quantum field theory and statistical mechanics because they allow for perturbative expansion [119, 128], which we will introduce in the following Sect. 4, and the formulation of the functional renormalization group [138, 139], which will be discussed in Sect. 5.

The main idea behind the formalism is to rewrite the partition function of a general Hamiltonian of the form Equ. (3.1) using the Trotter decomposition [119]

$$\exp^{-\lambda H} = \lim_{N\to\infty} \Big(:\, e^{-\lambda H/N} \,: \Big)^N , \tag{3.74}$$

where $:\cdot:$ brings an arbitrary operator into normal order, meaning all creation operators will end up to the left of the annihilation operators. In the decomposition, one inserts unities in the basis of coherent states

$$|\psi\rangle = \exp\left(-\sum_{\upsilon} \psi_{\upsilon} c^{\dagger}_{\upsilon} \right) |\text{vac}\rangle \,. \tag{3.75}$$

$|\text{vac}\rangle$ is the vacuum state and $|\psi\rangle$ a general state of the Fock space. The coherent states are the right eigenstate of the annihilation operator c_{υ} with eigenvalues ψ_{υ} and the left eigenstates of the creation operator $c^{\dagger}_{\upsilon}$ with eigenvalues $\bar{\psi}_{\upsilon}$. In the continuum limit, $N \to \infty$, the partition function can then be written as a functional integral of the continuous Grassmann (fermionic) or complex (bosonic) fields $\psi_{\upsilon}(t,\tau)$ and $\bar{\psi}_{\upsilon}(t,\tau)$, which replace the annihilation and creation operators. The partition function then takes the form:

$$Z = \int \mathcal{D}[\bar{\psi},\psi]\ \exp\big(\{\mathrm{i}\} S_0(\bar{\psi}_{\upsilon},\psi_{\upsilon}) - \{\mathrm{i}\} S_{\text{int}}(\bar{\psi}_{\upsilon},\psi_{\upsilon}) \big) \,, \tag{3.76}$$

with all expression in $\{\cdot\}$ only considered in the Keldysh approach. The full derivation can for example be found in [118, 119]. The differential element is defined as $\mathcal{D}[\bar{\psi},\psi] = \prod_{\upsilon} \mathrm{d}\bar{\psi}\,\mathrm{d}\psi/\mathcal{N}$, with $\mathcal{N} = 2\pi\mathrm{i}$ for fermions and $\mathcal{N} = 1$ for bosons. The argument of the exponential function is called the action and depends on all fields $\psi_{\upsilon}(t,\tau)$ and $\bar{\psi}_{\upsilon}(t,\tau)$. It is comprised of a non-interacting part

$$\begin{aligned} S_0 &= -\sum_{\upsilon',\upsilon} \int_0^{\beta} \mathrm{d}\tau\, \bar{\psi}_{\upsilon'}(\tau) \left[\partial_{\tau}\delta_{\upsilon',\upsilon} + \varepsilon_{\upsilon'\upsilon} \right] \psi_{\upsilon}(\tau) && \text{Matsubara,} \\ S_0 &= \sum_{\nu} \operatorname{sgn}(\nu) \int_{t_0}^{t_{\max}} \mathrm{d}t\ \sum_{\upsilon'\upsilon} \bar{\psi}^{\nu}_{\upsilon'}(t) [\mathrm{i}\,\partial_t \delta_{\upsilon',\upsilon} - \varepsilon_{\upsilon'\upsilon}(t)] \psi^{\nu}_{\upsilon}(t) && \text{Keldysh.} \end{aligned} \tag{3.77}$$

and an interacting part

$$S_{\text{int}} = \frac{1}{4} \int_{0 \text{ or } t_0}^{\beta \text{ or } t_{\max}} \mathrm{d}(\tau \text{ or } t) \left\{ \sum_{\nu} \right\} \sum_{\substack{\upsilon_1',\upsilon_2' \\ \upsilon_1,\upsilon_2}} \{\operatorname{sgn}(\nu)\} \left[\bar{\psi}^{\{\nu\}}_{\upsilon_1'} \bar{\psi}^{\{\nu\}}_{\upsilon_2'} \bar{v}^{\{\nu,\nu|\nu,\nu\}}_{\upsilon_1',\upsilon_2'|\upsilon_1,\upsilon_2} \psi^{\{\nu\}}_{\upsilon_2} \psi^{\{\nu\}}_{\upsilon_1} \right] (\tau \text{ or } t). \tag{3.78}$$

Besides the time and quantum number, the Keldysh formulation also depends on the contour index v, which places the operator on the forward or backward branch of the time contour.

In the steady-state limit, it is convenient to work in frequency space and therefore we Fourier transform the fields according to

$$\begin{aligned} \psi_v(\tau) &= \frac{1}{\beta}\sum_{n=-\infty}^{\infty} e^{-\mathrm{i}\,\omega_n\tau}\psi_v(\mathrm{i}\,\omega_n), && \text{Matsubara,} \\ \psi_v(t) &= \frac{1}{2\pi}\int_{-\infty}^{\infty} \mathrm{d}\,\omega\, e^{-\mathrm{i}\,\omega\tau}\psi_v(\omega), && \text{Keldysh.} \end{aligned} \tag{3.79}$$

Further, we introduce again the multi-index $x = \{\mathrm{i}\,\omega_n, v\}$ for Matsubara and $x = \{\omega, v, \nu\}$ for Keldysh parameters, and define the free propagator $[G_0^{-1}]_{v'v} = [\partial_\tau\delta_{v'v} + \varepsilon_{v'v}]$ in the Matsubara formulation and $[G_0^{-1}]_{v'v} = [\mathrm{i}\,\partial_t\delta_{v',v} - \varepsilon_{v'v}]$ for the Keldysh formulation. The free propagator is equivalent to the single-particle Green function in the non-interacting case. With this, the action takes the simple form

$$S_0 = \sum\!\!\!\!\!\!\!\int_{x,x'} \bar{\psi}_{x'}[G_0]^{-1}_{x'x}\psi_x, \qquad S_{\mathrm{int}} = \frac{1}{4}\sum\!\!\!\!\!\!\!\int_{\substack{x_1',x_2' \\ x_1,x_2}} \bar{\psi}_{x_1'}\bar{\psi}_{x_2'}\bar{v}(x_1', x_2'|x_1, x_2)\psi_{x_2}\psi_{x_1}. \tag{3.80}$$

3.6.1. Integrating-out the bosonic degrees of freedom

The generalized coupling Equ. (2.21) of fermionic and bosonic degrees of freedom is linear in the bosonic operators and can simply be integrated out, as presented in Appendix A. To this end, we used the functional integral representation, similar to [92, 119]. The calculation is slightly different in the Matsubara or Keldysh formalism, but both yield an effective two-particle interaction for the fermions. The interaction vertex in Matsubara formalism and in the steady-state limit reads

$$\begin{aligned} \bar{v}_{i_1',i_2'|i_1,i_2}(\mathrm{i}\,\omega_1', \mathrm{i}\,\omega_2'|\,\mathrm{i}\,\omega_1, \mathrm{i}\,\omega_2) &= \frac{1}{\beta}\delta(\omega_1' + \omega_2' - \omega_1 - \omega_2) \\ &\Big[D\big(\mathrm{i}\,\omega_1' - \mathrm{i}\,\omega_1\big)\, A^*_{i_1i_1'}A_{i_2'i_2} - D\big(\mathrm{i}\,\omega_1' - \mathrm{i}\,\omega_2\big)\, A^*_{i_2i_1'}A_{i_2'i_1}\Big]\,. \end{aligned} \tag{3.81}$$

Here, $i'_{1/2}$ are the site indices and $\omega'_{1/2}$ the frequencies. $D(\mathrm{i}\,\omega)$ is the bosonic propagator in frequency space

$$D(\mathrm{i}\,\omega) = \frac{1}{\mathrm{i}\,\omega - \omega_0} - \frac{1}{\mathrm{i}\,\omega + \omega_0} = -\frac{2\omega_0}{\omega^2 + \omega_0^2}. \tag{3.82}$$

Here, we directly neglected the dissipation $\kappa \to 0$, which will be utilized in the following studies.

On the forward-backward contour, indicated by the contour indices $\nu'_{1/2}$, the vertex reads

$$\begin{aligned} \bar{v}^{\nu_1',\nu_2'|\nu_1,\nu_2}_{i_1',i_2'|i_1,i_2}(\omega_1', \omega_2'|\omega_1, \omega_2) &= \frac{1}{2\pi}\,\mathrm{sign}(\nu_1')\,\mathrm{sign}(\nu_2')\delta(\mathrm{i}\,\omega_1' - \mathrm{i}\,\omega_1 + \mathrm{i}\,\omega_2' - \mathrm{i}\,\omega_2 = 0)\times \\ &\Big[D^{\nu_1'\nu_2'}(\omega_1' - \omega_1)\delta_{\nu_1',\nu_1}\delta_{\nu_2',\nu_2}A^*_{i_1,i_1'}A_{i_2',i_2} - D^{\nu_1'\nu_2'}(\omega_1' - \omega_2)\delta_{\nu_1',\nu_2}\delta_{\nu_2',\nu_1}A^*_{i_2,i_1'}A_{i_2',i_1}\Big] \end{aligned} \tag{3.83}$$

Since we will work later directly in the rotated Keldysh space, we here give the bosonic propagator on this contour. The retarded component is given by

$$D^{\mathrm{R}}(\omega) = \big[D^{\mathrm{A}}(\omega)\big]^* = \sum_{s=\pm1}\frac{1}{\omega - s\omega_0 + \mathrm{i}\,\kappa} \xrightarrow{\kappa\to0^+} \sum_{s=\pm1}\left[\mp\,\mathrm{i}\,\pi\delta(\omega - s\omega_0) + P\left[\frac{1}{\omega - s\omega_0}\right]\right] \tag{3.84}$$

in frequency space in the steady-state limit. We directly applied the limit for small κ here as well. $P[\cdot]$ indicates the Cauchy principal value. The Keldysh component takes the form

$$\begin{aligned} D^{\mathrm{K}}(\omega) &= -2\,\mathrm{i}(1+2b(\omega_0))\left[\frac{\kappa}{(\omega+\omega_0)^2+\kappa^2}+\frac{\kappa}{(\omega-\omega_0)^2+\kappa^2}\right] \\ &\xrightarrow{\kappa\to 0^+} -2\pi\,\mathrm{i}\,[1+2b(\omega_0)]\sum_{s=\pm 1}\delta(\omega-s\omega_0). \end{aligned} \tag{3.85}$$

$b(\omega_0) = n_+(\omega_0)$ is the Bose-Einstein distribution Equ. (3.30) for the bosonic bath with chemical potential $\mu_{\mathrm{b}} = 0$ and temperature T_{b} evaluated at the mode frequency ω_0.

4. Perturbation Theory

For the system described in Sect. 2, the existence of an exact solution that simultaneously accounts for the fermion-boson coupling and the Coulomb interaction is not known. One approximate approach to study the effective fermionic interaction, introduced in Eqs. (3.81) and (3.83), alongside the Coulomb interaction in Eq. (2.6), is perturbation theory. This is the method primarily used in the present thesis, where we only consider the lowest order in the interaction strengths $A_{ij}A_{i'j'}$ and U. Thus, there are also no mixing effects of e.g. the form $\mathcal{O}\left(UA^2\right)$ included. This approach has previously been applied to study correlated fermions interacting with a bosonic degree of freedom [140–142].

The lowest-order perturbation theory for the self-energy is given by the Hartree and Fock diagram shown in Fig. 4.1. For a comprehensive introduction to diagrammatics, the reader is referred to the wide range of literature available, e.g. [119, 128]. For this approximation, the self-energies for bosonic or fermionic degrees of freedom can be calculated as

$$\Sigma(x_1'|x_1) = -\zeta\{-\mathrm{i}\} \sum_{x_2,x_2'} G_0(x_2|x_2')\bar{v}(x_1', x_2'|x_1, x_2), \tag{4.1}$$

where the x_i are multi-indices containing all quantum numbers, the time or frequency components, and the Keldysh or contour indices for the non-equilibrium case as described in Sect. 3. ζ is again $+1$ for bosonic degrees of freedom and -1 for fermionic ones. Because we are considering fermionic self-energies in the following, we set $\zeta = -1$ from now on. The vertex $\bar{v}$ is given by the aforementioned interactions and G_0 is the fermionic propagator of the impurity including the lead contributions, cf. Equs. (3.40) and (3.41). The $\{-\mathrm{i}\}$ is only considered in the case of Keldysh variables, see Sect. 3.2.

In the following, we will evaluate Equ. (4.1) for the Matsubara self-energy in the zero-temperature limit and for the Keldysh self-energies separately.

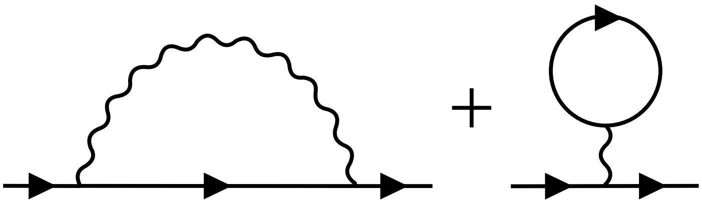

Figure 4.1.: Hartree and Fock diagram. The solid lines represent the fermionic propagators, only dressed by the lead self-energies. The vertices are given by the nearest-neighbor Coulomb interaction and the effective fermion-fermion interaction induced by the fermion-boson coupling. For the effective interaction, this means that the wiggly lines indicate the bosonic propagators and the crossing are proportional to the couplings A_{ij}.

4.1. Matsubara formalism

The Matsubara self-energy in first-order perturbation theory in the zero-temperature limit reads:

$$
\begin{aligned}
\Sigma_{i_1',i_1}(\mathrm{i}\,\omega) = \int_{-\infty}^{\infty} \frac{\mathrm{d}\,\omega'}{2\pi} \Bigg\{ & D(\mathrm{i}\,0) A^*_{i_1 i_1'} \sum_{i_2',i_2} A_{i_2',i_2} G_{0,i_2,i_2'}(\mathrm{i}\,\omega') \\
& - D(\mathrm{i}\,\omega - \mathrm{i}\,\omega') \sum_{i_2',i_2} A^*_{i_2 i_1'} A_{i_2' i_1} G_{0,i_2,i_2'}(\mathrm{i}\,\omega') \Bigg\} e^{\mathrm{i}\,\omega' 0^+} \\
+ U \int_{-\infty}^{\infty} \frac{\mathrm{d}\,\omega'}{2\pi} \Bigg\{ & \left[G_{0,i_1'-1,i_1-1}(\mathrm{i}\,\omega') + G_{0,i_1'+1,i_1+1}(\mathrm{i}\,\omega') \right] \delta_{i_1',i_1} \\
& - G_{0,i_1',i_1}(\mathrm{i}\,\omega') \left[\delta_{i_1'+1,i_1} + \delta_{i_1',i_1+1} \right] \Bigg\} e^{\mathrm{i}\,\omega' 0^+} .
\end{aligned}
\tag{4.2}
$$

We plugged in the effective fermionic interaction vertex from the bosonic degrees of freedom, given by Equ. (3.81), and the vertex arising from the Coulomb interaction, given by Equ. (2.6), into Equ. (4.1). The first term corresponds to the Hartree diagram, while the second term stems from the Fock diagram for each respective interaction. $D(\mathrm{i}\,\omega)$ is the bosonic propagator defined in Equ. (3.82). The exponential factor ensures convergence of the integral.

4.2. Keldysh formalism

In non-equilibrium, we want to evaluate the self-energies in the Keldysh basis. To this end, the vertex Equ. (3.83) in the contour basis is rotated as stated in Equ. (3.26) and the sum in Equ. (4.1) runs over the Keldysh indices α instead of the forward-backward contour index. The self-energies in first-order perturbation theory then take the form

$$
\begin{aligned}
\Sigma^{\mathrm{R}}_{i_1',i_1}(\omega) = & -\frac{\mathrm{i}}{2} D^{\mathrm{R}}(0) A^*_{i_1',i_1} \sum_{i_2',i_2} \int \frac{\mathrm{d}\,\omega'}{2\pi} G^{\mathrm{K}}_{0,i_2,i_2'}(\omega') A_{i_2',i_2} \\
& + \frac{\mathrm{i}}{2} \sum_{i_2',i_2} \int \frac{\mathrm{d}\,\omega'}{2\pi} \left[D^{\mathrm{R}}(\omega-\omega') G^{\mathrm{K}}_{0,i_2,i_2'}(\omega') + D^{\mathrm{K}}(\omega-\omega') G^{\mathrm{R}}_{0,i_2,i_2'}(\omega') \right] A^*_{i_1',i_2} A_{i_2',i_1} \\
& - \frac{\mathrm{i}\,U}{2} \int \frac{\mathrm{d}\,\omega'}{2\pi} \left[G^{\mathrm{K}}_{0,i_1'+1,i_1+1}(\omega') + G^{\mathrm{K}}_{0,i_1'-1,i_1-1}(\omega') \right] \delta_{i_1',i_1} \\
& + \frac{\mathrm{i}\,U}{2} \int \frac{\mathrm{d}\,\omega'}{2\pi} G^{\mathrm{K}}_{0,i_1',i_1}(\omega') \left[\delta_{i_1'+1,i_1} + \delta_{i_1',i_1+1} \right]
\end{aligned}
\tag{4.3}
$$

$$
\begin{aligned}
\Sigma^{\mathrm{A}}_{i_1',i_1}(\omega) = & -\frac{\mathrm{i}}{2} D^{\mathrm{A}}(0) A^*_{i_1',i_1} \sum_{i_2',i_2} \int \frac{\mathrm{d}\,\omega'}{2\pi} G^{\mathrm{K}}_{0,i_2,i_2'}(\omega') A_{i_2',i_2} \\
& + \frac{\mathrm{i}}{2} \sum_{i_2',i_2} \int \frac{\mathrm{d}\,\omega'}{2\pi} \left[D^{\mathrm{A}}(\omega-\omega') G^{\mathrm{K}}_{0,i_2,i_2'}(\omega') + D^{\mathrm{K}}(\omega-\omega') G^{\mathrm{A}}_{0,i_2,i_2'}(\omega') \right] A^*_{i_1',i_2} A_{i_2',i_1} \\
& - \frac{\mathrm{i}\,U}{2} \int \frac{\mathrm{d}\,\omega'}{2\pi} \left[G^{\mathrm{K}}_{0,i_1'+1,i_1+1}(\omega') + G^{\mathrm{K}}_{0,i_1'-1,i_1-1}(\omega') \right] \delta_{i_1',i_1} \\
& + \frac{\mathrm{i}\,U}{2} \int \frac{\mathrm{d}\,\omega'}{2\pi} G^{\mathrm{K}}_{0,i_1',i_1}(\omega') \left[\delta_{i_1'+1,i_1} + \delta_{i_1',i_1+1} \right]
\end{aligned}
\tag{4.4}
$$

$$\begin{aligned}\Sigma^{\mathrm{K}}_{i_1',i_1}(\omega) =& \frac{\mathrm{i}}{2} D^{\mathrm{A}}(0) A^*_{i_1',i_1} \sum_{i_2',i_2} \int \frac{\mathrm{d}\,\omega'}{2\pi} \left[G^{\mathrm{R}}_{0,i_2,i_2'}(\omega') + G^{\mathrm{A}}_{0,i_2,i_2'}(\omega')\right] A_{i_2',i_2} \\ &+ \frac{\mathrm{i}}{2} \sum_{i_2',i_2} \int \frac{\mathrm{d}\,\omega'}{2\pi} \Big[D^{\mathrm{R}}(\omega-\omega') G^{\mathrm{R}}_{0,i_2,i_2'}(\omega') + D^{\mathrm{A}}(\omega-\omega') G^{\mathrm{A}}_{0,i_2,i_2'}(\omega') \\ &\qquad + D^{\mathrm{K}}(\omega-\omega') G^{\mathrm{K}}_{0,i_2,i_2'}(\omega')\Big] A^*_{i_1',i_2} A_{i_2',i_1}.\end{aligned} \tag{4.5}$$

Now, we show how these expressions can be further simplified.

For the Keldysh component, we can directly use that the retarded Green function is analytic in the upper half complex plane, to evaluate the integrals

$$\int_{-\infty}^{\infty} \mathrm{d}\,\omega'\, G^{\mathrm{R}}_{0,ij}(\omega') = \int_{\Phi} \mathrm{d}\,z\, G^{\mathrm{R}}_{0,ij}(z) = 0, \tag{4.6}$$

where Φ is a positively oriented path along the x-axis and closing in the upper half plane. The same holds for the integral over the advanced Green function, which is analytic in the lower half plane when considering a negatively oriented path closing in the lower half plane. Additionally, when using the residue theorem, see e.g. [143], one can show

$$\int_{-\infty}^{\infty} \mathrm{d}\,\omega' \frac{G^{\mathrm{R}}_0(\omega')}{\omega-\omega'-s\omega_0+\mathrm{i}\,\kappa} = \int_{\Gamma} \mathrm{d}\,z \frac{G^{\mathrm{R}}_0(z)}{\omega-z-s\omega_0+\mathrm{i}\,\kappa} \xrightarrow{\kappa\to 0^+} -2\pi\mathrm{i}\, G^{\mathrm{R}}_0(\omega-s\omega_0). \tag{4.7}$$

This identity can alternatively be shown utilizing the Kramers-Kronig relation, see e.g. [123]. The term on the left-hand side occurs in Σ^{K} in Equ. (4.5), when plugging in the definition of the retarded bosonic propagator Equ. (3.84) in the $\kappa \to 0^+$ limit. An analogous calculation can be performed for the convolution of the advanced Green function $G^{\mathrm{A}}_0(\omega')$ with the advanced bosonic propagator Equ. (3.84). This term, however, experiences a change of sign due to the different orientation of the line-integral. Finally, the remaining Keldysh bosonic propagator in Equ. (4.5) is evaluated in the limit $\kappa \to 0^+$ as given in Equ. (3.85). The Keldysh self-energy then takes the form

$$\begin{aligned}\Sigma^{\mathrm{K}}_{i_1'i_1}(\omega) =& \frac{1}{2} \sum_{i_2,i_2'} \sum_{s} s\left[G^{\mathrm{R}}_{0,i_2i_2'}(\omega-s\omega_0) - G^{\mathrm{A}}_{0,i_2i_2'}(\omega-s\omega_0)\right] A^*_{i_2i_1'} A_{i_2'i_1} \\ &+ \frac{1}{2}\left(1+b(\omega_0)\right) \sum_{i_2,i_2'} \sum_{s} G^{\mathrm{K}}_{0,i_2i_2'}(\omega-s\omega_0) A^*_{i_2i_1'} A_{i_2'i_1}.\end{aligned} \tag{4.8}$$

The retarded and advanced component of the self-energy, Equs. (4.3) and (4.4), can also be further evaluated. We consider again the bosonic propagator in the limit of no bosonic dissipation $\kappa \to 0^+$, as seen in Equs. (3.84) and (3.85). This leads to

$$\begin{aligned}
\varSigma^{\mathrm{R}}_{i_1' i_1}(\omega) = &+ \frac{\mathrm{i}}{\omega_0} \sum_{i_2,i_2'} \int \frac{\mathrm{d}\,\omega'}{2\pi}\, G^{\mathrm{K}}_{0,i_2 i_2'}(\omega') A^*_{i_1 i_1'} A_{i_2' i_2} \\
&+ \frac{1}{4} \sum_{i_2,i_2'} \sum_{s} s G^{\mathrm{K}}_{0,i_2 i_2'}(\omega - s\omega_0) A^*_{i_2 i_1'} A_{i_2' i_1} \\
&+ \frac{\mathrm{i}}{2} \sum_{i_2,i_2'} \sum_{s} \mathcal{P}\!\!\int \frac{\mathrm{d}\,\omega'}{2\pi} \frac{s G^{\mathrm{K}}_{0,i_2 i_2'}(\omega')}{\omega - \omega_1 - s\omega_0} A^*_{i_2 i_1'} A_{i_2' i_1} \\
&+ \frac{1}{2} \left(1 + 2b(\omega_0)\right) \sum_{i_2,i_2'} \sum_{s} G^{\mathrm{R}}_{0,i_2 i_2'}(\omega - s\omega_0) A^*_{i_2 i_1'} A_{i_2' i_1} \\
&- \frac{\mathrm{i}U}{2} \int \frac{\mathrm{d}\,\omega'}{2\pi} \left[G^{\mathrm{K}}_{0,i_1'+1,i_1+1}(\omega') + G^{\mathrm{K}}_{0,i_1'-1,i_1-1}(\omega') \right] \delta_{i_1',i_1} \\
&+ \frac{\mathrm{i}U}{2} \int \frac{\mathrm{d}\,\omega'}{2\pi} G^{\mathrm{K}}_{0,i_1',i_1}(\omega') \left[\delta_{i_1'+1,i_1} + \delta_{i_1',i_1+1} \right] ,
\end{aligned} \tag{4.9}$$

and

$$\begin{aligned}
\varSigma^{\mathrm{A}}_{i_1' i_1}(\omega) = &+ \frac{\mathrm{i}}{\omega_0} \sum_{i_2,i_2'} \int \frac{\mathrm{d}\,\omega'}{2\pi}\, G^{\mathrm{K}}_{0,i_2 i_2'}(\omega') A^*_{i_1 i_1'} A_{i_2' i_2} \\
&- \frac{1}{4} \sum_{i_2,i_2'} \sum_{s} s G^{\mathrm{K}}_{0,i_2 i_2'}(\omega - s\omega_0) A^*_{i_2 i_1'} A_{i_2' i_1} \\
&+ \frac{\mathrm{i}}{2} \sum_{i_2,i_2'} \sum_{s} \mathcal{P}\!\!\int \frac{\mathrm{d}\,\omega'}{2\pi} \frac{s G^{\mathrm{K}}_{0,i_2 i_2'}(\omega')}{\omega - \omega_1 - s\omega_0} A^*_{i_2 i_1'} A_{i_2' i_1} \\
&+ \frac{1}{2} \left(1 + 2b(\omega_0)\right) \sum_{i_2,i_2'} \sum_{s} G^{\mathrm{A}}_{0,i_2 i_2'}(\omega - s\omega_0) A^*_{i_2 i_1'} A_{i_2' i_1} \\
&- \frac{\mathrm{i}U}{2} \int \frac{\mathrm{d}\,\omega'}{2\pi} \left[G^{\mathrm{K}}_{0,i_1'+1,i_1+1}(\omega') + G^{\mathrm{K}}_{0,i_1'-1,i_1-1}(\omega') \right] \delta_{i_1',i_1} \\
&+ \frac{\mathrm{i}U}{2} \int \frac{\mathrm{d}\,\omega'}{2\pi} G^{\mathrm{K}}_{0,i_1',i_1}(\omega') \left[\delta_{i_1'+1,i_1} + \delta_{i_1',i_1+1} \right] .
\end{aligned} \tag{4.10}$$

The evaluation of the self-energies until now was conducted analytically. However, the frequency integrals in the expressions in Equs. (4.8), (4.9) and (4.10) can only be treated analytically in certain limits. Some of which, we will see in Sects. 8 and 10.2. In general, the self-energies can only be calculated numerically. The same holds for the integrals in the perturbative Matsubare self-energy Equ. (4.2), Thus, we specify the numerical implementation in the following.

4.3. Implementation

The most numerically demanding part of calculating the self-energies in first-order perturbation theory is solving the frequency integrals on the right-hand side. This can be done using adaptive integral-solving tools in e.g. python or other languages. The first problem arising with this approach is the convergence-inducing factor $e^{\mathrm{i}\,\omega' 0^+}$ for large frequencies that appears in the Matsubara formalism and which is highly non-trivial to treat numerically. Secondly, although most adaptive integral routines are generally well-optimized, they can still be very slow. Especially treating the poles in the Cauchy principle integral in the Keldysh formalism, where existing routines are relatively unstable for large integration intervals.

Therefore, we decided to use a finite and discretized frequency grid and evaluate the integrals with a simple Riemann-sum

$$\int \mathrm{d}\,\omega F(\omega) \to \sum_k \frac{F(\omega_{k+1}) + F(\omega_k)}{2} (\omega_{k+1} - \omega_k)\,, \tag{4.11}$$

with ω_k being the frequency grid points. The Cauchy principle integral in Equs. (4.9) and (4.10) is evaluated by symmetrizing the frequency grid around the pole with additional logarithmically spaced frequency points. We obtain the same results with this method compared to adaptive methods when considering appropriate frequency grids. However, the Riemann sum approach was approximately 100 times faster.

Note that the ω_k are not equivalent to the discrete Matsubara frequencies introduced earlier in Equ. (3.13). Rather, we consider the zero-temperature limit for the Matsubara case, where the frequencies become continuous, and the grid points can be chosen freely, in analogy to the Keldysh formalism.

4.3.1. Discretized frequency grid

The grid must cover a broad frequency range to ensure that the Green functions are sufficiently decayed at the large frequencies, while also providing enough resolution at small frequencies to capture the detailed frequency dependence of all components. To achieve this, we employed a logarithmic grid that spans the entire frequency space as a base grid and overlaid it with several finer logarithmic grids at high-resolution points. A logartihmic grid with $(N + 1)$ grid points $\omega_k \in [-\omega_{\max}, \omega_{\max}]$ is constructed with

$$\omega_k = \omega_{\max} \frac{2k - N}{N} \exp\left[\frac{|N - 2k| - N}{S}\right], \qquad k = 0, 1, .., N. \tag{4.12}$$

Chosing an odd N excludes $\omega_k = 0$. S gives the resolution of the grid and therefore defines the minimal frequency spacing $\min\{|\omega_k|\} = \omega_{\min}$. The choice of the exact frequency grid depends on the considered problem and parameter regime of the physical system and was always tested for convergence. We will here give a rough approximation for a typical frequency grid. The basic grid is symmetrized around $\omega = 0$ with $N \in [3000, 6000]$, $\omega_{\min} \approx 10^{-2}\Gamma$ and $\omega_{\max} \approx 1000\Gamma$. Additional grids are set around the real part of the single-particle eigenergies of the effective, non-interacting Hamiltonian $H_{\text{eff}} = \left[G_0^{\mathrm{R}}(0)\right]^{-1}$ including the lead contributions, see Sect. 3.5.4. To take into account the features arising from inelastic processes due to the fermion-boson coupling, additional grids are added around the high-resolution points at $n\omega_0 \pm V/2$ with $n \in \mathbb{N}$. We considered only $n = 1, 2$, which we found to be sufficient in perturbation theory for small coupling strengths A_{ij}. These additional grids have around $N \approx 500$ points with $\omega_{\min} \approx 10^{-2}\Gamma$ and $\omega_{\max} \approx 2\Gamma$. Broadly speaking, the computation on the Keldysh contour needs more frequency points than for the Matsubara case.

4.3.2. Finite frequency grid

The integral cannot be analyzed numerically for infinite frequencies because it would require an infinitely large gid. Therefore, the integral is seperated into parts $\int_{-\infty}^{\infty} \mathrm{d}\,\omega = \int_{-\infty}^{-\omega_{\max}} \mathrm{d}\,\omega + \int_{-\omega_{\max}}^{\omega_{\max}} \mathrm{d}\,\omega + \int_{\omega_{\max}}^{\infty} \mathrm{d}\,\omega$ for large $\omega_{\max} \to \infty$. The integral $\omega \in (-\infty, -\omega_{\max}]$ and $\omega \in [\omega_{\max}, \infty)$ can be analyzed analytically, which we will present in the following and which is possible due to the decay of the fermionic and bosonic propagator for large frequencies. However, due to the slow decay of some components of the propagators, as we will see shortly, the frequency integrals do not vanish completely even for large frequencies. $\omega \in [-\omega_{\text{max}}, \omega_{\text{max}}]$ will be treated numerically with the discretized frequency grid. ω_{max} is the largest frequency considered numerically and has to be much larger than all physical energy scales of the system.

We consider the analytic evaluation of the integral containing the Matsubara Green functions in more detail. To this end, we rewrite the free Green function as

$$G_0(\mathrm{i}\,\omega) = \frac{1}{\mathrm{i}\,\omega}\left\{\mathbb{1} + \sum_{k=1}^{\infty}\frac{1}{(\mathrm{i}\,\omega)^k}\begin{pmatrix} -\varepsilon_1 + \mathrm{i}\,\Gamma\operatorname{sign}(\omega) & -t & & \\ -t & -\varepsilon_2 & -t & \\ & & \dots & \\ & & -t & -\varepsilon_M + \mathrm{i}\,\Gamma\operatorname{sign}(\omega) \end{pmatrix}^{k}\right\} \tag{4.13}$$

to see that the diagonal terms vanish only with $\mathcal{O}\left(\frac{1}{\omega}\right)$, while the off-diagonal terms vanish with $\mathcal{O}\left(\frac{1}{\omega^2}\right)$. Further, the bosonic propagator $D(\mathrm{i}\,\omega) = \mathcal{O}\left(\frac{1}{\mathrm{i}\,\omega}\right)$, for large ω. Therefore, high-frequency tails of the integrals in Equs. (4.8), (4.9) and (4.10) including off-diagonal elements always vanish. Also, convolutions containing the propagator $D(\mathrm{i}\,\omega - \mathrm{i}\,\omega')$ and diagonal elements of the Green function will vanish as well, due to the aforementioned scaling. The remaining high-frequency integrals with diagonal Green function components can be evaluated analytically and depend on the form of the interaction vertex. We now treat these terms explicitly.

The third term in the Matsubara self-energy Equ. (4.2) always provides a non-vanishing contribution. So does the third term exactly when $A_{i_2' i_2} \sim \delta_{i_2',i_2}$. These two terms contain both high-frequency integrals of the form

$$\lim_{\omega_{\text{max}}\to\infty}\left[\int_{-\infty}^{-\omega_{\text{max}}}\frac{\mathrm{d}\,\omega'}{2\pi}\,\frac{e^{\mathrm{i}\,\omega' 0^+}}{\mathrm{i}\,\omega'} + \int_{\omega_{\text{max}}}^{\infty}\frac{\mathrm{d}\,\omega'}{2\pi}\,\frac{e^{\mathrm{i}\,\omega' 0^+}}{\mathrm{i}\,\omega'}\right] = \lim_{\omega_{\text{max}}\to\infty}\int_{\omega_{\text{max}}}^{\infty}\frac{\mathrm{d}\,\omega'}{2\pi}\,\frac{2\sin(\omega' 0^+)}{\omega'} = -\frac{1}{2}. \tag{4.14}$$

So the self-energy can numerically be evaluated as

$$\begin{aligned} \Sigma_{i_1',i_1}(\mathrm{i}\,\omega) = &\int_{-\omega_{\text{max}}}^{\omega_{\text{max}}}\frac{\mathrm{d}\,\omega'}{2\pi}\left\{D(\mathrm{i}\,0)A^*_{i_1',i_1}\sum_{i_2',i_2}A_{i_2',i_2}G_{0,i_2,i_2'}(\mathrm{i}\,\omega')\right. \\ &\qquad\left. - D(\mathrm{i}\,\omega - \mathrm{i}\,\omega')\sum_{i_2',i_2}A^*_{i_1',i_2}A_{i_2',i_1}G_{0,i_2,i_2'}(\mathrm{i}\,\omega')\right\} \\ &+ U\int_{-\omega_{\text{max}}}^{\omega_{\text{max}}}\frac{\mathrm{d}\,\omega'}{2\pi}\left\{\left[G_{0,i_1'-1,i_1-1}(\mathrm{i}\,\omega') + G_{0,i_1'+1,i_1+1}(\mathrm{i}\,\omega')\right]\delta_{i_1',i_1}\right. \\ &\qquad\left. - G_{0,i_1',i_1}(\mathrm{i}\,\omega')\left[\delta_{i_1'+1,i_1} + \delta_{i_1',i_1+1}\right]\right\} \\ &- \frac{D(\mathrm{i}\,0)}{2}A^*_{i_1',i_1}\sum_{i_2}A_{i_2,i_2} - \delta_{i_1',i_1}\begin{cases} U, & \text{if } i_1 = 1, M, \\ U/2, & \text{else} \end{cases} \quad . \end{aligned} \tag{4.15}$$

For the Keldysh Green function, a similar analysis can be conducted, using the scaling behavior

$$G_0^{\mathrm{R}}(\omega) = \frac{1}{\omega}\left[\mathbb{1} + \sum_{k=1}^{\infty}\mathcal{O}\left(\frac{\left(T^{\mathrm{R}}\right)^k}{\omega^k}\right)\right], \qquad G_0^{\mathrm{K}}(\omega) = \mathcal{O}\left(\frac{\left(T^{\mathrm{K}}\right)^2}{\omega^2}\right) \tag{4.16}$$

for large frequencies and with T^{R} and T^{K} being frequency independent single-particle operators. Using this, the high-frequency tails of the integrals in Equs. (4.8), (4.9) and (4.10) can be treated analytically.

4.4. Current conservation in first-order perturbation theory

Physical systems generally obey certain symmetries and therefore conservation laws, such as for example energy or particle conservation. The respective conserved observables commute with the Hamiltonian of the system. So, it is easily shown that the interacting impurity Hamiltonian described in Sect. 2 of the closed system ($\Gamma = 0$) is fermion-conserving. Therefore, when opening the system ($\Gamma \neq 0$), the right and left particle current Equ. (3.63) should be equal and $\Delta I^N = 0$, in Equ. (3.65). However, approximate treatment of the system, such as the first-order perturbation theory introduced here, can break these symmetries and therefore the conservation. Using this method, the particle conservation was already found to be broken for the simple system containing one quantum dot capacitively coupled to a resonator [144]. This also holds for the generalized system under consideration in the present thesis. However, as first-order perturbation theory neglects only terms in second order in the interaction and all terms in first order are taken into account, the violation is at least of second order in the interaction. Thus, when considering small interaction strength, for which the perturbative treatment is feasible, the violation is also minute. Nevertheless, this unphysical behavior is important to keep in mind when applying perturbation theory. It can provide an indicator if the approximate treatment is able to reproduce the correct behavior of the real system and is therefore worth discussing.

Ref. [144] showed that the current through an open and interacting quantum dot system is preserved, when

$$\int \frac{\mathrm{d}\,\omega}{2\pi} \operatorname{Tr}\left[\Sigma_{ij}^{>}(\omega) G_{ji}^{<} \omega - \Sigma_{ij}^{<} G_{ji}^{>} \omega\right] = 0. \tag{4.17}$$

<and > indicate the lesser and greater component of the self-energy or Green function and Σ is the self-energy due to the interaction. Changing into the Keldysh basis and using the symmetries of the Green functions and self-energies, this can be written as

$$\int \frac{\mathrm{d}\,\omega}{2\pi} \operatorname{Tr}\left[\operatorname{Re}\left(\Sigma^{\mathrm{R}}(\omega) G^{\mathrm{K}}(\omega) - \Sigma^{\mathrm{K}}(\omega) G^{\mathrm{R}}(\omega)\right)\right] = 0. \tag{4.18}$$

Besides ΔI^N, this quantity can be studied to analyze the spurious breaking of the conservation of particle conservation.

It is useful to note that the self-consistent Hartree-Fock equation, also called self-consistent Born approximation, where all bare propagators of the right-hand side in Equ. (4.1) are replaced by the full ones dressed with the self-energies, conserve the particle current. These equations can be solved in an iterative process. The conservation has been shown for the capacitively coupled system in [144]. However, this method holds the risk of other spurious symmetry breaking [23]. In the present thesis, we will not further consider this approximation. Instead, we will introduce different methods, including the functional renormalization group method in the next section.

5. Functional Renormalization Group Theory

Perturbation theory, which treats all energy scales of the system at once often gives rise to divergencies at low energies, especially when considering low dimensional systems. More specifically, loop diagrams in perturbation theory, which include the free propagator times a sharp Fermi function at low temperatures, can produce logarithmic terms, which diverge for low energies [124, 145]. In these cases, perturbation theory breaks down. This has, for example, been shown for the g-ology model of a one-dimensional Fermi-gas [146], in the Kondo model [23] or in the interacting resonant level model [13, 30]. We will show that the logarithmic divergence also occurs when the coupling to the bosonic mode is considered in first-order perturbation theory in Sects. 9.4 and 10.3. One possible solution to this problem are so-called renormalization group methods. These methods effectively lead to a self-consistent resummation of a certain class of diagrams. For some systems, the method resums the so-called leading-logs to a power-law, curing the divergence [145, 147]. The origin of the resummation will become clear below. In the following, we will apply the functional renormalization group method which uses the functional integral formulation introduced in Sect. 3.6.

In functional renormalization group (FRG) [138, 139], the problematic low energy scales are artificially cut off, by introducing the so-called flow parameter Λ into the free propagator $G_0 \to G_0^\Lambda$, such that the problem is solvable for an initial Λ_i, where the low energies are cut off, and the original problem is recovered for a final Λ_f. Starting from the solvable system, the low-energy scales are subsequently reintroduced by 'flowing' from Λ_i to Λ_f. To this end, the vertex generating functional is expressed in the functional integral framework and the derivate with respect to the flow-parameter Λ is taken. The functional depends on Λ directly through the cut-off in G_0^Λ. Considering that the one-particle-irreducible n-particle vertex functions γ_n^Λ are the Taylor coefficients of the vertex generating functional, this gives rise to an infinite hierarchy of differential equations for γ_n^Λ of the form

$$\dot{\gamma}_n^\Lambda = F_n\left[\gamma_{n+1}^\Lambda, \gamma_n^\Lambda, ..., \gamma_1^\Lambda\right], \tag{5.1}$$

for $n > 0$. The dot indicates the derivative with respect to Λ. The differential equation for the zero-particle vertex function, on the other hand, only depends on the one-particle function and can easily be integrated. The flow of the one-particle vertex function is described by

$$\dot{\gamma}_1^\Lambda(x_1'|x_1) = \sum\!\!\!\!\!\!\!\int_{x_2', x_2} S^\Lambda(x_2|x_2')\gamma_2^\Lambda(x_1', x_2'|x_1, x_2), \tag{5.2}$$

where the single-scale propagator $S^\Lambda := -\partial_\Lambda^* G^\Lambda$, with $G^\Lambda = \left[\left[G_0^\Lambda\right]^{-1} + \gamma_1^\Lambda\right]^{-1}$ was introduced. The general derivation of the flow equations, including Equ. (5.2), can be found in e.g. [124, 127, 130, 148]. An introduction to vertex functions can for example be found in [119]. The partial derivate ∂_Λ^* acts explicitly only on the Λ-dependence in G_0^Λ. As the single-scale propagator, depends itself on the one-particle vertex function, the derivative of γ_1 with respect to Λ depends on γ_2 and γ_1 itself.

The set of differential equations Equ. (5.1) is exact in general. However, in practice, the infinite hierarchy is not solvable. For practical calculations, the hierarchy has therefore to be truncated at order n_c, so that for all n-particle vertex functions for $n > n_\mathrm{c}$, the function is just set to its initial value. This means $\gamma_n^\Lambda = \gamma_n^{\Lambda_\mathrm{i}}$ and $\dot{\gamma}_n^\Lambda = 0$ for all $n > n_\mathrm{c}$. In this thesis, we focus on a fist-order truncation $n_c = 1$, so that the n-particle vertex functions are given by

$$\dot{\Sigma}^\Lambda(x_1'|x_1) = \zeta\{-\mathrm{i}\} \sum_{x_2,x_2'} S^\Lambda(x_2|x_2')\bar{v}(x_1', x_2'|x_1, x_2), \tag{5.3}$$

and

$$\gamma_2^\Lambda(x_1', x_2'|x_1, x_2) = \{-\mathrm{i}\}\bar{v}(x_1', x_2'|x_1, x_2), \qquad\qquad \gamma_{n>2}^\Lambda = 0 \tag{5.4}$$

where the self-energy is given by $\Sigma = \zeta\gamma_1$. The results from this truncation are exact in first order in the two-particle vertex function, and thus in first order in the interaction strengths.

It is striking that the right-hand side of the FRG flow Equ. (5.3) resembles the right-hand side of the perturbation theory Equ. (4.1). In the first-order truncated FRG approximation, the derivative of the self-energy with respect to the flow parameter is diagrammatically described by the Hatree-Fock diagrams in Fig. 4.1, where the contracted lines are replaced by dressed lines indicating the minus the single-scale propagator. The resemblance becomes more clear when considering the FRG flow while neglecting the self-feedback of Σ into S^Λ on the right-hand side of Equ. (5.2). Then the selective partial derivate ∂_Λ^* in the single-scale propagator becomes the normal partial derivate ∂_Λ

$$\dot{\Sigma}^\Lambda(x_1'|x_1) = \zeta\{-\mathrm{i}\} \sum_{x_2,x_2'} \left(-\underbrace{\dot{G}^\Lambda(x_2|x_2')(\Sigma_\mathrm{i}^\Lambda)}_{\dot{G}_0^\Lambda(x_2|x_2')} \right) \bar{v}(x_1', x_2'|x_1, x_2). \tag{5.5}$$

The flow equation can just be integrated from Λ_i to Λ_f leading to the self-energy given by first-order perturbation theory Equ. (4.1). The feedback in the first-order truncated FRG flow of the self-energy itself includes arbitrary higher-order into the self-energy along the flow. This means that, even though the first-order truncated FRG scheme is an approximate method taking into account all terms in the first order in the interaction, higher orders are also included. The resulting effective resummation of higher-order terms due to feedback of the self-energy can also cure the logarithmic divergencies in FRG compared to ordinary perturbation theory, described above. This is the case when the summation of leading logs includes the logs and prefactors in the right order and leads to power law dependence instead. Nevertheless, the treatment of the higher-order terms is not exact, which means that not all terms including more than one two-particle vertex are being accounted for. FRG as an approximate method holds the risk of violation of conservation laws, analog to first-order perturbation theory.

Finally, we must specify how the cut-off Λ is introduced into the free Green function. Here, we choose different cut-off schemes for the Matsubara and Keldysh formulations, which will be specified further below. Solving the full hierarchy of differential equations provides the exact results of the many-body problem under consideration at Λ_f, where the cut-off vanishes. Thus, the results are independent of the specific choice of the cut-off. However, when considering the truncation of the hierarchy, the results may differ depending on the cut-off procedure employed. Nevertheless, since the first-order truncation scheme is exact in first order in the two-particle vertices, the difference due to cut-off schemes is at least in second order in the interaction strengths. Thus, the difference in the results for distinct cut-off schemes is negligible for small interaction strengths. The interested reader is referred to e.g. [118, 130, 149, 150] for a more thorough discussion of the effect of different cut-off procedures on the symmetries of the system. In general, the impact on results depends on the specifics of the problem and observables being calculated.

5.1. Matsubara formalism

For equilibrium setups, we employ the Matsubara formalism again and plug in the vertices Equ. (3.81) from the fermion-boson coupling and the one from the Coulomb interaction Equ. (2.6) into the flow equation Equ. (5.2). Additionally, the cut-off scheme has to be specified. In the equilibrium case, we stated that we would concentrate on the zero-temperature limit, where the Matsubara frequencies become continuous. It is therefore straightforward to introduce a step-like cut-off, excluding all frequencies lower than the cut-off parameter $|\omega| < \Lambda$. So the free propagator becomes

$$G_0^\Lambda(\mathrm{i}\,\omega) = \theta(|\omega| - \Lambda) G_0(\mathrm{i}\,\omega), \tag{5.6}$$

with $\Lambda_\mathrm{i} = \infty$ and $\Lambda_\mathrm{f} = 0$. With Morris' Lemma [151], it can be shown that the single-scale propagator then takes the form

$$S^\Lambda(\mathrm{i}\,\omega) = \delta(|\omega| - \Lambda)\left[[G_0(\mathrm{i}\,\omega)]^{-1} - \Sigma^\Lambda(i\omega)\right] =: \delta(|\omega| - \Lambda)\tilde{G}^\Lambda(\mathrm{i}\,\omega), \tag{5.7}$$

where the free propagator G_0 in $\tilde{G}^\Lambda = \left[[G_0]^{-1} - \Sigma_\mathrm{res} - \Sigma^\Lambda\right]$ does not contain the sharp cut-off anymore. S^Λ is only finite at the frequency $\omega = \pm\Lambda$, where also the name single-scale propagator originates from. This simplifies the calculations greatly.

The flow of the self-energy takes the form

$$\begin{aligned}\dot{\Sigma}^\Lambda(\mathrm{i}\,\omega) = &- \frac{1}{2\pi}\sum_{s=\pm}\sum_{i_2,i_2'}\left[D(\mathrm{i}\,0)A^*_{i_1 i_1'}A_{i_2' i_2}\tilde{G}_{i_2,i_2'}(\mathrm{i}\,s\Lambda) - D(\mathrm{i}\,\omega - is\Lambda)A^*_{i_2 i_1'}A_{i_2' i_1}\tilde{G}_{i_2,i_2'}(is\Lambda)\right] e^{\mathrm{i}\,s\Lambda 0^+} \\ &- \frac{U}{2\pi}\sum_{s=\pm}\left[\left[\tilde{G}_{i_1'-1,i_1-1}(\mathrm{i}\,s\Lambda) + \tilde{G}_{i_1'+1,i_1+1}(\mathrm{i}\,s\Lambda)\right]\delta_{i_1',i_1} - \tilde{G}_{i_1',i_1}(\mathrm{i}\,s\Lambda)\left[\delta_{i_1'+1,i_1} + \delta_{i_1',i_1+1}\right]\right] e^{\mathrm{i}\,s\Lambda 0^+}.\end{aligned} \tag{5.8}$$

The exponential term ensures convergence. As mentioned above, the right-hand side is analog to the one from perturbation theory in Equ. (4.2) with the free propagator swapped with minus the single-scale propagator. The flow equation cannot be solved analytically for all frequencies and we will resort to numerical methods.

Analog to what we discussed for perturbation theory in Sect. 4.3.2, we cannot treat the integration for infinite Λ numerically. As some components of the fermionic propagators only decay slowly, the large-Λ tails of the integral do not vanish, but the numerical evaluation of an infinite integral boundary is not possible. Therefore, the integral is split into two parts

$$\Sigma^{\Lambda_\mathrm{i}=0}(i\omega) - \Sigma^{\Lambda_\mathrm{f}=\infty}(i\omega) = \int_\infty^0 \mathrm{d}\,\Lambda\dot{\Sigma}^\Lambda(i\omega) = \int_\infty^{\Lambda_\mathrm{max}} \mathrm{d}\,\Lambda\dot{\Sigma}^\Lambda(i\omega) + \int_{\Lambda_\mathrm{max}}^0 \mathrm{d}\,\Lambda\dot{\Sigma}^\Lambda(i\omega), \tag{5.9}$$

where Λ_max is to be chosen much larger than any other energy scale of the system. The flow starting from the finite Λ_max, which is the second part in Equ. (5.9), is treated numerically. The first term of Equ. (5.9), containing large $|\Lambda|$s, can be evaluated analytically using that

$$\tilde{G}^\Lambda(\mathrm{i}\,s\Lambda) = \frac{1}{\mathrm{i}\,s\Lambda}\left[\mathbb{1} + \sum_{k=1}^{\infty}\mathcal{O}\left(\frac{T}{\Lambda^k}\right)\right], \tag{5.10}$$

with a frequency-independent operator T. So, all off-diagonal elements decay at least with $\sim 1/\Lambda^2$ for large Λ. Then the analytic analysis is analog to the one in perturbation theory using Equ. (4.14). The result then provides the initial conditions for the numerical flow. A generalized discussion of the treatment of the large Λ terms can be found in [130, 133], with the amendment that for the interactions under consideration in this thesis, the effective interaction vertex due to the bosonic coupling is frequency-dependent. Thus the scaling of the vertex with the frequency, which is given by the bosonic propagators, must also be considered. This is why, similar to the treatment in perturbation theory, only the term proportional to $D(\mathrm{i}\,0)$ contributes to large Λ.

5.2. Keldysh formalism

For the non-equilibrium system, we use the FRG flow equations in the Keldysh formulation. For the Keldysh formalism, it was shown that applying the sharp cut-off leads to unphysical behavior, violating causality, such that the dissipation-fluctuation theorem no longer holds in the equilibrium limit [120]. Instead, a reservoir cut-off is used, which preserves the theorem [120]. Auxiliary reservoirs, where the hybridization is given by Λ are coupled to each level of the quantum dot region. They give additional self-energy terms analog to Equ. (3.38) for the physical leads with $\Gamma \to \Lambda$ instead

$$\Sigma^{\mathrm{R/A},\Lambda}_{\mathrm{cut}}(\omega) = \pm\,\mathrm{i}\,\Lambda\mathbb{1}, \qquad \Sigma^{\mathrm{K},\Lambda}_{\mathrm{cut}}(\omega) = -2\,\mathrm{i}\,\Lambda\left[\mathbb{1} - 2F(\omega)\right]. \tag{5.11}$$

$F(\omega)$ is a diagonal matrix, containing the Fermi functions of the auxiliary reservoirs coupling to each site of the impurity. At $\Lambda_{\mathrm{i}} = \infty$, the coupling to the reservoirs is infinitely large, leading to the Green function decaying with $\mathcal{O}(1/\Lambda)$. Decreasing Λ subsequently decouples the auxiliary leads from the physical system, so that they are separated at $\Lambda_{\mathrm{f}} = 0$, and the original system is recovered. The single-scale propagators can then be determined as

$$S^{\mathrm{R},\Lambda}(\omega) = \left[S^{\mathrm{A},\Lambda}(\omega)\right]^{\dagger} = \mathrm{i}\left[G^{\mathrm{R},\Lambda}(\omega)\right]^{2}, \qquad \text{with } G^{\mathrm{R},\Lambda}(\omega) = \left[\omega - \Sigma^{\mathrm{R}}_{\mathrm{res}} - \Sigma^{\mathrm{R},\Lambda}_{\mathrm{cut}} - \Sigma^{\mathrm{R},\Lambda}\right] \tag{5.12}$$

and

$$S^{\mathrm{K},\Lambda}(\omega) = \left[G^{\mathrm{R},\Lambda}\tilde{\Sigma}^{\mathrm{K},\Lambda}G^{\mathrm{A},\Lambda}\right](\omega), \qquad \text{with } \tilde{\Sigma}^{\mathrm{K},\Lambda}(\omega) = \left[\Sigma^{\mathrm{K}}_{\mathrm{res}} - \Sigma^{\mathrm{K},\Lambda}_{\mathrm{cut}} - \Sigma^{\mathrm{K},\Lambda}\right](\omega). \tag{5.13}$$

The FRG flow equations in Keldysh formalism can be derived by plugging in the interaction vertex of the Coulomb repulsion Equ. (2.6) and the effective vertex from the coupling to the resonator Equ. (3.83) into the flow equation Equ. (5.2). As we aim for the self-energies on the Keldysh contour, we rotate the vertices according to Equ. (3.26) and run the sum in the flow equation over the Keldysh contour indices. However, here we take a different approach. To write down the FRG flow equations in Keldysh formalism, we use the discussed similarity of the right-hand side of the flow equation Equs. (5.2) and perturbation theory Equ. (4.1). We interpolate the differential equation for the given interactions from the perturbation theory equations Equs. (4.3), (4.4) and (4.5) by replacing the free propagator by minus the single-scale propagator on the right-hand side. Using that both, the free and the single-scale propagator, have the same analytic properties, the flow equations, in analogy to Equs. (4.8), (4.9) and (4.10), are

$$\begin{aligned}\dot{\Sigma}^{\mathrm{K}}_{i_1' i_1}(\omega) = &-\frac{1}{2}\sum_{i_2,i_2'}\sum_{s=\pm} s\left[S^{\mathrm{R}}_{i_2 i_2'} - S^{\mathrm{A}}_{i_2 i_2'}\right](\omega - s\omega_0)A^{*}_{i_2 i_1'}A_{i_2' i_1} \\ &-\frac{1}{2}\left(1 + b(\omega_0)\right)\sum_{i_2,i_2'}\sum_{s=\pm} S^{\mathrm{K}}_{i_2 i_2'}(\omega - s\omega_0)A^{*}_{i_2 i_1'}A_{i_2' i_1},\end{aligned} \tag{5.14}$$

$$
\begin{aligned}
\dot{\Sigma}^{\mathrm{R}}_{i'_1 i_1}(\omega) = &- \frac{\mathrm{i}}{\omega_0} \sum_{i_2, i'_2} \int \frac{\mathrm{d}\,\omega'}{2\pi} S^{\mathrm{K}}_{i_2 i'_2}(\omega') A^*_{i_1 i'_1} A_{i'_2 i_2} \\
&- \frac{1}{4} \sum_{i_2, i'_2} \sum_{s=\pm} s S^{\mathrm{K}}_{i_2 i'_2}(\omega - s\omega_0) A^*_{i_2 i'_1} A_{i'_2 i_1} \\
&- \frac{\mathrm{i}}{2} \sum_{i_2, i'_2} \sum_{s=\pm} \mathcal{P}\!\!\int \frac{\mathrm{d}\,\omega'}{2\pi} \frac{s S^{\mathrm{K}}_{i_2 i'_2}(\omega')}{\omega - \omega_1 - s\omega_0} A^*_{i_2 i'_1} A_{i'_2 i_1} \\
&- \frac{1}{2} (1 + 2b(\omega_0)) \sum_{i_2, i'_2} \sum_{s=\pm} S^{\mathrm{R}}_{i_2 i'_2}(\omega - s\omega_0) A^*_{i_2 i'_1} A_{i'_2 i_1},
\end{aligned}
\tag{5.15}
$$

$$
\begin{aligned}
\dot{\Sigma}^{\mathrm{A}}_{i'_1 i_1}(\omega) = &- \frac{\mathrm{i}}{\omega_0} \sum_{i_2, i'_2} \int \frac{\mathrm{d}\,\omega'}{2\pi} S^{\mathrm{K}}_{i_2 i'_2}(\omega') A^*_{i_1 i'_1} A_{i'_2 i_2} \\
&+ \frac{1}{4} \sum_{i_2, i'_2} \sum_{s=\pm} s S^{\mathrm{K}}_{i_2 i'_2}(\omega - s\omega_0) A^*_{i_2 i'_1} A_{i'_2 i_1} \\
&- \frac{\mathrm{i}}{2} \sum_{i_2, i'_2} \sum_{s=\pm} \mathcal{P}\!\!\int \frac{\mathrm{d}\,\omega'}{2\pi} \frac{s S^{\mathrm{K}}_{i_2 i'_2}(\omega')}{\omega - \omega_1 - s\omega_0} A^*_{i_2 i'_1} A_{i'_2 i_1} \\
&- \frac{1}{2} (1 + 2b(\omega_0)) \sum_{i_2, i'_2} \sum_{s=\pm} S^{\mathrm{A}}_{i_2 i'_2}(\omega - s\omega_0) A^*_{i_2 i'_1} A_{i'_2 i_1}.
\end{aligned}
\tag{5.16}
$$

The change in initial condition due to the large Λ integration can be treated analog to the one in the Matsubara formalism, see e.g. [130, 133].

5.3. Implementation

The FRG flow equation is a set of differential equations that couple every frequency ω with every other frequency ω' via the convolution on the right-hand side of Equs. (5.14), (5.15) and (5.16). Therefore, the flow equation is evaluated on a discrete frequency grid. The integrals on the right-hand side of the flow equations are evaluated with the Riemann sums as explained in Sect. 4.3. Besides, this procedure additionally leads to an increased numerical performance evaluating the integrals, as compared to the usage of interpolation and adaptive integration routines.

The grid is constructed similarly to the one for the perturbation theory, introduced in Sect. 4.3. During the solution of the differential equation for the self-energy, the result of the current flow step is fed back into the calculation, leading to an accumulation of numerical errors. Thus, the calculations are very sensitive to the choice of the frequency grid and larger grid sizes, $N \in [6000, 10000]$ with higher resolution $\omega_{\mathrm{min}} \approx 10^{-3}\Gamma$ are needed to obtain converged results. Unfortunately, we were not able to reach a stable convergence in the solution of the flow equations when considering scenarios deeper in the non-equilibrium limit $V > \Gamma$ and effective interaction of the form Equ. (3.83) for more than one interacting quantum dot. This regime will therefore not be discussed in this thesis.

The system of coupled differential equations is solved with the use of the ode class of scipy [152] in Python. The integration uses an explicit Runge-Kutta method. To this end, we define a logarithmic grid of $\{\Lambda_\lambda\}$ starting at a large initial $\Lambda_{\lambda_{\mathrm{i}}}$ and a small final $\Lambda_{\lambda_{\mathrm{f}}}$ between which we split the calculations so that the differential equation is solved sequential from Λ_λ to $\Lambda_{\lambda+1}$. Finally, the last step $\Lambda_{\lambda_{\mathrm{i}}} \to \Lambda_{\mathrm{f}} = 0$ is considered as well. This is done, so that the adaptive solver does not jump over any part of the flow. It is known, that the FRG flow is cut by different energy scales in different regimes [28]. Thus, the chosen initial and finite Λ depends on the other energy parameters of the system.

So far, we have discussed two methods that can be applied in the regime of small interaction strength. In the following section, we will introduce two complementary methods to compare results. These methods contain, in contrast to perturbation theory and FRG all orders in the interaction, but the applicability will be constrained by other approximations.

6. Complementary Methods

So far, we have introduced two methods, which allow us to treat interacting quantum mechanical systems with weak interaction strengths. In the following, we present two additional methods that rely on different approximations and are suited for distinct parameter regimes. (i) The exact diagonalization provides access to the exact many-body eigenstates and eigenenergies. However, the calculations are very inefficient and further limited to finite-size systems and thus, the infinite leads and full bosonic Fock space cannot be treated in this method. (ii) The Lindblad master equation allows the calculation of the density matrix for open quantum systems. It therefore provides access to many-body expectation values of all observables of interest. Unfortunately, it is restricted to weakly coupled Markovian leads and thus is not able to treat the frequency dependence of the reservoirs. In the following, we will introduce both methods in more detail.

6.1. Exact diagonalization

Exact diagonalization (ED) is a widely used and the most straightforward method to study an isolated quantum mechanical system [153, 154]. By diagonalizing the many-body Hamiltonian H, it provides the solution of the eigenvalue problem

$$H|v_\alpha\rangle = E_\alpha\,|v_\alpha\rangle\,. \tag{6.1}$$

The many-body eigenvalues E_α and eigenvectors $|v_\alpha\rangle$ contain all information of the system, which allows the calculation of expectation values for any arbitrary observable. In most practical applications, the matrix H is sparse but grows exponentially with system size, and the diagonalization is conducted numerically. Therefore, in the most straightforward implementation, which we will consider here, the computational effort rapidly exceeds that of other methods. Further, the Fock space for bosonic degrees of freedom has to be truncated and only a finite number of lead sites can be taken into account. In our calculation, we will, thus, focus on the closed system ($\Gamma = 0$, $\kappa = 0$), cf. Sect. 2 in equilibrium without any leads or dissipation of the resonator. In this scenario, the expectation value of an arbitrary observable A is given by the canonical density matrix ρ, with

$$\langle A\rangle = \mathrm{Tr}\left[A\rho\right], \qquad \rho = \frac{\sum_\alpha e^{-E_\alpha/T}\,|v_\alpha\rangle\,\langle v_\alpha|}{\sum_\alpha e^{-E_\alpha/T}}. \tag{6.2}$$

6.1.1. Implementation

The main task of ED comes back to the question of how we generate the many-body Hamiltonian in the second quantization in numerical implementations. For this purpose, we show here how to construct many-body creation and annihilation operators and how to combine them for numerical calculations, see e.g. [153] for a more thorough discussion. We will consider a general system containing fermionic and bosonic degrees of freedom, which can interact arbitrarily.

We start with the fermionic ones. Defining the basis of a single state as

$$|1\rangle = \begin{pmatrix} 1 \\ 0 \end{pmatrix}, \qquad |0\rangle = \begin{pmatrix} 0 \\ 1 \end{pmatrix} \tag{6.3}$$

for a filled ($|1\rangle$) and empty ($|0\rangle$) state, the single-particle annihilation and creation operators read

$$c = \begin{pmatrix} 0 & 0 \\ 1 & 0 \end{pmatrix}, \qquad c^\dagger = \begin{pmatrix} 0 & 1 \\ 0 & 0 \end{pmatrix}. \tag{6.4}$$

We will indicate the basis elements with the indices $\sigma^{(\prime)}$. The many-body operator $c_n^{(\dagger)}$, which annihilates (creates) a particle in state n, is defined by the tensor-product $\otimes$:

$$c_n^{(\dagger)} = JW_{(1)} \otimes JW_{(2)} \otimes ... \otimes c_{(n)}^{(\dagger)} \otimes ... \otimes \mathbb{1}_{(M-1)} \otimes \mathbb{1}_{(M)}, \tag{6.5}$$

where the index (i) labels the ordering of the states, which can be chosen freely. JW is the Jordan-Wigner operator and is introduced for fermionic operators to ensure the correct anticommutation relation in Equ. (3.2). It is defined as

$$JW = \begin{pmatrix} -1 & 0 \\ 0 & 1 \end{pmatrix}. \tag{6.6}$$

We now introduce the bosonic degree of freedom in a similar manner. In practical applications, a bosonic mode can only be included approximately by truncating the Fock space. The annihilation and creation operators are given by

$$a = \begin{pmatrix} 0 & 0 & 0 & ... & 0 & 0 \\ \sqrt{1} & 0 & 0 & ... & 0 & 0 \\ 0 & \sqrt{2} & 0 & ... & 0 & 0 \\ ... & ... & ... & ... & ... & ... \\ 0 & 0 & 0 & ... & \sqrt{N} & 0 \end{pmatrix}, \qquad a^\dagger = [a]^\dagger, \tag{6.7}$$

with N being the maximal number of bosons taken into account. The index of the bosonic matrix will be indicated by $\tilde{\sigma}^{(\prime)}$.

To treat the fermionic and the bosonic systems together, we place the bosonic operators just in front of the fermionic ones in the tensor product expression, so that the first $N+1$ positions in the matrix are reserved for the bosonic degrees of freedom. Thus, the Hamiltonian including the coupling, can simply be expressed by combining the corresponding many-body operators. So an example many-body coupling term becomes

$$c_{i+1}^\dagger c_i e^{\mathrm{i}\, g(a+a^\dagger)} = e^{\mathrm{i}\, g(a+a^\dagger)} \otimes \mathbb{1}_{(1)} \otimes ... \otimes JW_{(i+1)} \cdot c_{(i)} \otimes c_{(i+1)}^\dagger \otimes \mathbb{1}_{(i+2)} \otimes ... \otimes \mathbb{1}_{(M)}. \tag{6.8}$$

In this manner, the whole Hamiltonian under consideration can be constructed. The tensor-product gives a many-body Hamiltonian H in tensor form with elements $H_{(\tilde{\sigma},\tilde{\sigma}'),(\sigma_1,\sigma_1'),(\sigma_2,\sigma_2'),...}$, which is a $((N+1) \times (N+1) \times 2 \times 2 \times 2 \times 2 ...)$ tensor. For easy diagonalization this has to be reshaped into $H_{(\tilde{\sigma},\sigma_1,\sigma_2,...),(\tilde{\sigma}',\sigma_1',\sigma_2',...)}$ to obtain a square $(((N+1) \cdot 2 \cdot 2 \cdot ...) \times ((N+1) \cdot 2 \cdot 2 \cdot ...))$ matrix. In the present thesis, the scheme is applied to the full Hamiltonian discussed in Sect. 2.

6.2. Lindblad master equation

The (Lindblad) master equation is another fundamental tool in quantum mechanics, particularly in the study of open quantum systems. It is used in a wide range of fields, such as condensed matter physics [117, 155–157], quantum optics [71, 158] or quantum computation [159, 160]. The master equation describes the time evolution of the density matrix, providing a complete description of the quantum state of the system without having to treat the environment explicitly. It allows for the non-unitary evolution of the density matrix, which is necessary to account for the loss of coherence and energy due to the system's interaction with its environment.

The Hamiltonian of the total setup is split into

$$H = H_0 + V = H_\mathrm{s} + H_\mathrm{e} + H_\mathrm{se}, \tag{6.9}$$

containg the system (s) and environment (e) part, providing the non-interacting Hamiltonian H_0, together with the interaction between the two $H_\mathrm{se} = V$. For our model described in Sect. 2, H_s contains the impurity and the resonator degrees of freedom, and H_e the fermionic leads and the bosonic bath. The complete setup is described by the density operator ρ_full which evolves following the Liouville equation [161]

$$\frac{\partial \rho_\mathrm{full}(t)}{\partial t} = -\mathrm{i}\,[H, \rho_\mathrm{full}(t)] =: \mathcal{L}_\mathrm{full} H, \tag{6.10}$$

for $t > 0$. We assume that for $t < 0$, the system and environment are decoupled for $V = 0$. We are ultimately only interested in the expectation values of the system observables, e.g. $A = A_\mathrm{s} \otimes \mathbb{1}_\mathrm{e}$, which can be calculated by

$$\langle A(t) \rangle = \mathrm{Tr}_\mathrm{full}\left[(A_\mathrm{s} \otimes \mathbb{1}_\mathrm{e})\, \rho_\mathrm{full}(t) \right] =: \mathrm{Tr}_\mathrm{s}\left[A_\mathrm{s} \rho_\mathrm{s}(t) \right] = \langle A(t) \rangle_\mathrm{s}. \tag{6.11}$$

Here, the reduced density matrix $\rho_\mathrm{s}(t)$ was introduced by integrating out the environment degrees of freedom:

$$\rho_\mathrm{s}(t) = \mathrm{Tr}_\mathrm{e}\left[\rho_\mathrm{full}(t) \right], \tag{6.12}$$

which we will refer to as $\rho_\mathrm{s}(t) = \rho(t)$ from now on. This shows that by knowing the reduced density matrix, we can compute the observables of interest. Thus, our objective is to derive the equation of motion for this quantity.

This can be done by applying projection techniques and some approximations, which we will specify in a moment. The derivation can be found in literature, see e.g. [71, 117, 162–164]. We will briefly outline the main steps to arrive at the master equation, following [164], before introducing the short, but instructive example of a damped quantum dot.

To arrive at an equation of motion for $\rho(t)$, it is usefull to utelize the interaction picture Equ. (3.6):

$$\rho_\mathrm{I}(t) = e^{-\mathrm{i}\, H_\mathrm{s} t} \rho(t) e^{\mathrm{i}\, H_\mathrm{s} t}. \tag{6.13}$$

By integrating Equ. (6.10) in the interaction picture and iteratively evaluating it, the Born series is obtained

$$\rho_\mathrm{I,full}(t) = \rho_\mathrm{I,full}(0) + \sum_{n=1}^{\infty} (-\mathrm{i})^n \int_0^t \mathrm{d}\,t_1 \int_0^{t_1} \mathrm{d}\,t_2 \ldots \int_0^{t_{n-1}} \mathrm{d}\,t_n \left[V_\mathrm{I}(t_1), \left[V_\mathrm{I}(t_2), \ldots \left[V_\mathrm{I}(t_1), \rho_\mathrm{I,full}(0) \right]_- \right]_- \right]_-, \tag{6.14}$$

with V in the interaction picture. To obtain the equation of motion for the reduced density, the environment is traced over. Differentiation leads to

$$\frac{\partial \rho_{\mathrm{I}}(t)}{\partial t} = \left[\frac{U_1(t)}{\partial t} + \frac{U_2(t)}{\partial t} + \mathcal{O}(V^3)\right] [U_1(t) + U_2(t) + \mathcal{O}(V^3)]^{-1} \rho(t), \tag{6.15}$$

where

$$U_n(t) := (-\mathrm{i})^n \int_0^t \mathrm{d}t_1 \int_0^{t_1} \mathrm{d}t_2 \ldots \int_0^{t_{n-1}} \mathrm{d}t_n \ \mathrm{Tr}_{\mathrm{e}} \left[V_{\mathrm{I}}(t_1), \left[V_{\mathrm{I}}(t_2), \ldots [V_{\mathrm{I}}(t_1), \rho_{\mathrm{e}} \otimes (\cdot)]_-\right]_-\right]_- . \tag{6.16}$$

We now assume V is such that $\mathrm{Tr}_{\mathrm{e}}\,[V_I(t)\rho_{\mathrm{e}}(t)]$ and therefore $U_1(t) = 0$. In the following example in Sect. 6.2.2, it will become clear why this is a reasonable assumption. Then further applying the Born-approximation [163], stating that the coupling between the system and environment is small, all terms in $\mathcal{O}(V^3)$ are neglected, leading to

$$\frac{\partial \rho_{\mathrm{I}}(t)}{\partial t} \approx -\int_0^t \mathrm{d}t_1 \ \mathrm{Tr}_{\mathrm{e}} \left[V_{\mathrm{I}}(t) \left[V_{\mathrm{I}}(t_1), \rho_{\mathrm{I,full}}(t)\right]_-\right]_- . \tag{6.17}$$

For weak coupling, we can further assume that the correlation time between the system and the environment is much shorter than the characteristic time scale of the system's dynamics. Consequently, it is reasonable to approximate, on the right-hand side of Equ. (6.17), that the environment remains in a thermal state and is only minimally affected by the interaction. Therefore, the environment and system densities can be treated as approximately uncorrelated, $\rho_{\mathrm{I,full}}(t) \approx \rho_{\mathrm{I,e}} \otimes \rho_{\mathrm{I}}(t)$, for all times t. This is a relatively strong restriction on the setup and leads to the Redfield equation [163, 165]

$$\frac{\partial \rho_{\mathrm{I}}(t)}{\partial t} \approx -\int_0^t \mathrm{d}t_1 \ \mathrm{Tr}_{\mathrm{e}} \left[V_{\mathrm{I}}(t) \left[V_{\mathrm{I}}(t_1), \rho_{\mathrm{I,e}} \otimes \rho_{\mathrm{I}}(t)\right]_-\right]_- . \tag{6.18}$$

Another strong restriction we impose on the system is the Markov approximation, which states that the environment is memoryless. This means that the time scale on which the correlations of the reservoir decay is much smaller than the typical time scale of the system. With this, the kernel of the integration decays fast enough to extend the upper integration bound to infinity. This leads to the Born-Markov master equation:

$$\frac{\partial \rho_{\mathrm{I}}(t)}{\partial t} \approx -\int_0^\infty \mathrm{d}t_1 \ \mathrm{Tr}_{\mathrm{e}} \left[V_{\mathrm{I}}(t) \left[V_{\mathrm{I}}(t_1), \rho_{\mathrm{I,e}} \otimes \rho_{\mathrm{I}}(t)\right]_-\right]_- . \tag{6.19}$$

Note that the Markov approximation implies that we can only treat reservoirs with two-time correlation functions being quasi-delta peaked in time. Equivalently, this corresponds to a flat or constant spectral density in frequency space, where the environment responds uniformly across all frequencies.

Finally, we want to impose that the master equation preserves the trace and the complete positivity of the density operator. It can be shown, which we will not do here but which can be found in e.g. [162, 163], that the most general master equation has to take the form

$$\frac{\mathrm{d}\rho(t)}{\mathrm{d}t} = \mathcal{L}\rho(t), \tag{6.20}$$

with the Liouvillian superoperator

$$\mathcal{L}\rho(t) = -\mathrm{i}[H, \rho(t)] + \sum_\nu \gamma_\nu \left(L_\nu \rho(t) L_\nu^\dagger - \frac{1}{2}[L_\nu^\dagger L_\nu, \rho(t)]_+\right). \tag{6.21}$$

L_i are called the jump operators and γ_i the dissipative rates. Given the jump operators, the rates can be determined using Fermi's Golden Rule. The first term in Equ. (6.20) with Equ. (6.21) is analog to the Liouville equation Equ. (6.10), describing the coherent dynamics of the isolated system. The sum describes the dissipative part of the system due to the environment and is called the dissipator acting on $\rho(t)$.

The master equation can practically only be solved analytically for a handful of systems. In the present thesis, we will use the QuTiP package from Python [166, 167] to numerically evaluate the master equation Equ. (6.20).

6.2.1. Jump operators and rates

In contrast to the Green function formalism, which is directly based on a microscopic Hamiltonian, the jump operators are most often chosen in a physically intuitive manner and the rates follow by Fermis Golden rule. In the following Sect. 6.2.2, we will, however, see that also the jump operators can be constructed more methodologically. Further, we will discuss in Sect. 6.2.3 that by choosing the right rates, it can be shown that a mapping between the master equation and the Keldysh action exists and that Green functions can be calculated using the Liouville super operator Equ. (6.21).

First, however, we choose the jump rate and operator pairs in the usual physically intuitive manner, as e.g. seen in [168]. Due to the Markov approximation, the master equation can only treat reservoirs that react to the system uniformly over the whole frequency space. Thus, the jump rates and operators $\{\gamma_\nu, L_\nu\}$ have to be frequency-independent. For the system under consideration in the present thesis, the Markovian assumption only holds when the single-particle distribution is frequency-independent. Thus, when utilizing the master equation, we consider the infinite-bias limit $V \to \infty$. To compare to the Hamiltonian Equ. (2.1), the jump operators and rates are then chosen as

1. Electron tunneling in from the left lead: $\{2\Gamma, c_1^\dagger\}$
2. Electron tunneling out into the right lead: $\{2\Gamma, c_M\}$
3. Photon annihilation $\{2\kappa(1 + b(\omega_0)), a\}$
4. Photon creation $\{2\kappa b(\omega_0), a^\dagger\}$.

We choose again symmetric coupling to the right and left lead. In contrast to the analysis within the other methods presented, we also include a finite dissipation rate κ for the resonator, which will, however, be assumed to be small. When further considering the zero temperature limit, the fourth process can be neglected due to low occupation in the resonator $b(\omega_0) \approx 0$ for bosonic temperatures $T_\mathrm{b} \ll \kappa\omega_0$.

6.2.2. A damped quantum dot

As an instructive example of how the master equation is applied, we consider a single spinless quantum dot coupled to a fermionic reservoir. The system and environment Hamiltonians are given by

$$H_\mathrm{s} = \varepsilon d^\dagger d, \qquad H_\mathrm{e} = \sum_k \varepsilon_k c_k^\dagger c_k, \tag{6.22}$$

with the coupling between the two systems

$$V = \frac{\tau}{\sqrt{N}} \sum_k \left[d^\dagger c_k + c_k^\dagger d \right]. \tag{6.23}$$

This represents a reduced version of the system described in Sect. 2.1. The reservoir is assumed to be in equilibrium. The calculations presented here follow the derivation in [71, 164], done for a damped harmonic oscillator instead of a quantum dot.

In the interaction picture, the coupling reads

$$V_\mathrm{I}(t) = \frac{\tau}{\sqrt{N}} \sum_k \left[d^\dagger c_k e^{\mathrm{i}(\varepsilon-\varepsilon_k)t} + c_k^\dagger d e^{\mathrm{i}(\varepsilon_k-\varepsilon)t} \right] = d^\dagger F(t) + F^\dagger(t) d, \tag{6.24}$$

with $F(t) := \frac{\tau}{\sqrt{N}} \sum_k c_k e^{\mathrm{i}(\varepsilon-\varepsilon_k)t}$. The $U_1(t)$-term, which is defined by Equ. (6.16) and neglected in Equ. (6.17), leads to expectation values of the form $\mathrm{Tr}_\mathrm{e}\left[F(t)\rho_\mathrm{e}\right] = \langle F(t)\rangle_\mathrm{e}$. When considering the environment to remain in equilibrium and not be affected by the coupling to the system, similar to the assumption of infinitely large leads in Sect. 3.3.1, these expectation values vanish. This validates the assumption $U_1(t) = 0$. Evaluating the commutators in the master equation Equ. (6.19), we obtain

$$\begin{aligned} \frac{\partial \rho_\mathrm{I}(t)}{\partial t} = -\int_0^\infty \mathrm{d}\,t_1 \; \mathrm{Tr}_\mathrm{e} \Big[& V_\mathrm{I}(t)V_\mathrm{I}(t_1)\left(\rho_\mathrm{e} \otimes \rho(t)\right)_\mathrm{I} + \left(\rho_\mathrm{e} \otimes \rho(t)\right)_\mathrm{I} V_I(t_1) V_\mathrm{I}(t) \\ & - V_\mathrm{I}(t)\left(\rho_\mathrm{e} \otimes \rho(t)\right)_\mathrm{I} V_\mathrm{I}(t_1) - V_\mathrm{I}(t_1)\left(\rho_\mathrm{e} \otimes \rho(t)\right)_\mathrm{I} V_\mathrm{I}(t) \Big]. \end{aligned} \tag{6.25}$$

Plugging in Equ. (6.24), we must evaluate terms containing the two-time correlation functions of F and $F^\dagger$. Terms like $\langle F(t)F(t_1)\rangle_\mathrm{e}$ and $\langle F^\dagger(t)F^\dagger(t_1)\rangle_\mathrm{e}$, containing correlations such as $\langle c_k c_{k'}\rangle_\mathrm{e}$ or $\langle c_k^\dagger c_{k'}^\dagger\rangle_\mathrm{e}$, can be reasonably negelected when considering thermal reservoirs. The other correlation functions can be calculated for a given reservoir. Exemplarily, we evaluate the correlation function

$$\begin{aligned} \int_0^t \mathrm{d}\,t_1 \; \langle F^\dagger(t)F(t)\rangle_\mathrm{e} &= \frac{|\tau|^2}{N} \int_0^\infty \mathrm{d}\,t_1 \; \sum_{k,k'} \langle c_k c_{k'}^\dagger \rangle e^{\mathrm{i}(\varepsilon-\varepsilon_k)t} e^{\mathrm{i}(\varepsilon-\varepsilon_{k'})t_1} \\ &\xrightarrow{N\to\infty} |\tau|^2 \int_0^\infty \mathrm{d}\,t_1 \; \int \mathrm{d}\,\omega \; \rho(\omega) \underbrace{\langle c(\omega)c^\dagger(\omega)\rangle_\mathrm{e}}_{f(\omega)} e^{\mathrm{i}(\varepsilon-\omega)(t-t_1)}, \end{aligned} \tag{6.26}$$

where we introduced the density of states $\rho_\mathrm{res}(\omega) = \frac{1}{N}\sum_k \delta(\omega-\varepsilon_k)$ in the thermodynamic limit, and assumed that the density operator is diagonal in the energy representation $\langle c_k c_{k'}^\dagger\rangle_\mathrm{e} = \langle c_k c_k^\dagger\rangle_\mathrm{e}\delta_{kk'}$. $f(\omega)$ is the Fermi distribution. We can use the relation

$$\int_0^\infty \mathrm{d}\,t e^{\pm\,\mathrm{i}\,\omega t} = \pi\delta(\omega) \pm P\left[\frac{\mathrm{i}}{\omega}\right] \tag{6.27}$$

to evaluate the time integral. The principle part $P[\cdot]$ leads to a shift in the quantum dot energy, analog to the Lamb shift, cf., for example, [63], and will not be further discussed here. The delta distribution leads to

$$\int_0^t \mathrm{d}\,t_1 \; \langle F^\dagger(t)F(t)\rangle_\mathrm{e} = \pi|\tau|^2\rho_\mathrm{res}(\varepsilon)f(\varepsilon), \tag{6.28}$$

where we recognize the frequency independent reservoir hybridization $\Gamma = \pi|\tau|^2\rho_\mathrm{res}(\varepsilon)$ from Equ. (3.42). Similarly, the other correlation functions can be evaluated. In the interaction picture, Equ. (6.25) then takes the form

$$\frac{\partial \rho_\mathrm{I}(t)}{\partial t} = \Gamma f(\varepsilon)\left[2d^\dagger\rho_\mathrm{I}(t)d - [dd^\dagger, \rho_\mathrm{I}(t)]_+\right] + \Gamma(1-f(\varepsilon))\left[2d\rho_\mathrm{I}(t)d^\dagger - [d^\dagger d, \rho_\mathrm{I}(t)]_+\right] \tag{6.29}$$

and in the Schrödinger picture

$$\frac{\partial\rho(t)}{\partial t} = -\mathrm{i}\,[H,\rho(t)] + \Gamma f(\varepsilon)\left[2d^\dagger\rho(t)d - [dd^\dagger,\rho(t)]_+\right] + \Gamma(1-f(\varepsilon))\left[2d\rho(t)d^\dagger - [d^\dagger d,\rho(t)]_+\right]. \quad (6.30)$$

This is the general form of the Lindblad master equation Equ. (6.20) with jump rates and operators

$$\{2\Gamma f(\varepsilon), d^\dagger\} \qquad \text{and} \qquad \{2\Gamma(1-f(\varepsilon)), d\}. \quad (6.31)$$

This is equivalent to the form of the jump operators chosen above in Sect. 6.2.1 in the infinite bias limit when considering only one quantum dot $M = 1$.

6.2.3. From Lindblad to Green functions

We saw in Sect. 3.6 that the Green function formalism is based on the microscopic Hamiltonian. As previously mentioned, the jump operators and rates for the Lindblad master equation are often selected intuitively, although they can also be derived more rigorously. However, the question remains how to choose the parameters in the Lindblad master equation method, so it describes the same underlying system as the Green function approach. For this purpose, we present two equations which link the two formalisms.

Firstly, considering a limit where the Markovian approximation of frequency independent reservoirs hold, there exists a direct mapping between the Markovian Lindblad formalism to the action, which directly follows from the microscopic Hamiltonian, as a Keldysh path integral [169–171]:

$$\begin{aligned} S &= \int \mathrm{d}t\, \left[\bar{\phi}_+\,\mathrm{i}\,\partial_t\phi_+ - \bar{\phi}_-\,\mathrm{i}\,\partial_t\phi_- - \mathrm{i}\,\mathcal{L}(\bar{\phi}_+,\bar{\phi}_-,\phi_+,\phi_-)\right], \\ \mathcal{L}(\bar{\phi}_+,\bar{\phi}_-,\phi_+,\phi_-) &= -\mathrm{i}(H_+ - H_-) + \sum_\nu \gamma_\nu \left[\bar{L}_{\nu,-}L_{\nu,+} - \frac{1}{2}\left(\bar{L}_{\nu,+}L_{\nu,+} + \bar{L}_{\nu,-}L_{\nu,-}\right)\right]. \end{aligned} \quad (6.32)$$

Here, the mapping holds for a purely fermionic or bosonic system, where $\phi_\pm$ are the fermionic or bosonic fields. ± indicates that the operator is evaluated on the forward or backward branches of the time contour respectively. Exemplarily, [171] showed, how this equation can be applied to the damped harmonic oscillator.

Additionally, the quantum regression theorem (QRT) [163, 172] allows the calculation of two-time correlation functions, such as Green functions, from the Liouvillian superoperator. For times $t \geq 0$ it takes the form [173]

$$\langle A(t)B\rangle = \mathrm{Tr}\left(Ae^{\mathcal{L}t}B\rho_{\mathrm{ss}}\right), \qquad \langle BA(t)\rangle \;= \mathrm{Tr}\left(Ae^{\mathcal{L}t}\rho_{\mathrm{ss}}B\right), \quad (6.33)$$

for two arbitrary operators A and B and the steady-state density operator ρ_{ss}. Due to the anticommutation of fermionic operators, the Liouvillian in Equ. (6.21) has to be adapted with an additional sign $\zeta_\nu = -1$ in front of the first dissipative term, whenever the jump operator is fermionic [174, 175]. By introducing the eigenspace of the Liouvollian

$$\mathcal{L}r_\alpha = \lambda_\alpha r_\alpha, \qquad \mathcal{L}^\dagger l_\alpha = \lambda_\alpha^* l_\alpha, \quad (6.34)$$

a spectral decomposition, similar to the Lehman representation [128] in closed systems, can be found [176]. The retarded Green function Equ. (3.23) of two arbitrary bosonic or fermionic operators d_x, d_y can therefore be written as

$$G^{\mathrm{R}}_{xy}(t) = -\mathrm{i}\,\theta(t)\sum_\alpha e^{\lambda_\alpha t}\left(\mathrm{Tr}\,[d_x r_\alpha]\,\mathrm{Tr}\left[l_\alpha^\dagger d_y^\dagger\,\rho\right] - \zeta\,\mathrm{Tr}\,[d_x r_\alpha]\,\mathrm{Tr}\left[l_\alpha^\dagger d_y^\dagger\,\rho\right]\right). \quad (6.35)$$

The Fourier transformation in the steady-state limit leads to

$$G^{\mathrm{R}}_{xy}(\omega) = \sum_{\alpha} \frac{\mathrm{Tr}\left[d_x r_\alpha\right] \mathrm{Tr}\left[l_\alpha^\dagger \left[d_y^\dagger, \rho_{\mathrm{ss}}\right]_{-\zeta}\right]}{\omega - i\lambda_\alpha}, \tag{6.36}$$

with $\zeta = +1$ for the bosonic Green function and $\zeta = -1$ for fermionic one. We refer to appendix C for more details on the calculation. A similar expression can also be found for the lesser Green function

$$G^{<}_{xy}(\omega) = \zeta \sum_{\alpha} \left(\frac{\mathrm{Tr}\left[d_x r_\alpha\right] \mathrm{Tr}\left[l_\alpha^\dagger \rho_{\mathrm{ss}} d_y^\dagger\right]}{\omega - i\lambda_\alpha} - \frac{\mathrm{Tr}\left[d_y^\dagger r_\alpha\right] \mathrm{Tr}\left[l_\alpha^\dagger d_x \rho_{\mathrm{ss}}\right]}{\omega + i\lambda_\alpha} \right). \tag{6.37}$$

In our following studies of the interacting model described in Sect. 2, we aim to compare the Lindblad master equation results with the perturbative results, compare Sect. 4, within the Green function formalism. It is however important to note, that even though both methods are capable of describing the same underlying physics, there are differences in the field of applicability. In the limit of small interaction U and A_{ij}^2, small resonator dissipation κ, and large voltages V, both approaches are well controlled and lead to comparable results. However, we will see that even in this part of the parameter space, a direct comparison of the two methods is not possible, due to the underlying different character of the description in first-order perturbation theory and Lindblad master equation. This will be specified in Sects. 9 and 11. Furthermore, different observables are more or less efficiently determined in either method. We will address this further in Sect. 11. Here, we just remark that the frequency-dependent observables, such as e.g. the spectral function Equ. (3.56), are straightforwardly derived from the Green function formalism, while it is numerically more cumbersome to derive them from the Lindblad master equation. Further, the Green functions allow in general for more analytic insights. On the other hand, we will see that other observables, such as, e.g., the many-body spectrum, are more easily obtained with the master equation approach.

6.2.4. Observables

In general, all expectation values of system parameters can be obtained as introduced in Equ. (6.11), when the reduced density matrix is known. This includes, for example, the average system energy or the mean occupation of different system states. Here, we want to briefly comment on how to obtain dynamical variables such as the currents within the Lindblad master equation formalism.

The particle current through the fermionic system can be calculated by examining the change in particle number on one of the quantum dots, cf. [168]. The dynamics of the mean occupation of state j is directly given by the Liouvillian Equ. (6.21) and the particle current through the state is given by

$$I_j^N = \frac{\mathrm{d}\langle n_j\rangle}{\mathrm{d}t} = \frac{\mathrm{d}}{\mathrm{d}t}\left[\left(n_j \otimes \mathbb{1}_{\mathrm{e}}\right) \rho_{\mathrm{full}}\right] = \mathrm{Tr}\left[n_j \mathcal{L} \rho\right]. \tag{6.38}$$

The evaluation of this quantity depends on the setup. For the model introduced in Sect. 2 with the jump operators from Sect. 6.2.1, the particle current from the left or right lead through the last or first dot takes the form

$$I_L^N = 2\Gamma\left(1 - \langle c_1^\dagger c_1\rangle\right), \qquad I_R^N = -2\Gamma\langle c_M^\dagger c_M\rangle, \tag{6.39}$$

which is shown in appendix B in more detail.

On a similar footing, the energy current from the fermionic system into the bosonic one can be analyzed by considering the change in energy in the latter, which is the general energy current into the resonator and given by

$$I_{\mathrm{b}}^{E} = \frac{\mathrm{d}\langle H_{\mathrm{b}} \rangle}{\mathrm{d}t} = \mathrm{Tr}\left[H_{\mathrm{b}} \mathcal{L} \rho \right]. \tag{6.40}$$

In appendix B, it is shown that the energy current for our given system described in Sect. 2 is

$$\begin{aligned} I_{\mathrm{b}}^{E} &= -\mathrm{i}\,\omega_0 \sum_{i,j} \left[A_{ij} \langle c_i^{\dagger} c_j a^{\dagger} \rangle + A_{ij}^{*} \langle c_j^{\dagger} c_i a \rangle \right] - 2\kappa (1 + b(\omega_0)) \omega_0 \left\langle a^{\dagger} a \right\rangle + 2\kappa b(\omega_0) \omega_0 \left(1 + \left\langle a^{\dagger} a \right\rangle \right) \\ &= I_{\mathrm{f}\to\mathrm{b}}^{E} + I_{\mathrm{e}\to\mathrm{b}}^{E}. \end{aligned} \tag{6.41}$$

This expression has two contributions. The first one ($I_{\mathrm{f}\to\mathrm{b}}^{E}$) is the energy current from the fermionic system into the resonator due to the coupling. This provides an expression for the current, which can be compared with the energy dissipation of the fermionic system Equ. (3.68) from the Green function formalism. The other term ($I_{\mathrm{e}\to\mathrm{b}}^{E}$) originates from the dissipation into or from the bosonic bath in Equ. (2.17). In a steady state, we expect no change in energy of the bosonic system and therefore a balance between the terms reached, so that $I_{\mathrm{b}}^{E} = 0$.

Part III.

Coupling Matter to a Quantum Cavity

In the following part, we discuss the light-matter coupling occurring when a linear impurity system is placed in a light cavity. First, we show how the light mode couples to the lattice fermions using the Peierls substitution in Coulomb gauge in Chapter 7. We extend the well-known substitution in homogenous systems to the impurity system under consideration and see, how the finite extent of the light field, in the latter case, leads to additional boundary terms. We also discuss the expansion of the exponential containing the Peierls phase in orders of the vector potential and develop a method to include the second-order terms in the perturbative treatment. Additionally, we study the Power-Zienau-Wooley transformation into the dipole gauge, which we also apply to the inhomogenous impurity system. In Chapter 8, we study the effect of the effective fermion-fermion long-range interaction stemming from the light-matter coupling on the electronic conductance through the impurity. We see that it can lead to interference effects, which appear as dips in the linear conductance. Finally, we study the energy transfer between the fermionic and bosonic systems within a non-equilibrium setup in Chapter 9. To this end, we consider a finite particle current through a double quantum dot, which is embedded in a light cavity.

7. Quantum Peierls Substitution

As outlined in the introductory Sect. 1.2, the control of matter using light has emerged as a burgeoning field within the condensed matter community in recent years. To circumvent unwanted heating effects that arise when pumping with coherent lasers, a promising pathway is to couple solids with quantum light confined inside a cavity. This coupling presents the need for a robust theoretical framework capable of describing the coupling of matter with quantum light [177, 178].

One widely applied approach to model light-matter coupling was introduced by Peierls [179], who proposed a method where the electronic degrees of freedom of a solid, which are described quantum mechanically, couple to a classically described electromagnetic field within the cavity. In this semi-classical approach, the electromagnetic field is incorporated into the system by introducing a phase factor into the hopping parameter of the tight-binding model, with this phase being dependent on the vector potential. A more detailed discussion of this method will follow in the subsequent Sect. 7.1.1. The Peierls substitution can be extended to a fully quantum mechanical description by quantizing the vector potential of the light field, as done e.g. in Ref. [82, 86, 180], leading to the hopping in Equ. (2.18). However, several challenges arise when adopting this quantum description, many of which are currently the focus of active discussions within the field.

An important assumption in the derivation of the Peierls substitution is the smoothness of the vector potential. One, thus, has to prevent abrupt changes associated with boundaries and, consequently, this approach is most commonly applied to systems with periodic boundary conditions [81, 83–85]. In such cases, the vector potential is assumed to vary smoothly across the entire solid. However, in the present thesis, we focus on systems where only a small region of the solid is coupled to the cavity. As a result, the vector potential must vanish outside this localized region, and it can no longer be considered quasi-constant on the scale of the entire system. There have been studies on these finite open systems interacting with light [142, 181, 182]. We aim here at a more thorough discussion on how light couples to such systems, which will be discussed in Sects. 7.1.2 and 7.4.

Another issue concerning the light-matter coupling relates to the truncation of the Hilbert space and maintaining gauge invariance. In practice, the Hilbert space of the solid has to be truncated by only considering a limited number of bands within the tight-binding model, a strategy that is commonly adopted and also used in the present thesis. Similarly, the Hilbert space of the electromagnetic field is truncated by restricting the analysis to a few modes of the field. Although the general theory is gauge-invariant, this is not necessarily true for the truncated description [83, 85, 183]. Specifically, Wannier orbitals can take on different shapes and meanings in different gauges [83, 184, 185], raising the question of which degrees of freedom have to be considered in which gauge to best represent the observables of interest. These issues will be explored in more depth in Sect. 7.4.

Another critical problem is the perturbative treatment of the Peierls phase. When considering weak couplings between the solid and the light field, it may be tempting to expand the Peierls phase, only taking into account low orders in the interaction. However, this approach can introduce artifacts and lead to unphysical phenomena, such as spurious superradiance [84, 186] and violations of the gauge invariance [85]. This issue will be addressed in more detail in Sect. 7.3.

In the following chapter, we neglect the nearest-neighbor Coulomb interaction $U = 0$ in Equ. (2.6).

7.1. Derivation of Peierls substitution

To obtain a better understanding of the Peierls substitution and which approximations are applied, we take a closer look at its derivation, closely following Ref. [81]. First, we consider a general three-dimensional solid in a cavity within the dipole approximation, where the vector potential of the electromagnetic field $\vec{A}$ is assumed to change smoothly over space. Subsequently, we analyze the case where only a finite part of the fermionic system is emerged in the cavity and the dipole approximation is not satisfied. We focus particularly on the linear chain in this scenario. First, the electromagnetic fields are treated classically, whereas the lattice fermions are treated quantum mechanically, before quantizing the light fields as well.

7.1.1. In the dipole approximation

The description of the fermionic system on a lattice without the cavity was introduced in Sect. 2.1.2. The coupling of the fermions with an electromagnetic field can be introduced via the minimal coupling and the single-particle Hamiltonian Equ. (2.11) takes the form

$$H = \frac{\left(\vec{p} - q\vec{A}(\vec{r})\right)^2}{2m} + V(\vec{r}) + q\phi(\vec{r}), \tag{7.1}$$

with the scalar potential ϕ and the vector potential $\vec{A}$. $\vec{p}$ and $\vec{r}$ are the canonical momentum and position operators respectively. q is the general charge of the electronic particle, which we will specify further below. The expansion in the Wannier orbitals Equ. (2.12) is no longer possible straightforwardly due to the mixing of the fermionic and bosonic degrees of freedom. Alternatively, an additional phase is included in the expansion of the wave function $\Psi(\vec{r})$ which consequently removes the vector-potential contribution from the kinetic term.

$$\Psi(\vec{r}) = \sum_m \psi_m \exp\left(\mathrm{i}\, qG_m(\vec{r})\right) a_m(\vec{r}), \qquad G_m(\vec{r}) = \int_{\vec{R}_m}^{\vec{r}} \mathrm{d}\vec{r}' \cdot \vec{A}(\vec{r}'), \tag{7.2}$$

with the integral following a straight path from $\vec{R}_m$ to $\vec{r}$. The single-orbital approximation was used. This truncation of the Hilbert space is subject to discussions [83, 85, 86] and will be explored in more detail in the context of the gauge freedom in Sect. 7.4. In this expansion, the orbitals are hybrid light-matter objects.

It can be shown, see. [81] for more details, that the Hamiltonian acting on $\Psi(\vec{r})$ takes the form

$$H\Psi(\vec{r}) = \sum_m \psi_m \exp\left(\mathrm{i}\, qG_m(\vec{r})\right) \left[\frac{\left[\vec{p} - q(\vec{A}(\vec{r}) - \vec{\nabla}G_m(\vec{r}))\right]^2}{2m} + V(\vec{r}) + q\phi(\vec{r}) \right] a_m(\vec{r}). \tag{7.3}$$

By applying the dipole approximation, which assumes that the vector potential does not change significantly over the lattice, $\vec{\nabla}G_m$ can further be evaluated. We use the parametrization $\vec{r}' = \vec{R}_m + \lambda(\vec{r} - \vec{R}_m)$ with $\lambda \in [0,1]$ to describe the straight line between $\vec{R}_m$ and $\vec{r}$. The integral then reads

$$\begin{aligned}
\vec{\nabla}G_m &= \int_0^1 \mathrm{d}\lambda\, \vec{\nabla}\left[(\vec{r} - \vec{R}_m) \cdot \vec{A}\left(\vec{R}_m + \lambda(\vec{r} - \vec{R}_m)\right)\right] \\
&= \int_0^1 \mathrm{d}\lambda\, \left[(\vec{r} - \vec{R}_m) \times (\vec{\nabla} \times \vec{A}) + \vec{A} \times (\vec{\nabla} \times (\vec{r} - \vec{R}_m)) + (\vec{A} \cdot \vec{\nabla})(\vec{r} - \vec{R}_m) + ((\vec{r} - \vec{R}_m) \cdot \vec{\nabla})\vec{A}\right] \\
&= \int_0^1 \mathrm{d}\lambda\, \left[\lambda(\vec{r} - \vec{R}_m) \times \vec{B} + \vec{A} + \left((\vec{r} - \vec{R}_m) \cdot \vec{\nabla}\right)\vec{A}\right],
\end{aligned} \tag{7.4}$$

where $\vec{B}$ is the magnetic field. Note, that we did not write out the $\vec{r}'$ dependence of $\vec{A}$ explicitly in every expression here. By applying integration by parts, the integral over the vector potential can be evaluated as

$$\begin{aligned}\int_0^1 \mathrm{d}\lambda\, \vec{A}\left(\vec{R}_m + \lambda(\vec{r} - \vec{R}_m)\right) &= \lambda \vec{A}\left(\vec{R}_m + \lambda(\vec{r} - \vec{R}_m)\right)\Big|_0^1 - \int_0^1 \mathrm{d}\lambda\, \lambda \frac{\mathrm{d}}{\mathrm{d}\lambda} \vec{A}\left(\vec{R}_m + \lambda(\vec{r} - \vec{R}_m)\right) \\ &= \vec{A}(\vec{r}) - \int_0^1 \mathrm{d}\lambda\, \left((\vec{r} - \vec{R}_m)\cdot\vec{\nabla}\right)\vec{A}. \end{aligned} \tag{7.5}$$

So, the second term of Equ.(7.5) cancels the last term in Equ. (7.4) and the total expression reads

$$\vec{\nabla} G_m = \vec{A}(\vec{r}) + \int_0^1 \mathrm{d}\lambda\, \lambda(\vec{r} - \vec{R}_m) \times \vec{B}(\vec{R}_m + \lambda(\vec{r} - \vec{R}_m)). \tag{7.6}$$

When assuming that the fields do not vary significantly over the span of the system and using the localization of the Wannier function $a_m(\vec{r})$ in Equ. (7.3), we can approximately take $\vec{r} \approx \vec{R}_m$ in Equ. (7.6) and therefore neglect the integral over the magnetic field. For this to hold exactly, the magnetic field $\vec{B}$ must vanish. It remains unclear what this implies for the ability of the Peierls substitution to accurately describe the interaction with magnetic fields. Nevertheless, in the case of a linear system, which we are ultimately interested in in the present thesis, the magnetic field and therefore the second term in Equ. (7.6), always vanishes. Thus, we will not comment further on this.

Using $\vec{\nabla} G_m \approx \vec{A}$, the Hamiltonian acting on the wave function Equ. (7.3) can be written as

$$H\Psi(\vec{r}) = \sum_m \psi_m \exp(\mathrm{i}\, q G_m) \left[\frac{\vec{p}^2}{2m} + V(\vec{r}) + q\phi(\vec{R}_m)\right] a_m(\vec{r}) \tag{7.7}$$

where the dependence on the vector potential was moved from the kinetic term into an additional phase in the orbitals.

The additional phase in the wave function leads to a renormalization of the matrix elements Equ. (2.13) in the tight-binding Hamiltonian. The diagonal terms do not change. But the off-diagonal hopping parameters change compared to the parameters without an electromagnetic field:

$$\begin{aligned} t_{mm'} &= -\int \mathrm{d}\vec{r}\, a_m^*(\vec{r}) H a_{m'}(\vec{r}) \\ &\to -\int \mathrm{d}\vec{r}\, a_m^*(\vec{r}) H a_{m'}(\vec{r}) e^{-\mathrm{i}\, q G_m(\vec{r}) + \mathrm{i}\, q G_{m'}(\vec{r})} \\ &= -e^{\mathrm{i}\, q \int_{\vec{R}_{m'}}^{\vec{R}_m} \mathrm{d}\vec{r}\cdot\vec{A}(\vec{r})} \int \mathrm{d}\vec{r}\, a_m^*(\vec{r}) H a_{m'}(\vec{r}) e^{\mathrm{i}\, q \Phi_{\vec{R}_{m'},\vec{r},\vec{R}_m}}. \end{aligned} \tag{7.8}$$

The change in the hopping parameter due to the first phase factor is called Peierls substitution and is often considered in the literature, see e.g. [84, 86, 180], to describe light-matter coupling. The additional phase is given by the plaquette integral $\Phi_{\vec{R}_{m'},\vec{r},\vec{R}_m} := \oint_{\vec{R}_{m'}\to\vec{r}\to\vec{R}_m\to\vec{R}_{m'}} \mathrm{d}\vec{r}'\, \vec{A}(\vec{r}')$. This corresponds to the flux through the triangle enclosed by the path $\vec{R}_{m'} \to \vec{r} \to \vec{R}_m \to \vec{R}_{m'}$. When using that the Wannier orbitals are well localized at the lattice sites, the contribution in the integral in Equ. (7.8) is of the order of the magnetic flux per lattice plaquette [187]. This term is generally very small in practical applications [83]. However, when we consider a finite impurity model, as discussed in the following, this is no longer true when the vector potential changes significantly between two lattice sites, and one has to consider Peierls substitution more carefully. Fortunately, the two phase factors G_m and $G_{m'}$

can more easily be added for linear systems as the integral over the path $\vec{R}_{m'} \to \vec{r} \to \vec{R}_m \to \vec{R}_{m'}$ on a straight line always vanishes. Thus, the plaquette term is zero in linear systems, which are the systems under consideration in the present thesis. In one dimension, when the lattice is directed in x-direction, the hopping parameters then read

$$t_{ij} \to t_{ij} e^{\mathrm{i}\, q \int_{R_j}^{R_i} \mathrm{d}x'\, A(x')} . \tag{7.9}$$

Here A and R_i are the x-component of $\vec{A}$ and $\vec{R}_i$ respectively. We will only consider linear systems in the present thesis, so the discussion of the (non-)vanishing flux is a concern for future research.

Additionally to the renormalized hopping, the scalar potential in Equ. (7.7) has to be included in the tight-binding formulation. When applying the Coulomb gauge ($\vec{\nabla} \cdot \vec{A} = 0$), the electromagnetic field can purely be described by the transverse vector potential [83, 188]. This gauge is often considered in condensed matter studies, cf. [189] and references therein. The last term in Equ. (7.7), containing ϕ, therefore dissapears. In the Coulomb gauge, the electromagnetic field can hence be included by simply renormalizing the hopping parameter with the Peierls phase Equ. (7.9) including the transverse vector potential. Still, in this formulation, the light-matter coupling enters in a highly non-linear way entangling the matter and light degrees of freedom. It further only includes local, on-site orbital contributions. These issues will be discussed in Sect. 7.4 in more detail.

Finally, Peierls substitution Equ. (7.9) can easily be extended to quantum light when considering a constant vector potential A. The substitution can then describe the interactions of a tight-binding model introduced in Sect. 2.1 with quantum light from a cavity. At this point, we also set $q = -e = -1$. In the present thesis, we choose the vector potential in negative x-direction. We point out that this orientation is different from what is often found in literature [84, 86, 180]. The quantization of the vector-potential $A = -A_0(a + a^\dagger)$, where $A_0 := \frac{1}{\sqrt{2\omega_0 \varepsilon_0 V}}$ [180], leads to the hoppings

$$t_{ij} \to t_{ij} \begin{cases} e^{\mathrm{i}\, g_{ij}(a+a^\dagger)} & \text{for } R_j > R_i \\ e^{-\mathrm{i}\, g_{ij}(a+a^\dagger)} & \text{for } R_j < R_i \end{cases} \tag{7.10}$$

for the tight-binding model with $g_{ij} = g_{ji} := A_0 |R_i - R_j|$. The phase is, thus, given by the angular mode frequency ω_0, the free permittivity ε_0, and the quantization volume V, which are defined by the cavity under consideration. We call the exponential function containing the Peierls phase, the Peierls factor in the present thesis.

This formulation is equivalent to the Peierls substitution appearing in the introduction of the model in Equ. (2.18) when considering only finite nearest-neighbor hopping with $t_{i(i+1)} \neq 0$. This is a reasonable assumption when considering well-localized orbitals. For completeness, we reproduce the coupling Hamiltonian at this point

$$H_\mathrm{f} + H_\mathrm{fb} = \sum_j \varepsilon_j c_j^\dagger c_j + t \sum_{j=1}^{M-1} \left[e^{\mathrm{i}\, g_{j(j+1)}(a+a^\dagger)} c_{j+1}^\dagger c_j + \text{h.c.} \right] . \tag{7.11}$$

7.1.2. Peierls substitution in the impurity system - violating the dipole approximation

A very important assumption in the derivation of Peierls substitution is that the electromagnetic field does not change significantly over the extent of the system. In our studies, however, we consider a system, where interaction with the electromagnetic field, only takes place in a small region of the overall system: the fermionic system is split into a central quantum dot region and leads. Hence, for small central impurities, where the vector potential is suddenly ramped up, the dipole approximation no longer holds.

Therefore, we will take a closer look, at how the presented derivation applies to a system, where the electromagnetic field is only applied on a finite part of an infinite lattice. For this discussion, we will focus on the linear chain, which is ultimately the system under consideration and presented in Sect. 2. This means that the leads in Equ. (2.4) are modeled by half-infinite linear chains. In this case, we assume a coordinate system, so the lattice is oriented in x-direction. Thus, we only consider the x-component of the lattice vector (R_m) and we choose a vector potential with $\vec{A}(\vec{r}) = A(x)\vec{e}_x$. In the derivation in the previous section, the integrals in Equs.(7.4)-(7.6) are then evaluated on the x-axis and $\vec{\nabla} G_m = \partial_x G_m$. In Equ. (7.8) for the linear system, the y and z component can be integrated out, leading to an effective x-integral.

The interacting impurity quantum dots are assumed to be located within the spacial interval $x \in [0, L]$. The electromagnetic field is thus given by a vector potential of the form

$$A(x) = \begin{cases} A_0(x), & \text{if } x \in [0, L] \\ 0, & \text{otherwise.} \end{cases} \tag{7.12}$$

$A_0(x)$ is assumed to fulfill the dipole approximation. So the vector potential varies sizeable only at the boundaries of the impurity region $x = 0, L$. The calculation of

$$\partial_x G_m(x) = \partial_x \int_{R_m}^{x} \mathrm{d}\, x'\, A(x') \tag{7.13}$$

analog to Equ. (7.4) for the linear chain has to be performed more carefully. Especially, the integration by parts analog to Equ. (7.5) cannot be performed without considering the boundary of the vector potential with more care.

When evaluating the integral over the vector potential, three different scenarios have to be distinguished: (i) x is outside the part of the lattice embedded in the cavity and R_m is arbitrary, (ii) x and R_m are inside and (iii) x is inside and R_m is outside. For the first scenario, we consider the exemplary case where $x < 0$ and $R_m \in [0, L]$. The other cases are evaluated analogously. With this

$$\partial_x G_m(x) = \partial_x \int_{R_m}^{0} \mathrm{d}\, x'\, A_0(x') = 0 \tag{7.14}$$

vanishes. So does the vector potential at x and, thus, $\partial_x G_m(x) = A(x)$ holds. In the second scenario, the evaluation is analog to Equs. (7.4)-(7.6) in one dimension, as the vector potential is homogenous between x and R_m. Therefore $\partial_x G_m(x) = A(x)$ also holds. For the third scenario, we consider again an examplary case with $R_m < 0$ and

$$\partial_x G_m(x) = \partial_x \int_{0}^{x} \mathrm{d}\, x'\, A_0(x'). \tag{7.15}$$

$R_m > L$ is evaluated analogously. In this case, the integral G_m can still be calculated analogously to Equs. (7.4)-(7.6) in one dimension, while replacing $R_m \to 0$ and $\partial_x G_m(x) = A(x)$ follows. Therefore, the additional term $\partial_x G_m$ analog to Equ. (7.3) cancels out the vector potential as well and the derivation still holds so far. At this point, it is important to note that due to $A(x)$ being discontinuous, G_m is technically not differentiable directly at the borders $x = 0, L$. However, because at these points, also A

is not well defined, it is reasonable to bridge the definition at these points with $\partial_x G_m(x)|_{x=0} = A(0)$ and $\partial_x G_m(x)|_{x=L} = A(L)$.

Now, we determine the renormalization in the hopping parameter in Equ. (7.10) for the linear chain, where we directly assume, that only nearest neighbor hopping contributes in the non-interacting fermionic system, $t_{m,m'} = 0$ for $m \neq m' \pm 1$. This is a reasonable assumption when considering well-localized orbitals. So, we only consider nearest neighbor $R_m, R_{m'}$, where we still have to distinguish between three cases: either both sites are outside the interacting region, both are inside, or one is inside the interacting region and one is outside. The first case is trivial and the phase vanishes with vanishing vector potential. In the second case, we recover the result of the general Peierls substitution for linear systems and the hopping obtains the Peierls phase depending on the vector potential

$$t_{m(m\pm1)} \to t_{m(m\pm1)} e^{\mathrm{i}\, q \int_{R_{m\pm1}}^{R_m} A_0(x)\, \mathrm{d}x}, \tag{7.16}$$

which is analog to Equ. (7.8) for the linear chain. In the last case, however, the phase depends on how and the exact position, where the vector potential vanishes. Assuming the exemplary case of nearest neighbors with $R_m < L$ and $R_{m+1} > L$, the hopping takes the form

$$t_{m(m+1)} \to t_{m(m+1)} e^{\mathrm{i} \int_{L}^{R_m} A_0(x)\, \mathrm{d}x}. \tag{7.17}$$

This implies that the hopping from the impurity region to the leads, which are no longer embedded in the cavity will also be renormalized by the electro-magnetic field.

In the following, we extend the impurity region to include the boundary sites of the leads. Specifically, we redefine the impurity region to consist of the M quantum dots embedded in the cavity, along with the first two boundary sites of the leads. Consequently, the number of sites is redefined by absorbing the two lead sites, such that $M + 2 \to M$. The Peierls substitution is then applied exclusively to this expanded impurity region, while the remaining lead sites remain interaction-free. As a result, the Peierls phase differs between the bulk of the impurity region and its boundary.

As a simple example, we consider the case, where the vector potential is considered to be constant in the impurity region $A_0(x) = -A_0$ and $x = 0, L$ are points directly in the middle between two lattice sites. All lattice sites are separated by the lattice constant R_0. We obtain

$$t_{m(m\pm1)} \to \begin{cases} t_{m(m\pm1)} e^{\mp\mathrm{i}\, q R_0 A_0} & \text{in the bulk,} \\ t_{m(m\pm1)} e^{\mp\mathrm{i}\, q R_0 / 2 A_0} & \text{at the boundaries.} \end{cases} \tag{7.18}$$

Conclusion

In this section, we have shown that the Peierls substitution, which describes light-matter coupling and is usually applied for homogenous systems, can also be extended to inhomogenous impurity systems. For the latter, the vector potential is assumed to only be finite in a finite part of the lattice. This results in the violation of the dipole approximation, a key assumption in deriving the Peierls phase, leading to differing phase magnitudes at the impurity boundary compared to the bulk. The Peierls phase at the boundary strongly depends on how exactly the vector potential is varied. We provided an example, where the Peierls phase at the boundaries is given by half the Peierls phase of the bulk.

It is worth noting, that the step-like vector potential assumed in this example, is not necessarily applicable in practical systems. A more realistic approach would for example gradually increase the vector potential over the extent of a handful of lattice sites. This would lead to a varying Peierls phase over an extended region at the boundaries and is subject to future research.

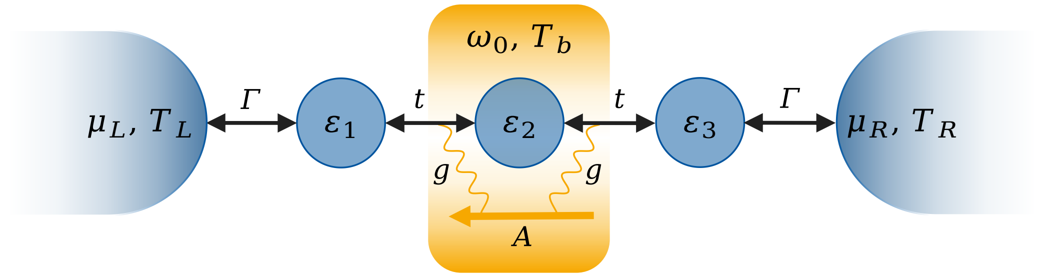

Figure 7.1.: Sketch of the impurity model coupled to a light cavity. One quantum dot with on-site energy ε_2 is placed into a single-mode cavity with frequency ω_0 at temperature T_b. Additionally, two auxiliary quantum dots with on-site energies ε_1 and ε_3, together with the other quantum dot form the impurity. They are coupled by the hopping amplitude t, which is renormalized by the Peierls phase $\sim g$ due to the electromagnetic field with vector potential. The vector potential has only a non-vanishing component (A) along the linear impurity system. The impurity is coupled on either side to two non-interacting leads with chemical potential $\mu_{L,R}$ and temperature $T_{L,R}$.

7.2. Particle-hole symmetry

To determine how the PHS point changes when considering Peierls coupling, we perform the transformation discussed in Sect. 2.1.1 together with $a \to \tilde{a} = -a$. The Hamiltonian of the central interacting part is transformed as

$$\tilde{H}_{1\mathrm{D}} + \tilde{H}_\mathrm{b} + \tilde{H}_\mathrm{fb} = -\sum_{j=1}^{M} \varepsilon_j c_j^\dagger c_j + \omega_0 a^\dagger a + t \sum_{j=1}^{M-1} \left[e^{-\mathrm{i}\, g_{j(j+1)}\left(a+a^\dagger\right)} c_j^\dagger c_{j+1} + e^{\mathrm{i}\, g_{j(j+1)}\left(a+a^\dagger\right)} c_{j+1}^\dagger c_j \right], \tag{7.19}$$

where we directly neglected all emerging constant terms. Thus, the Peierls substitution does not shift the PHS point $\vec{\varepsilon}_\mathrm{PHS} = (0, 0, ...0)$. This also holds for the truncated expansion of the Peierls factor Equ. (2.19). In contrast to the Coulomb interaction in Sect. 2.1.1, which is proportional to the filling of the quantum dot, in the Peierls coupling, the light couples to the hopping between the dots. It is plausible that this is the reason why the PHS point is not affected by the presence of the cavity. On the other hand, the capacitive coupling introduced in Sect. 2.2.2 couples the resonator mode to the occupation of the site. As we will see in Sect. 10.1, this indeed shifts the PHS point.

7.3. Expansion of the Peierls phase

When considering weak electromagnetic fields, an intuitive approach to treat the light-matter coupling is only accounting for the paramagnetic term linear in the vector potential [180, 190–192]. When considering only the linear term in the vector potential of the Peierls factor Equ. (2.18), the coupling is brought in the general form Equ. (2.21) with $A_{ij} = \mathrm{i}\, g_{ij} t \left(\delta_{i,j+1} - \delta_{i+1,j}\right)$. We have seen in Sect. 3.6.1 that the photonic degrees of freedom can be integrated out, leading to an effective fermionic interaction. This interaction can be treated perturbatively as described in Sects. 4 and 5.

However, it is known that approximating the Peierls phase by expanding the exponential and truncating it for small orders of the couplings g can lead to unphysical behavior [84, 193]. The importance of including higher orders for strong coupling and the regime of high-photon-occupation has been discussed in [85]. Further, an artificial superradiant phase emerges, when only considering the phase approximated in the first order in the coupling [84]. These phenomena are accompanied by the aforementioned breaking of the gauge invariance of the system [84, 182], which will be further discussed in Sect. 7.4.

The spurious superradiance is closely related to the superradiance reported in the equilibrium Dicke model, cf. [77–79, 88, 89], in which higher-order couplings are neglected. In this model, one distinguishes between two superradiant phases: (i) in equilibrium, where a second-order phase transition breaks the parity symmetry of the system [53], and (ii) in non-equilibrium, where a continuous transition is found for dissipative systems [79]. The latter is a real superradiant phase and has been experimentally verified [194, 195]. On the other hand, the superradiance in equilibrium was found to be artificial due to only including contributions in the first order in the vector potential. However, including the diamagnetic term in second order g^2 removes the transitions [186].

In this section, we show the general importance of the second-order term even for small couplings. As an examplary model, we focus on the system depicted in Fig. 7.1, where one quantum dot is placed in the cavity and is coupled via two additional quantum dots to the non-interacting leads. The system is therefore described by the Hamiltonian introduced in Sect. 2.1 with $M = 3$ coupled via the Peierls phase Equ. (2.18) to the electromagnetic field. Because we only consider one quantum dot inside the cavity, we do not have to distinguish between a Peierls phase in the bulk and the boundary of the impurity and can choose the coupling at the boundaries to be constant $g_{12} = g_{21} := g$. Additionally, we define $\lambda := \mathrm{i}\, gt$. We tune the three quantum dots simultaneously $\varepsilon_1 = \varepsilon_2 = \varepsilon_3 = \varepsilon$.

In the following, we present the different physical behaviors arising when only considering the linear term in the coupling of the Peierls factor compared to when including all orders in the coupling for this setup. Our goal is to understand why this difference occurs, even within the small coupling regime. To this end, we analyze the influence of the light-matter coupling on the mean occupation of the quantum dots as an example. Finally, we aim to provide an approach extending the perturbative method introduced in Sect. 4, which includes the second order of the vector potential systematically in the light-matter coupling.

7.3.1. Lowest-order expansion

First, we analyze the system within ED, introduced in Sect. 6.1. To minimize the numerical effort, we decouple the fermionic leads, $\Gamma = 0$. For the chosen parameter set, it was established that the truncated bosonic Fock space with $N = 10$ leads to converged results. In Fig. 7.2(a), the mean dot occupation for the impurity quantum dots is shown as a function of the detuning ε. The Peierls factor is expanded and truncated in different orders of g according to Equ. (2.19), which we reproduce here up to the second order in the coupling for completeness:

$$H_\mathrm{f} + H_\mathrm{fb} = \sum_j \varepsilon_j c_j^\dagger c_j + t \sum_{j=1}^{M-1} \left[\left(1 + \mathrm{i}\, g_{j(j+1)} \left(a + a^\dagger\right) - \frac{g_{j(j+1)}^2}{2} \left(a + a^\dagger\right)^2 \right) c_{j+1}^\dagger c_j + \text{h.c.} \right] + \mathcal{O}(g^3), \quad (7.20)$$

The light-matter coupling shifts the energy on which the quantum dots are emptied or filled. This means the coupling changes the effective level spacing of the fermionic system. However, as seen in the plots, the first order (yellow dashed line) shows a qualitatively wrong behavior, compared to the result with the full Peierls factor (blue solid line). It is apparent that the second-order (red dashed line) already reproduces the exact result well enough, and in particular shows the right qualitative dependency. We have verified that this effect is robust against changes of g. In general, for $g \to 0$, the shift of the step does vanish. However, even for small g, which we assume to be well in the perturbative regime, the shift due to the quadratic term does not become negligible compared to the one of the linear

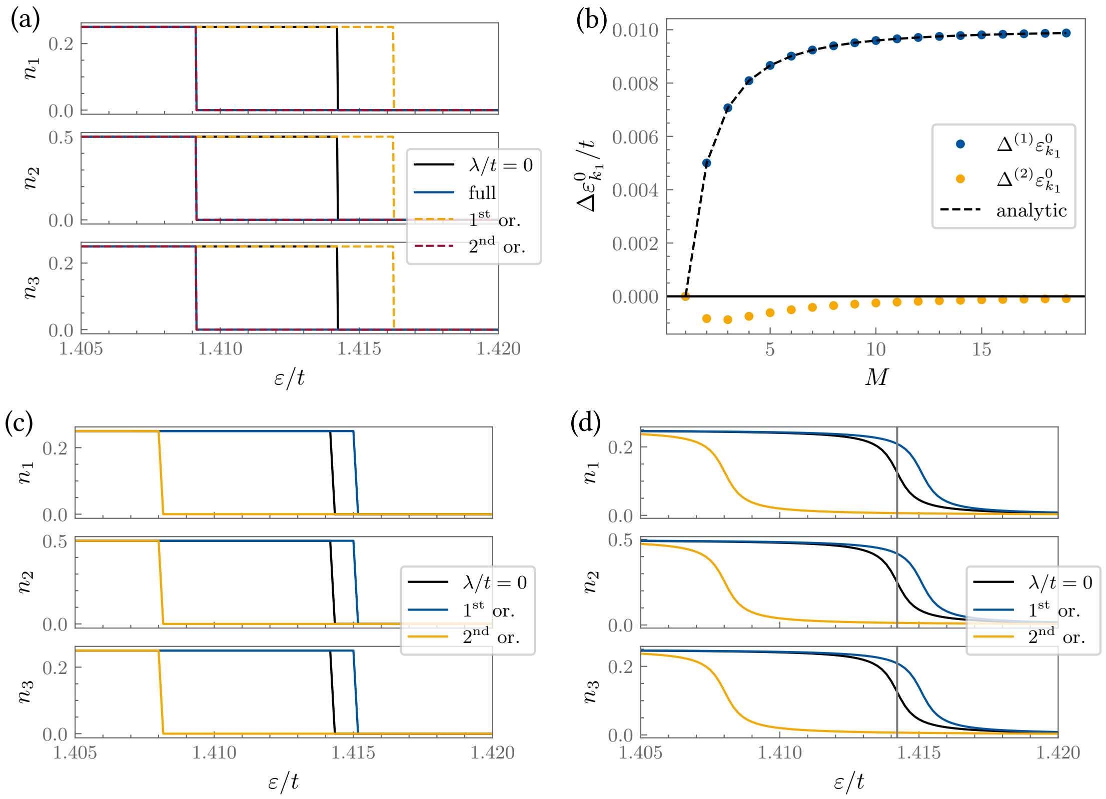

Figure 7.2.: (a), (c), (d) Mean occupation of the different quantum dots n_i of the impurity region as a function of the on-site energies $\varepsilon_1 = \varepsilon_2 = \varepsilon_3 = \varepsilon$ for $\omega_0/t = 10$ and $\lambda/t = 0.1\,\mathrm{i}$. (a) ED results for different orders of the exponential function. The lower row shows the perturbative results with MF correction for the decoupled system $\Gamma = 0$ in (c) and for the coupled one with $\Gamma/t = 10^{-3}$ in (d). (b) First- and second-order correction of the single-particle ground state ($n = M, m = 0$) in perturbation theory as a function of the chain length M for the same parameters as in (a), (c), (d).

term. The reason for this will become clear in the following chapter, where we discuss the coupling in single-particle perturbation theory.

7.3.2. First and second order expansion in one-particle perturbation theory

To obtain an initial understanding of how the interaction enters and why the second-order expansion term of the exponential function seems to be significant, even for small couplings g, we study the single-particle Hamiltonian perturbatively. We are interested in the change in the fermionic eigenenergies in the second order in g due to the electromagnetic field. Here, we consider the first- and second-order perturbation theory and the first- and second-order expansion of the Peierls factor according to Equ. (7.20). The Hamiltonian is given by $h = h_0 + v$, where

$$h_0 = \varepsilon \sum_{j=1}^{M} |j\rangle\langle j| + t \sum_{j=1}^{M-1} \left[|j\rangle\langle j+1| + |j+1\rangle\langle j|\right] \tag{7.21}$$

is the free Hamiltonian given by a tight binding chain and

$$v = t\left[\mathrm{i}\, g(a + a^\dagger) - \frac{g^2}{2}(a + a^\dagger)^2 + \mathcal{O}(g^3)\right] \sum_j \left[|j+1\rangle\langle j|\right] + \text{h.c.} \tag{7.22}$$

is the perturbation due to the coupling with the cavity bosons, expanded in orders of g. At this point, we reproduce the definition of $\lambda = \mathrm{i}\, gt$ for the coupling in the linear term. $|j\rangle$ is the single-particle Wannier state of the j^{th} quantum dot. We neglect the coupling to the leads ($\Gamma = 0$) and only consider the closed fermionic system described by h_0 with unperturbed fermionic eigenstates Equ. (2.15) and eigenvalues Equ. 2.14 given by:

$$\varepsilon_{k_n} = \varepsilon + 2t\cos(k_n), \qquad k_n = \frac{n\pi}{M+1},\ n \in \{1, 2, ..., M\}, \tag{7.23}$$

$$\langle j|\psi_{k_n}\rangle = \sqrt{\frac{2}{M+1}}\sin(k_n j). \tag{7.24}$$

The eigenstates of the complete system, including fermionic and bosonic degrees of freedom, are then given by the product states $|k_n, m\rangle = |\psi_{k_n}\rangle \otimes |m\rangle$ with energy $\varepsilon^m_{k_n} = \varepsilon + 2t\cos(k_n) + \omega_0(m + 1/2)$ and $m \in \mathbb{N}_0$ being the number of photons with which the cavity is occupied. In first-order perturbation theory, the first-order expansion term in Equ. (7.20) does not contribute to the change in energy, due to the vanishing matrix element $\langle m|a + a^\dagger|m\rangle = 0$. Though, the second-order term in Equ. (7.20) provides a correction in first-order perturbation theory

$$\Delta^{(1)}\varepsilon^m_{k_n} = \langle k_n, m|v|k_n, m\rangle = -\frac{2tg^2}{M+1}(m+1)\sum_{j=1}^{M-1}\sin(k_n j)\sin(k_n(j+1)), \tag{7.25}$$

which is of order g^2. The sum over j can be analytically evaluated, giving

$$\Delta^{(1)}\varepsilon^m_{k_n} = -\frac{tg^2}{2(M+1)}(m+1)\frac{M\sin(2k_n) - \sin(2Mk_n)}{\sin(k_n)}. \tag{7.26}$$

A second contribution arises in second-order perturbation theory due to the first-order term in the expansion of the Peierls factor and is given by

$$\begin{aligned}\Delta^{(2)}\varepsilon^m_{k_n} &= \sum_{n\neq l=1}^{M}\sum_{m\neq m'=0}^{\infty}\frac{|\langle k_n, m|v|k_l, m'\rangle|^2}{\varepsilon^m_{k_n} - \varepsilon^{m'}_{k_l}}\\ &= \frac{4t^2g^2}{(M+1)^2}\sum_{n\neq l=1}^{M}\left\{\sum_{j=1}^{M-1}\left[\sin(k_n(j+1))\sin(k_l j) - \sin(k_n j)\sin(k_l(j+1))\right]\right\}^2\\ &\times\left\{\frac{m+1}{2t[\cos(k_n) - \cos(k_l)] + \omega_0} + \frac{m}{2t[\cos(k_n) - \cos(k_l)] - \omega_0}\right\},\end{aligned} \tag{7.27}$$

which is also of order g^2. This demonstrates that both the linear and quadratic terms in the expansion of the Peierls factor contribute to a perturbative correction of order g^2 to the one-particle eigenenergies. Therefore, neglecting the second-order term, even for small couplings g, results in an inconsistent treatment of the Peierls factor.

In general, the corrections in Equ. (7.25) and Equ. (7.27) can have different signs. This is illustrated in Fig. 7.2(b), where the first- and second-order perturbative corrections are plotted as a function of the chain length M for the ground state $n = M$ and $m = 0$. Here, the first-order expansion term of the Peierls factor leads to a second-order perturbative correction, which is negative for all values of M. On the other hand, the second-order expansion term contributes to the first-order perturbative correction, which is positive for all M. Thus, the one-particle perturbation theory already hints at the qualitative different physical behaviors observed in the previous section. It is worth noting that this behavior does not necessarily hold for all states k_n, where for smaller M, the first-order correction perturbative correction can become negative.

7.3.3. Mean-field approach for the second-order term

We have seen that one cannot simply neglect the second-order term in the vector potential of the Peierls factor. Thus, the goal of this section is to extend the first-order perturbation theory method to include the Peierls phase up to order g^2 systematically. To this end, we utilize a non-self-consistent mean-field (MF) approach. This is similar to the calculation performed in [193]. We consider the coupling term of the many-body Hamiltonian H_{fb} in the second-order expansion of the Peierls factor, $H_{\text{fb}}^{(2)}$ as in Equ. (7.20) and approximate the term of order g^2 on the MF level. This gives

$$\begin{aligned} H_{\text{b}} + H_{\text{fb}}^{(2)} =& \omega_0 a^\dagger a + \mathrm{i}\, gt(a+a^\dagger) \sum_{j=1}^{M-1} \left[c_{j+1}^\dagger c_j - c_j^\dagger c_{j+1}\right] - \frac{g^2 t}{2}(a+a^\dagger) \sum_{j=1}^{M-1} \left[c_{j+1}^\dagger c_j + c_j^\dagger c_{j+1}\right] \\ \approx& \omega_0 a^\dagger a + \mathrm{i}\, gt(a+a^\dagger) \sum_{j=1}^{M-1} \left[c_{j+1}^\dagger c_j - c_j^\dagger c_{j+1}\right] - \frac{g^2 t}{2}\langle (a+a^\dagger)^2\rangle_0 \sum_{j=1}^{M-1} \left[c_{j+1}^\dagger c_j + c_j^\dagger c_{j+1}\right] \\ &- \frac{g^2 t}{2}(a+a^\dagger)^2 \left\langle \sum_{j=1}^{M-1} \left[c_{j+1}^\dagger c_j + c_j^\dagger c_{j+1}\right] \right\rangle_0 , \end{aligned} \tag{7.28}$$

where $\langle \cdot \rangle_0$ is the expectation value in the absence of light-matter coupling ($g = 0$). We must evaluate $\langle (a+a^\dagger)^2\rangle_0$ and $\left\langle c_{j+1}^\dagger c_j + c_j^\dagger c_{j+1}\right\rangle_0$ with $j \in \{1, .., M-1\}$, to obtain an effective model including the second-order terms. This approach contains all contributions up to order g^2.

Renormalized hopping parameter

The first term of order g^2 in Equ. (7.28) containing $\langle (a+a^\dagger)^2\rangle_0$ is evaluated for a cavity with chemical potential $\mu = 0$ and without dissipation $\kappa = 0$. The terms read

$$\langle (a+a^\dagger)^2\rangle_0 = \mathrm{Tr}\left[\rho_0 (a+a^\dagger)^2\right] = \coth\left(\frac{\beta}{2}\omega_0\right), \tag{7.29}$$

with ρ_0 being the equilibrium distribution for a non-coupled bosonic cavity. In the zero-temperature limit, which we consider in all Matsubara calculations, this gives the constant value $\langle (a+a^\dagger)^2\rangle_0 \to 1$. This term renormalizes the hopping t to

$$\tilde{t} = t\left(1 - \frac{g^2}{2}\coth\left(\frac{\beta}{2}\omega_0\right)\right) \xrightarrow{T\to 0} t\left(1 - \frac{g^2}{2}\right), \tag{7.30}$$

and will be included in the fermionic part of the Hamiltonian H_{f}. It leads to a decrease in the hopping. This relates to the so-called dynamical localization in Floquet theory [53, 86], which refers to the suppression of electron transport in a lattice under the influence of a time-periodic field, such as a light field.

Renormalized cavity parameters

The second term containing $\left\langle \sum_{j=1}^{M-1} \left[c_j^\dagger c_{j+1} + c_{j+1}^\dagger c_j\right]\right\rangle_0$ in Equ. (7.28) is slightly more complicated to evaluate when considering the additional coupling to the leads ($\Gamma \neq 0$). This term changes the boson propagator and can be evaluated using the Bogoliubov transformation, see e.g. [71] by introducing the bosonic operators b and $b^\dagger$ fulfilling

$$a = xb + yb^\dagger, \qquad \text{with } (x, y) = (\cosh(\varphi), \sinh(\varphi)),\ \varphi \in \mathbb{R} \tag{7.31}$$

Further, we define the renormalization factor

$$p := -\frac{g^2 t}{2} \sum_{j=1}^{M-1} \left\langle c^\dagger_{j+1} c_j + c^\dagger_j c_{j+1} \right\rangle_0 . \tag{7.32}$$

The transformation which eleminates the terms proportional to bb and $b^\dagger b^\dagger$ is given by $\varphi = \ln\left(\frac{\omega_0}{\omega_0+4p}\right)$. The part of the Hamiltonian containing the bosonic degrees of freedom can be written as

$$H_\mathrm{b} + H_\mathrm{fb}^{(2)} = \sqrt{\omega_0^2 - 4p\omega_0}\, b^\dagger b + \lambda(b + b^\dagger)\frac{\omega_0}{\omega_0 + 4p} \sum_{j=1}^{M-1} \left[c^\dagger_{j+1} c_j - c^\dagger_j c_{j+1}\right], \tag{7.33}$$

which is equivalent to $H_\mathrm{b} + H_\mathrm{fb}$ in Equs. (2.16) and (2.21) with $A_{ij} = \lambda\left(\delta_{i,j+1} - \delta_{i,j-1}\right)$, both with renormalized ω_0 and λ

$$\tilde{\omega}_0 = \omega_0\sqrt{1 - 4p/\omega_0} \qquad \text{and} \qquad \tilde{\lambda} = \lambda\frac{1}{1 + 4p/\omega_0}. \tag{7.34}$$

This approximation is only valid for small couplings with $4p < \omega_0$. Finally, the factor p has to be evaluated. To this end, we distinguish between an open and closed quantum dot chain.

In the case of decoupled leads ($\Gamma = 0$), an analytic expression for the many-body expectation value in p can be found. The expectation value is given by the sum over the wavefunctions of the tight-binding chain with closed boundaries, cf. Sect. 2.1.2, weighted by the Fermi function

$$\left\langle c^\dagger_{j+1} c_j + c^\dagger_j c_{j+1} \right\rangle_0 = \sum_k \left[\langle\psi_k|j\rangle\langle j+1|\psi_k\rangle + \langle\psi_k|j+1\rangle\langle j|\psi_k\rangle\right] \frac{1}{1 + e^{\varepsilon_k/T}}. \tag{7.35}$$

For $T = 0$, only the non-interacting ground state is occupied and, therefore, the expectation value can be calculated by

$$\begin{aligned} \left\langle c^\dagger_{j+1} c_j + c^\dagger_j c_{j+1} \right\rangle_0 &= \frac{4}{M+1} \sum_{E(k_n)\leq\varepsilon_\mathrm{F}} \sin\left(k_n(j+1)\right)\sin\left(k_n j\right) \\ &= -\frac{1}{M+1}\left[\frac{\sin\left(\frac{2j+1}{M+1}\pi(n_F + 1/2)\right)}{\sin\left(\frac{2j+1}{2M+2}\pi\right)} - \frac{\sin\left(\frac{1}{M+1}\pi(n_F + 1/2)\right)}{\sin\left(\frac{1}{2M+2}\pi\right)}\right]. \end{aligned} \tag{7.36}$$

The sum includes all states, in which the energy is smaller than the Fermi energy. This defines n_F, which holds $E(k_n) \leq \varepsilon_\mathrm{F}$ for all $n \geq n_\mathrm{F}$.

To evaluate the quality of this approximation, we compare directly with the ED results. The occupation when including this second-order correction is shown in Fig. 7.2(c). We see that when taking into account only the linear order in $g \sim A$ in the Peierls factor, the first-order perturbation theory shows a shift of the step towards larger on-site energies compared to the case without light-matter coupling. This is consistent with what we found in the ED calculation when considering only the first order of the vector potential in the Peierls factor. However, the shift due to the full Peierls phase or taking into account the linear and quadratic order in A was shown to be towards smaller energies. Including the quadratic order in A^2 in the perturbative treatment with the MF approach introduced above, reproduces this behavior. This result is still only perturbatively correct and, therefore, does not fully agree with the exact ED results. However, the formalism treats all terms of second order in g systematically and therefore describes the same physical behavior for small couplings.

In the case of coupled leads ($\Gamma \neq 0$), we utilize the equal-time Green functions Equ. (3.7) dressed by the self-energies with the Dyson equation Equ. (3.36) and $G^< = 1/2\left(G^\mathrm{K} - G^\mathrm{R} + G^\mathrm{A}\right)$ due to the reservoirs to calculate the one-particle correlation functions in p:

$$\left\langle c_{j+1}^\dagger c_j + c_j^\dagger c_{j+1}\right\rangle_0 = -\mathrm{i}\left[G^<_{j,j+1}(t=0) + G^<_{j+1,j}(t=0)\right] = -\frac{\mathrm{i}}{2\pi}\int \mathrm{d}\,\omega\,\left[G^<_{j,j+1}(\omega) + G^<_{j+1,j}(\omega)\right]. \tag{7.37}$$

The lesser component of the Green function $G^< = G^\mathrm{R}\Sigma^< G^\mathrm{A}$ is calculated via the lesser component of the self energy

$$\Sigma^<(\omega) = \mathrm{i}\,\Gamma\begin{pmatrix} f_L(\omega) & & \\ & 0 & \\ & & \dots & \\ & & & f_R(\omega)\end{pmatrix} \tag{7.38}$$

as $G^<_{ij} = \mathrm{i}\,\Gamma f_L G^R_{i1} G^A_{1j} + \mathrm{i}\,\Gamma f_R G^R_{iM} G^A_{Mj}$, which will be evaluated numerically.

The result for the mean occupation with finite Γ, obtained by this approach is shown in Fig. 7.2(d). As for the impurity region decoupled from the leads, the inclusion of the second-order term in the vector potential shows a qualitatively different behavior compared to when this term is neglected. The energies at which the quantum dots are filled or emptied are shifted as well due to the light-matter coupling. The coupling to fermionic reservoirs merely leads to a smoothening of the step observed in the mean occupation at $\Gamma = 0$.

Conclusion

In this section, we showed the importance of taking into account at least the second order in the vector potential A of the light-matter coupling when expanding the exponential of the Peierls factor to low orders of A. To this end, we utilized ED to study the closed quantum dot region decoupled from the fermionic leads with $\Gamma = 0$. Already for the closed system, only considering the linear term in A leads to qualitative different physical behavior than when considering the Peierls factor in all orders of the vector potential. We supported this observation, by studying the single-particle perturbation theory of the fermionic ground state in first and second order in the interaction. We demonstrated that when expanding the Peierls factor to linear order in the coupling $g \sim A$, the second-order perturbation theory leads to a correction to the ground state in second-order in the coupling (g^2). On the other hand, when considering the quadratic term of the expansion of the Peierls factor, it leads in first-order perturbation theory to a correction in order g^2 as well. Importantly, we found that both corrections can have different signs. This shows that the second-order term of the exponential function provides corrections of the same order in the coupling as the linear term, which can lead, however, to qualitative different perturbative corrections to the eigenenergies and, thus, different physical behavior.

Subsequently, we presented a non-self-consistent MF approach, which includes the quadratic terms of the expansion of the Peierls factor. The MF method leads to a renormalization of the light frequency ω_0, the light-matter coupling g, and the fermionic nearest-neighbor hopping t. For the system decoupled from the leads, $\Gamma = 0$, we obtained results comparable to the ED results. We showed additionally that the MF approach is also applicable when coupling to the leads, $\Gamma \neq 0$, and, thus, can also be used to study open and even non-equilibrium setups.

7.4. Gauge invariance

The physical electromagnetic fields are invariant under gauge transformations of the vector and scalar potentials. This means that all physical observables stay invariant under the transformation of the form [196]

$$\vec{A}(\vec{r},t) \to \vec{A}(\vec{r},t) + \vec{\nabla} X(\vec{r},t), \qquad \phi(\vec{r},t) \to \phi(\vec{r},t) - \partial_t X(\vec{r},t), \tag{7.39}$$

with an arbitrary scalar and differentiable function $X(\vec{r},t)$ for a three-dimensional solid. Thus, to accurately represent physical behavior, the Hamiltonian governing the light-matter coupling must be formulated to preserve this gauge invariance.

In the localized orbital expansion Equ. (2.12), with one orbital per site, the gauge transformation is described by the unitary transformation

$$H \to UHU^\dagger - \mathrm{i}\, U\frac{\partial U}{\partial t}, \qquad \text{with}\, U = \exp\left[\mathrm{i}\sum_m X(\vec{r},t) c_m^\dagger c_m\right] \tag{7.40}$$

in second quantization or equivalent

$$c_m \to c_m e^{-\mathrm{i}\, X(\vec{r},t)}. \tag{7.41}$$

c_m annihilates a particle in state $|m\rangle$ in Wannier space.

However, straightforwardly truncating the Hilbert space, for example, by considering only a subset of orbitals of the matter system or a finite number of modes of the resonator, breaks the gauge invariance. This artifact originates from a carelessly applied Coulomb gauge neglecting that the lattice potential becomes position- and momentum-dependent in the truncated Hilbert space. So the minimal coupling has to be included as well in the potential and not only in the kinetic part. Ref. [85, 188] proposed a corrected version of the Coulomb gauge, where the projected gauge transformation is applied to the projected Hamiltonian, leading to the Peierls substitution

$$\tilde{t}_{mm'}^{\mu\mu'} = \sum_{m_1,m_1'\mu_1\mu_1'} \left(e^{-\mathrm{i}(a+a^\dagger)\chi}\right)_{mm_1}^{\mu\mu_1} t_{m_1m_1'}^{\mu_1\mu_1'} \left(e^{\mathrm{i}(a+a^\dagger)\chi}\right)_{m_1'm'}^{\mu_1'\mu'}, \tag{7.42}$$

with

$$\chi_{mm'}^{\mu\mu'} = \int \mathrm{d}\vec{r}\, a_{m,\mu}^*(\vec{r})\chi(\vec{r})a_{m',\mu'}(\vec{r}), \qquad \vec{\nabla}\chi(\vec{r}) = -\vec{A}(\vec{r}). \tag{7.43}$$

μ are the additional orbital indices. Ref. [85] showed that electron-electron interaction can take on an even more intricate inter-orbital dependency when considering light-matter coupling. This will not be further discussed in the present thesis. In the single-orbital approximation, Equ. (7.42) takes the form of the Peierls substitution Equ. (7.9). But already by considering two orbitals per lattice sites, the Peierls substitutions and Equ. (7.42) lead to very different energy spectra, cf. [85], and can influence e.g. the optical conductivity [197]. In the present thesis, we focus on the one-orbital approximation, thus these additional terms are not taken into account. One should, however, be aware that this neglects effects such as inter-orbital transitions induced by the light field.

But not only the truncation of the Hilbert space breaks the gauge invariance. The expansion of the Peierls factor in orders of the vector potential, which was just discussed in Sect. 7.3, also leads to the breaking of the gauge-invariance [83, 85]. Due to the highly non-linear light-matter coupling, a perturbative treatment of the Peierls phase can quickly lead to artifacts, such as the previously mentioned superradiance. This holds, however, primarily for the ultra-strong coupling regime, and we have shown in Sect. 7.3 that perturbative treatment up to second order in the vector potential can recover the correct results even in the strong coupling regime, where the coupling is larger than the loss rate of the cavity and the quantum dot system $g \gg \kappa, \Gamma$.

In general, different gauges express the Hamiltonian in different canonical variables. In the Coulomb gauge, the electromagnetic field is represented by the transverse vector potential proportional to $(a+a^\dagger)$ and its corresponding canonical conjugate momentum [71]. Within this framework, the coupling between the light field and the electronic system is included in the orbitals in the free-electron part of the Hamiltonian with the highly non-linear Peierls factor, cf. Sect. 7.1.1. Due to the entanglement of the fermionic and bosonic degrees of freedom, a truncation in orbital space is non-trivial and the Coulomb gauge is highly sensitive to this approximate treatment [83, 85].

In contrast, when switching to the dipole gauge, the coupling is described using the displacement field, proportional to $(a - a^\dagger)$, alongside the magnetic field [71]. In the dipole gauge, the light-matter interaction takes on a different form. It is expressed through an instantaneous fermionic self-interaction term and a linear light-matter coupling term. This formulation is less sensitive to Hilbert space truncation because the coupling can be interpreted as a mere shift in the bosonic degrees of freedom, the so-called depolarization shift. Unlike the Coulomb gauge, where the bosonic and fermionic degrees of freedom are highly entangled in orbital space, the dipole gauge offers a cleaner separation. Thus, we hope that the light-matter coupling in the dipole gauge will also be easier to treat mathematically [198], particularly within the first-order perturbation theory that we aim to apply in this thesis.

The transition to this gauge can be accomplished through the Power-Zienau-Wooley (PZW) transformation [199, 200] by introducing a photonic pseudopotential. We provide a detailed discussion of this transformation in the following sections. The aim is to adapt the PZW transformation such that it can be applied to our inhomogeneous system in the single-orbital approximation. The dipole gauge has already been applied to systems consisting of only a few quantum dots in other works [181, 182]. There, the light-matter coupling was introduced to the closed ($\Gamma = 0$) impurity and transformed into the dipole gauge for the closed system. To the best of our knowledge, the incorporation of leads in such systems has not yet been explored. Here, we consider the impurity together with the leads, when applying the transformation, so it acts on the entire system. To this end, we consider first the system in the dipole gauge in the continuum limit and subsequently project the Hamiltonian on a subset of localized orbitals. The approach in the continuum limit is motivated by [201]. As a second approach, we directly consider the Peierls substitution in Coulomb gauge and the tight-binding formulation and transform the Hamiltonian via the PZW transformation in the tight-binding picture.

7.4.1. PZW in continuum formulation

The dipole gauge is often used in atomic cavity electro-dynamics and can be obtained by applying the PZW transformation. The transformation is applied in the literature when considering solids completely embedded in the cavity [83, 85, 201–204] and with electromagnetic fields in the dipole approximation, where the vector potential is assumed to be spatially invariant on the scale of the solid. The continuum Hamiltonian Equ. (7.1) in Coulomb gauge and with considering only one photon mode reads in second quantization

$$H = \int \mathrm{d}x \left\{ \psi^\dagger(x) \frac{\left[-\mathrm{i}\,\partial_x + A(x)\right]^2}{2m} \psi(x) \; + V(x)\psi^\dagger(x)\psi(x) + \frac{1}{2}\left[\omega_0^2 \pi^2 + q^2\right] \right\}. \tag{7.44}$$

We focus on the one-dimensional case, assuming the solid is oriented along the x-axis. $\psi^{(\dagger)}(x)$ annihilates or creates a fermion at position x. $V(x)$ denotes the lattice potential. The canonical boson coordinate operator q and the canonical boson momentum operator π are given by

$$q = 1/\sqrt{2\omega_0}\left(a + a^\dagger\right), \qquad \pi = \mathrm{i}\sqrt{\omega_0/2}\left(a^\dagger - a\right) \tag{7.45}$$

and with $A \sim q$. A more thorough discussion on the quantization of the electromagnetic field can be found in e.g. [71, 164]. For a spatially dependent vector potential, a regularized generator for the PZW was proposed by Ref. [201]:

$$S = q\int \mathrm{d}x\,\theta(x)\psi^\dagger(x)\psi(x), \tag{7.46}$$

where $A(x) := -q\partial_x\theta(x)$ is introduced. In the following, we will take a closer look at how this approach can be applied to our open system. In the present thesis, we are interested in a system, where the electromagnetic field is spatially restricted to the impurity region described in Sect. 2. The vector potential is defined as in Equ. (7.12), where we directly chose a constant vector potential for $A(x) = A_0(x) = -A_0$ in the central region $x \in [0, L]$ and zero otherwise. Thus, such a regularization has to be considered. Supplementary calculations are found in Appendix D.

For this purpose, we split the Hamiltonian Equ. (7.44) into three parts $H = H_\mathrm{f} + H_\mathrm{b} + H_\mathrm{fb}$, containing either only fermionic (f) or bosonic (b) fields or both (fb). We calculate how each part transforms independently under the generator in Equ. (7.46) using the Baker-Campell-Hausdorff formula [205]. The fermionic part is the most straight-forward transformation because the generator S commutes with H_f

$$e^{-\mathrm{i}S}H_\mathrm{f}e^{\mathrm{i}S} = H_\mathrm{f} \tag{7.47}$$

For the bosonic part, using that only π transforms, leads to

$$e^{-\mathrm{i}S}H_\mathrm{b}e^{\mathrm{i}S} = \frac{1}{2}\left[\omega_0^2q^2 + (\pi + \mathcal{P})^2\right], \tag{7.48}$$

where the polarization

$$\mathcal{P} = \int \mathrm{d}x\,\theta(x)\psi^\dagger(x)\psi(x) \tag{7.49}$$

was introduced.

The mixed part H_fb is however a little more complicated. It is important to keep in mind which operators the derivative in Equ. (7.44) is acting on. Using the Baker-Campbell-Hausdorff formula, the transformation takes the form

$$\begin{aligned} e^{-\mathrm{i}S}H_\mathrm{fb}e^{\mathrm{i}S} =& \frac{1}{2m}\int \mathrm{d}x\,e^{-\mathrm{i}\theta(x)}\psi^\dagger(x)\left[\mathrm{i}\,\partial_x - A(x)\right]^2\psi(x) \\ &+ \frac{1}{2m}\int \mathrm{d}x\int \mathrm{d}x'\,e^{-\mathrm{i}(\theta(x)-\theta(x'))}\psi^\dagger(x)\psi(x)\left[\mathrm{i}\,\partial_x - A(x)\right]^2\delta(x-x') \\ &- \frac{1}{2m}\int \mathrm{d}x\int \mathrm{d}x'\,e^{-\mathrm{i}\theta(x)}\psi^\dagger(x)\psi(x')\left[\mathrm{i}\,\partial_x - A(x)\right]^2\delta(x-x'). \end{aligned} \tag{7.50}$$

With the help of integration by parts, the derivative acting on the δ-distribution can be shifted to the other terms. This is trivial in the case when all functions are smooth and periodic boundary conditions are considered. We will see, however, that when considering our impurity system, the inhomogeneity in the vector potential between the impurity and the fermionic reservoirs leads to additional boundary terms different from the form often found in literature, see e.g. [83, 85, 201–204]. When considering a general function $f(x)$ which is defined partwise to be non-zero on just a finite part $x \in [0, L]$ and vanishing otherwise, just like the vector potential A, the integration by parts to shift the derivative obtains boundary terms at $x = 0$ and $x = L$

$$\int \mathrm{d}\,x\, f(x)\partial_x\delta(x' - x) = f(x)\delta(x' - x)\Big|_{x=0}^{x=L} - \underbrace{\int \mathrm{d}\,x\, \left(\partial_x f(x)\right)\delta(x' - x)}_{\partial_{x'} f(x')}. \tag{7.51}$$

Applying this to Equ. (7.50), keeping in mind that

$$\left[\mathrm{i}\,\partial_x - A(x)\right]^2 \delta(x - x') = \left[-\partial_{x'}^2 + 2\,\mathrm{i}\,A(x)\partial_{x'} - \mathrm{i}\,(\partial_x A(x)) + A^2(x)\right]\delta(x - x'), \tag{7.52}$$

we obtain the following expression

$$\begin{aligned} e^{-\mathrm{i}\,S} H_{\mathrm{fb}}\, e^{\mathrm{i}\,S} &= \frac{1}{2m}\int \mathrm{d}\,x \psi^\dagger(x)\,(\mathrm{i}\,\partial_x)^2\,\psi(x) \\ &+ \frac{1}{2m}\int \mathrm{d}\,x \psi^\dagger(x) e^{-\mathrm{i}\,\theta(x)}\Big\{ -\left(e^{\mathrm{i}\,\theta(x')} - 1\right)\psi(x')\partial_{x'}\delta(x - x')\Big|_{x'=0}^{L} \\ &+ \left[-\left(e^{\mathrm{i}\,\theta(x')} - 1\right)\psi(x')\partial_{x'} + \left(\partial_{x'}\left(e^{\mathrm{i}\,\theta(x')} - 1\right)\psi(x')\right) - 2\,\mathrm{i}\,A(x')\left(e^{\mathrm{i}\,\theta(x')} - 1\right)\psi(x')\right]\delta(x - x')\Big|_{x'=0}^{L}\Big\}. \end{aligned} \tag{7.53}$$

This includes the aforementioned boundary terms and the fully transformed Hamiltonian is

$$\begin{aligned} e^{-\mathrm{i}\,S} H e^{\mathrm{i}\,S} = &\int \mathrm{d}\,x \psi^\dagger(x)\frac{(-\mathrm{i}\,\partial_x)^2}{2m}\psi(x) + \int \mathrm{d}\,x V(x)\psi^\dagger(x)\psi(x) + \frac{1}{2}\left[\omega_0^2 q^2 + (\pi + \mathcal{P})^2\right] \\ &+ \text{boundary terms}. \end{aligned} \tag{7.54}$$

The first line recovers the results from the calculations for a homogeneous system with periodic boundary conditions, see e.g. [83, 85, 201–204]. In this form, the light-matter coupling does not enter in the form of an exponential function such as through the Peierls phase. Instead, the interaction between the fermions and the bosons is fully captured via the polarization term Equ. (7.49) in the bosonic part of the Hamiltonian. However, additional boundary terms arise due to the sharp step in the vector potential, which can no longer be treated straightforwardly. This challenge arises for two distinct reasons. First, at the points $x = 0, L$ where the vector potential vanishes, the derivative of the δ-function diverges and the first part of the boundary terms cannot be evaluated at these points. Further, it is not clear how exactly to define θ at the boundaries. In general, the discussion of the boundary terms is similar to the discussion of the Peierls substitution for non-homogeneous vector potentials in Sect. 7.1.2 starting underneath Equ. (7.15): the additional terms strongly depend on the exact point where the potential vanishes. Because it is not clear, how to further evaluate these expressions in the continuum limit, we will later come back to the boundary terms, when considering the tight-binding formulation of the solid, see Sect. 7.4.2. But first, we discuss the projection of Equ. (7.54) onto the tight-binding space, when neglecting the boundary terms.

Back to the tight-binding model

Analog to the non-interacting tight-binding model, see Sect. 2.1.2 and e.g. [109, 110], we rewrite the Hamiltonian again in the basis of localized orbitals around the lattice sites. Note that the Coulomb interaction Equ. (2.6) is still not taken into account ($U = 0$). As an example, we project here on the 1s orbital [206], so that basis transforms as

$$\psi^\dagger(x) = \sum_j \langle x|j\rangle\, c_j^\dagger, \qquad\qquad \langle j|x\rangle = \phi_j^{1s}(x) = \frac{1}{\sqrt{\pi a_0}} e^{-|x - R_0 j|/a_0}, \tag{7.55}$$

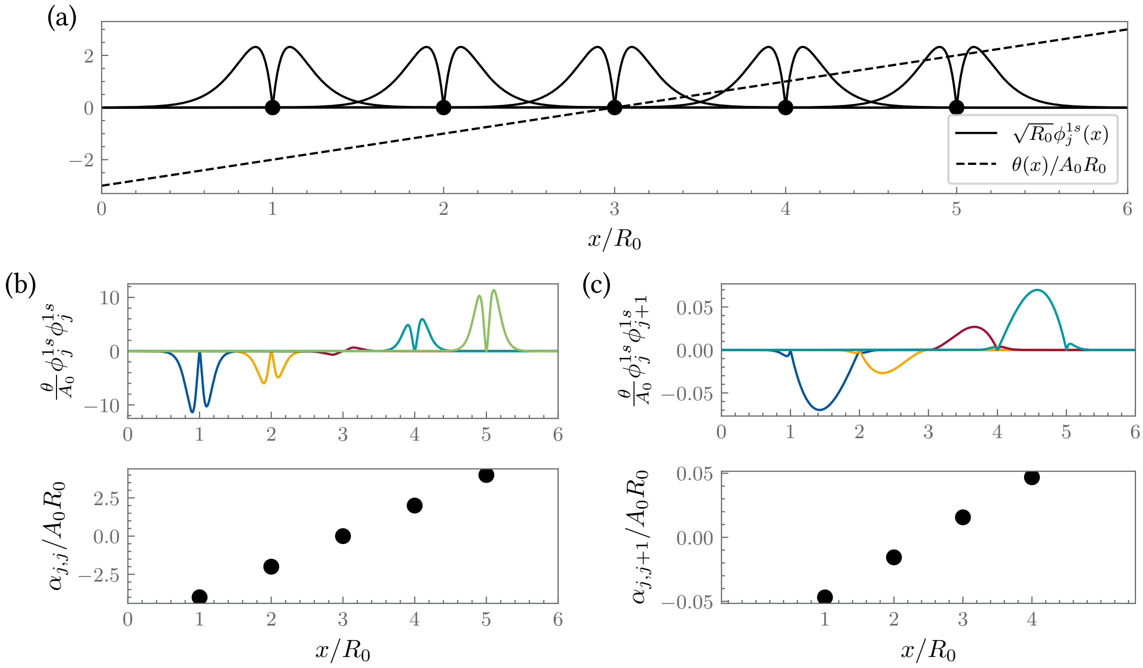

Figure 7.3.: Evaluation of the α-integrals for the PZW transformation to retain the tight-binding formulation for a lattice of size $M = 5$. (a) The dots indicate the lattice sites. Additionally, the $1s$-orbital wave function $\phi_j^{1s}(x)$ (solid lines) and θ (dashed line), defining the vector potential $A(x) = -\partial_x\theta(x)$, are shown. (b) and (c) show the on-site integrals and the nearest-neighbor integrals respectively in the lower panels and the integrand in the upper ones. The lattice constant is taken as $R_0/a_0 = 10$.

where j are the lattice sites, seperated by the lattice constant R_0 and a_0 being the Bohr radius [207]. In physical systems, the lattice constant is around 1-2 orders of magnitude larger than the Bohr radius [109]. Note that we are applying the one-orbital approximation again at this point. As discussed above, in the dipole gauge, the light-matter coupling appears linearly in the Hamiltonian, in contrast to the Coulomb gauge. Hence, the formulation in Equ. (7.54) without the boundary terms should provide good results in the one-orbital approximation.

The part of the Hamiltonian in dipole gauge Equ. (7.54) containing the fermions, $H_{\text{fb}} + H_{\text{f}}$, takes the form of free fermions on a lattice, that was discussed in Sect. 2.1.2. The light-matter coupling is included in the bosonic part through the polarization $\mathcal{P}$. We, therefore, only take a closer look at how $\mathcal{P}$ is projected onto the truncated localized basis. Considering again the simple case where $A(x)$ is given by the step function Equ. (7.12) for $A_0(x) \to -A_0$, so that

$$\theta(x) = \begin{cases} A_0\left(x - R_0\frac{M+1}{2}\right) & \text{for } x \in [0, L], \\ 0 & \text{else.} \end{cases} \tag{7.56}$$

We directly symmetrized θ around the middle point of the impurity region to keep the spatial symmetry of the system in equilibrium. The polarization in the tight-binding picture in one dimension takes the form

$$\mathcal{P} = \sum_{i,j=1}^{M} \alpha_{ij} c_i^{\dagger} c_j, \tag{7.57}$$

where $i, j \in [1, M]$ are the lattice sites in the interacting region $x \in [0, L]$. The matrix elements are given by

$$\alpha_{ij} = \int \mathrm{d}\, x \theta(x)\, \phi_i^{1s}(x)\, \phi_j^{1s}(x) \qquad \in \mathbb{R}. \tag{7.58}$$

In Fig. 7.3, the numerical evaluation of the integrals is shown together with the 1*s*-orbitals and the function $\theta(x)$. We omit the integrals of higher than nearest-neighbor overlap. This is based on the premise that the orbitals do not overlap strongly, similar to what is assumed when considering only nearest-neighbor hopping in the tight-binding model. Hence, only the on-site and nearest-neighbor integrals are shown. The weighted overlap integrals are, analog to θ, linearly increasing over the chain. Due to the localization of the orbitals, the on-site overlap is greater and leads to greater matrix elements than the nearest-neighbor ones. To describe the system, we therefore define the slopes as new parameters $\alpha_o > 0$ and $\alpha_n > 0$ with

$$\alpha_{jj} = \begin{cases} \alpha_\mathrm{o} \left(j - \frac{M+1}{2}\right) & \text{for } i = j, \\ \alpha_{ji} = \alpha_\mathrm{n} \left(j - \frac{M}{2}\right) & \text{for } i = j - 1, \\ 0 & \text{else}, \end{cases} \tag{7.59}$$

with $|\alpha_\mathrm{o}| > |\alpha_\mathrm{n}|$.

Thus, in the tight-binding formulation, we can rewrite the coupling term of the Hamiltonian as follows

$$\begin{aligned} H_\mathrm{fb} &= \omega_0 \left(a^\dagger - \frac{\mathrm{i}}{\sqrt{2\omega_0}} \sum_{i,j} \alpha_{ij} c_i^\dagger c_j \right) \left(a + \frac{\mathrm{i}}{\sqrt{2\omega_0}} \sum_{i,j} \alpha_{ij} c_i^\dagger c_j \right) \\ &\to \omega_0 a^\dagger a + \mathrm{i} \sqrt{\frac{\omega_0}{2}} (a^\dagger - a) \sum_{ij} \alpha_{ij} c_i^\dagger c_j + \frac{1}{2} \sum_{i,i'j,j'} \alpha_{ij} \alpha_{i'j'} c_i^\dagger c_{i'}^\dagger c_{j'} c_j \end{aligned} \tag{7.60}$$

where the energy offset of the ground state was neglected in the last line. The shift in the bosonic operators in the first line is called the depolarization shift.

The last term in the second line of Equ. (7.60) is an additional two-particle fermionic interaction term and can simply be incorporated into the perturbative treatment. To treat the second term, due to the bosonic fields occurring only quadratic in the highest order in the transformed Hamiltonian, we can integrate out the bosonic fields again as described in Sect. 3.6.1. By introducing

$$A_{ij} = \mathrm{i} \sqrt{\frac{\omega_0}{2}} \alpha_{ij}, \tag{7.61}$$

the resulting vertices of the effective fermionic interaction are given by Equ. (3.81) for the Matsubara formalism and by Equ. (3.83) on the Keldysh contour. Both terms together then lead to the full vertex

$$\bar{v}_{i_1' i_2' | i_1 i_2}(\mathrm{i}\,\omega_1', \mathrm{i}\,\omega_2' | \,\mathrm{i}\,\omega_1, \mathrm{i}\,\omega_2) = \frac{1}{\beta} \delta(\omega_{1'} + \omega_{2'} - \omega_1 - \omega_2) \left\{ \left[1 + \frac{\omega_0}{2} D(\mathrm{i}\,\omega_1' - \mathrm{i}\,\omega_1) \right] \alpha_{i_1 i_1'} \alpha_{i_2' i_2} - (1 \leftrightarrows 2) \right\}, \tag{7.62}$$

in the Matsubara formalism and

$$\begin{aligned} \bar{v}_{i_1', i_2' | i_1, i_2}^{\nu_1', \nu_2' | \nu_1, \nu_2}(\omega_1', \omega_2' | \omega_1, \omega_2) = \frac{1}{2\pi} \operatorname{sign}(\nu_1') \operatorname{sign}(\nu_2') \delta(\omega_1' - \omega_1 + \omega_2' - \omega_2 = 0) \times \\ \left\{ \left[1 + \frac{\omega_0}{2} D(\mathrm{i}\,\omega_1' - \mathrm{i}\,\omega_1) \right] \delta_{\nu_1', \nu_1} \delta_{\nu_2', \nu_2} \alpha_{i_1 i_1'} \alpha_{i_2' i_2} - (1 \leftrightarrows 2) \right\} \end{aligned} \tag{7.63}$$

on the Keldysh contour. In this approach, we obtain an effective fermion-fermion interaction with long-range interactions due to coupling with the bosonic resonator. This method allows the direct application of first-order perturbation theory to a homogeneous system, without additional approximations of the light-matter coupling first. This is in contrast to the coupling in the Coulomb gauge, where the Peierls factor does not lead straightforwardly to an effective two-particle vertex. However, boundary terms must still be considered, as they arise from the inhomogeneity of the impurity system, which we aim to study. We will examine these terms more closely in the following section.

7.4.2. PZW in tight-binding formulation

In the following, we use the PZW transformation on the Hamiltonian Equ. (2.1) with the Peierls substitution Equ. (7.11) in the Coulomb gauge directly in the tight-binding picture. When considering only one orbital per site, the Hamiltonian was shown to be gauge invariant [85], and this approach is reasonable. To this end, we assume again an infinite linear tight-binding chain, where the electromagnetic field is only present in a finite part of the lattice for lattice sites $j \in [1, M]$. This means the leads Equ. (2.4) are modeled by half-infinite linear chains. This setup is the tight-binding model analog to what was done in Sect. 7.1.2, with the two boundary sites of the leads not yet included in the impurity. From this approach, we learned that the hopping between the $j = 0$ to the $j = 1$ site and the $j = M$ to the $j = M + 1$ site are also renormalized by the Peierls phase which we chose to be half of the bulk phase g. The generator of transformation in the tight-binding formulation takes the form

$$S_j = \begin{cases} -g(a + a^\dagger)\left(j - \frac{M+1}{2}\right) & \text{for } j \in [1, M], \\ 0 & \text{else} \end{cases}, \tag{7.64}$$

which is of the general form Equ. (7.40). The transformation was directly symmetrized around the middle point of the impurity region to preserve the spatial symmetry of the system. The fermionic and bosonic annihilation operators of the system transform as follows

$$c_j \to \begin{cases} e^{\mathrm{i}\, g(a+a^\dagger)\left(j-\frac{M+1}{2}\right)} c_j & \text{for } j \in [1, M], \\ c_j & \text{else,} \end{cases} \qquad a \to a + \mathrm{i}\, g \sum_{j=1}^{M} \left(j - \frac{M+1}{2}\right) c_j^\dagger c_j, \tag{7.65}$$

where the Baker–Campbell–Hausdorff formula was used to derive the transformation of a. Therefore, the full Hamiltonian Equ. (2.1) transforms as

$$\begin{aligned} H \to & \sum_{j=-\infty}^{\infty} \varepsilon_j c_j^\dagger c_j + t \sum_{j \neq \{0,M\}} \left[c_j^\dagger c_{j+1} + \text{h.c.}\right] \\ & + \omega_0 \left(a^\dagger - \mathrm{i}\, g \sum_{j=1}^{M} \left(j - \frac{M+1}{2}\right) c_j^\dagger c_j\right)\left(a + \mathrm{i}\, g \sum_{j=1}^{M} \left(j - \frac{M+1}{2}\right) c_j^\dagger c_j\right) \\ & + t\left[e^{\mathrm{i}\, g(a+a^\dagger)\frac{M}{2}} c_1^\dagger c_0 + e^{\mathrm{i}\, g(a+a^\dagger)\frac{M}{2}} c_{M+1}^\dagger c_M + \text{h.c.}\right] \end{aligned} \tag{7.66}$$

To relate this result to the previous approach in Sect. 7.4.1, where we projected the continuum Hamiltonian in the dipole gauge without the boundary terms on the 1s orbital space, we compare the second line in Equ. (7.66) with the first line in Equ. (7.60). By choosing $\alpha_{ij} = \sqrt{2\omega_0} g\left(j - \frac{M+1}{2}\right)\delta_{i,j}$, the Hamiltonians coincide. As discussed before, α_{jj} is proportional to the site index as seen in Equ. (7.59). The nearest-neighbor or even more long-range coupling components are neglected in the derivation directly from the tight-binding picture, which is, as seen when comparing the lower plots in Figs. 7.3(b) and

7.3(c), a reasonable assumption for the sufficiently localized orbitals. This means that both approaches are consistent when neglecting the boundary terms.

In general, this transformation deals with the exponential term in the Peierls factor by including the electro-magnetic coupling via a polarization term $P = g \sum_j j c_j^\dagger c_j$, which is equivalent to Equ. (7.49) in the tight-binding formulation. This term can straightforwardly be treated with a Bogoliubov transformation, renormalizing the bosonic propagator when integrating out the bosonic degrees of freedom as described in Sect. 3.6.1. It leads directly to an effective two-particle interaction vertex for the fermionic degrees of freedom without any approximations, which can be treated in first-order perturbation theory.

However, due to the vector potential A being confined to the impurity region and not acting on the leads, the inhomogeneity leads to a phase being rotated into the boundaries during the transformation. These boundary terms, again, contain the exponential of the potential, which cannot be integrated out exactly. The problem was merely shifted.

At this point, a word of caution is in order. The system coupled to the leads has to be considered in full when performing the PZW transformation. When considering the system decoupled from the leads, $\Gamma = 0$, in the transformation and later including the leads without transforming would ignore the boundary terms. Therefore, it is important to take into account the complete system, even though the electromagnetic field and, hence, the gauge transformation does not act on the non-interacting leads. If considering a system with closed or periodic boundary conditions, these phases do not arise and the PZW transformation is a good tool to treat the exponential phase.

Conclusion

In this section, we transformed the Hamiltonian with light-matter coupling into the dipole gauge using the PZW transformation. We did so in the continuum as well as in the tight-binding formulation. In the dipole gauge, the light-matter coupling leads merely to a linear shift in the bosonic field, called the depolarization shift, for a homogenous system. Thus, compared to the Peierls substitution, where the light-matter coupling is highly non-linear, the coupling is easily treated in all orders of the vector potential and straightforwardly leads to an exact effective fermion-fermion two-particle interaction vertex when integrating out the bosonic degrees of freedom. Thus, it has been validated, that the light-matter coupling in dipole gauge for a homogenous system can be directly treated in first-order perturbation theory.

The general aim of this section was to apply the PZW transformation to our impurity model, where only a part of an infinite lattice is emerged in the cavity leading to a sharp step in the vector potential and, thus, a violation of the dipole approximation. In the dipole gauge, the violation of the dipole approximation leads to additional boundary terms. We thus, showed the importance of treating the system with impurity and leads as a whole, when including the light-matter coupling. Applying the light-matter coupling only to the impurity region would ignore the boundary terms. Unfortunately, these boundary terms are not well-defined in the continuum limit. Instead, we performed the PZW transformation directly in the tight-binding formulation. Here, the light-matter coupling leads to additional terms at the boundaries of the impurity, which include a vector-potential dependent exponential function. Similar to the Peierls substitution, these highly non-linear terms are not trivial to treat. The treatment of the depolarization shift together with the highly non-linear boundary terms are however non-trivial in first-order perturbation theory and is left for future research.

8. Interference Effects in the Linear Conductance

As seen in the vertices in Equs. (3.81) and (3.83), the coupling to the cavity leads to an effective long-range interaction in the fermionic system [52]. This results in effective long-range hopping between quantum dots, which opens multiple transport channels through the quantum dot system, which can interfere with each other. Interference effects due to long-range hopping have already been studied in multiple experimental and theoretical works [45–50]. They are shown to lead to features in the transport observables, such as the suppression of the current or the linear conductance.

In this chapter, we cover the emergence of a Fano-like conductance node due to the effective long-range interaction resulting from the coupling with the cavity [208]. Fano-like interference effects have already been observed in other contexts within cavity QED [209, 210]. The case with $M = 3$ sites, cf. Fig. 7.1, is the minimal case where such long-range effects can arise and will therefore be our main exemplary configuration. The results are easily translated to larger system sizes. For the triple dot system, we consider two different parameter sets to study the linear conductance using first-order perturbation theory (Sect. 4), as well as the extended MF method to include the second order in the vector potential of the Peierls factor (Sect. 7.3.3). The reason for revisiting this inconsistent approximation is twofold. First, it provides additional examples demonstrating that the non-systematic inclusion of terms in second order in the vector potential leads to vastly different physical behavior compared to the systematic treatment. Second, the first-order perturbation theory can be solved analytically in certain parameter regimes. The analytic expressions can then be utilized within the MF approach by considering the renormalized parameter. But first, we examine the interference based on fundamental principles by considering a simple double dot system without coupling to the cavity.

In the following chapter, we focus on the equilibrium ($V = 0$) and the zero-temperature limit ($T_L = T_R = T_\mathrm{b} = 0$). In this regime, we apply the Matsubara Green function formalism, introduced in Sect. 3.1. We do not consider Coulomb interaction ($U = 0$) in this chapter.

8.1. Interference of a two-level system

Interference effects in the transport can only occur when two distinct transport channels are available. To understand when such interference is possible and how it affects the linear conductance, we will analyze the interference in energy space. To this end, we begin by studying a system of two quantum dots coupled in parallel to a left and right lead. This represents the simplest model where two transport channels across a finite region are present. We focus on the scenario where the two energy levels are simultaneously located at the Fermi level, bringing them into resonance concurrently and how this affects the conductance through the double dot.

Specifically, we examine a simple effective two-level model, as shown in the inset of Fig. 8.1. Besides the two main quantum dots under consideration, we treat the two first lead sites explicitly as auxiliary dots and consider the scaling limit $\Gamma \gg t$, where the auxiliary dots are re-incorporated into the leads. The first dot is chosen to be in resonance with the Fermi level ($\varepsilon_1 = 0$), while the second dot, with energy

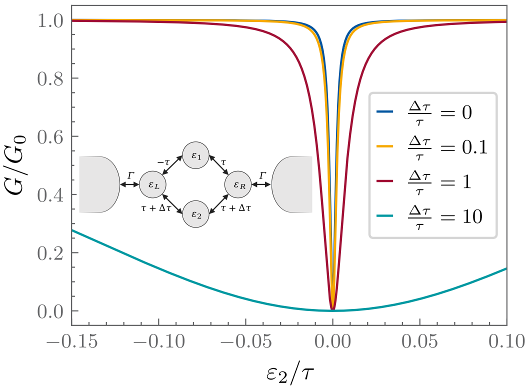

Figure 8.1.: Linear conductance trough the two-level system shown in the inlet with $\Gamma \gg \tau$ and $\varepsilon_1 = \varepsilon_L = \varepsilon_R = 0$ as a function of ε_2 and for different $\Delta\tau$.

ε_2, is tuned through this region, crossing degeneracy with the first dot and allowing for interference of the two transport channels through either level. The first dot is coupled via $-\tau$ to the first dot of the left/right lead and the second dot with $\tau + \Delta\tau$. The additional minus sign in the coupling to the left is necessary to obtain a destructive interference between the two transport channels through the dot [16] and is analog to the scenario, we encounter for the triple-dot system, which we will see in Sect. 8.2.

In Fig. 8.1, the linear conductance Equ. (3.73) is shown as a function of ε_2 and for different coupling differences $\Delta\tau$. As clearly seen, the conductance has a node when both energy levels are in resonance with the Fermi level simultaneously ($\varepsilon_1 = \varepsilon_2 = 0$). The node occurs independent of the difference in coupling to the leads $\Delta\tau$.

At this point, it is interesting to note that the case $\Delta\tau \gg \tau$ corresponds to the so-called Fano effect [211]. This phenomenon was initially discussed in the context of the inelastic scattering of electrons from helium in the weak coupling, where an asymmetric line shape appears in the cross-section. In general, it occurs when a very narrow energy level is coupled to a continuum and can occur in all sorts of nanoscale structures, particularly in quantum dots with electron-phonon coupling and in Aharonov-Bohm interferometers, cf. [208, 212, 213] and references therein.

Finally, we show the necessity of the minus sign in front of the hopping by considering the conductance in the case $-\tau \to \pm\tau$ for the hopping from the left lead onto the first dot. The linear conductance Equ. (3.73) is given by

$$\frac{G}{G_0} = 4\Gamma^2 \left| \frac{\pm\varepsilon_2}{(\pm 1 - 1)^2 (\tau + \Delta\tau)^2 - 2i\Gamma\varepsilon_2} \right|^2 \tag{8.1}$$

which becomes 1 in the case of the plus sign, independent of ε_2. So no interference is observed when considering hoppings without a sign difference in the hoppings. In the case of a sign difference with $-\tau$, the linear conductance reads

$$\frac{G}{G_0} = \frac{(\varepsilon_2)^2}{4\Gamma^2(\varepsilon_2)^2 + 16\,(\tau + \Delta\tau)^2}, \tag{8.2}$$

which depends on the on-site energy ε_2 and becomes zero when the second dot crosses the Fermi-energy $\varepsilon_1 = \varepsilon_3 = 0$.

In summary, we found that a node in the linear conductance can arise from interference between two transport channels. Two conditions are necessary for this to occur. First, fermions must be able to traverse both channels simultaneously. In the double dot example, this happens when both energy levels are resonant with the Fermi level at the same time. Second, the tunneling from the left and right leads of a given channel must have opposite signs. When both criteria are met, destructive interference can occur.

8.2. Triple dot system - detuning the central dot

After examining how the interference between two energy levels affects the linear conductance, we now turn to the linear chain described in Sect. 2. We investigate how the coupling of the fermionic system to light via the Peierls substitution, Equ. (2.18), and how the resulting effective long-range interaction influences the conductance through the system. We focus on an impurity consisting of $M = 3$ quantum dots, representing the minimal system in which long-range interactions and multiple transport channels can occur. A schematic of the system is provided in Fig. 7.1. Only the central quantum dot is embedded in the cavity, and the adjacent hopping parameters are renormalized via the Peierls phase with constant coupling $g_{12} = g_{23} = g$, see Sect. 7.1.2. In this section, we only tune the on-site energy of the central dot ε_2, while the on-site energies of the left ($i = 1$) and right ($i = 3$) dots are fixed at the Fermi level, $\varepsilon_1 = \varepsilon_3 = 0$.

Before considering the interacting system, we briefly analyze the transport through the system decoupled from the cavity ($g = 0$). Concurrently, we couple the fermions to the cavity mode via the Peierls substitution in Coulomb gauge to analyze the effect of the effective long-range interaction on the linear conductance. In this case, we compare the results obtained when taking only the first order in the vector potential of the exponential into account with the ones obtained when including the second-order term within the MF approach.

8.2.1. Non-interacting system

As we have seen in Sect. 8.1, the interference can be understood by analyzing it in energy space. Therefore, we first diagonalize the Hamiltonian of the isolated fermionic quantum dot system $H_{1\mathrm{D}}$ in Equ. (2.3), with $\Gamma = 0$ and $g = 0$. The eigenenergies are given by

$$E_0 = 0, \qquad\qquad E_\pm = \frac{1}{2}\left(\varepsilon_2 - \sqrt{8t^2 + (\varepsilon_2)^2}\right). \tag{8.3}$$

Rotating the lead-hopping into the left and right reservoirs, defined in Equ. (2.4), in the eigenbasis of $H_{1\mathrm{D}}$ results to

$$\begin{aligned} \tau_0^L &= -\frac{\tau}{\sqrt{2}} \qquad\qquad \tau_0^R = \frac{\tau}{\sqrt{2}} \\ \tau_\pm^{R/L} &= \frac{2\tau}{\sqrt{8 + \left|\frac{\varepsilon_2 - \sqrt{(\varepsilon_2)^2 + 8t^2}}{t}\right|^2}}. \end{aligned} \tag{8.4}$$

The hopping τ_ϵ^s is the hopping contribution from lead $s \in \{L, R\}$ into the E_ϵ state of the quantum dot system. Note the difference between the on-site energy ε and the energy-index $\epsilon \in \{-, 0, +\}$. The hopping from the leads onto energy level $E_\pm$ is always positive. However, the hopping onto E_0 has a sign difference between the left and right lead. As discussed in the previous chapter, this is the requirement to obtain a dip in the linear conduction due to interference effects. A finite Γ results in more complex analytical expressions; however, the overall conclusion remains unchanged.

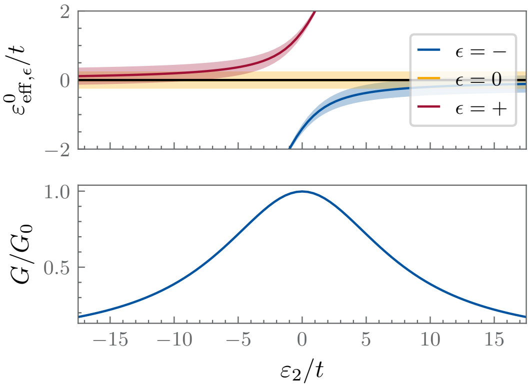

Figure 8.2.: The upper plot shows the effective energy $\varepsilon^0_{\mathrm{eff},\epsilon}$ (lines) and broadening $\Gamma^0_{\mathrm{eff},\epsilon}$ (filled areas) of the triple dot system as a function of ε_2 with $\varepsilon_1 = \varepsilon_3 = 0$ and $\Gamma/t = 0.1$ without coupling to the cavity $g = 0$. The lower plot shows the linear conductance with the same parameters.

For coupling the impurity to the leads ($\Gamma \neq 0$), the linear conductance G/G_0 as a function of the detuning ε_2 is shown in Fig. 8.2. Additionally, we show the effective eigenenergies $\varepsilon^0_{\mathrm{eff}}$ and the broadening Γ^0_{eff}, as introduced in Sect. 3.5.4. These are the eigenenergies already containing the lead contributions. The eigenenergy $\varepsilon^0_{\mathrm{eff},0}$ (yellow), is for all ε_2 in resonance with the Fermi-level, and a finite conductance is expected for all ε_2. However, the linear conductance vanishes for large detuning $\varepsilon_2 \to \pm\infty$. In these cases, the level $\varepsilon^0_{\mathrm{eff},\mp}$ (blue and red) move into the Fermi-level and thus simultaneously into resonance with $\varepsilon^0_{\mathrm{eff},0}$. This scenario is therefore similar to the interference discussed in Sect. 8.1 with the lead-hopping τ_0 exhibiting a sign difference between the hopping into the left and the right lead and $\varepsilon^0_{\mathrm{eff},0}$ and $\varepsilon^0_{\mathrm{eff},\pm}$ being simultaneously in resonance at the Fermi level. Contrary to a single energy level moving through the Fermi level, the linewidth of the linear conductance is no longer directly related to the broadening of the level [214], but is also strongly dependent on how the energies move into each other. The peak is therefore much broader than Γ^0_{eff} in the upper plots of Fig. 8.2 would suggest. Thus, we see that interference effects already dictate the line shape of the linear conductance without the effective long-range interaction present.

8.2.2. Coupling to the cavity

Now, the cavity light field is turned on, with $g \neq 0$. We treat the resulting Peierls phase perturbatively using the expanded form in Equ. (7.20). First, we consider only the contribution linear in the vector potential, which gives the effective interaction vertex in Equ. (3.81) with $A_{ij} = \mathrm{i}\, gt\left(\delta_{i,j+1} - \delta_{i,j-1}\right) =: \lambda\left(\delta_{i,j+1} - \delta_{i,j-1}\right)$. The interaction provides the Matsubara self-energy terms in Equ. (4.2) within the first-order perturbation theory. Subsequently, we include the second-order term in the vector potential from Equ. (7.20) within the MF approach introduced in Sect. 7.3.3, leading to renormalized parameters which are then considered in the first-order perturbative calculations. We show that the inconsistent treatment of the second-order term in the first approach leads to spurious behavior. In equilibrium, the spatial symmetry of the system imposes that $\Sigma_{12} = \Sigma_{21} = \Sigma_{23} = \Sigma_{32}$, $\Sigma_{13} = \Sigma_{31}$, and $\Sigma_{11} = \Sigma_{33}$.

For this setup, we explore the interference from a different perspective and we analyze the linear conductance Equ. (3.73) of the interacting system, for which we have to evaluate the retarded Green function at $\omega = 0$. Having access to the Green function in Matsubara space generally poses the problem of analytical continuation back onto the real axis, which is a numerically involved and delicate

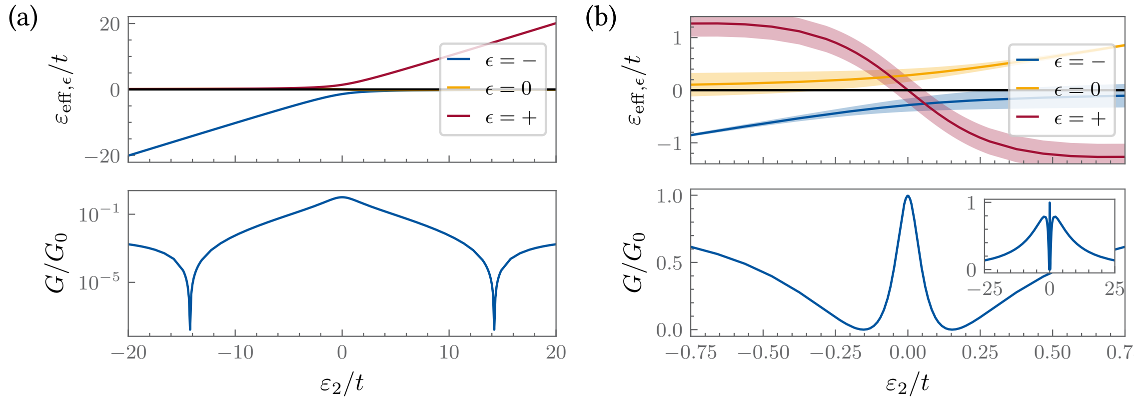

Figure 8.3.: Effective eigenenergies $\varepsilon_{\mathrm{eff},\epsilon}$ (lines) and broadening $\Gamma_{\mathrm{eff},\epsilon}$ (filled areas) of the interacting system in the upper and the linear conductance G/G_0 in the lower plots. Both are plotted as a function of on-site energy of the central quantum dot ε_2 and for $\varepsilon_1 = \varepsilon_2 = 0$, $\lambda/\omega_0 = 0.167\,\mathrm{i}$, $\omega_0/t = 7.5$ and $\Gamma/t = 0.25$. (a) For perturbation theory without second-order terms in the expansion of the Peierls factor and (b) with the corrections of the MF procedure introduced in Sect. 7.3.3. Note the different y scaling. The inlet in (b) shows the same ε_2-range as in (b).

calculation [92, 127] when the Green functions are only known numerically for a finite set of frequencies. In the posed limit, where we only consider the retarded Green function for $\omega = 0$ and for continuous Matsubara frequencies ($T = 0$), we can approximate

$$\left|G^{\mathrm{R}}_{ii'}(\omega = 0)\right| = \lim_{\eta \searrow 0} G(\mathrm{i}\,\eta) \approx G(\mathrm{i}\min[|\omega|]). \tag{8.5}$$

The Green function has to be evaluated at $\min[|\omega|]$, which is the smallest frequency for which the Green function is numerically known and must be smaller than any other energy of the system. So, we do not have to consider the analytic continuation for this calculation. The linear conductance Equ. (3.73) then takes the form

$$\frac{G}{G_0} = \left\{4\Gamma^2\left[(t+\Sigma_{12})^2 - \Sigma_{13}(\varepsilon+\Sigma_{22})\right]^2\right\} / \tag{8.6}$$
$$\left\{\left[(\varepsilon+\Sigma_{22})((\varepsilon+\Sigma_{11})^2 - \Sigma_{13}^2 - \Gamma^2) - 2(t+\Sigma_{12})^2(\varepsilon+\Sigma_{11}-\Sigma_{13})\right]^2 + 4\Gamma^2\left[(t+\Sigma_{12})^2 - \Sigma_{13}(\Sigma_{22}+\varepsilon)\right]^2\right\}.$$

All self-energies are evaluated at $\mathrm{i}\,\omega = \mathrm{i}\,0^+$. We see that to obtain $G = 0$ it is sufficient that $(t+\Sigma_{12})^2 = \Sigma_{13}(\varepsilon+\Sigma_{22})$. It is not evident that such a point exists and strongly depends on the exact setup. Therefore, a sufficient condition for the occurrence of a Fano-like interference is $t + \Sigma_{12} \neq 0 \neq \Sigma_{13}$. Considering a fermion traveling from the first to the last site, two transport channels can interfere. First, a fermion hopping from the first to the second and then to the third site, or secondly, the fermion tunnels directly from the first to the third site.

Because the linear conductance in equilibrium does not contain any frequency dependence due to evaluating the Green function at $\mathrm{i}\,\omega = \mathrm{i}\,0^+$, the behavior can be entirely understood through the effective energy spectrum E_{eff} introduced in Sect. 3.5.4, including lead as well as interaction contributions $\Sigma_{\mathrm{res}}(\mathrm{i}\,0^+)$ and $\Sigma(\mathrm{i}\,0^+)$. Figure 8.3 shows the linear conductance G/G_0 as a function of the detuning ε_2 together with the effective eigenenergies $\varepsilon_{\mathrm{eff}}$ and broadenings Γ_{eff}. In Fig. 8.3(a), only the first-order term in the expansion of the Peierls factor Equ. (7.20) is considered. The linear conductance shows a minor interference node, where $\varepsilon_{\mathrm{eff},0}$ (yellow) and $\varepsilon_{\mathrm{eff},\pm}$ (blue or red) are crossing the Fermi-level simultaneously within their respective broadenings $\Gamma_{\mathrm{eff},\epsilon}$ and interference effects arise. The crossing only occurs, due to the interaction-induced self-energy contributions Σ with $(t+\Sigma_{12})^2 = \Sigma_{13}(\varepsilon+\Sigma_{22})$. However, this node arises in a region, where the conductance is rather small and thus only observable on a logarithmic scale (see lower plot).

As discussed in Sect. 7.3, neglecting the second-order correction in the expansion of the Peierls substitution is not a consistent approximation and can result in unphysical behavior. The first-order perturbation theory without this correction takes into account g^2-terms inconsistently. Including the second-order correction within the MF approach, introduced in Sect. 7.3.3, causes the node to vanish completely. Although another node appears closer to $\varepsilon_2 = 0$, it is not due to the interference of two energies at the Fermi level. Instead, both energies are pushed out of the transport region, primarily due to the renormalization of the self-energies, leading to the condition $(t+\Sigma_{12})^2 = \Sigma_{13}(\varepsilon+\Sigma_{22})$, but without degeneracy. While the underlying cause of transport suppression in both cases is the renormalization of energy scales, the conductance nodes arise from different mechanisms in each approach. Thus, we have shown again that neglecting the second-order corrections in the Peierls coupling can lead to potentially incorrect conclusions about the system's behavior.

Conclusion

In this section, we studied the linear conductance in the triple dot system, where only the central energy level is detuned from the Fermi level. We saw that the linear conductance is generally well understood by the effective energy spectrum of the impurity system.

The interference effects occur already for the case, where no light-matter coupling is involved. In this case, the interference dictates the line shape of the conductance. Subsequently, we introduced light-matter coupling in the Coulomb gauge via the Peierls substitution. We compared the linear conductance when only taking the first-order in the vector potential A of the Peierls factor into account with the one where also the second-order term is considered. For the latter, we used perturbation theory in lowest order and extended it with the MF approach, to obtain expressions for the self-energies describing the light-matter coupling. In both scenarios, we found dips in the linear conductance accompanied by $(t+\Sigma_{12})^2 = \Sigma_{13}(\varepsilon+\Sigma_{22})$. However, when neglecting the quadratic terms in A in the Peierls factor, which is an inconsistent approximation, we found that the dips resulted from interference effects. In contrast, when the quadratic terms were included, the dips arose from the renormalization of the effective energy spectrum, causing the energy levels to shift away from resonance due to the light-matter coupling. This demonstrated again, the different physical behavior resulting when neglecting the second-order term of the exponential function of the Peierls factor. Nevertheless, we note that an interference node due to the effective long-range interaction considering the A^2 term cannot be ruled out in other parameter regimes, which we were not able to identify.

8.3. Triple dot system - detuning all dots simultaneously

Next, all on-site energies of the triple dot system (see Fig. 7.1) are shifted simultaneously, such that $\varepsilon_1 = \varepsilon_2 = \varepsilon_3 = \varepsilon$. Once again, we study how the light-matter coupling affects the linear conductance. To understand the underlying mechanism, we also closely examine the self-energies, which can be analyzed analytically using first-order perturbation theory for certain parameter regimes. Thus, the analytic expressions obtained in first-order perturbation theory can simply be adapted to the MF approach by considering the renormalization of the parameters. We then compare these results to those

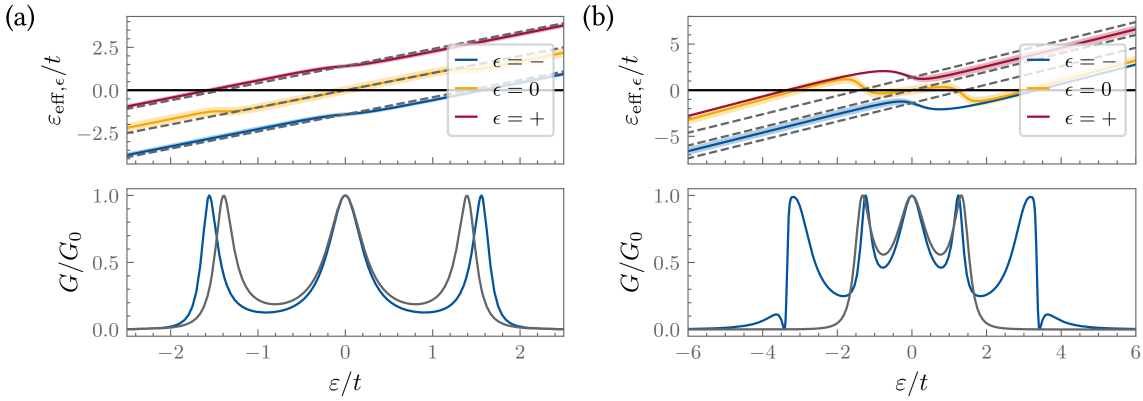

Figure 8.4.: Effective eigenenergies $\varepsilon_{\mathrm{eff},\epsilon}$ (lines) and broadening $\Gamma_{\mathrm{eff},\epsilon}$ (filling) of the interacting system in the upper and the linear conductance in the lower plots. Only the first order in the coupling was considered in the expansion of the Peierls factor. Both are plotted as a function of $\varepsilon_1 = \varepsilon_2 = \varepsilon_3 = \varepsilon$. In the upper plots, the black vertical line indicates the Fermi level. The grey dotted lines indicate the non-interacting case ($\lambda = 0$). (a) $\lambda/t = 0.99\,\mathrm{i}$, $\omega_0/t = 4$, $\Gamma/t = 0.25$. (b) $\lambda/t = 6\,\mathrm{i}$, $\omega_0/t = 20$, $\Gamma/t = 0.5$.

obtained numerically from the combined perturbative-MF approach, which includes all second-order terms in the vector potential for the light-matter coupling and is, therefore, a consistent approximation.

8.3.1. Linear conductance in first-order perturbation theory

In this section, only the linear order in g of the Peierls factor, Equ. (7.20), is analyzed. We consider again this inconsistent approach to first obtain a set of analytic expressions, which can be used in the systematic MF approach and further demonstrate the consequences of the inconsistent treatment. In Fig. 8.4, the linear conductance, along with the effective eigenenergies $\varepsilon_{\mathrm{eff}}$ and their respective broadenings Γ_{eff}, is presented as a function of the detuning ε. The coupling to the cavity is treated using first-order perturbation theory, as discussed in Sect. 4, with the effective interaction given by Equ. (3.81), where $A_{ij} = \lambda\left(\delta_{i,j+1} - \delta_{i,j-1}\right)$, with $\lambda = \mathrm{i}\,gt$, for constant $g_{12} = g_{23} = g$.

In Fig. 8.4(a), a small coupling is considered such that $\lambda^2/\omega_0\Gamma < 1$. The effective energies exhibit slight steps as a function of ε, which shift the detuning at which the Fermi level is crossed. As a result, the outer peaks in the linear conductance are slightly shifted outward compared to the non-interacting case, similar to what occurs in Coulomb-blockaded systems.

When λ is increased, a crossing of the effective eigenenergies due to the induced steps can be observed. This phenomenon is seen in Fig. 8.4(b). In this case, the effective eigenenergies are degenerate and in resonance with the Femi level simultaneously, leading to interference, which is observed as a distinct dip in the linear conductance. While we could not identify a parameter regime where this interference occurs for smaller couplings, we cannot rule out its occurrence in different parameter regimes for arbitrary λ.

In the static case $\mathrm{i}\omega = \mathrm{i}\,0^+$, used to calculate the linear conductance, and when decoupling the triple-dot system from the leads ($\Gamma = 0$), the self-energies can be calculated analytically. These analytic expressions provide a better understanding of how the energies are renormalized, and thus, how the interaction influences the conductance. For this setup, these calculations are carried out in the following section before returning to the study of the linear conductance, including the second-order term in g in the Peierls factor, Equ. (7.20). These expressions can be used for the systematic combined

MF-perturbative approach. However, it is helpful to first understand the effects without the MF renormalization.

8.3.2. Perturbation theory in site space

In the static case $\mathrm{i}\,\omega = \mathrm{i}\,0^+$, the perturbation theory in site space, Equ. (4.2), can be treated analytically. Due to the left-right symmetry of the system in equilibrium, the tunneling interactions $\Sigma_{12} = \Sigma_{21} = \Sigma_{23} = \Sigma_{32} = t$ remain constant and are not renormalized by the cavity. The equality of the self-energy components $\Sigma_{11} = \Sigma_{33}$ and $\Sigma_{13} = \Sigma_{31}$ follow from the same symmetry considerations. Using the general symmetry property $G^\dagger(\mathrm{i}\,\omega) = G(-\mathrm{i}\,\omega)$, Equ. (3.48), the remaining self-energies are given by

$$\operatorname{Re}\Sigma_{11}(\mathrm{i}\,0^+) = -\varepsilon\frac{\lambda^2}{\pi}\int_0^\infty \mathrm{d}\,\omega' \frac{2\omega_0}{\omega'^2+\omega_0^2}\frac{\varepsilon^2-2t^2+\Gamma^2+2\omega'\Gamma+\omega'^2}{\left[\varepsilon^2-\omega'(\Gamma+\omega')-2t^2\right]^2+\varepsilon^2\left[\Gamma+2\omega'\right]^2}, \tag{8.7}$$

$$\operatorname{Re}\Sigma_{13}(\mathrm{i}\,0^+) = -\operatorname{Re}\Sigma_{11}(\mathrm{i}\,0^+), \tag{8.8}$$

$$\operatorname{Re}\Sigma_{22}(\mathrm{i}\,0^+) = -\varepsilon\frac{\lambda^2}{\pi}\int_0^\infty \mathrm{d}\,\omega' \frac{2\omega_0}{\omega'^2+\omega_0^2}\frac{1}{\varepsilon^2+(\Gamma+\omega')^2}. \tag{8.9}$$

The imaginary parts vanish. An additional long-range tunneling term $\Sigma_{13} \neq 0$ emerges, indicating that the cavity induces a second transport channel via the effective long-range interaction.

We first consider the case $\Gamma = 0$, where the chain is decoupled from the leads, focusing solely on the chain's degrees of freedom. Solving the integral in Equ. (8.9) yields

$$\Sigma_{22}(\mathrm{i}\,0^+, \Gamma = 0) = 2\frac{\lambda^2}{\omega_0}\operatorname{sign}(\varepsilon)\frac{1}{\frac{|\varepsilon|}{\omega_0}+1} \overset{|\varepsilon|\ll\omega_0}{\approx} 2\frac{\lambda^2}{\omega_0}\operatorname{sign}(\varepsilon). \tag{8.10}$$

Since the perturbative correction is proportional to the sign of ε, this results in a sharp step at $\varepsilon = 0$. In the anti-adiabatic limit, where $\omega_0 \gg \varepsilon$, the energy varies only slowly with ε. The effective long-range hopping term Equ. (8.8) takes the form

$$\begin{aligned}\Sigma_{13}(i0^+, \Gamma = 0) = {} & \omega_0\varepsilon\lambda^2\frac{\frac{4(2t^2+\omega_0^2-\varepsilon^2)}{\omega_0}}{4\left[(\varepsilon-\omega_0)^2-2t^2\right]\left[(\varepsilon+\omega_0)^2-2t^2\right]} \\ & + \omega_0\varepsilon\lambda^2\frac{\operatorname{sign}(\varepsilon^2-2t^2)\frac{\left[\sqrt{2}\varepsilon^2-4\varepsilon t+\sqrt{2}(2t^2-\omega_0^2)\right]\operatorname{sign}(\varepsilon-\sqrt{2}t)+\left[\sqrt{2}\varepsilon^2+4\varepsilon t+\sqrt{2}(2t^2-\omega_0^2)\right]\operatorname{sign}(\varepsilon+\sqrt{2}t)}{\varepsilon/\sqrt{2}}}{4\left[(\varepsilon-\omega_0)^2-2t^2\right]\left[(\varepsilon+\omega_0)^2-2t^2\right]}\end{aligned} \tag{8.11}$$

This expression can be simplified by considering two distinct limits for the on-site energy ε relative to the hopping t. For $|\varepsilon| \gg \sqrt{2}t$, the perturbative result simplifies to

$$\Sigma_{13}(\mathrm{i}\,0^+, \Gamma = 0) \approx -\frac{\lambda^2}{\omega_0}\frac{\operatorname{sign}(\varepsilon)}{\frac{|\varepsilon|}{\omega_0}+1} \overset{|\varepsilon|\ll\omega_0}{\approx} -\frac{\lambda^2}{\omega_0}\operatorname{sign}(\varepsilon), \tag{8.12}$$

which takes the same form as $\Sigma_{22}(\mathrm{i}\,0^+)$ in Equ. (8.10) in the anti-adiabatic limit. For $|\varepsilon| \ll \sqrt{2}t$, we find

$$\Sigma_{13}(\mathrm{i}\,0^+, \Gamma = 0) \approx \frac{\varepsilon\lambda^2}{\sqrt{2}}\frac{2t^2+\omega_0^2}{\left(\omega_0^2-2t^2\right)^2} \overset{\sqrt{2}t\ll\omega_0}{\approx} \frac{\lambda^2}{\omega_0}\frac{|\varepsilon|\operatorname{sign}(\varepsilon)}{\sqrt{2}\omega_0}. \tag{8.13}$$

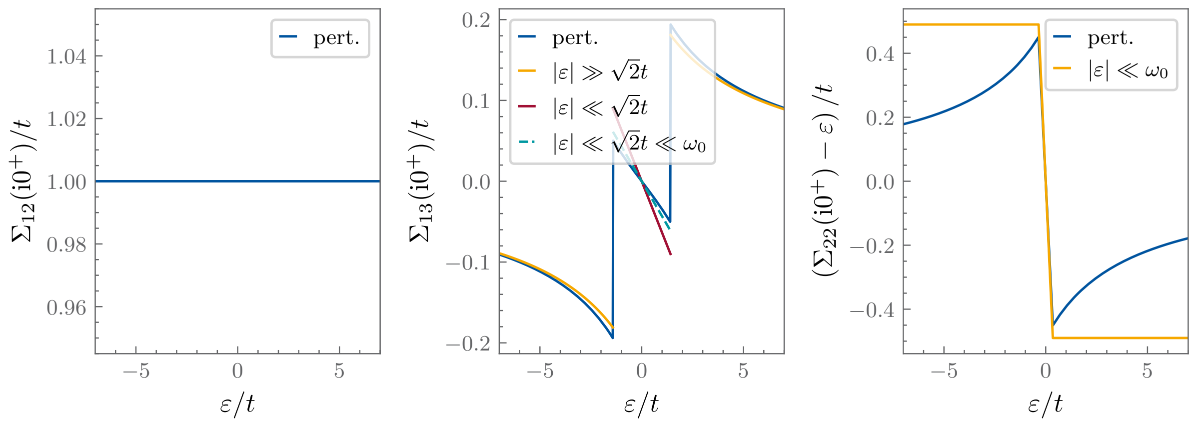

Figure 8.5.: Self-energy components in first-order perturbation theory for coupling to the cavity together with analytic approximations. Same parameters as in Fig. 8.4(a) with $\Gamma = 0$.

The self-energies and their corresponding approximations are displayed in Fig. 8.5. The approximations agree well with the numerical data within their respective parameter ranges. In particular, in the anti-adiabatic limit for large ω_0, $\Sigma_{13}(\mathrm{i}\,0^+)$ becomes progressively smaller in the region $|\epsilon| < \sqrt{2}t$, vanishing linearly with $|\epsilon|/\omega_0$ and proportional to λ^2/ω_0, which, by definition, is small within the perturbative method. This effect becomes more pronounced as one moves deeper into the anti-adiabatic regime. In contrast, in the outer region, we obtain a finite Σ_{13}, which only vanishes in the limit where $|\varepsilon|$ becomes significantly larger than the polaronic shift $E_p = \lambda^2/\omega_0$. We thus conclude that a second transport channel can only open in the outer regions where $|\varepsilon| > \sqrt{2}t$, comparable in magnitude to the first channel, allowing for an antiresonance with $(t + \Sigma_{12})^2 = \Sigma_{13}(\varepsilon + \Sigma_{22})$ to occur.

Introducing a finite coupling to the leads, $\Gamma \neq 0$, smears out the step-like behavior of the self-energies as a function of the detuning ε. Additionally, slight renormalization of both the real and imaginary parts may occur. Interestingly, as Γ increases, we observed the emergence of an additional conductance zero with $(t + \Sigma_{12})^2 = \Sigma_{13}(\varepsilon + \Sigma_{22})$, which does not arise from interference between two effective eigenenergies.

8.3.3. Perturbation theory in energy space

In the static case, it is further insightful to consider perturbation theory in energy space. This allows a deeper analysis and different points of view on where the step-like shift seen in the upper plots of Fig. 8.4 originate from. For this purpose, we rotate in the diagonal basis of the non-interacting one-particle impurity Hamiltonian, decoupled from the leads ($\Gamma = 0$) and the resonator ($\lambda = 0$) in Equ. (2.3). The non-interacting single-particle Hamiltonian H_{1D} of Equ. (2.3) in site space is given by

$$H_{1\mathrm{D}} = \begin{pmatrix} \varepsilon & t & 0 \\ t & \varepsilon & t \\ 0 & t & \varepsilon \end{pmatrix}. \tag{8.14}$$

The rotation into the eigenbasis is governed by

$$U = U^{-1} = U^{\dagger} = \begin{pmatrix} 1/2 & -1/\sqrt{2} & 1/2 \\ -1/\sqrt{2} & 0 & 1/\sqrt{2} \\ 1/2 & 1/\sqrt{2} & 1/2 \end{pmatrix} \tag{8.15}$$

leading to the eigenvalues $E_0 = \varepsilon$ and $E_\pm = \varepsilon \pm \sqrt{2}t$ with energy indices $\epsilon \in \{-, 0, +\}$, not to confuse with the on-site energy ε. At this point, it is important to note that this basis is different from the diagonal basis in the interacting case giving the effective energy spectrum of $H_{\mathrm{eff}} = -\left[G^{\mathrm{R}}(0)\right]$ and denoted by E_{eff}, cf. appendix E. Still considering the static case $\mathrm{i}\,\omega = \mathrm{i}\,0^+$, perturbation theory in first order Equ. (4.1) in the energy basis gives

$$\Sigma_{\epsilon_1',\epsilon_1}(\mathrm{i}\,0^+) = \int \mathrm{d}\,\omega' \sum_{\epsilon} \bar{v}_{\epsilon_1',\epsilon|\epsilon_1,\epsilon}(\mathrm{i}\,\omega') G_{0,\epsilon,\epsilon}(\mathrm{i}\,\omega'), \tag{8.16}$$

with $\epsilon_i \in \{-, 0, +\}$. We used that the free propagator G_0 is diagonal in the E-basis. The interaction vertex takes the form

$$\bar{v}_{\epsilon_1',\epsilon_2'|\epsilon_1,\epsilon_2} = U_{\epsilon_1',i_1'} U_{\epsilon_2',i_2'} \bar{v}_{i_1',i_2'|i_1,i_2} U_{i_1,\epsilon_1} U_{i_2,\epsilon_2} = \frac{\lambda^2}{2\pi} D(-i\omega') \cdot (*)_{\epsilon_1',\epsilon_2'|\epsilon_1,\epsilon_2} \tag{8.17}$$

with $(*)_{\epsilon_1',\epsilon_2'|\epsilon_1,\epsilon_2} \in \{-1, 0, 1\}$, depending on $\epsilon_1', \epsilon_2', \epsilon_1, \epsilon_2$ and not further specified here. For all self-energy components, the same integral has to be evaluated. Solving the real and imaginary parts separately with the help of Mathematica [215] leads to

$$\begin{aligned} &\int_{-\infty}^{\infty} \mathrm{d}\,\omega \frac{1}{\omega^2 + \omega_0^2} \operatorname{Re}\left[\frac{1}{\mathrm{i}\,\omega - E}\right] = \frac{E\left[\omega_0 \tan^{-1}(\omega/E) - E \tan^{-1}(\omega/\omega_0)\right]_{\omega=-\infty}^{\infty}}{E\omega_0(E^2 - \omega_0^2)} = -\frac{\pi}{\omega_0} \frac{\operatorname{sign}(E)}{|E| + \omega_0} \\ &\int_{-\infty}^{\infty} \mathrm{d}\,\omega \frac{1}{\omega^2 + \omega_0^2} \operatorname{Im}\left[\frac{1}{\mathrm{i}\,\omega - E}\right] = 0. \end{aligned} \tag{8.18}$$

and the general result

$$\Sigma_{\epsilon_1',\epsilon_1}(\mathrm{i}\,0^+) = \lambda^2 \sum_{\epsilon} (*)_{\epsilon_1',\epsilon|\epsilon_1,\epsilon} \frac{\operatorname{sign}(E_\epsilon)}{|E_\epsilon| + \omega_0}. \tag{8.19}$$

Concretely this reads

$$\begin{aligned} \Sigma_{--} &= -|\lambda|^2 \frac{\operatorname{sign}(E_0)}{|E_0| + \omega_0} \\ \Sigma_{00} &= -|\lambda|^2 \left[\frac{\operatorname{sign}(E_-)}{|E_-| + \omega_0} + \frac{\operatorname{sign}(E_+)}{|E_+| + \omega_0}\right] \\ \Sigma_{++} &= -|\lambda|^2 \frac{\operatorname{sign}(E_0)}{|E_0| + \omega_0} \\ \Sigma_{+-} = \Sigma_{-+} &= +|\lambda|^2 \frac{\operatorname{sign}(E_0)}{|E_0| + \omega_0} \\ \Sigma_{-0} = \Sigma_{0-} = \Sigma_{+0} = \Sigma_{0+} &= 0. \end{aligned} \tag{8.20}$$

The self-energies obtain steps where $E_0 = \varepsilon$ or $E_\pm = \varepsilon \pm \sqrt{2}t$ cross the Fermi level.

Now, changing into the diagonal E_{eff}-basis of the interacting ($\lambda \neq 0$) but still uncoupled ($\Gamma = 0$) problem, cf. Sect. 3.5.4, we obtain the relation

$$\begin{aligned} \varepsilon_{\mathrm{eff},0} &= \Sigma_{00} + E_0 \\ \varepsilon_{\mathrm{eff},\pm} &= \frac{1}{2}\left[\Sigma_{++} + E_+ + \Sigma_{--} + E_- \pm \sqrt{(\Sigma_{++} - \Sigma_{--} + E_+ - E_-)^2 + 4\Sigma_{+-}}\right]. \end{aligned} \tag{8.21}$$

Hence, we obtain the step-like features in $\varepsilon_{\mathrm{eff},0}$ directly from the crossing from $E_\pm$ with the Fermi level. Where $\varepsilon < -\sqrt{2}t$ $\left(\varepsilon > -\sqrt{2}t\right)$, perturbation theory for Σ_{00} gives two positive (negative) addends to E_0.

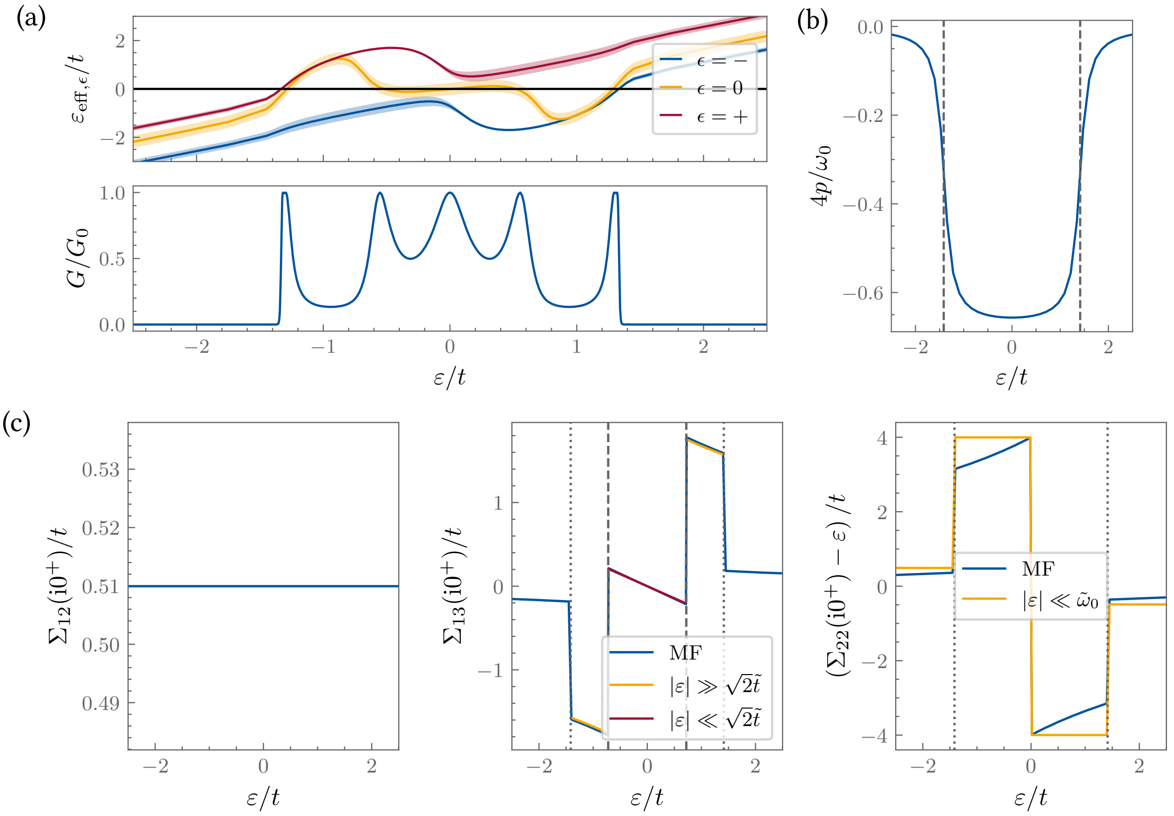

Figure 8.6.: (a) Effective eigenenergies $\varepsilon_{\mathrm{eff},\epsilon}$ (lines) and broadening $\Gamma_{\mathrm{eff},\epsilon}$ (filling) of the interacting system together with the linear conductance. The coupling to the cavity is included within the combined perturbative-MF approach. (b) The MF induced renormalization factor p. The renormalization of the hopping is given by $\tilde{t} \approx 0.51t$. (c) Components of the static self-energy $\Sigma(\mathrm{i}\,0^+)$ within the MF-approach for the blue solid line. The yellow and red line indicate the analytic expressions Equs. (8.10), (8.12) and (8.13) respectively, where the MF renormalized $\tilde{\omega}_0$, $\tilde{\lambda}$ and $\tilde{t}$ are plugged in. All quantities are plotted as a function of $\varepsilon_1 = \varepsilon_2 = \varepsilon_3 = \varepsilon$ and for $\lambda/\omega_0 = 0.25\,\mathrm{i}$, $\omega_0/t = 4$. (a) and (b) are plotted for $\Gamma/t = 0.25$ and (c) for $\Gamma = 0$. The grey dashed lines in (b) and (c) indicate $\varepsilon = \sqrt{2}t$ and the dotted lines $\varepsilon = \sqrt{2}\tilde{t}$.

For $\varepsilon \in \left[-\sqrt{2}t, \sqrt{2}t\right]$, we have one positive and one negative contribution canceling each other and giving an addend of $\frac{-2\varepsilon}{(\omega_0+\sqrt{2}t)^2-\varepsilon^2}$. For $\omega_0 \gg t, \varepsilon$, this becomes relatively small, leading to $\varepsilon_{\mathrm{eff},0} \approx E_0$. The self-energy components Σ_{--},Σ_{++} and Σ_{+-} contributing to $\varepsilon_{\mathrm{eff},\pm}$ exhibit steps of equal amplitude all at the same position $\varepsilon = 0$, where E_0 crosses the Fermi level. However, due to the different prefactor, Σ_{+-} leads to the asymmetry of stepsize. This asymmetry is hard to observe in the energy-spectrum plots in Fig. 8.4(a) due to small steps. Artificially increasing the coupling λ in Fig. 8.4(b), however, shows this quite clearly.

These observations can easily be extrapolated to the case with $\Gamma \neq 0$, which foremost leads to the eigenenergies of $H^0_{\mathrm{eff}} = [G_0(\mathrm{i}\,\omega = 0)]^{-1}$ becoming complex. Thus, also the imaginary part of the integral in Equ. (8.18) becomes finite, leading to an imaginary part of the self-energies $\Sigma_{\epsilon\epsilon'}$. Additionally, the real part of $\Sigma_{\epsilon\epsilon'}$ are slightly shifted. In general, $\Gamma \neq 0$ leads, thus, to a smearing out of the steps in the effective energy spectrum E_{eff} and also slightly shifting the position of the steps.

8.3.4. Mean-field approach

Finally, we incorporate the second-order term in g from the expansion of the Peierls factor, Equ. (7.20), by applying the MF approach introduced in Sect. 7.3.3. This results in the renormalization of the hopping parameter $t \to \tilde{t} = t\left(1 - \frac{g^2}{2}\right)$ (Equ. (7.34)), as well as in modifications of the mode frequency $\omega_0 \to \tilde{\omega}_0 = \omega_0\sqrt{1 - 4p/\omega_0}$ and coupling $\lambda \to \tilde{\lambda} = \lambda\frac{1}{1+4p/\omega_0}$ (Equs. (7.34)), which are then used in the first-order perturbation theory. This approach contains all terms up to order g^2 systematically. The renormalization factor p (Equ. (7.32)) is shown in Fig. 8.6(b), where further t is reduced to $\tilde{t} = 0.51t$. We consider a small coupling with $\lambda^2/\omega_0\Gamma < 1$, utilizing the same parameters as in Fig. 8.4(a). The region where the renormalization takes effect is confined to $|\varepsilon| < \sqrt{2}\,t$, within the broadening proportional to Γ.

Using the MF corrections, the renormalized variables $\tilde{\omega}_0$, $\tilde{\lambda}$ and $\tilde{t}$ can be plugged in the analytic expressions for the self-energies obtained in Sect. 8.3.2. These expressions then include all terms in g^2 of the Peierls factor. They are plotted together with the numerically obtained self-energy components in Fig. 8.6(c) for $\Gamma = 0$. The analytic expressions, thus, allow for a better understanding of the form of the self-energy components even for the combined perurbative-MF approach.

First and most straightforward, $\Sigma_{12}(\mathrm{i}\,0^+)$ is shifted due to $t \to \tilde{t}$. Second, the self-energy component $\Sigma_{22}(\mathrm{i}\,0^+)$ is increased in the region $|\varepsilon| < \sqrt{2}\,t$, where the renormalization p leads to an effective increase of the prefactor $\tilde{\lambda}^2/\tilde{\omega}_0 > \lambda^2/\omega_0$ in the analytic expression Equ. (8.10). Finally, in the $\Sigma_{13}(\mathrm{i}\,0^+)$ component, we observe three distinct regions $|\varepsilon| > \sqrt{2}t$, $\sqrt{2}t > |\varepsilon| > \sqrt{2}\tilde{t}$ and $\varepsilon < \sqrt{2}\tilde{t}$. For $|\varepsilon| > \sqrt{2}t$, p vanishes and no renormaliztion takes place. The self-energy is thus simply given by first-order perturbation theory and the same as in Fig. 8.5. For $\sqrt{2}t > |\varepsilon| > \sqrt{2}\tilde{t}$, the renormalization takes effect and the approximate expression Equ. (8.12) for $|\varepsilon| \gg \sqrt{2}t \to \sqrt{2}\tilde{t}$ describes the self energy component quiete well. We see again that due to the effectively increased $\tilde{\lambda}^2/\tilde{\omega}_0 > \lambda^2/\omega_0$, the self-energy is increased compared to when only considering the first-order perturbative approach. Finally, for $\varepsilon < \sqrt{2}\tilde{t}$, the approximate expression for $\varepsilon \ll \sqrt{2}\tilde{t}$ in Equ. (8.13) agrees well with the numerical results. In this case, we observe again a depleted self-energy component analog to Fig. 8.5. Additionally, the renormalization $\tilde{\omega}_0 > \omega_0$ leads to a further decrease of the self-energy component described by Equ. (8.13). Again, these observations are easily interpolated to finite Γ, where the steps are smeared out and a slight shift of the step position occurs.

Thus, the self-energies change notably for different detuning ε, as seen in Fig. 8.6(c) for $\Gamma = 0$, leading to a more intricate structure in the linear conductance, as shown in Fig. 8.6(a) for $\Gamma \neq 0$. The effective eigenenergies now exhibit a more involved dependence on ε, crossing the Fermi level multiple times, which in turn increases the number of conductance peaks. Additionally, there are points where two eigenenergies cross the Fermi level simultaneously within their corresponding broadening, resulting in a reduction of the conductance due to the interference effects discussed previously. This can be seen at on-site energies around $\varepsilon \approx \pm 1.3t$. The interference effect of the two energy levels leads to the asymmetric line shape of the resonance peak in the conductance, compared to the familiar Lorentz peak [216, 217].

We can also utilize the analytic expressions for the self-energies in energy space in Sect. 8.3.3 to understand the steps occurring in the effective energy spectrum, in the lower plot Fig. 8.6(a). Due to the renormalization of $t > \tilde{t}$, the original step which was observed in the perturbative approach without the MF correction is shifted to $|\varepsilon| = \sqrt{2}\tilde{t}$. This becomes clear from the renormalization of $E_\pm$ in Equ. (8.20). A second step-like feature occurs due to the renormalization of $\tilde{\lambda} > \lambda$ within the MF approach for $|\varepsilon| < \sqrt{2}t$. Looking at Equ. (8.21) together with Equ. (8.20), it is clear that this leads to step in the effective self-energies at $|\varepsilon| = \sqrt{2}t$ and generally increasing its magnitude.

In comparison to simple perturbation theory based on the effective vertex, the self-energies when considering the MF corrections are larger in magnitude. This observation is consistent with the fact that we found in single-particle perturbation theory that the second-order term from the Peierls factor contributes more significantly, cf. Sect. 7.3.2. In this case, the region of significant change is primarily restricted to $|\varepsilon| < \sqrt{2}\,t$. Consequently, in contrast to the discussion in Sect. 8.3.2, we expect interference effects to predominantly manifest in this region. This shows again the importance of including the second-order term of the Peierls factor, which cannot be neglected in first-order perturbation theory and which seems to lead to different physical behavior compared to taking only the linear term into account.

Conclusion

In this section, we studied the linear conductance of a triple quantum dot, where all energy levels are simultaneously detuned away from the Fermi level. We found that step-like features in the effective energy spectrum due to light-matter coupling lead to intricate line shapes in the linear conductance, including several resonance peaks and interference effects.

The effective energy spectrum can be understood through the self-energies, which we studied analytically for the case where the impurity region is decoupled from the leads ($\varGamma = 0$) using first-order perturbation theory while considering only the linear order in the vector potential A in the Peierls factor. We observed that the self-energy corrections are most significant for $\varepsilon > \sqrt{2}t$, where interference effects, governed by $(t + \varSigma_{12})^2 = \varSigma_{13}(\varepsilon + \varSigma_{22})$, were also found in first-order perturbation theory. Furthermore, the shift and step-like features in the effective energy spectrum were directly linked to where the eigenenergies of the non-interacting impurity cross the Fermi energy.

When the second order in A from the Peierls factor was included, which we treated at the MF-level, the self-energies remained significant mostly for $\varepsilon < \sqrt{2}t$. In this regime, interference effects were observed. Thus, although the inclusion of second-order contributions from the Peierls coupling leads to similar effects in the linear conductance as when neglecting it, these effects occur on different energy scales. Thus, we can say again that the inconsistent treatment of the Peierls factor leads to spurious physical behavior. Furthermore, we demonstrated that the analytical results from first-order perturbation theory can be extended to the MF approach by incorporating renormalization of t, ω_0, and λ. This allowed for a deeper understanding of the structure of the self-energy terms.

9. Energy Pumping of a Double Quantum Dot

By coupling a fermionic system to a bosonic cavity, energy transfer between the two systems will occur. In the well-known Dicke model, see for example [78, 79], this coupling results in periodic energy exchange, characterized by the so-called Rabi frequency. This occurs when a two-level system in an excited state is placed in a vacuum cavity, as described in [164, 218]. Similarly, the energy transfer between the lattice electrons and its vibrational excitations has been extensively studied, revealing its impact on the transport properties of solids [96, 99, 212, 219, 220]. We will revisit this specific problem in Sects. 11 and 12, where we also provide more in-depth context to current research in this field.

But also the coupling of matter systems with a light cavity was shown to lead to a change in the properties of the solid. These effects are related to the energy transfer between both systems. In particular and similar to the effects we will discuss in this section, this includes an increase in particle transport [72, 73]. A broader overview of the research in the field of light-matter coupling is given in the introductory Sect. 1.2.

In this chapter, we aim to analyze the energy transfer between a finite impurity system in non-equilibrium and a light cavity. Besides the energy transfer itself, we study how it affects the transport properties of the fermionic system by analyzing the particle current through the impurity region. Additionally, we use this as an easy example to apply the MF approach derived in Sect. 7.3.3 to include second-order contributions of the Peierls phase in the perturbative treatment in a non-equilibrium setup. We compare these calculations with results obtained by the Lindblad master equation, see Sect. 6.2, where all orders of the vector potential in the Peierls phase are taken into account. To this end, we couple the double quantum dot to a single-mode cavity, utilizing the Peierls substitution, as outlined in Equ. (7.20), up to the second order in the vector potential A. The first-order term in this expansion is incorporated via first-order perturbation theory Equs. (4.8)-(4.10), while the second-order term is addressed using the non-self-consistent MF approach. Because we consider a finite bias voltage across the impurity, we evaluate the Green funtions on the Keldysh contour, cf. Sect. 3.2. Finally, we examine the differences between coupling to a zero-temperature vacuum cavity and an excited cavity. This comparison enables us to demonstrate the feedback effects from the cavity. While the Lindblad master equation accounts for these effects, they are not captured by perturbation theory in the lowest order. Throughout this analysis, we neglect Coulomb interaction, assuming $U = 0$.

9.1. The non-interacting double quantum dot

First, let us briefly recap some helpful spectral properties of the double dot system $M = 2$ decoupled from the cavity $\lambda = 0$. We consider the fermionic Hamiltonian described in Sect. 2.1 with $M = 2$ and refer to the first dot as the left ($i = 1 \rightarrow L$) and the second as the right ($i = 2 \rightarrow R$) dot with energies ε_L and ε_R respectively. The effective one-particle eigenenergies $E^0_{\mathrm{eff},\epsilon}$, see Sect. 3.5.4, of the double dot

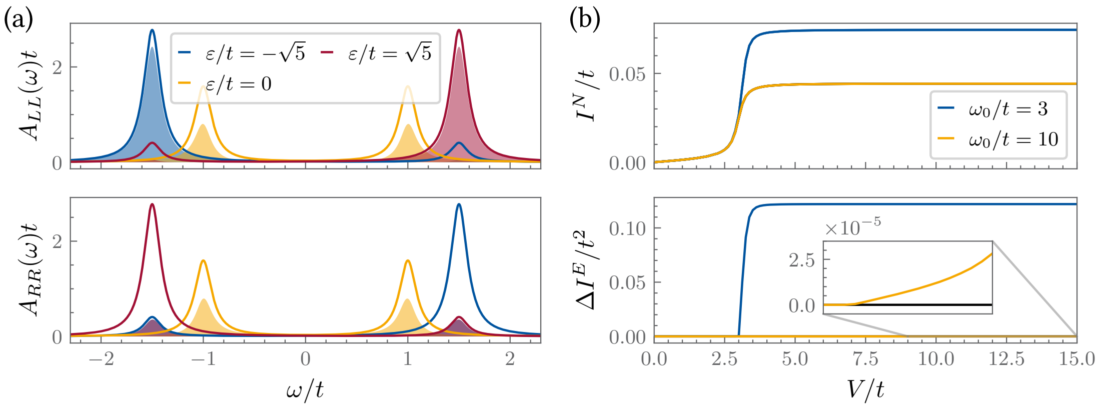

Figure 9.1.: (a) Spectral function (lines) and weight (filled area) of two coupled quantum dots for asymmetric detuning $\varepsilon_L = -\varepsilon_R = \varepsilon/2$ decoupled from the cavity $\lambda = 0$. We consider the small temperature limit $T_L = T_R = T_b = 10^{-4}t$ and the large bias limit $V/t = 20$ and couple to the right and left leads with $\Gamma/t = 0.1$. (b) Particle current I^N and energy dissipation ΔI^E through the double dot system coupled to the cavity, $\lambda/t = 0.1\,\mathrm{i}$, with different frequencies ω_0 as a function of the bias-voltage V and for $\varepsilon/t = \sqrt{5}$. The black line (hidden under the yellow one in the upper plot) indicates the uncoupled case, $\lambda = 0$.

decoupled from the resononator ($\lambda = 0$) but coupled to the leads ($\Gamma \neq 0$) are given by

$$E^0_{\text{eff},\pm} = \frac{1}{2}\left(\varepsilon_L + \varepsilon_R - 2\,\mathrm{i}\,\Gamma \pm \sqrt{(\varepsilon_L - \varepsilon_R)^2 + 4t^2}\right). \tag{9.1}$$

In the case of simultaneously detuning all dots where $\varepsilon_L = \varepsilon_R = \varepsilon$, as considered in Sect. 8 for $M = 3$, the excitation energy $\Delta E = |E^0_{\text{eff},+} - E^0_{\text{eff},-}|$ depends only on the hopping parameter t. As we will see shortly, the excitation energy is the relevant energy scale, when tuning the fermionic system in resonance with the cavity mode. However, from Equ. (9.1) it is clear that for this setup the excitation energy is independent of ε and, thus, the system is not controllable by the easily bias-detunable on-site energy. Hence, we choose an asymmetric detuning instead with $\varepsilon_L = -\varepsilon_R = \varepsilon/2$, where the excitation energy becomes $\Delta E = \sqrt{\varepsilon^2 + 4t^2}$.

In Fig. 9.1(a), we show the spectral function Equ. (3.56) and the corresponding spectral weight Equ. (3.59) for the left and right quantum dot at different values of ε, considering the large-bias limit where V is larger than any other energy scale. We see that positive detuning ($\varepsilon > 0$) can lead to a global population inversion, where higher energy levels are more populated than lower ones across both dots. As we will demonstrate shortly, this population inversion can be harnessed to transfer energy from the fermionic system to the cavity, when both systems are coupled. Conversely, for negative detuning ($\varepsilon < 0$), the lower energy levels are more populated than the higher-lying ones.

Note that the spectral weight is only finite within the transport window for frequencies $|\omega| < V/2$. The large-bias limit is chosen here to broaden the transport window, allowing it to cover all eigenenergy peaks.

9.2. Coupling to a zero-temperature cavity

We now introduce the coupling between the quantum dot and the cavity via Peierls substitution Equ. (7.11) with $\lambda \neq 0$ to investigate how the cavity influences the transport through the fermionic

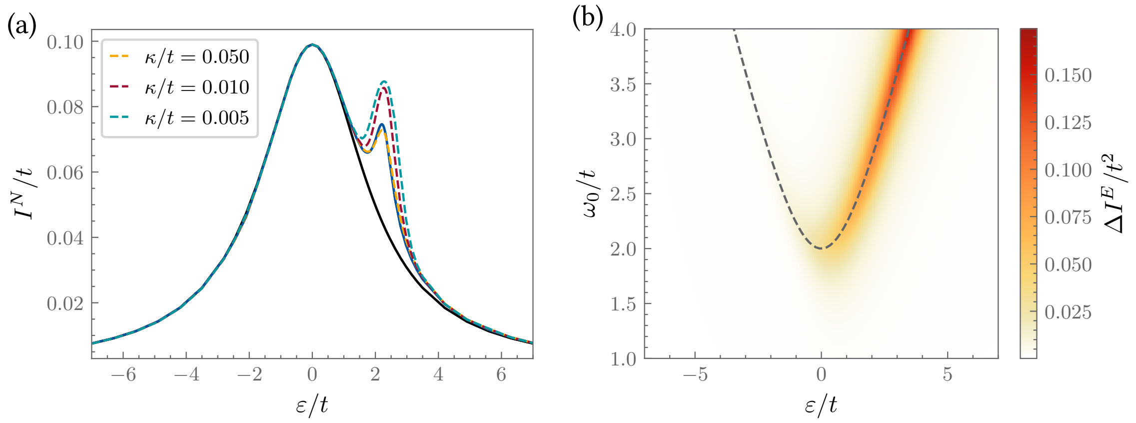

Figure 9.2.: (a) Particle current I^N through the double quantum dot as a function of the asymmetric detuning ε for $\Gamma/t = 0.1$. The black line shows the decoupled case $\lambda = 0$, and the colored plots show $\lambda/t = 0.1\,\mathrm{i}$ and $\omega_0/t = 3$. The solid blue line is obtained by the combined perturbation theory-MF approach and the dashed lines result from the Lindblad master equation for different cavity dissipation κ. (b) The energy dissipation of the double dot ΔI^E into the cavity as a function of the detuning ε and the cavity mode frequency ω_0 for $\lambda/t = 0.1\,\mathrm{i}$ calculated with the perturbation theory-MF approach. The grey dashed line indicates the excitation energies of the fermionic system ΔE.

system. For now, we focus on the low-temperature limit, where $T_L = T_R = T_\mathrm{b}$ is much smaller than any other energy scale in the system.

In the upper plot of Fig. 9.1(b), the particle current is shown as a function of the bias voltage $\mu_L = -\mu_R = V/2$ for the double quantum dot both in resonance with the cavity ($\omega_0/t = 3$) and out of resonance ($\omega_0/t = 3$). Resonance occurs when the transition energy matches the mode frequency, $\Delta E = \omega_0 = 3t$. In our setup, this condition is met when $\varepsilon = \sqrt{\omega_0^2 - 4t^2}$ (here, $\varepsilon = \sqrt{5}t$ as shown in Fig. 9.1(b)). These plots are obtained using lowest-order perturbation theory for the lowest-order expansion of the Peierls phase in the vector potential and including the second-order term A^2 within the non-self consistent MF scheme, see Sect. 7.3.3. As expected, there is a small impact on the current due to the coupling when the cavity is off-resonance. However, when tuned to resonance, the current increases significantly once the transport window becomes large enough to encompass both spectral peaks, $V/2 > |E^0_{\mathrm{eff},\pm}|$. This increase is due to inelastic tunneling processes, where fermions can deposit energy into the cavity, allowing them to tunnel into a lower energy state. Thus, this process is also called photon-assisted tunneling.

The energy transfer between the two systems is evident in the energy dissipation of the fermionic system, as shown in the lower plot in Fig. 9.1(b). In the resonant case, the double dot begins to pump energy into the cavity as soon as fermions start to flow through it, i.e., when $\Delta E = \omega_0 > V/2$. Even when away from resonance, the fermionic system still deposits energy into the cavity once the bias is sufficiently large, $V > \omega_0$. However, the energy transferred in this non-resonant case is significantly smaller, resulting in only a slight increase in the particle current (see inset in Fig. 9.1(b)).

We now examine the electric and energy transport through the fermionic system in the large-bias limit. In Fig. 9.2(a), the particle current is plotted as a function of the asymmetric detuning ε. Compared to the non-coupled double quantum dot system, the current through the system coupled to the cavity shows a peak at resonance $\varepsilon = \sqrt{5}t \approx 2.24t$. This peak is attributed to photon-assisted coupling. Resonance is observed only for positive ε. This is due to the fact that in the zero-temperature regime, the Bose distribution becomes small $b(\omega_0) \to 0$, rendering the cavity effectively empty. In first-order perturbation theory, where feedback effects are neglected and changes in the cavity are not considered, the cavity can only absorb energy. Consequently, only transitions where energy is transferred from the fermions to the cavity, i.e. transitions across population-inverted levels, can enhance the tunneling process. As illustrated in Fig. 9.1(a), population inversion occurs only for positive detunings. To observe an increase in particle current at negative detuning $\varepsilon = -\sqrt{\omega_0^2 - 4t^2}$, one could, for instance, drive the cavity by setting the bosonic distribution to a finite value at the cavity mode frequency ($b(\omega_0) \neq 0$) or by raising the cavity temperature T_b in our calculations. This will be studied in more detail in Sect. 9.3.

But first, we compare the results of perturbation theory with those from the Lindblad master equation, also shown in Fig. 9.2(a), and find the same qualitative behavior, although the quantitative values differ between the two methods. At this point, we refer to the comment in Sect. 6.2.3 that the two methods are inherently different and cannot be compared straightforwardly. In perturbation theory, we neglect the feedback effect of the filled cavity, which is included in the master equation approach: in the steady state, there is a balance between the energy pumped into and out of the bosonic system [91]

$$\frac{\mathrm{d}}{\mathrm{d}t}\langle n_\mathrm{b}(\omega_0)\rangle = \frac{\Delta I^E}{\omega_0} - \kappa\left[\langle n_\mathrm{b}(\omega_0)\rangle - b(\omega_0)\right] \to 0. \tag{9.2}$$

Here, n_b is the mode occupation, which remains constant in a steady state. This balancing mechanism is absent in perturbation theory. Instead, the cavity is considered always empty, which is equivalent to infinite dissipation κ. On the other hand, the boson spectral function is infinitely narrow around ω_0 in the limit of $\kappa \to 0$. This inconsistency means that no trivial limit in κ can be found where the two methods coincide. We note additionally, that the Lindblad master equation contains all orders in the vector potential in the Peierls phase. However, this should not have a great impact on the results as we work in the perturbative regime for small couplings. For this regime, we found in Sect. 7.3 that including the second-order terms in the expansion with the MF approach well reproduces the results of not expanding the exponential function at all.

In Fig. 9.2(b), the energy dissipation of the fermionic system is shown as a function of the detuning ε and the cavity mode frequency ω_0. As expected, the region with significant energy dissipation coincides with the resonance condition where the excitation energy equals the mode frequency $\Delta E = \omega_0$, indicated by the grey dashed lines. Again, we observe energy dissipation only for positive ε. Moreover, the energy transfer disappears as $\varepsilon \to 0$, where no population inversion occurs as seen in Fig. 9.1(a). Calculating the energy transfer with the master equation Equ. (6.41) showed the same result. These are the parameter regimes where boson-assisted tunneling occurs.

9.3. Coupling to an excited cavity

As stated above, in perturbation theory and the zero-temperature regime, the fermionic system experiences an always-empty cavity and can therefore only absorb energy from the bosonic system. However, if driving the cavity by pumping or increasing its temperature to obtain a finite filling, bosons can also be absorbed by the quantum dot system. As seen in the upper plot of Fig. 9.3(a), increasing the temperature indeed leads to a boson-assisted transport at negative $\varepsilon = -\sqrt{\omega_0^2 - 4t^2}$ as well, increasing the particle current through the dot. Comparing this to the energy dissipation, shown in the lower plot of Fig. 9.3(a), it is clear that this process originates from the absorption of a boson, giving a negative energy dissipation of the dot system. This is also consistent with the spectral function and filling shown in Fig. 9.1(a). At negative energies, the transition of the two non-population inverted energy

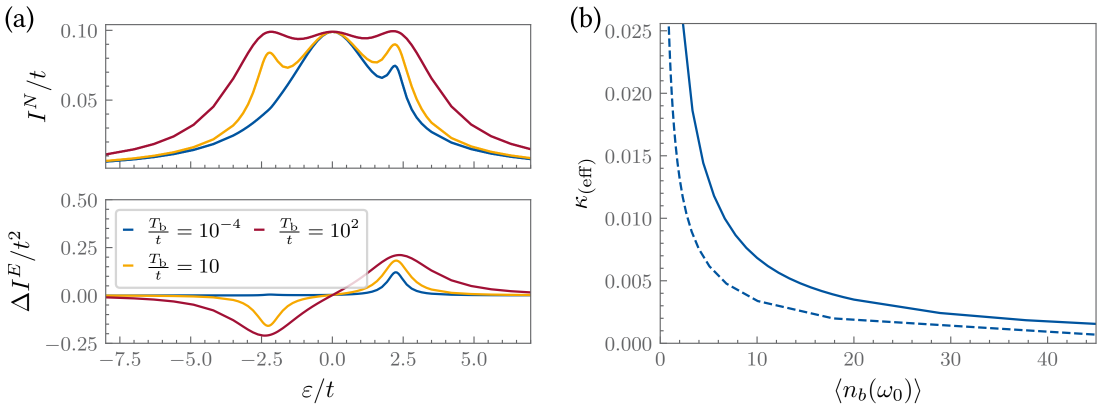

Figure 9.3.: (a) Particle current I^N through the double quantum dot and energy dissipation ΔI^E into the cavity as a function of the detuning ε for different temperatures of the bosonic cavity T_b. The temperature of the fermionic leads stays constant in the zero-temperature limit $T_L = T_R = 0$ and the large bias-voltage limit $V/t = 20$ is considered. Parameters as in Fig. 9.2 for $\lambda/t = 0.1\,\mathrm{i}$ and calculated with perturbation theory with MF-renormalized parameters. The average of the filling with the given temperatures is $b(\omega_0) = \{0, 2.86, 32.81\}$ from lowest to highest temperature. (b) Effective dissipation κ_{eff} from the perturbative calculation with MF-corrections (solid line) and κ for the Lindblad master equation (dashed line) for a given bosonic occupation in the cavity.

states is in resonance, so that energy is absorbed by the quantum dot system in the process, just as we expected.

We have discussed that the balancing mechanism in Equ. (9.2) is not included in the perturbation theory approach. However, when driving the cavity and no longer assuming the thermal distribution $b(\omega_0) \approx 0$ but instead a finite $\langle n_b(\omega_0)\rangle$, one can define an effective broadening κ_{eff} from this equation in steady state

$$\kappa_{\mathrm{eff}} = \frac{\Delta I^E}{\omega_0 \langle n_b(\omega_0)\rangle}. \tag{9.3}$$

The effective dissipation rate as a function of the cavity filling is plotted in Fig. 9.3(b) (solid line) in comparison with the average cavity occupation for a given κ calculated with the Lindblad master equation (dashed line). We see again good qualitative agreement, but a deviation for the quantitative values. There are multiple factors, why this is the case, which are related to the statement above that there is no straight-forward κ limit in which the two methods agree. First, the balancing mechanism between the different energy dissipation channels is still not taken into account in the perturbative treatment. This means that the cavity is not changed due to the fermionic system. This also includes the broadening of the cavity mode which leads to $\langle N_b\rangle \neq \langle b(\omega_0)\rangle$. It is important to note that this dissipation only reflects the effective filling of the cavity and does not take into account the broadening of the bosonic spectrum. Therefore, κ_{eff} is not equivalent to the broadening used in the Lindblad master equation. It shows, however, that the balancing mechanism can be reasonably well represented in perturbation theory, leading to the same qualitative dependence of filling and dissipation in the steady-state limit as the Lindblad results.

Conclusion

In this chapter, we examined the energy transfer between a cavity and a double quantum dot system, with a finite bias voltage applied across the impurity region and asymmetrically detuned energy levels ($\varepsilon_1 = -\varepsilon_2 = \varepsilon/2$). The light-matter coupling is modeled by the Peierls substitution, where we utilized the combined perturbative-MF approached and the Lindblad master equation. First, we analyzed the zero-temperature limit ($T_L = T_R = T_\mathrm{b}$), where significant energy transfer was observed only for positive detuning ($\varepsilon > 0$) when the cavity mode was tuned into resonance with the excitation energies of the fermionic system ($\Delta E = \omega_0$) and for a bias voltage $V/2 > |E_\pm|$. The energy transfer into the cavity is explained by a population inversion, where the spectral peak of the higher-lying eigenenergy of the fermionic system is more occupied than the lower one. This effect simultaneously leads to boson-assisted tunneling processes, as indicated by an increase in particle current.

When the cavity is excited by increasing its temperature, a resonance peak in the particle current was also observed for negative detuning ($\varepsilon < 0$), where the energetically lower-lying states are more occupied than the higher-lying ones, leading to energy transfer into the fermionic system. Finally, we discussed that the perturbative approach, unlike the Lindblad master equation, cannot model the balancing of energy between the fermionic system and the cavity, as it does not account for the influence of the quantum dot system on the cavity. However, we demonstrated that in the limit of small coupling λ and large bias V, the two methods exhibit the same qualitative behavior, albeit with quantitatively different results. In general, we can however say that the combined perturbative-MF approach well reproduces the physical behavior from the Lindblad master equation approach.

9.4. Short excurse on logarithmic divergencies in perturbation theory and in the functional renormalization group method

At this point, we want to utilize the double quantum system, considered in this part of the thesis, to briefly comment on the logarithmic divergencies mentioned in Sect. 5, which can occur in perturbation theory and can in some instances be cured by applying FRG. A full discussion can be found in appendix F.1. Note that we only consider the linear term in the vector potential in first-order perturbation theory without the MF corrections. The reason for this is also outlined in the appendix.

For the system under consideration, we find a logarithmic divergence in the real part of the retarded self-energy for frequencies $\omega \to \omega_0$ when using first-order perturbation theory. When comparing the scaling of the perturbative self-energy components for frequencies close to the cavity mode frequency with the retarded self-energy components obtained with FRG, it becomes apparent that the FRG approach does not cure the divergencies for the system at hand. Instead, the self-energy components of both methods exhibit the same logarithmic scaling $\sim \log(\omega - \omega_0)$.

Additionally, we find that the singularity in the self-energy components directly translates to a zero in the spectral function and, thus, physical observables. Nevertheless, the sharp features have little impact on integrated variables, such as the occupation and currents introduced in Sect. 3.5. Therefore, we expect that perturbation theory can reliably capture the correct physical behavior of these quantities.

Part IV.

Coupling Matter to a Vibrational Mode

In this part, we discuss the coupling of the fermionic degrees of freedom to a bosonic resonator via a capacitive coupling, which describes a phonon-fermion coupling or a coupling with a *LC*-circuit. In Chapter 10, we provide a brief overview of this coupling and typical effects arising from it. This also includes interference effects emerging due to the fermion-boson coupling, similar to what was discussed for the light-matter coupling. Subsequently, in Chapter 11, we discuss a triple-dot system in non-equilibrium with additional long-range hopping, which leads even in the non-interacting system to interference effects. When coupling to the resonator, these interferences can be used to control the energy transfer between the two systems. We compare this setup with a system without long-range hopping and explain the underlying mechanisms of the transfer. Finally, we discuss a combination of the interacting resonant level model and the spinless Anderson-Hohlstein model by including a nearest-neighbor Coulomb interaction besides the coupling to the resonator in Chapter 12. We discuss, how the transport characteristics of both individual models translate to the one of the combined model.

10. Capacitive Coupling - an Overview

The second type of fermion-boson interaction, we study in the present thesis, is a capacitive coupling of the bosonic mode to the fermionic chain. In this case, the bosons couple directly to the local occupation of the fermions, as introduced in Sect. 2.2.2. In general, this model can describe the quantum dot system coupled to an electric *LC* circuit or a phonon mode, as discussed in the introductory Sect. 1.3. The coupling takes the form of Equ. (2.20), which we reproduce here for convenience:

$$H_{\mathrm{fb}} = \left(a + a^\dagger\right) \sum_{j=1}^{M} \lambda_j c_j^\dagger c_j. \tag{10.1}$$

It is of the general form of Equ. (2.21) with $A_{ij} = \lambda_i \delta_{i,j}$ and the effective fermionic interaction can directly be obtained by plugging this into Equ. (3.81) or Equ. (3.83). We consider here that the resonator can couple differently to each quantum dot i with strength λ_i.

The purpose of this chapter is twofold. First, it serves as an introductory chapter for the capacitive coupling and second as a comparison to the aforementioned discussed light-matter coupling. To this end, we discuss how the capacitive coupling influences the particle-hole symmetric point by effectively shifting the on-site energies of the quantum dot region. Furthermore, we explore the possibility of the capacitive coupling inducing interference effects in the transport properties, similar to what was observed for the light-matter coupled system. Finally, we comment on the logarithmic divergence arising when analyzing the capacitive coupling in first-order perturbation theory.

10.1. Particle-hole symmetry

In contrast to the Peierls substitution, cf. Sect. 7.2, and analogous to the Coulomb interaction, cf. Sect. 2.1.1, the capacitive coupling breaks the particle-hole symmetry. Considering the transformation $d_i \to \tilde{d}_i = d_i^\dagger$ and $c_{k_s} \to \tilde{c}_{k_s} = -c_{k_s'}^\dagger$ as described in Sect. 2.1.1 together with $a \to \tilde{a} = -a - \frac{\sum_j \lambda_j}{\omega_0}$, the part of the Hamiltonian introducing the bosons takes the form

$$\tilde{H}_{\mathrm{b}} + \tilde{H}_{\mathrm{fb}} = \omega_0 a^\dagger a + \left(a + a^\dagger\right) \sum_j \lambda_j d_j^\dagger d_j + 2\frac{\sum_i \lambda_i}{\omega_0} \sum_j \lambda_j d_j^\dagger d_j, \tag{10.2}$$

where all constant terms were omitted. The first two terms are the same as in the non-transformed Hamiltonian $H_{\mathrm{b}} + H_{\mathrm{fb}}$, Equs. (2.16) and (10.1), but the last part effectively shifts the on-site energies of the quantum dots. So the PHS point is then given by $\vec{\varepsilon}_{\mathrm{PHS}} = \left(\frac{\lambda_1 \sum_i \lambda_i}{\omega_0}, \frac{\lambda_2 \sum_i \lambda_i}{\omega_0}, ..., \frac{\lambda_M \sum_i \lambda_i}{\omega_0}\right)$, which is related to the polaronic shift $E_p = \lambda^2/\omega_0$ in the spinless Anderson Holstein model, cf. [92]. We include the shift in the renormalization of the energy space of the Hamiltonian $\varepsilon_j \to \varepsilon_j - \frac{\lambda_j \sum_i \lambda_i}{\omega_0}$ or equivalently redefine

$$H_{\mathrm{fb}} = \left[a + a^\dagger - \frac{\sum_{i=1}^{M} \lambda_i}{\omega_0}\right] \sum_{j=1}^{M} \lambda_j c_j^\dagger c_j \tag{10.3}$$

to obtaine again the PHS point at $\vec{\varepsilon}_{\mathrm{PHS}} = (0, 0, ..., 0)$.

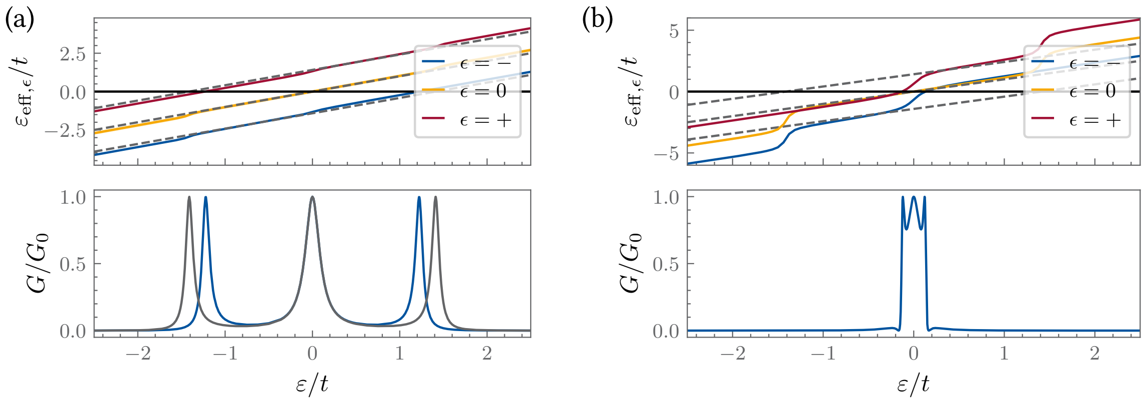

Figure 10.1.: Effective eigenenergies $\varepsilon_{\mathrm{eff},\epsilon}$ (lines) and broadening $\Gamma_{\mathrm{eff},\epsilon}$ (filling, very small) of the interacting system in the upper and the linear conductance G/G_0 in the lower plots calculated with first-order perturbation theory. Both are plotted as a function of $\varepsilon_1 = \varepsilon_2 = \varepsilon_3 = \varepsilon$. The resonator frequency is $\omega_0 = 10t$ and the broadening $\Gamma = 0.1t$. In the upper plots, the black vertical line indicates the Fermi level and the grey dotted lines the non-interacting effective eigenenergies, $\lambda = 0$. The grey line in the lowe plot of (a) indicates the conductance for $\lambda = 0$. (a) $\lambda/t = 0.99$, (b) $\lambda/t = 2.97$.

10.2. Interference effects in the linear conductance

In Sect. 8, we have seen that the effective long-range interaction due to the light-matter coupling can lead to Fano-like interference effects in the linear conductance. The capacitive coupling leads to a long-range fermionic interaction as well, which introduces effective long-range hopping between the quantum dots and, thus, opens different transport channels across the dot system. We briefly show that interference between the channels can also be observed in the case of the capacitive coupling.

In this section, we again employ a triple dot system ($M = 3$) of the form described in Sect. 2.1 as a minimal example and consider a constant coupling to the resonators $\lambda_i = \lambda$ for all sites $i = \{1, 2, 3\}$. The resonator is described by Equ. (2.16) as a single-mode harmonic oscillator. Additionally, we consider the case where all quantum dots are detuned simultaneously with $\varepsilon_1 = \varepsilon_2 = \varepsilon_3 = \varepsilon$. To this end, we utilize perturbation theory in first order (cf. Sect. 4) to treat the coupling between the fermions in the quantum dot system and the bosons in the resonator. We study the linear conductance and simultaneously analyze the effective energy space to understand the effects occurring in the fermionic transport. Analog to Sect. 8.3.1, we provide analytic expressions for the self-energies to determine, in which parameter regime long-range hopping occurs.

The linear conductance G/G_0 together with the effective eigenenergies of the interacting system, as described in Sect. 3.5.4, are shown in Fig. 10.1 as a function of the detuning. In Fig. 10.1(a), we consider a small phonon-fermion coupling, so that the perturbative approach is assumed to produce reliable results. Step-like features in the effective eigenenergies also arise from the capacitive coupling, similar to the behavior observed in the light-matter coupling. For the capacitive coupling, they lead to an inward shift of the outer peaks of the linear conductance, in contrast to what occurs for a repulsive Coulomb interaction. For the small coupling strength, a crossing of the different energies cannot be seen, and thus, no interference effect takes place.

Similar to Fig. 8.4(b) for the light-matter coupling, we can increase the coupling strength to shift the effective eigenenergies into degeneracy and induce interference effects. Note, however, that it is unclear whether the perturbative method provides reliable results at larger λ. We nonetheless employ large

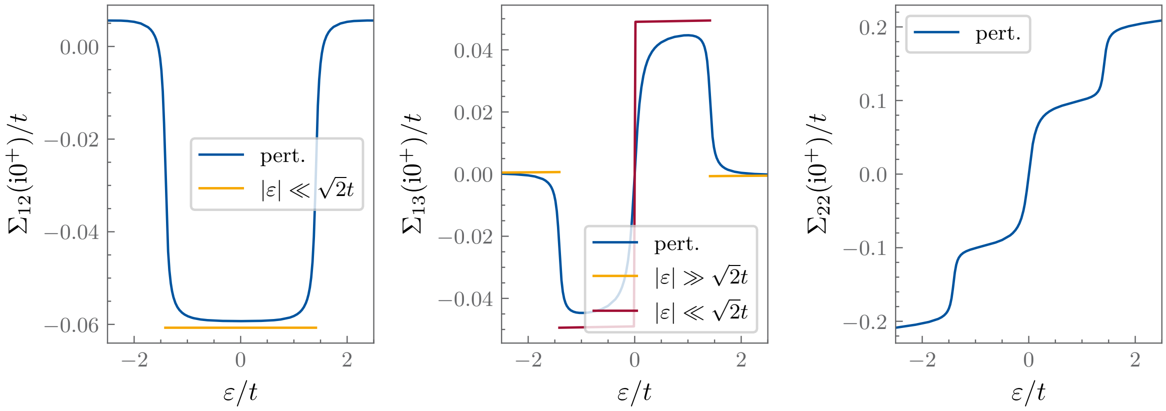

Figure 10.2.: Self-energy components in first-order perturbation theory (blue) for coupling to the cavity together with the analytic approximations (yellow and red). Same parameters as in Fig. 10.1(a).

couplings to illustrate the possibility of interference effects due to the capacitive coupling. The results are shown in Fig. 10.1(b). Indeed, an interference effect leading to a zero in the linear conductance can be observed in this case. Similar to what was observed for the light-matter coupling in Fig. 8.6, the interference occurs in a region $\varepsilon < \sqrt{2}t$. Thus, the capacitive and the light-matter coupling can introduce interference effects in the same detuning regime.

To understand this phenomenon, it is important to recall the necessity of a finite long-range hopping term, Σ_{13}, for interference to occur (see Sect. 8.2). More specifically, we have established that $(t+\Sigma_{12})^2 = \Sigma_{13}(\varepsilon+\Sigma_{22})$ is sufficient for zero linear conductance (cf. Equ. (8.6)), with the same symmetries applying to systems with either Peierls or capacitive coupling. Thus, we take a closer look at the stationary self-energies in Matsubara formalism $\Sigma(\mathrm{i}\,0^+)$ obtained with first-order perturbation theory Equ. (4.2), which can be treated analytically when decoupling the quantum dots from the leads, $\Gamma = 0$. We only give an analytic expression for the renormalized hoppings Σ_{12} and Σ_{13}. Using Mathematica [215], we obtain

$$\Sigma_{13}(\mathrm{i}\,0^+, \Gamma=0) = -\frac{\lambda^2\omega_0\varepsilon t^2}{8}\left[\frac{4\,\mathrm{sign}(\varepsilon)}{\varepsilon t^2(\varepsilon^2-\omega_0^2)} + \frac{-\,\mathrm{sign}(\varepsilon^2-2t^2)\frac{\left[\sqrt{2}\varepsilon^2-4\varepsilon t+\sqrt{2}(2t^2-\omega_0^2)\right]\mathrm{sign}(\varepsilon-\sqrt{2}t)+\left[\sqrt{2}\varepsilon^2+4\varepsilon t+\sqrt{2}(2t^2-\omega_0^2)\right]\mathrm{sign}(\varepsilon+\sqrt{2}t)}{\varepsilon t^2/\sqrt{2}} - \frac{8\left[2t^2-3\omega_0^2-\varepsilon^2\right]}{\omega_0(\varepsilon^2-\omega_0^2)}}{4\left[(\varepsilon-\omega_0)^2-2t^2\right]\left[(\varepsilon+\omega_0)^2-2t^2\right]}\right] \tag{10.4}$$

and

$$\Sigma_{12}(\mathrm{i}\,0^+, \Gamma=0) = -\lambda^2\omega_0 t\left[\frac{-4\frac{\varepsilon^2-2t^2+\omega_0^2}{\omega_0} + \frac{\varepsilon^3+\sqrt{2}\varepsilon^2 t-\varepsilon(2t^2+\omega_0^2)+\sqrt{2}t(\omega_0^2-2t^2)}{t/\sqrt{2}|\varepsilon-\sqrt{2}t|} + \frac{-\varepsilon^3+\sqrt{2}\varepsilon^2 t+\varepsilon(2t^2+\omega_0^2)+\sqrt{2}t(\omega_0^2-2t^2)}{t/\sqrt{2}|\varepsilon+\sqrt{2}t|}}{(4(\varepsilon^4-2\varepsilon^2(\omega_0^2+2t^2)+(\omega_0^2-2t^2)^2))}\right]. \tag{10.5}$$

The results can be simplified again in different limits for ε. For the component Σ_{12}, we approximate the results from Equ. (10.5) for $|\varepsilon| \ll \sqrt{2}t$:

$$\Sigma_{12}(\mathrm{i}\,0^+, \Gamma = 0) \approx -\frac{\lambda^2}{\omega_0} \frac{1}{\sqrt{2}\left(1 + \frac{\sqrt{2}t}{\omega_0}\right)}. \tag{10.6}$$

For Σ_{13}, we use Equ. (10.4) to obtain for $|\varepsilon| \ll \sqrt{2}t$:

$$\Sigma_{13}(\mathrm{i}\,0^+, \Gamma = 0) \approx -\frac{\lambda^2}{\omega_0} \left[\frac{1}{2} + \frac{|\varepsilon| t^2}{\omega_0^3} \frac{3 - \frac{2t^2}{\omega_0^2}}{\left(1 - \frac{2t^2}{\omega_0^2}\right)^2} \right] \mathrm{sign}(\varepsilon), \tag{10.7}$$

and for $|\varepsilon| \gg \sqrt{2}t$:

$$\Sigma_{13}(\mathrm{i}\,0^+, \Gamma = 0) \approx -\frac{\lambda^2}{\omega_0} \frac{\frac{t^2}{\omega_0^2}\,\mathrm{sign}(\varepsilon)}{\left(\frac{|\varepsilon|}{\omega_0} + 1\right)^3}. \tag{10.8}$$

The approximation, along with the numerical and full analytic results, is shown in Fig. 10.2. In the outer regions, where $|\varepsilon| > \sqrt{2}t$, Σ_{13} vanishes as $\omega_0^3/|\varepsilon|^3$. As a result, the second transport channel becomes relatively insignificant, preventing any interference with the first channel. In contrast, within the region $|\varepsilon| < \sqrt{2}t$, Σ_{13} increases with a term proportional to the polaronic shift $E_p = \lambda^2/\omega_0$, remaining constant in ε. Simultaneously, Σ_{12} decreases within this parameter regime, bringing the two channels closer in strength. As a consequence, Fano interference is expected to occur in this region, as illustrated in Fig. 10.1.

Conclusion

In this section, we observed that, similar to light-matter coupling, capacitive coupling induces long-range hopping in the quantum dot system. Consequently, the fermionic conductance can exhibit a node due to the destructive interference of two transport channels. We studied this effect in a triple dot, where all energy levels are detuned simultaneously. Comparing this to the phenomenon observed for the same setup with light-matter coupling when consistently including the second-order term in the vector potential, we found that interference occurs at similar detuning scales in both cases. More specifically, two active transport channels were mainly found for $|\varepsilon| < \sqrt{2}t$. Therefore, we conclude that, even though the specific details of both systems are quite different, particularly when considering the energy space, similar interference phenomena can still be observed in the linear conductance.

10.3. Short excurse on logarithmic divergencies in perturbation theory and in the functional renormalization group method

Analogous to the logarithmic divergence encountered in first-order perturbation theory for the Peierls coupling, mentioned in Sect. 9.4 and discussed in Sect. F.1, a similar logarithmic divergence in the self-energies can also be observed for the capacitive coupling. This phenomenon has already been addressed in [92]. In the present thesis, we want to check if FRG is able to cure these divergencies. Here, we only provide the result and the full discussion can be found in apendix F.2. In the appendix, we study the divergence for a double dot system ($M = 2$) capacitively coupled to a resonator with equal coupling strengths, $\lambda_1 = \lambda_2 = \lambda$. The double dot is tuned asymmetrically ($\varepsilon_1 = -\varepsilon_2 = \varepsilon/2$) close to resonance with the resonator. We find that similar to the Peierls coupling, the self-energies calculated with FRG in first-order truncation exhibit the same scaling as the first-order perturbation theory. Therefore, the FRG approach does not cure the logarithmic divergence of the self-energies components occurring in perturbation theory.

11. Energy Pumping in a Triangular Setup

This chapter is based on the following publication, where the main results were already published: [221] C. Hermansen et al., “Simulating electron-vibron energy transfer with quantum dots and resonators”, Phys. Rev. B **110**, 205424 (2024)
For this project, I performed the numerical analysis of the first-order perturbative approach when studying the fermionic degrees of freedom. Further, C. Hermansen and I both performed Lindblad calculations. I specifically provided the analysis of the nearest-neighbor Coulomb interaction, to obtain the energy-dissipation and the application of the quantum regression theorem. Further, I contributed to the interpretation of the results. Finally, I provided the analytic expressions in the appendix of the paper.

In the work presented here we perform minor adjustments to the notation for consistency within the present thesis. I produced most results in this chapter, while contributions from co-authors are explicitly marked. It should be noted that some of the figures in the publication were created independently by C. Hermansen and me. In the present thesis, however, only figures produced solely by myself are included unless otherwise stated.

In the previous chapters, we have considered a simple linear chain, where the tight-binding Hamiltonian Equ. (2.3) only contains nearest-neighbor hopping t. For $M > 2$ also longer-range hoppig t_{ij} can be taken into account. In this chapter, we study the triple quantum dot system $M = 3$ with additional next-nearest neighbor hopping $t_{13} = t_{31} =: s$. This additional longer-range hopping allows for a more intricate energetical structure within the fermionic system. As described in the introductory Sect. 1.3, the quantum dot-resonator system within a circuit QED setup can be used as a simulator of artificial atoms [17]. By including additional long-range hopping in the quantum dot system, the simulators can represent more involved internal structures of the artificial molecular orbitals [46], originating, for example, from different spatial configurations. This structure can lead to additional interference

Parameters	**linear**	**triangle**
Next-nearest neighbor hopping s	0	$0.5t$
Left/right detuning $\varepsilon_L = -\varepsilon_R$	$\varepsilon/2$	0
Central dot energy ε_C	0	ε_C
Hybridization due to reservoir $\Gamma_L = \Gamma_R = \Gamma$	$0.1t$	
Temperature T	$10^{-4}t$	
Voltage bias $\mu_L = -\mu_R = V/2$	$10t$	
Resonator frequency ω_0	$3t$	
Resonator decay rate κ	$0.005t$	
Coupling strength λ	$0.1t$	

Table 11.1.: Model parameters. These parameters are always used in this section unless stated otherwise.

effects [222, 223]. To this end, we compare two different layouts of the quantum dot system focusing on the energy transfer between the two systems and how this influences the fermionic particle transport.

In particular, we consider a triple quantum dot, described by the fermionic model in Sect. 2.1 in two different configurations: (i) the linear one, in which only nearest-neighbor hopping $t_{ij} = t(\delta_{i,j+1} + \delta_{i,j+1})$ is considered, and the triangular one with nearest- and next nearest-neighbor hopping $t_{ij} = t(\delta_{i,j+1} + \delta_{i,j-1}) + s(\delta_{i,j+2} + \delta_{i,j-2})$. In the following, we denote the sites as L for $i = 1$ site, C for $i = 2$, and R for $i = 3$. For the linear configuration, we symmetrically detune the left and right quantum dot $\varepsilon_L = -\varepsilon_R = \varepsilon/2$, while leaving the central dot fixed at the Fermi level $\varepsilon_C = 0$. The triangular setup is the minimal model allowing for single-particle interference to occur. In this case, the left and right dots remain fixed at the Fermi level $\varepsilon_L = \varepsilon_R = 0$ and we only detune the central dot ε_C.

For reasons that will become clear in the following, we couple only the right quantum dot to the resonator ($\lambda_R = \lambda$ and $\lambda_L = \lambda_C = 0$). Additionally, we always consider the infinite-bias limit, where V is much larger than any other energy scale of the system, and the zero-temperature limit. In this limit, we can compare results obtained by perturbation theory, cf. Sect. 4, with calculations with the Lindblad master equation, cf. Sect. 6.2. We will see that for large biases, all states of the fermionic system are within the transport window and the spectral weight can be controlled by bias-tuning the on-site energies. The general set of parameters under consideration is shown in Table 11.1. These parameters are used in all calculations if not stated otherwise. The resonator under consideration has a Q-factor of $Q = f/\kappa \approx 100$, which is relatively low for currently used resonators, c.f. to [20], but is of the order of dominant underdamped vibrational modes in biochemistry [224].

In the following, we first examine the two setups without coupling to the resonator ($\lambda = 0$). We primarily focus on the spectral properties of the fermionic system, while also considering the current and transmission through the impurity system. Next, we introduce the coupling ($\lambda > 0$) and investigate the energy transfer between the two systems, which leads to boson-assisted tunneling in the quantum dot system. We also comment on the increase in the mean occupation of the resonator as energy is pumped into it. Finally, we introduce Coulomb interactions between the fermionic degrees of freedom to assess how robust the observed characteristics are in the presence of these interactions.

11.1. Triple quantum dot system

To assess the quantum dot system's ability to exchange energy with the resonator, it is useful to first examine the voltage-biased triple quantum dot in the absence of interaction with the bosonic degrees of freedom, i.e., with $\lambda = 0$. As discussed in Sect. 9, the excitation energy plays a pivotal role in this context. The one- and two-particle energy spectrum of the quantum dot system described by $H_{1\mathrm{D}}$ Equ. (2.3) as a function of the detuning can be seen in Fig. 11.1 for both setups under consideration. For the linear configuration, the one-particle eigenenergies read

$$E_\pm = \pm\frac{1}{2}\sqrt{8t^2 + \varepsilon^2}, \qquad E_0 = 0 \tag{11.1}$$

and $E_\pm$ are always equidistant to E_0, independently of the detuning ε, as also seen in Fig. 11.1(a). So, two excitation energies ΔE, being the difference of two eigenenergies, are always degenerate. Further, the two-particle eigenergies are identical to the one-particle ones.

In the case of the triangular setup, the one-particle eigenenergies are given by

$$E_\pm = \left(s + \varepsilon_C \pm \sqrt{8t^2 + (\varepsilon_C - s)^2}\right)/2, \qquad E_0 = -s, \tag{11.2}$$

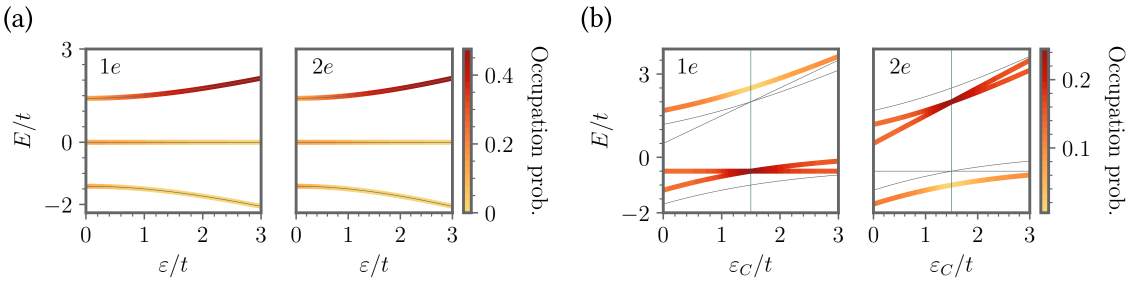

Figure 11.1.: The one- and two-particle energy spectra ($1e$ and $2e$) for the linear (a) and triangular (b) configurations are shown. Thin solid lines represent the two-particle and one-particle energies, respectively, while the color map illustrates the occupation probabilities. The vertical line in (b) indicates the degeneracy point $\varepsilon_C = 1.5t$. These plots are taken from [221] and were produced by C. Hermansen.

so E_- can be tuned into degeneracy with E_0 for $\varepsilon_C = (t^2 - s^2)/s$, see Fig. 11.1(b). At this energy, also two excitation energies are degenerate. The two-particle eigenenergies are different but show the same degeneracy point as the one-particle eigenenergies. The excitation energies are identical for both sectors.

Similar to lasers [225], a population inversion within the fermionic system is of great importance for it to be able to act as a gain medium for the resonator, such that energy transfer occurs. This has also been discussed in Sect. 9. Intuitively, a transition from a high-lying energy to a lower one frees up energy, which can be transferred to the resonator. At this point, it is important to note that the fermion-boson coupling, which we will introduce later, is fermion-conserving and transitions between the particle sectors do not have to be considered. We also show the occupation probability of the corresponding many-body eigenstates in Fig. 11.1 to check for population inversion for the setups under consideration. These quantities are calculated using the Lindblad master equation, described in Sect. 6.2. To clarify, we note that the eigenstates are calculated for $\lambda = 0$ and $\Gamma = 0$, whereas the occupation of these eigenstates is calculated using the steady-state density of the infinitely biased system with $\Gamma \neq 0$. For the linear setup in Fig. 11.1(a), a population inversion arises for a wide range of detuning ε and in both one- and two-particle sectors. On the other hand, there is a population inversion only for the two-particle sector for the triangular configuration, which is strongly peaked at the degeneracy point as a function of the detuning ε_C, as seen in Fig. 11.1(b). This could lead to the conclusion that only the linear configuration provides a population inversion usable for energy transfer. As we will see in the following analysis, this is not true.

Next, we aim to gain insights about the dynamics of the fermionic system and examine the transmission function $T(\omega) = \left|G^{\mathrm{R}}_{13}(\omega)\right|^2$ in Equ. (3.73), the particle current I^N Equ. (3.64) and the spectral function $A_{ii}(\omega)$ Equ. (3.56) together with the spectral weight $n_i^A(\omega)$ Equ. (3.59) of the triple-dot system. In addition to the spectral properties of the distinct quantum dots, we also show the total spectral function $A(\omega) = \sum_i A_{ii}(\omega)$ and the total spectral weight $n^A(\omega) = \sum_i n_i^A(\omega)$. These quantities are calculated for the fermionic system decoupled from the resonator ($\lambda = 0$) but coupled to the leads ($\Gamma \neq 0$). We focus first on the linear setup, displayed in Fig. 11.2. The transmission function $T(\omega)$ in the upper plot of Fig. 11.2(a) shows three well-separated peaks at the single-particle eigenenergies, where the central peak is significantly larger than the two satellites. The transmission is closely related to the particle current, cf. Equ. (3.63), and is shown in the lower plot of Fig. 11.2(a) to be peaked as a function of the detuning ε around zero-detuning. The spectral function in Fig. 11.2(b) exhibits three distinct peaks which are population inverted on all sites. In the context of the one-particle spectral function, this implies that the peaks at higher frequencies carry more spectral weight (i.e., have a larger filled area) than those at lower frequencies. For the linear configuration, this corresponds to a population inversion across all three quantum dots, which we refer to as a global population inversion. Integrating over the spectral weight, see Equ. (3.58), shows that the quantum dot system is half-filled $\sum_i n_i = 1.5$

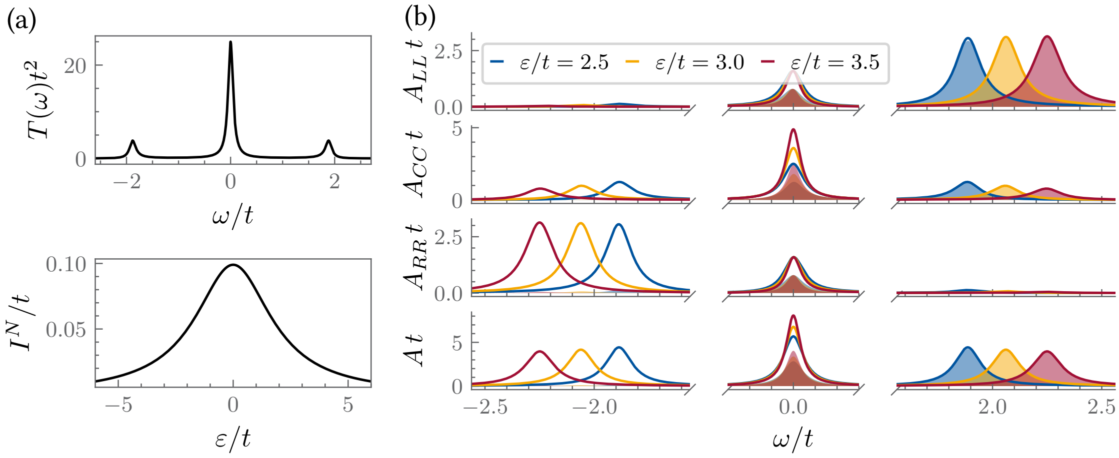

Figure 11.2.: Properties of the non-interacting ($\lambda = 0$) fermionic system in the linear setup. (a) Transmisson function $T(\omega) = |G^R_{13}(\omega)|^2$ as a function of the frequency for $\varepsilon/t = 1.25$ and particle current I^N as a function of ε. (b) Spectral function $A_{ii}(\omega)$ (lines) and weight $n^A_{ii}(\omega)$ (filled area) as a function of the frequency ω for different ε. The lowest panel shows the total spectral function $A(\omega) = \sum_i A_{ii}(\omega)$ (lines) and the total spectral weight $n^A(\omega) = \sum_i n^A_i(\omega)$ (filled area). These figures are adapted from [221].

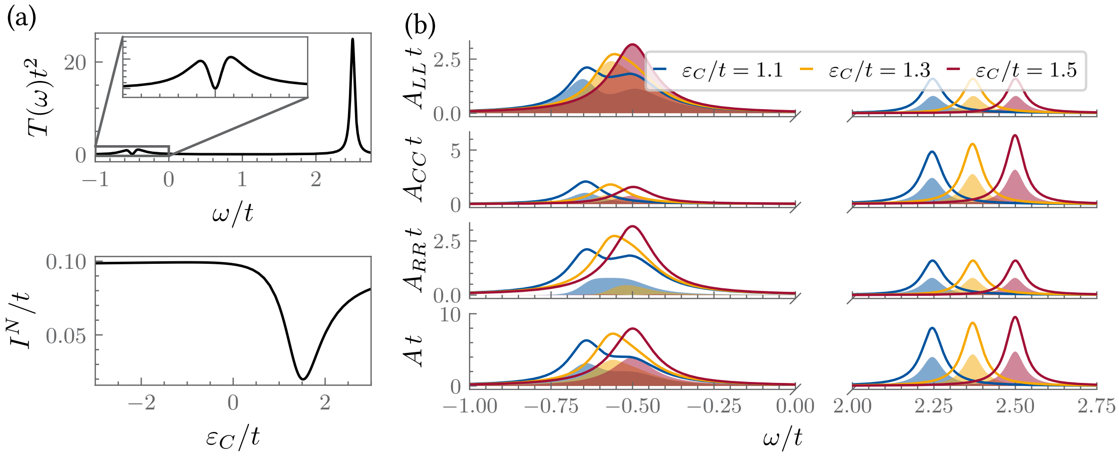

Figure 11.3.: As in Fig. 11.2 for the triangular configuration. The current is plotted as a function of ε_C. The transmission is shown for $\varepsilon_C/t = 1.5$ and the spectral function for different ε_C. These figures are adapted from [221].

We compare this behavior now to the triangular setup, where Fig. 11.3 shows the same quantities for varying detuning ε_C. First, we notice the distinct zero point in the transmission function in the upper plot of Fig. 11.3(a) at the frequency $\omega = \varepsilon_C - t^2/s = -0.5t$ where two eigenenergies become degenerate. This dip occurs due to the interference of the two degenerate eigenstates shown in Fig. 11.1(b) and causes the decrease in the particle current [45] seen in the lower plot in Fig. 11.3(a). The same interference

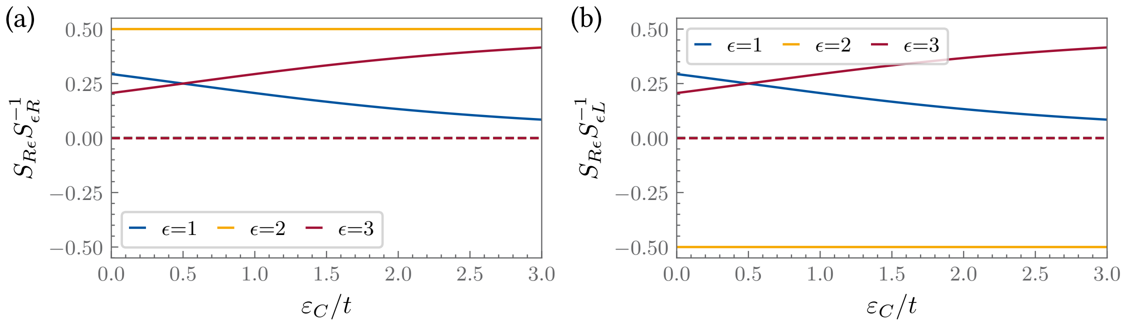

Figure 11.4.: Product of elements of the transformation matrix S, which diagonalizes the dissipative effective Hamiltonian H^0_{eff} containing the lead contributions for finite, but small $\Gamma/t = 0.01$ without coupling to the resonator $\lambda = 0$. The eigenenergies given by the indices $\epsilon = 2$ and $\epsilon = 3$ are the degenerate ones at $\varepsilon_C/t = 1.5$. (a) products contained in the retarded Green function, (b) products contained in the lesser Green function.

effect at the degeneracy point is also found in the spectral weight in Fig. 11.3(b), which leads to a population inversion on the right quantum dot so that the high-frequency state has more spectral weight than the lower lying one. This population inversion is, contrary to the linear setup, only local on the right quantum dot. Compared to the spectral function and weight on the left dot, where the lower frequencies have more weight compared to the higher ones, and the central dot, where all peaks are half-filled. In contrast to the many-body picture in Fig 11.1, it becomes clear, that the population inversion can only be used for resonator gain when coupling to the right quantum dot. The coupling to the left dot instead, would lead to a pumping of energy, which is a process neglected in our setup, due to the resonator being nearly depleted for small temperatures. We have found that coupling to both dots, the energy transfer into and from the resonator is balanced out, and therefore no net energy is pumped.

We see, therefore, how the two methods based on the Green function formalism and the master equation are complementary. Even though Green functions do not provide straightforward access to the one- and two-particle spectrum shown in Fig. 11.1, it allows the straightforward calculation of local spectral properties of the system. It is also possible to calculate the spectral function and weight within the master equation formalism with the QRT as shown in Sect. 6.2.3. However, the calculations are numerically far more involved.

To understand the local population inversion arising in Fig. 11.3(b) of the triangular setup, we study analytically the spectral function and the weight. Using the Green function approach and focusing on the small-Γ regime, we show how the interference of two eigenenergies influences the spectral properties.

First, we analyze how the two peaks of the spectral function interfere in the R-component. To achieve this, the retarded Green function is rotated into the eigenspace of the effective non-Hermitian Hamiltonian $H^0_{\text{eff}} = -\left[G^{\text{R}}(0)\right]^{-1}$ as introduced in Sect. 3.5.4, containing the lead self-energy ($\Gamma \neq 0$) but no contribution from the coupling to the reservoirs ($\lambda = 0$). The rotation is conducted using the non-unitary transformation matrix S. The spectral function can be written as the sum over the eigenspace $\epsilon = \{1, 2, 3\}$ of H^0_{eff}

$$A_{RR}(\omega) \sim \operatorname{Im} G^{\text{R}}_{RR}(\omega) = \sum_{\epsilon=1}^{3} \operatorname{Im}\left(S_{R\epsilon}\frac{1}{\omega - E^0_{\text{eff},\epsilon}}\left(S^{-1}\right)_{\epsilon R}\right), \tag{11.3}$$

with complex eigenenergies $E^0_{\text{eff},\epsilon}$. The contributions are weighted by the product of two matrix elements of the transformation matrix S, which are plotted in Fig. 11.4(a). The imaginary parts are negible compared to the real ones and the products are always positive, so that the addends always add up and the peaks merge constructively.

This is different for the lesser Green function, which gives the occupational weights. It can be simplified assuming the infinite-bias limit, where the lesser self-energy becomes frequency-independent:

$$G^{<}_{RR}(\omega) = \left(G^{\mathrm{R}}\Sigma^{<}G^{\mathrm{A}}\right)_{RR} = \left(G^{\mathrm{R}}\begin{pmatrix} \mathrm{i}\Gamma & 0 & 0 \\ 0 & 0 & 0 \\ 0 & 0 & 0 \end{pmatrix}G^{\mathrm{A}}\right)_{RR} = \mathrm{i}\,\Gamma|G^{\mathrm{R}}_{RL}(\omega)|^2. \tag{11.4}$$

So, the lesser Green function is proportional to the transmission $T_{RL}(\omega) = T_{LR}(\omega)$ plotted in Fig. 11.3(a). Therefore, the node in the transmission function also leads to the population inversion. While the fermionic transport from L to R is suppressed, the fermions can still leave the right quantum dot into the right lead and the population decreases. This process is energy-dependent. The transmission can be written as

$$\left|G^{\mathrm{R}}_{RL}(\omega)\right|^2 = \left|\sum_{\epsilon=1}^{3} S_{R\epsilon}\frac{1}{\omega - E^{0}_{\mathrm{eff},\epsilon}}\left(S^{-1}\right)_{\epsilon L}\right|^2 . \tag{11.5}$$

Again the real part of the product $S_{R\epsilon}\left(S^{-1}\right)_{\epsilon L}$, shown in Fig. 11.4(b), are much larger than the imaginary parts. The real parts of the two degenerate eigenergies, $\epsilon = 2$ and $\epsilon = 3$, have different signs. So, the two contributions cancel each other and the destructive interference can lead to a zero in the transmission and concurrently in the population inversion.

11.2. Boson-assisted tunneling

Now, the quantum dot system is coupled to the resonator and we want to study the energy transfer between the two systems and how this influences the fermionic transport properties. Additionally, we will comment on the behavior of the bosonic system, which can be found in more detail in [221] and was studied C. Hermansen. In the previous discussion, it was shown that for both parameter configurations a population inversion emerges on the right quantum dot. Therefore, the resonator is coupled to this site via the coupling $\lambda > 0$. We will utilize first-order perturbation theory based on the Keldysh Green function formalism as introduced in Sect. 4, and the Lindblad master equation from Sect. 6.2. Simultaneously to the study of the physical phenomena, we will comment on the advantages and disadvantages of both methods.

11.2.1. Particle current

First, we take a closer look at the change in particle current I^N as a function when the coupling $\lambda > 0$ is turned on compared to the current for $\lambda = 0$, which is shown Figs. 11.2(b) and 11.3(b). The interacting case is shown in Fig. 11.5 calculated within the first-order perturbation theory Equ. (4.2) (solid lines) and the master equation Equ. (6.20) (dots). The corresponding equations for the current are given by Equ. (3.64) for the Green functions and Equ. (6.39) for the density operator. The two methods generally agree well for the parameters chosen here and show the same qualitative behavior. However, in the inset of Fig. 11.5, it is shown that perturbation theory slightly underestimates the effect of the coupling to the resonator on the fermionic system compared to the Lindblad master equation. As a reminder, the master equation contains all orders in the interaction, whereas the perturbation theory only contains

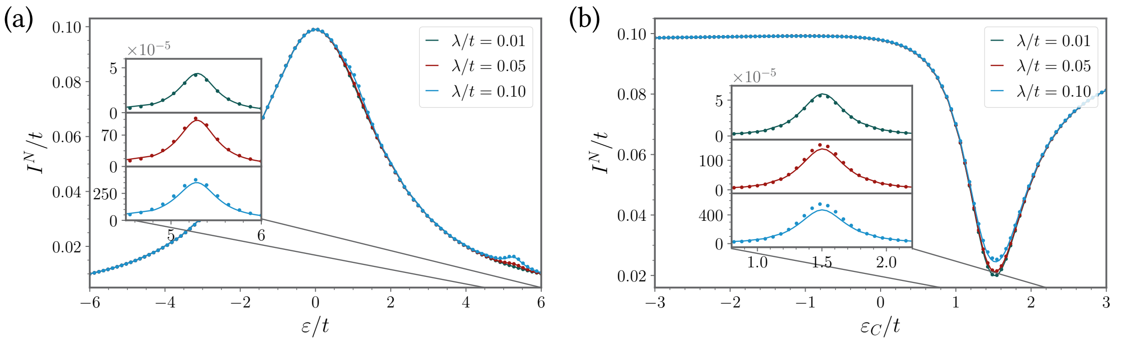

Figure 11.5.: Particle current I^N as a function of the detuning ε or ε_C for the linear (a) and triangular (b) configuration respectively and for different couplings λ. The solid lines result from first-order perturbation theory and the dots from the Lindblad master equation. The insets show the difference in current between the system coupled to the bosonic resonator ($\lambda \neq 0$) and the non-interacting ($\lambda = 0$) system. These figures are adapted from [221].

orders up to λ^2. Thus, the effect also becomes stronger at larger couplings. Furthermore, similar to the discussion in Sect. 9, we found that the agreement between the two methods strongly depends on the dissipation rate κ, which is accounted for in the master equation calculations. In particular, there is no straightforward limit where the agreement is consistently good. Instead, we observe that the level of agreement varies for different values of κ, with some leading to better alignment than others.

In the linear configuration shown in Fig. 11.5(a), we find a peak structure where the particle current as a function of the detuning ε is increased compared to the noninteracting current. This has also been observed in [155] in a study of the double quantum dot. Note that the narrow width of the peak in [155] originates from a smaller κ considered in this case. Those increases are due to photon-assisted inelastic tunnelings when the bosonic system is in resonance with the excitation energies of the quantum dot system $\mathit{\Delta} E = \omega_0$. The position of the increased current therefore depends on the resonator frequency. This means, that in resonance, the resonator frequency is as large as the distance of two spectral peaks in Fig. 11.2(b). When the resonant transition is between population inverted peaks, it occurs under the emission of energy in the form of a boson. As stated before, we observe only an additional peak in the current, when population inversion occurs, and the inelastic process deposits energy into the resonator. The process in which energy is absorbed and which would occur at negative detuning is not possible due to the zero-temperature limit assumed, which corresponds to an effectively empty resonator. This behavior was discussed in Sect. 9.3 when coupling to a cavity.

For the triangular configuration, we have seen that at the degeneracy point, the current in Fig. 11.3(a) experiences a dip and simultaneously, the spectral function in Fig. 11.3(b) shows a local population inversion at this detuning. When tuning the resonator in resonance with the quantum dot system with degenerated excitation energies $\mathit{\Delta} E = (2s^2 + t^2)/s = \omega_0 = 3t$ an increase of the current can be seen at this minimum, see Fig. 11.5(b). Thus, the local population inversion in the triangular configuration can also be utilized for the inelastic tunneling processes.

We know that the self-energies in first-order perturbation theory are exact in the second order in the coupling λ. Therefore, the range of validity for the perturbative regime can be studied by conducting a scaling analysis and seeing where the scaling deviates from the expected behavior. This is shown in Fig. 11.6 comparing the perturbative scaling with the scaling of the Lindblad results. Keep in mind that the Lindblad master equation includes all orders in the interaction. For small couplings, the scaling of the current enhancement is observed to be in the second order of the coupling up to $\lambda \approx \mathit{\Gamma}$. We

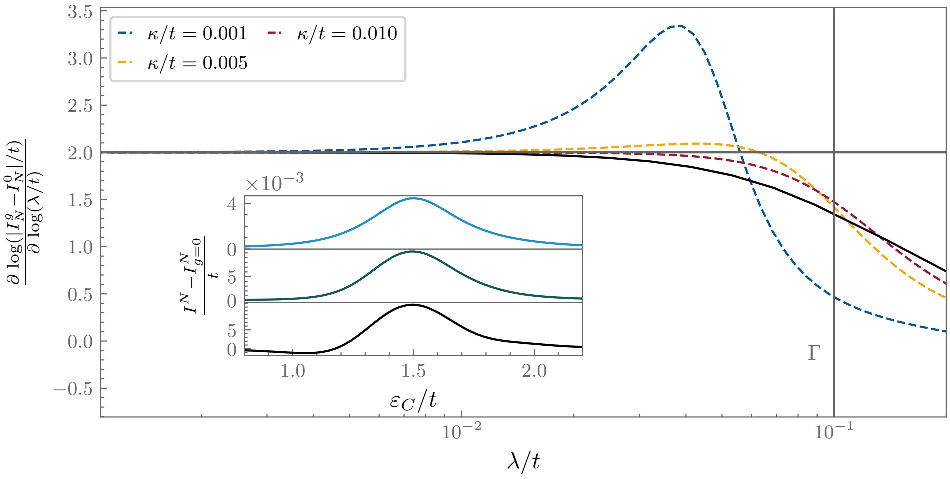

Figure 11.6.: Scaling analysis of the particle current for the triangular setup at the degeneracy point $\varepsilon_C = 1.5t$. The logarithmic derivative of the difference in current with coupling to the resonator ($\lambda \neq 0$) and no coupling ($\lambda = 0$) with respect to λ. The solid black line shows the perturbation theory results and the dashed lines are the ones obtained by the master equation for different values of κ. The tunneling rate Γ is marked by the vertical grey line and the horizontal line indicates the λ^2 scaling. In the inset, we show the difference in particle current between the coupled and uncoupled case, similar to the inset in Fig. 11.5, obtained with the Lindblad master equation close to the degeneracy point $\varepsilon_C = 1.5t$ for $\kappa/t = 0.01, 0.001, 0.0005$ from top to bottom. This figure is adapted from [221].

note, that the deviation from the perturbative result from the $\sim g^2$ behavior is due to the way in which we calculate the current. The Green functions appearing in the current Equ. (3.63) are dressed with the self-energies obtained by first-order perturbation theory using the Dyson equation Equ. (3.36). This leads to higher orders in λ being generated. The results from the master equation approach show very good agreement with the perturbative scaling for small coupling. However, especially at larger coupling, this strongly depends again on the dissipative rate κ. As also discussed in Sect. 9.2, the two methods inherently differ. The first-order perturbation theory does not consider a change in particle number in the resonator and the balancing effect Equ. (9.2), captured within the master equation, is not included. There is no straightforward κ limit in which the perturbative and Lindblad results agree, due to the master equation not being able to represent the effective always empty cavity with an infinitely narrow spectrum, which is assumed in perturbation theory.

11.2.2. Energy dissipation

As stated above, the current increase occurs due to boson-assisted tunneling processes. They arise when the emission of energy from the quantum dot system in the form of a boson leads to a tunneling process. It was already shown that a double quantum dot, when brought in resonance with the resonator can lead to an energy transfer, similar to a lasing effect [102, 140]. In particular, the biased double dot was shown to function as a gain medium, exhibiting resonant energy transfer into the resonator [20, 140, 155, 156, 226]. An experimental study with two double quantum dots in a microwave cavity has demonstrated gains reaching approximately 10^3, accompanied by a pronounced narrowing of the cavity mode linewidth [20]. To track the energy transfer of the fermions into the resonator, we calculate the energy dissipation ΔI^E of the fermionic system Equ. (3.68) in the Green function formalism or the energy transfer into the resonator $I^E_{\mathrm{f}\rightarrow\mathrm{b}}$ Equ. (6.41) with the Lindblad master equation. The dissipation is

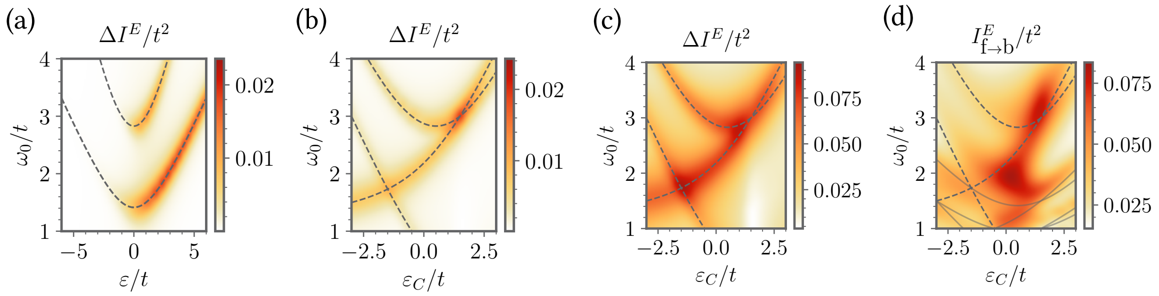

Figure 11.7.: Energy dissipation of the quantum dot system calculated in first-order perturbation theory ((a),(b),(c)) as a function of the resonator frequency ω_0 and the detuning ε or ε_C. For small coupling $\lambda = 0.1t$ ((a),(b)) and large coupling $\lambda = 0.6t$ ((c)). (d) shows the energy current into the resonator calculated with the Lindblad master equation for $\lambda = 0.6t$. The dashed lines indicate the one-particle excitation energies. These figures are adapted from [221].

shown in Fig. 11.7 as a function of the resonator frequency and the detuning for both configurations and two different couplings. For the small couplings $\lambda = 0.1t$, the shown results in Figs. 11.7(a) and 11.7(b), obtained with first-order perturbation theory, agree well with the results of the master equation found in appendix G. Even though the balancing effect described in Sect. 6.2.4, where the energy flow into the resonator is balanced out by the dissipation into the environment, is not included in the first-order perturbation theory. In both configurations, the regions where energy is pumped into the resonator follow the one-particle excitation energies, indicated by grey dashed lines. The maximal pumping is obtained, where the population inversion (cf. Figs. 11.1, 11.2(b) and 11.3(b)) are largest. For the linear setup in Fig. 11.7(a), this includes an extended region as a function of the detuning ε, whereas for the triangular configuration in Fig. 11.7(b), a sharply peaked maximum is observed at the degeneracy point $\varepsilon_c/t = 1.5$. The width of the pumping region is in general governed by the tunnel broadening Γ.

Increasing the coupling to $\lambda = 0.6t$, the perturbative results in Fig. 11.7(c) strongly deviate from the Lindblad results in Fig. 11.7(d). This shows the breakdown of first-order perturbation theory for large couplings. The energy-current calculated within the master equation approach exhibits sidebands from two- or more-boson processes. The new arising regions of higher energy-dissipation are close to the excitation energies of two- and three-boson processes indicated by the light-grey lines in Fig. 11.7(d). We assume these processes together with a slight shift due to a renormalization of the resonator frequency to be the origin of the changed behavior. Both effects are of higher order in the coupling, containing feedback effects, and are not included in first-order perturbation theory.

11.2.3. Decreasing the population inversion

The transition from higher-lying states to lower-lying ones causing the energy pumping into the resonator can also be seen in the spectral weight, which is shown in Fig. 11.8. The spectral function together with the spectral weight for the right quantum dot can be seen in Fig. 11.8(a) for the linear and in Fig. 11.8(b) for the triangular configuration. We calculate the spectral quantities from Green functions first with the help of perturbation theory (blue) and further compare it with the results of the Lindblad master equation (yellow) using the QRT introduced in Sect. 6.2.3. Compared to the decoupled case ($\lambda = 0$), indicated by the black dashed lines, both results show a general decrease in the spectral weight of the higher-lying states and an increase in the weight of the lower ones. Thus, the initial population inversion is decreased by the deexcitation process leading to the boson-assisted tunneling and the related energy transfer. Even though both methods show the same qualitative behavior, perturbation theory again underestimates the effects of the coupling, which is consistent

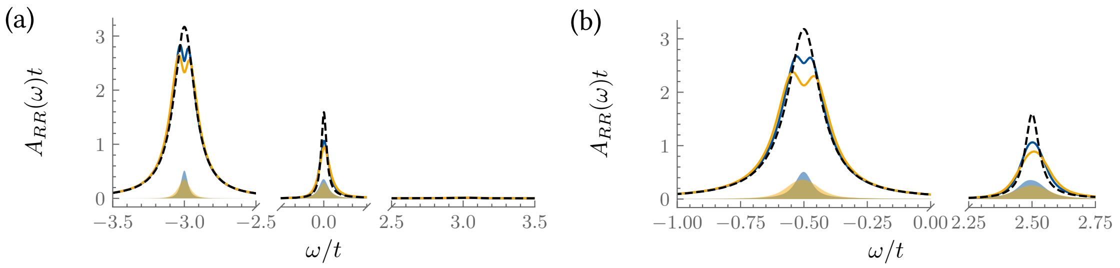

Figure 11.8.: Spectral function (lines) and spectral weight (filled areas) of the right quantum dot. The black dashed lines show the non-interacting case $\lambda = 0$ and the solid lines show the results for $\lambda = 0.1t$ and at resonance with the resonator. The Green functions calculated with first-order perturbation theory are shown in blue and with the Lindblad master equation in yellow. (a) for the linear configuration at $\varepsilon = 2\sqrt{\omega_0^2 - 2t^2} = 2\sqrt{7}t$, (b) for the triangular setup at $\varepsilon_C = 1.5t$. These figures are adapted from [221].

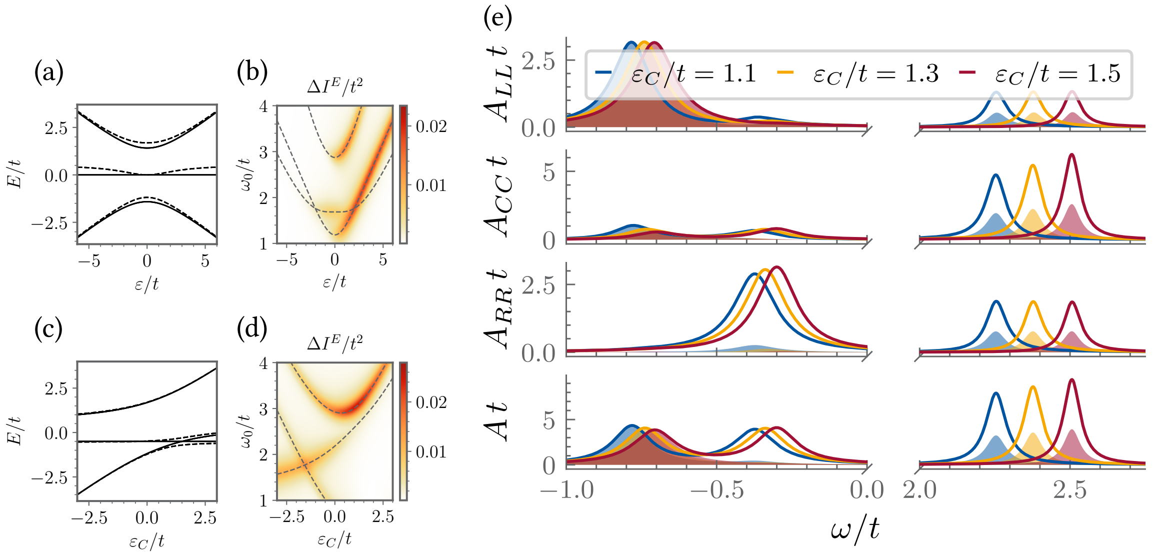

Figure 11.9.: Eigenenergies of the isolated quantum dot system ($\lambda = 0$, $\Gamma = 0$) as a function of the detuning ε or ε_C for the linear (a) and triangular configuration (c). The solid lines show the fine-tuned case of $\varepsilon_C = 0$ for the linear setting and $\varepsilon = 0$ for the triangular one. The dashed lines indicate the results for the slightly off-tuned scenario $\varepsilon_C = 0.5t$ and $\varepsilon = 0.5t$ respectively. (b) and (d) show the energy dissipation for the detuned setups and for finite $\lambda = 0.1t$ and $\Gamma = 0.1t$ for the linear and triangular setup respectively. The grey dashed lines indicate the one-particle excitation energies for the isolated quantum dot system ($\lambda = 0$, $\Gamma = 0$). (e) shows the spectral function (lines) and weight (filled area) for the triangular setup for detuned $\varepsilon = 0.5t$ and different ε_C.

with what was observed in Fig. 11.5.

11.2.4. Lifting the degeneracy

Up to this point, the system has been fine-tuned such that the excitation energy degeneracy is precisely achieved. This fine-tuning can be lifted by e.g. detuning ε_C or ε away from the Fermi level for the linear or triangular configuration respectively. This is shown in Fig. 11.9. The one-particle eigenenergies are plotted for the decoupled ($\lambda = 0$, $\Gamma = 0$), and slightly detuned case in Figs. 11.9(a) and 11.9(c). We see that for both configurations, the degeneracy of the excitation energies is broken when moving away from the fine-tuned system. For the linear configuration, this means, that the eigenenergies are no longer in a cascade-like order and two transitions can no longer be excited simultaneously.

Looking, however, at the energy dissipation, plotted in Figs. 11.9(b) and 11.9(d), this does not greatly influence the energy transfer out of the fermionic system. For the linear setup, the area of large energy transfer only follows one excitation energy and is not reduced in magnitude. This is consistent with the occupations found in Fig. 11.1(a), which suggests that only one transition is population inverted and can therefore be excited. In the triangular setup, the degeneracy at $\varepsilon_C = 1.5t$ is lifted, so that the excitation energies do no longer coincide. For the energy transfer, this leads to a wider region of high energy transfer, only following one of the excitation energies. The overall magnitude of the energy transfer also seems to be increased slightly compared to the fine-tuned case. This can be better understood when looking at the spectral function in Fig. 11.9(e). The population inversion is no longer local, and therefore more similar to the mechanism in the linear setup than to the one in the triangular fine-tuned configuration. The inversion further only occurs between the highest lying frequencies and the middle one and therefore only this transition can be excited, leading to the energy dissipation in Fig. 11.9(d).

11.2.5. Resonator gain

At this point, we briefly want to comment on the bosonic perspective. The resonator, coupled to the fermionic system, can be analyzed using either the Lindblad master equation, Equ. (6.20), or via first-order perturbation theory within the Keldysh Green function formalism. First-order perturbation theory for the bosonic degrees of freedom involves integrating out the fermionic degrees of freedom and evaluating the so-called bubble diagram shown in Fig. 11.10 to obtain the bosonic self-energy $\Pi(\omega)$. The full discussion, along with all associated plots, is available in [221] and was provided by C. Hermansen. For completeness, we summarize the main results here.

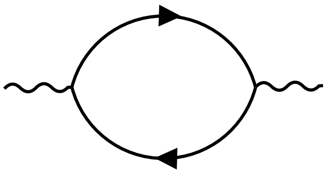

Figure 11.10.: Bubble diagram. The wiggly lines represent the bosonic propagators, the solid lines are the fermionic ones, and the crossings are the effective interaction vertices with strength λ. The propagators are only dressed by the bath and lead self-energies respectively.

The energy transfer from the fermionic system to the bosonic system, as discussed earlier, occurs in the form of bosonic excitations, which increase the mean occupation of the resonator N_b. In the bosonic calculations performed, a finite dissipation κ was assumed, see Table 11.1. In steady-state, the system reaches a balance between the net energy transferred from the fermionic system into the resonator and the losses into the bosonic bath. This balance determines the steady-state population of the resonator. The imaginary part of the perturbative calculated self-energy provides an estimate of the dissipative effect of the quantum dot system, given by

$$\mathrm{Im}\left[D^\mathrm{R}(\omega)\right]^{-1} = \frac{2\omega}{\omega_0}\kappa - \mathrm{Im}\Pi^\mathrm{R}(\omega) = \frac{2\omega}{\omega_0}\tilde{\kappa}(\omega). \quad (11.6)$$

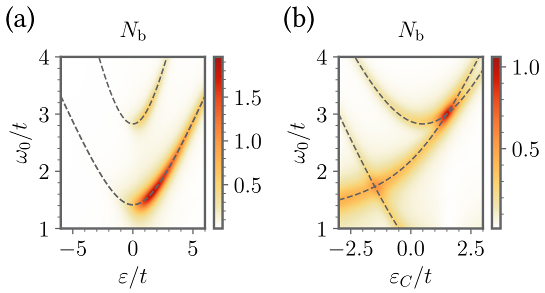

Figure 11.11.: The mean resonator occupation N_b as a function of the detuning ε or ε_C and the resonator frequency ω_0 for (a) the linear and (b) the triangular setup. The grey dashed lines indicate the one-particle excitation energies for the isolated quantum dot system ($\lambda = 0$, $\Gamma = 0$). The results are obtained with the Lindblad master equation and based on the plots provided by C. Hermansen in [221], but reproduced by myself.

This defines an effective dissipation rate $\tilde{\kappa}$, which controls the occupation of the resonator. The imaginary part of the self-energy therefore leads to either an effectively increased ($\tilde{\kappa} > \kappa$ for $\mathrm{Im}\Pi^\mathrm{R}(\omega) < 0$) or decreased ($\tilde{\kappa} < \kappa$ for $\mathrm{Im}\Pi^\mathrm{R}(\omega) > 0$) damping. A reduction in the dissipation rate results in a narrowing and filling of the resonator mode. It was demonstrated in [221] that areas of increased energy transfer from the fermionic system indeed coincide with regions of the positive imaginary part of the bosonic self-energy.

Additionally, the bosonic occupation N_b can be investigated using both methods. In Figs. 11.11(a) and 11.11(b), the occupation is shown as a function of detuning ε or ε_C and the resonator frequency ω_0 for both configurations. These plots are obtained by calculating the steady-state density matrix ρ_s using the Lindblad master equation, with $N_\mathrm{b} = \mathrm{Tr}[\rho_s a^\dagger a]$. It is clearly evident that regions of high occupation coincide with the areas of high energy dissipation shown in Figs. 11.7(a) and 11.7(b).

The calculation of bosonic self-energies within the Keldysh Green function formalism in first-order perturbation theory revealed limitations in the perturbative treatment when the coupling is chosen too large. Specifically, it was found that the imaginary part of the retarded Green function can become negative, which implies that the retarded Green function effectively becomes advanced [87, 221]. However, a comparison with the results obtained from the quantum regression theorem within the Lindblad formalism showed no such issues, suggesting that this spurious behavior stems from the perturbative approach. It was further observed that the results of the Green functions in first-order perturbation theory deviate significantly from the Lindblad results already for $\lambda = 0.05t$. This contrasts with the treatment of the fermionic degrees of freedom, where both methods remain in good agreement even for coupling strengths as large as $\lambda = 0.1t$.

The Green function formalism provides a framework for analytically studying the breakdown of perturbation theory, and it can further be employed for a stability analysis similar to [227]. To this end, we analyze the conditions under which the effective dissipation $\tilde{\kappa}$ changes sign. The full calculation is available in [221] and was provided by C. Hermansen. Here, we outline the main concept and results.

The spectral function is approximated by a sum of Lorentzians centered around the single-particle eigenenergies E_α with effective broadening γ_α. Similarly, the retarded Green function is approximated as

$$G^\mathrm{R}_{RR}(\omega) = \sum_\alpha \frac{Z_\alpha}{\omega - E_\alpha + \mathrm{i}\gamma_\alpha}. \tag{11.7}$$

Here, Z_α is the wave-function renormalization factor. The representation provides a good approximation when the spectral peaks are well separated, which is always the case for the linear configuration. For the triangular setup, however, this holds only true when the system is tuned into degeneracy with two peaks or far away from it with three peaks. This leads to the following approximate form of the self-energy:

$$\Pi^{\mathrm{R}}(\omega) = -2g^2 \sum_{E_\alpha > E'_\alpha} \frac{Z_\alpha Z_{\alpha'} \left(n_{R,\alpha} - n_{R,\alpha'}\right)}{\omega - |E_\alpha - E_{\alpha'}| + \mathrm{i}\left(\gamma_\alpha + \gamma_{\alpha'}\right)}, \tag{11.8}$$

where the non-equilibrium occupation of the right quantum dot $n_R(\omega)$ was approximated by a scaling factor $n_{R,\alpha}$ for the α-th spectral peak. The photon self-energy is determined by the local population inversion of the right dot $(n_{R,\alpha} - n_{R,\alpha'})$, which reflects the fermionic system's ability to act as a gain medium for the resonator, thereby influencing the efficiency of energy transfer. Additionally, a critical occupation value can be determined where one of the poles of the retarded Green function crosses the real axis.

In the triangular setup, at the degeneracy point where two spectral peaks (at $E_1 = E_2$ and E_3) are observed and the lower-lying ones are nearly depleted ($n_{R,1} = n_{R,2} \approx 0$), the critical occupation is given by

$$n^c_{R,3} \approx \frac{\kappa(\gamma_1 + \gamma_3)}{2g^2 Z_1 Z_3} \left[1 + \left(\frac{E_3 - E_1 - \omega_0}{\kappa + \gamma_1 + \gamma_3}\right)\right]. \tag{11.9}$$

Here, it was further assumed that $Z_1 = Z_2$ and $\gamma_1 = \gamma_2$. Thus, the critical point depends on the difference between the excitation energy and the resonator frequency $E_3 - E_1 - \omega_0 = \Delta E - \omega_0$, as well as the combined broadening $\gamma_1 + \gamma_3$. This was further analyzed in [221] for the specific parameter set shown in Table 11.1.

11.2.6. Including nearest and next-nearest neighbor Coulomb interaction

In small-scale systems, Coulomb interactions are significant and cannot be neglected [228]. Thus, we include both nearest and next-nearest neighbor Coulomb interactions in the spin-polarized quantum dots. The corresponding part of the Hamiltonian takes the form

$$H_U = U d_L^\dagger d_L d_C^\dagger d_C + U d_R^\dagger d_R d_C^\dagger d_C + \tilde{U} d_L^\dagger d_L d_R^\dagger d_R, \tag{11.10}$$

which includes an additional next-nearest neighbor term $\sim \tilde{U}$ compared to H_U in Equ. (2.6), accounting for the advanced spatial structure, similar to the hopping. We choose the interaction to preserve the mirror symmetry of the quantum-dot system. Breaking this symmetry lifts the degeneracy in the two-particle sector of the excitation energies. This situation is analogous to that discussed in Sect. 11.2.5, where the degeneracy is lifted due to the system not being finely tuned, thereby weakening the energy transfer if the degeneracy is lifted by more than Γ. Otherwise, the effect is minimal. In this form, the Coulomb interaction only renormalizes the two- and three-particle sectors but breaks particle-hole symmetry. In this study, we do not include the shift of the PHS point in the renormalization of the energy space as in Sect. 2.1.1 and 10.1.

Including Coulomb interaction such that it influences the coupling to the resonator in a non-trivial way would require higher-order feedback effects. This means that for the resonator to experience the effects of Coulomb interaction on the coupling, we would need to include terms of $\mathcal{O}\left(Ug^2\right)$. Such terms are not included in the first-order perturbation theory, so we use the Lindblad master equation, where including this interaction poses no additional challenges.

When $\tilde{U} = U$, the two- and three-particle eigenenergies are simply shifted by U and $3U$, respectively, and the excitation energies remain unchanged. However, for $\tilde{U} \neq U$, the one- and two-particle energies

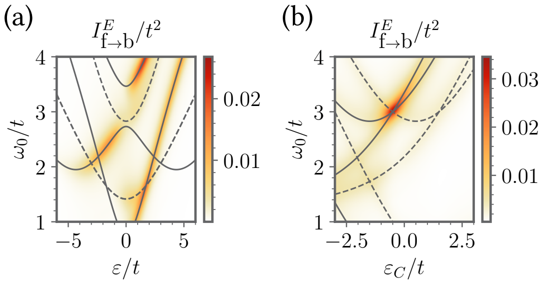

Figure 11.12.: The energy flow from the fermionic system into the bosonic one $I^E_{\mathrm{f}\to\mathrm{b}}$ as a function of the detuning ε or ε_C and the resonator frequency ω_0 for (a) the linear and (b) the triangular setup. Further, a nearest-neighbor Coulomb interaction $U = 20t$ and $\tilde{U} = 0.9U$ is assumed. The grey dashed lines indicate the single-particle excitation energies of the isolated Hamiltonian ($\lambda = 0$, $\Gamma = 0$). The two-particle excitation energies are indicated by solid grey lines. These figures are adapted from [221].

no longer coincide, and the degeneracy point in the triangular setup is found at different ε_C. In the two-particle sector, the degeneracy point is shifted to $\varepsilon_C = \left(t^2 - s(s + U - \tilde{U})\right)/s$, while in the one-particle sector, it remains at $\varepsilon_C = \left(t^2 - s^2\right)/s$. Thus, the shift scales with the difference $U - \tilde{U}$. Assuming $\tilde{U} < U$, the largest difference between the two sectors occurs for $\tilde{U} = 0$.

In Fig. 11.12, the energy current into the bosonic system Equ. (6.41) is shown for $\tilde{U} = 0.9U$. To achieve the Coulomb blockade regime, where the electron number sectors are energetically well-separated, which is a critical feature in realistic physical systems [229, 230], U is chosen to be much larger than all other energy scales, except for the voltage. In both configurations, we observe the described separation of the one- and two-particle excitation energies. For the linear setup in Fig. 11.12(a), the Coulomb interaction breaks the degeneracy of the two-particle excitation energies. The region of high energy transfer clearly follows only one of the excitations. This is consistent with the population probability shown in Fig. 11.1(a), where only one transition exhibits population inversion. In the triangular configuration in Fig. 11.12(b), the peak of maximal energy transfer shifts with the degeneracy point of the two-particle sector. This aligns with the population inversion seen in Fig. 11.1(b), which is only found in the two-particle sector. In general, we conclude that the symmetrically applied Coulomb interaction does not change the overall magnitude of energy transfer, but instead shifts the maxima in resonator frequency and detuning space.

11.3. Intradot Coulomb interaction and PERLind

For the energy scales typical for quantum dot systems and available magnetic fields, the spinpolarization of the system is not trivial to achieve, cf. [221]. Therefore, we briefly address the inclusion of spin degrees of freedom and examine whether the observed effects persist in a spinful system. In this case, each quantum dot can be occupied by two fermions with opposite spins, making the on-site Coulomb interaction a significant effect.

This investigation was carried out by C. Hermansen, with the full details available in [221]. The results were obtained using the position- and energy-resolved Lindblad master equation (PERLind) [168], which extends the approach introduced in 6.2 by allowing for the evaluation of frequency-dependent jump rates.

It was demonstrated that, for an infinite bias voltage, the isolated fermionic system ($\lambda = 0$, $\Gamma = 0$) with finite on-site Coulomb interaction does not exhibit the necessary population inversion. However, reducing the bias voltage leads to a recovery of population inversion in both the one- and two-particle sectors, similar to what is observed in spin-polarized systems. Thus, it is reasonable to expect similar behavior in this more realistic spinful system.

Nonetheless, it is important to highlight that, even though PERLind can be applied to finite bias systems, the Markovian approximation must still hold. In this method, the jump operators are expressed in the eigenbasis of the Hamiltonian. This formulation allows the tracking of filling and emptying of states by introducing a Fermi function into the jump operators, thereby incorporating memory effects. The validity of the method was tested against the exact non-interacting Green function for the case without Coulomb interaction. It was found that PERLind reasonably reproduces static or integrated variables, such as the current [168] and mean occupation [221]. However, for dynamic, frequency-dependent variables, PERLind shows significant deviations from the Green function results. In these cases, non-Markovian effects are more pronounced, and PERLind fails to capture the exact behavior.

Conclusion

In this section, we discussed a triple quantum dot system coupled to a resonator, which can be used as a quantum dot simulator for molecules. Beyond the nearest-neighbor hopping, we also included next-nearest-neighbor hopping in a triangular configuration. This more complex spatial structure better approximates a realistic artificial molecule. We compared this setup to the linear configuration with only nearest-neighbor hopping. While population inversion was observed in both setups, the linear configuration exhibited a global population inversion, whereas the triangular configuration showed a local population inversion on the right quantum dot. When the resonator was coupled to the right quantum dot, we observed energy transfer from the quantum dot system to the resonator driven by this population inversion. This process was accompanied by boson-assisted tunneling, which enhanced the fermionic current, and resonator gain, increasing the mean occupation of the resonator. Finally, we found that the energy transfer effects are robust against Coulomb interaction. These results provide a set of benchmarks that can be used in experimental setups to validate the system before exploring more complex parameter regimes where theoretical studies become more challenging or infeasible.

In this study, we employed first-order perturbation theory and compared the results to those obtained using the Lindblad master equation. The two methods yielded comparable results in the limit of small coupling λ and infinite bias $V \to \infty$. The Lindblad master equation approach captures all orders in the coupling λ and easily provides access to quantities such as the many-body energy spectrum, as well as the inclusion of Coulomb interactions in all orders. On the other hand, it is restricted by the Markov approximation for the fermionic leads, which the Green function approach is not. The perturbative treatment, thus, does not require the infinite bias limit and, further, provides easy access to dynamical variables, such as the spectral function. Moreover, it allows for valuable analytical insights. However, it does not take into account higher-order effects and breaks down when increasing the fermion-boson coupling. Both methods complement each other, providing a comprehensive framework for studying the full system by combining the advantages of each approach.

12. Coupling the Interacting Resonant Level Model to a Phonon Mode

This chapter is based on the following publication, where the main results were already published: [231] M. Caltapanides et al., "Finite-bias transport through the interacting resonant level model coupled to a phonon mode: a functional renormalization group study", Phys. Rev. B **104**, 085125 (2021)
For this project, I performed all calculations and contributed to the interpretation of the results.

In the work presented here we perform minor adjustments to the notation for consistency within the present thesis.

The interacting resonant level model (IRLM) is a well-established impurity model that is characterized by a nearest-neighbor Coulomb interaction. The electrons are assumed to be spin-polarized. As a well-controllable setup, it provides a good platform to study non-equilibrium transport properties of locally-correlated electronic systems [13, 28–32, 229]. A more thorough introduction to the model was given in Sect. 1.1. In this chapter, we want to further include the vibrational degrees of freedom, introduced in Sect. 1.3, into the IRLM. We focus on the transport properties of the fermionic system. This includes a discussion of the particle current through the quantum dot system. Specifically, we analyze how the current is affected by the two types of interactions and study the interplay of the electron-electron and the electron-boson interaction. Additionally, we investigate the differential transport coefficients, highlighting the role of the effective low-energy scale that emerges due to these interactions. Finally, we briefly address the violation of particle current conservation that occurs as a result of the approximate truncated FRG method used in this chapter.

A schematic of the system under consideration is shown in Fig. 12.1. The model consists of a central quantum dot with on-site energy ε_2, referred to as the central level in this chapter. This level is coupled to two non-interacting leads, positioned on the left (L) and right (R), with chemical potentials $\mu_{L/R}$ and

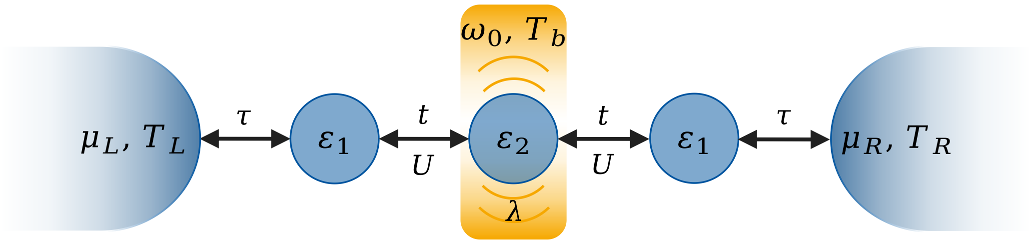

Figure 12.1.: Sketch of the combined model (CM) of the IRLM and SAHM. The system consists of three quantum dots with energies ε_j coupled via the hopping t. Fermions occupying the three dots experience a nearest-neighbor Coulomb interaction U. The central region is connected to two leads on the left and right side with chemical potentials $\mu_{L/R}$ and temperature $T_{L/R}$. By administering the scaling limit $\tau \gg t$ and $\varepsilon_1 = \varepsilon_3 = 0$, the first and third dot become part of the left and right lead respectively. The central dot is further coupled to a phonon mode with frequency ω_0 with the coupling strength λ.

temperatures $T_{L/R}$. The hopping from the central site to the leads, denoted by t, is assumed to be much smaller than the lead bandwidth, which is characterized by Γ. Additionally, dot-fermions experience a nearest-neighbor Coulomb interaction U with fermions in the leads. To maintain interaction-free leads computationally, the boundary levels of the leads that are assumed to mediate the Coulomb interaction are explicitly treated. These auxiliary quantum dots have energies $\varepsilon_1 = \varepsilon_3 = 0$ and are reintegrated into the leads by choosing the hopping onto the non-interacting part of the leads (τ) and, therefore, $\Gamma = \pi\rho_{\text{res}}(0)\tau^2$ to be much larger than t. This is known as the scaling limit. Thus, the model is identical to the one described in Sect. 2.1 for $M = 3$, with $t_{i,j} = t(\delta_{i,j+1} + \delta_{i,j-1})$, and finite U.

This setup results in an effective broadening for the central site. In the non-interacting case ($U = 0$) and within the wide-band limit ($\Gamma \gg t$), the broadening is given by $\tilde{\Gamma} = 2t^2/\Gamma$. When Coulomb interaction is introduced, the broadening becomes renormalized. Analogous to the Kondo model [23], this renormalization leads to an emergent low-energy scale, denoted as T_{K}. We will demonstrate that some observables become universal functions when rescaled by T_{K}. Perturbation theory predicts a renormalization of the low-energy scale of the form $-U\ln(\tilde{\Gamma}/\Gamma)$, which diverges in the scaling limit ($\tilde{\Gamma} \ll \Gamma$) [13, 34], where the central dot is well defined. This logarithmic divergence signifies the breakdown of perturbation theory, as noted in Sect. 5 [124]. It is known [13, 33] that this term is part of a logarithmic series, $U^n \log(\tilde{\Gamma}/\Gamma)^n$, and the resummation of these terms leads to a power-law dependence for the increased effective broadening ($T_{\mathrm{K}} > \tilde{\Gamma}$ for $U > 0$):

$$\frac{T_{\mathrm{K}}^{\mathrm{IRLM}}}{\tilde{\Gamma}} = \left(\frac{\tilde{\Gamma}}{\Gamma}\right)^{-\alpha_\Gamma(U)}, \tag{12.1}$$

where the exponent α_Γ is of order $\mathcal{O}(U)$. The Coulomb interaction generally increases the effective broadening. One method to obtain the correct scaling behavior through resummation is FRG, as introduced in Sect. 5.

In this chapter, we also include a vibrational degree of freedom in the IRLM by incorporating the coupling from Equ. (2.21), with $A_{i,j} = \lambda\delta_{i=j=2}$ at the central site. The total model, thus, combines the IRLM and the so-called spinless Anderson-Holstein model (SAHM) [87, 90, 96, 98–101]. The SAHM framework models the emission or absorption of a single-mode phonon, depending on the occupation of the central quantum dot. A more detailed description is provided in Sect. 1. The phonon introduces an additional energy scale, the mode frequency ω_0. One distinguishes two regimes: (i) the adiabatic and (ii) the anti-adiabatic ones. In the adiabatic regime, where the phonon frequency is much smaller than the lead broadening ($\omega_0 \ll \Gamma$), the interaction between the quantum dot and the phonon mode has only a slight impact on system behavior. The phonons are too slow to respond at the tunneling timescale. In this case, the interaction can be treated perturbatively [232], as the coupling induces only minor modifications to electronic properties. Conversely, in the anti-adiabatic regime, where the phonon frequency is much larger than the coupling strength ($\omega_0 \gg \Gamma$), the coupling induces significant many-body effects [97, 99, 219, 233]. The effects emerge due to the effective fermion-fermion interaction induced by the phonons, which is attractive and non-local in time. This stands in contrast to the Coulomb interaction, which is typically repulsive and time-local. The retardation of phonon interactions leads to frequency-dependent self-energies, even within first-order truncation schemes. This dependency prevents the SAHM from being described by a renormalized single-particle picture. In contrast, for the IRLM, the sum of the frequency-independent self-energy components corresponds to an effective non-interacting problem [234].

The coupling to the bosonic degree of freedom also renormalizes the effective hybridization T_{K}, but in this case, it reduces the low-energy scale ($T_{\mathrm{K}} < \tilde{\Gamma}$ for $\lambda > 0$) [34, 97]. In the anti-adiabatic limit, perturbation theory again incorrectly predicts a logarithmic scaling of T_K with λ^2. Resummation of these logarithms within the FRG method recovers the correct power-law dependence [97]:

$$\frac{T_\mathrm{K}^\mathrm{SAHM}}{\tilde{\Gamma}} = e^{-\left(\frac{\lambda}{\omega_0}\right)^2} \left(\frac{\tilde{\Gamma}}{\omega_0}\right)^{-\frac{4\tilde{\Gamma}}{\pi\omega_0}\left(\frac{\lambda}{\omega_0}\right)^2} \tag{12.2}$$

for $\tilde{\Gamma} \ll \omega_0$ and $\lambda \lesssim \omega_0$. The first term reflects the aforementioned reduction of the tunneling rate.

Therefore, we employ FRG on the Keldysh, which was discussed in Sect. 5.2, to investigate the transport properties of the combined model (CM) of the IRLM and SAHM. This chapter is based on the work published in [231], parts of which were already discussed in my master's thesis [118]. The latter parts will not be included in the present thesis or will be labeled accordingly.

12.1. The low energy scale

As stated above, in the effective single dot impurity model, the level-lead tunneling introduces the low energy scale T_K. It will be introduced in more detail now. In the non-interacting system ($U = 0$, $\lambda = 0$) and in the scaling limit $\Gamma \gg t$, the tunneling is given by $\tilde{\Gamma} = 2t^2/\Gamma$ [34, 92] with $\tilde{\Gamma}/\Gamma \ll 1$. The renormalized broadening can be defined as the slope of the central-level occupation n_2 with ε_2 at zero temperature

$$T_\mathrm{K} = \frac{1}{\pi\chi}, \qquad \text{with } \chi = -\frac{\mathrm{d}\,n_2}{\mathrm{d}\,\varepsilon_2}\Big|_{\varepsilon_2=V=T_L=T_R=0}. \tag{12.3}$$

This definition is analogous to the definition chosen in [13] with an additional factor of 1/2. However, because the numerical differentiation did turn out to be unstable in the FRG calculations, we use an alternative but equivalent definition of T_K as the half width at half maximum of the single-particle spectral function Equ. (3.56) of the central level.

It can be shown, cf. Refs. [34, 97], that the low energy scale of the combined model T_K^CM can be written as a product of the ones of the IRLM and the SAHM

$$\frac{T_\mathrm{K}^\mathrm{CM}}{\tilde{\Gamma}} = \frac{T_\mathrm{K}^\mathrm{IRLM}}{\tilde{\Gamma}} \frac{T_\mathrm{K}^\mathrm{SAHM}}{\tilde{\Gamma}} \tag{12.4}$$

up to corrections of order $\mathcal{O}\left(\left[U, \lambda^2\right]^2\right)$. We have seen that the effective interaction due to fermion-phonon coupling is attractive. This leads to a reduction of the effective hybridization compared to the non-interacting case, i.e. $T_\mathrm{K}^\mathrm{SAHM} < \tilde{\Gamma}$ for $\lambda^2 > 0$. On the other hand, the Coulomb interaction is repulsive, resulting in an increase $T_\mathrm{K}^\mathrm{IRLM} > \tilde{\Gamma}$ for $U > 0$. For the combined model, the energy scale can increase or decrease, depending on which of the two competing interactions prevails.

12.2. Thermo-electric transport

The IRLM and SAHM are known to exhibit intriguing features in their transport properties, as discussed in Sect. 1. For the IRLM, these features include a power-law decay of the particle current as a function of voltage bias in the large bias limit $V \gg T_\mathrm{K}^\mathrm{IRLM}$ [13, 28, 32], which leads to negative differential conductance in this regime. In the case of the SAHM, inelastic phonon processes result in shoulder-like features in the $I - V$ curves [99, 233]. Moreover, strong fermion-phonon coupling causes a suppression of the low-bias current, an effect known as the Franck-Condon blockade [90, 96, 101], which narrows

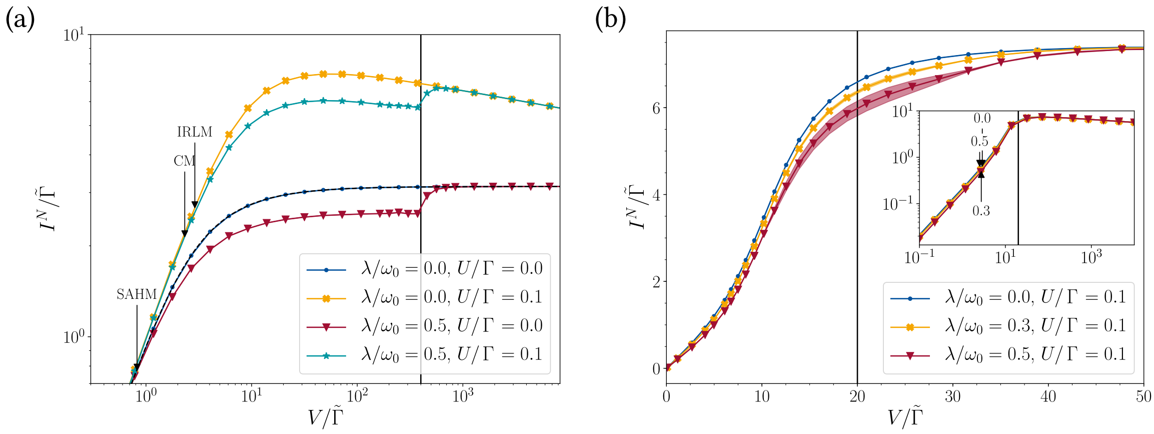

Figure 12.2.: (a) shows the Particle current I^N as a function of the bias-voltage V on a log-log scale for different combinations of interaction strength λ and U. The system is considered deep in the anti-adiabatic regime at $\omega_0/\tilde{\Gamma} = 200$, at the particle-hole symmetric point $\varepsilon_2 = 0$, in the zero-temperature limit $T_L = T_R = 0$ as well as in the scaling limit $\tilde{\Gamma}/\Gamma = 2 \cdot 10^{-8}$. The black dashed line, mostly hidden by the blue line, was calculated analytically for the interaction-free case. (b) shows the current as a function of V away from particle-hole symmetry $\varepsilon_2/\tilde{\Gamma} = 5$, for $\omega_0/\tilde{\Gamma} = 10$ and for fixed U on a linear scale. The filled area indicates the measure for violation of particle conservation ΔI^N. To show the power-law decay in the current, the inset shows a larger voltage range on a log-log scale. In all plots, the arrows indicate the low-energy scales for the SAHM, the IRLM and the CM and the black vertical line bias where $V = 2\omega_0$. The figures are adapted from [231].

the zero-bias conductance peak. Phonon-mediated structures also emerge in differential transport coefficients due to inelastic tunneling processes [99].

In this section, we investigate whether these transport characteristics of both models simply superimpose, similar to the behavior observed for the low-energy scale. We will analyze the fermionic particle current through the combined model (CM), cf. Equ. (3.64), as well as the differential transport coefficients in Equs. (3.70)-(3.72).

12.2.1. Particle current

The following is an extension of the discussion of the particle current through the CM found in [118]. The particle current I^N Equ. (3.64) as a function of the bias voltage is shown in Fig. 12.2. In Fig. 12.2(a), we considered particle-hole symmtry $\varepsilon_2 = 0$ and the antiadiabatic limit $\omega_0/\tilde{\Gamma} = 200$. Different combinations of interaction strength λ and U are compared and as a reference, we show the analytically calculated non-interacting current [127]

$$\frac{I^N}{\tilde{\Gamma}} = \tan^{-1}\left[\frac{\varepsilon_2 + V/2}{\tilde{\Gamma}}\right] - \tan^{-1}\left[\frac{\varepsilon_2 - V/2}{\tilde{\Gamma}}\right]. \tag{12.5}$$

Additionaly, the three low-energy scales $T_{\mathrm{K}}^{\mathrm{SAHM}}$, $T_{\mathrm{K}}^{\mathrm{IRLM}}$ and $T_{\mathrm{K}}^{\mathrm{CM}}$ are indicated by vertical arrows. For the chosen interaction strengths, the repulsive Coulomb interaction is dominant compared to the effectively attractive interaction due to the phonons, leading to an overall increased combined $T_{\mathrm{K}}^{\mathrm{CM}} > \tilde{\Gamma}$. In the case of the SAHM ($\lambda > 0$ and $U = 0$), the current exhibits the characteristic phonon-step at $V = 2\omega_0$, where the phonon satellites in the spectral function enter the transport window [99, 100]. For the IRLM ($\lambda = 0$ and $U > 0$), we find the characteristic power-law suppression of the current at large voltages $T_{\mathrm{K}} \ll V \ll \Gamma$ [13, 30]. In the combined model, both effects are robust against the inclusion

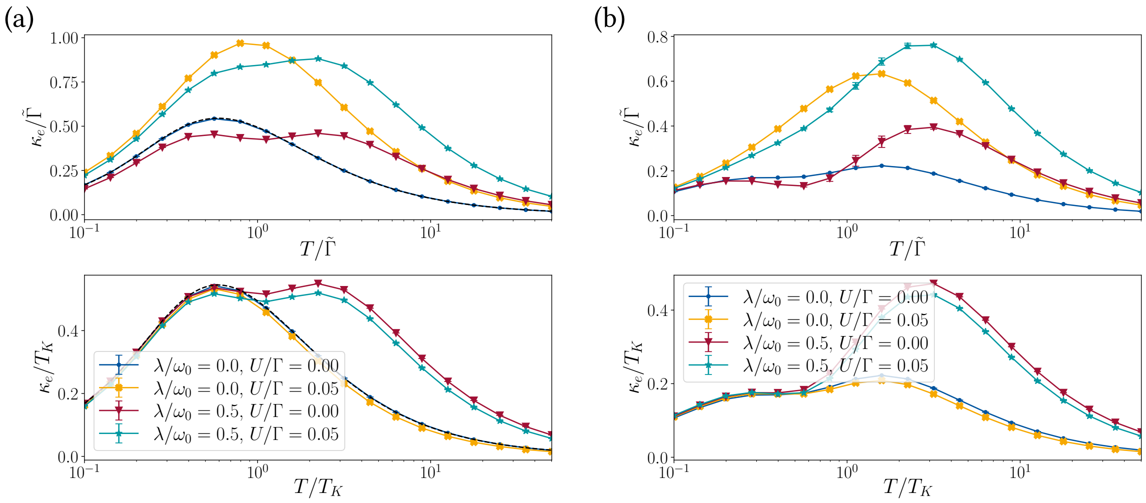

Figure 12.3.: The electron contribution to the thermal conductance κ_e as a function of the temperature $T_L \to T_R = T$ and for different interaction strengths. Upper: all energy scales are in units of the bare hybridization $\tilde{\Gamma}$ with $\varepsilon_2/\tilde{\Gamma} = -1$ and $\omega_0/\tilde{\Gamma} = 5$. Lower: the energies are renormalized by the small energy scale $T_\mathrm{K} = T_\mathrm{K}(\omega_0/\tilde{\Gamma} = 5)$ with $\varepsilon_2/T_\mathrm{K} = -1$, $\omega_0/T_\mathrm{K} = 5$. In (a), we consider the linear transport with $V = 0$ and in (b) the nonlinear one with $V/\tilde{\Gamma} = -1$ or $V/T_\mathrm{K} = -1$ respectively. Further, in (a), the analytically calculated free case is shown as the dotted black line, which is mostly hidden by the blue line.

of the other interaction. For $\omega_0 > T_\mathrm{K}$, the Coulomb interaction-induced suppression already sets in for voltages $V > 2\omega_0$, meaning before the phonon step. The characteristics occur on different energy scales and superimpose in a straightforward way. Only after the step, the current in the CM reaches the value of the IRLM. This is the point where all spectral weight, including the phonon satellites, is included in the transport window and therefore contributes to the current.

To analyze the current, when both effects occur on similar energy scales, we show the current for a smaller bosonic frequency in Fig. 12.2(b). Here, T_K^CM and ω_0 are less well seperated. Further, we move away from the PHS point. For increasing phonon coupling λ, the current is suppressed due to the Franck-Condon blockade. The phonon step is observable but for the given parameter far less pronounced and more shoulder-like than in Fig. 12.2(a). In the inset of Fig. 12.2(b), also the power-law suppression due to the Coulomb interaction is visible. Both effects set in at similar energy scales, however, still no additional feature due to the interplay of both effects is observable. In the following, we will see that also in the transport coefficients, the effects of the two interaction effects superimpose straighforwardly.

12.2.2. Differential transport coefficients

Now, we continue with studying the transport coefficients Equs. (3.70)-(3.72), first focusing on the linear case for $V \to 0$ and $T_L \to T_R = T$. We focus on the electron contribution to the thermal conductance κ_e because, in contrast to the conductance G and the Seebeck coefficient S, it contains information about the particle as well as the heat current with voltage and temperature difference on the leads. Hence, it shows the most interesting behavior, as shown in [219] for the SAHM. The linear κ_e as a function of the temperature is shown in the upper plot of Fig. 12.3(a) for different interaction strengths. The derivatives in Equ. (3.72) are calculated numerically. In the upper plot, we show the results, where all energies are scaled by the bare hybridization $\tilde{\Gamma}$ so that $\varepsilon_2/\tilde{\Gamma} = -1$ and $\omega_0/\tilde{\Gamma} = 5$. For the non-interacting case

($\lambda = 0, U = 0$), κ_e can be expressed by the polygamma function [235]. It is indicated by the black dashed lines for comparison. In this case, there is one maximum originating from resonant tunneling and, thus, it was found to scale with the detuning ε_2. When turning on the coupling to the bosonic degrees of freedom ($\lambda > 0$), a second peak emerges, which scales with ω_0 and thus stems from phononic resonances. The inclusion of the Coulomb interaction only renormalizes the peak positions and heights.

In the lower plot of Fig. 12.3(a), we rescale all energies with $T_\mathrm{K} = T_\mathrm{K}^\mathrm{CM}$ instead of $\tilde{\Gamma}$, so that $\varepsilon_2/T_\mathrm{K} = -1$ and $\omega_0/T_\mathrm{K} = 5$. Further, κ_e and T are rescaled by T_K. All curves for a fixed coupling λ, but different Coulomb strength U collapse onto the $U = 0$-curve. This means T_K acts as a universal energy scale and the effect of the Coulomb interaction on κ_e can be fully incorporated into the renormalization of T_K [14]. We see again that the effects of the two interactions are given by the phonon features of the SAHM ($U = 0$) superimposed by the renormalization of the central level-lead coupling, including all effects of finite U. At this point, it is interesting to note that the low energy scale with finite $\lambda > 0$ depends on the phonon frequency $T_\mathrm{K} = T_\mathrm{K}(\omega_0)$. Therefore, an iterative process, renormalizing ω_0 with T_K and recalculating the later scale, would be required to obtain a complete collapse of the curves for different U. This is likely the reason why the collapsed curves are not exactly overlapping. Because the corrections to the low-energy scale are however of higher order in the interaction, we neglect and use $T_\mathrm{K} = T_\mathrm{K}(\omega_0/\tilde{\Gamma} = 5)$ for the rescaling.

Finally, Fig. 12.3(b) shows the nonlinear κ_e, analogous to Fig. 12.3(a) for the normally scaled and rescaled energies, but for finite bias $V/\tilde{\Gamma} = 2$ or $V/T_\mathrm{K} = 2$. There, it becomes clear that the aforementioned collapse also occurs beyond the regime of linear response. The finite voltage mainly modifies the first peak resulting from resonant tunneling and only barely affects the second maximum due to the inelastic phonon scattering.

In general, the same behavior can be found for the other transport coefficients given in Equs. (3.70) and (3.71) in the linear regime as well as in the non-linear one. The results can be found in appendix H.

12.3. Comment on the conservation of the particle current

As stated before in Sects. 4.4 and 5, the approximate treatment of the interactions in first-order perturbation theory, as well as of the FRG can lead to the breaking of certain symmetries. This includes the violation of particle conservation, even for Hamiltonians that are particle conserving, such as the one introduced in Sect. 2. In my master's thesis [118], we already discussed the implications of the violation of particle conservation in FRG for the CM. In the present thesis, we want to comment on this matter for completeness briefly and further wish to include some minor additions based on [231].

As already discussed in [118], the CM suffers from this violation of particle conservation, already in the first-order truncation scheme of FRG. ΔI^N in Equ. (3.65) can be used as a measure for this violation. In the given approximation, not all terms of order U^2, λ^4, and $U\lambda^2$ are taken into account and, therefore, the violation has to be at least of this order. Therefore, the violation also vanishes for vanishing interaction strength. The self-energies in first-order in the IRLM ($\lambda = 0, U \neq 0$) are frequency independent and the system can be described by an effective single-particle picture with renormalized energies. The description is therefore particle conserving. On the contrary, the frequency dependence of the effective interaction due to the phonon-coupling in the SAHM ($\lambda \neq 0, U = 0$) leads to frequency-dependent self-energies and the single-particle picture no longer holds. These elastic processes are responsible for the violation. We found, that for certain parameter regimes, such as at particle-hole symmetry $\varepsilon_2 = 0$ as seen in Fig. 12.2(a), the violation vanishes. Even outside these regimes, there are parameter ranges where the current violation can be neglected, allowing for the

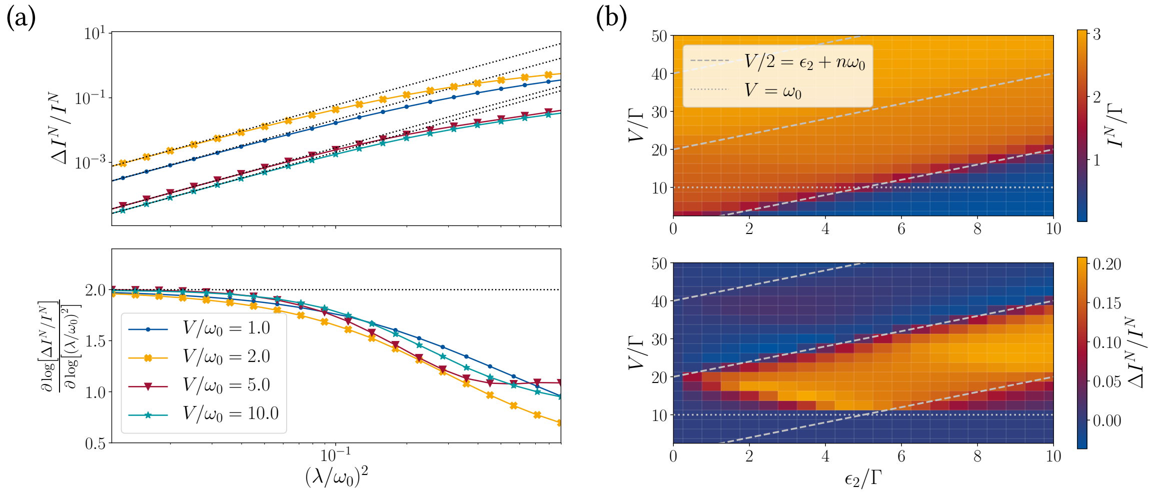

Figure 12.4.: (a) The relative violation of the current conservation as a function of the coupling λ^2/ω_0^2 for the SAHM ($U = 0$) in the anti-adiabatic regime $\omega_0/\tilde{\Gamma} = 10$ and away from particle-hole symmetry $\varepsilon_2/\tilde{\Gamma} = 5$. The temperature $T_L = T_R = \tilde{\Gamma}$ and the system is in non-equilibrium with different bias-voltages V. The expected power laws $\sim (\lambda/\omega_0)^4$ are displayed at black dotted lines. Upper plot: $\Delta I^N/I^N$ on a log-log scale. Lower plot: logarithmic derivative on a log-linear scale. (b) The particle current I^N in the upper and the vioaltion of particle conservation ΔI^N in the lower plot. Both as a function of the on-site energy ε_2 and the voltage V for $\omega_0/\tilde{\Gamma}$, in the anti-adiabatic limit, and in the zero-temperature limit $T_L = T_R = T_b = 0$. We neglect the Coulomb interaction $U = 0$ and only consider $\lambda/\omega_0 = 0.5$. The grey dashed lines indicate the position of the phononic shoulders in the particle current and the grey dotted line the bosonic frequency. The figures are adapted from [231].

observation of interesting non-equilibrium many-body physics, as illustrated in Fig. 12.2(b), indicated by the filled areas. This does not necessarily hold when increasing the coupling λ or going deeper into the anti-adiabatic limit [231]. A more thorough discussion can be found in [118] or [231].

As a reminder, we show ΔI^N for the SAHM ($U = 0$) in the anti-adiabatic regime $\omega_0/\tilde{\Gamma}$ as a function of the coupling strength λ^2/ω_0^2 in upper plot of Fig. 12.4(a), which can also be found in a similar form in [118]. As stated above, we expect a violation of order $\mathcal{O}(\lambda^4/\omega_0^4)$. Indeed, on the presented log-log scale, the power-law behavior of ΔI^N can be seen well, as all curves follow a straight line with a similar slope. This is especially clear for small couplings λ. For comparison, the dotted black lines indicate the expected power-laws with exponent 2.

This behavior becomes even more evident when plotting the logarithmic derivative, which becomes equal to the constant exponent in the case of power-law behavior. This is plotted in the lower plot in Fig. 12.4(a). As expected, the exponent approaches 2 for decreasing λ^2. This scaling analysis is similar to the one conducted in Sects. 9.4 and 10.3. The analysis of ΔI^N can be used to check the consistency of the approximate method in two ways. First, the reliability of the results can be checked by controlling the expected power-law behavior and eliminating regimes where unphysical behavior, such as a large violation of the particle conservation for a conserving Hamiltonian, can be found. Secondly, the logarithmic derivative is very sensitive to numerical errors and can thus be used to benchmark the accuracy of the numerical evaluation, which is non-trivial even for FRG in the first-order truncation. It might become even more important in numerically more involved higher-order truncation schemes [150].

In Fig. 12.4(b), the particle current and the relative violation of particle conservation are shown as a function of the central detuning ε_2 and the bias voltage V. This allows for a better understanding of how these quantities depend on the given parameter regime in the CM. As already shown in Fig. 12.2 and more thoroughly discussed in [118], the particle current saturates for $V > \varepsilon_2$. Further, the current exhibits shoulder-like plateaus for $V/2 \in [\varepsilon_2 + n\omega_0, \varepsilon_2 + (n+1)\omega_0]$, $n \in \mathbb{N}$, due to inelastic processes with the phonons, such as absorption or emission and are, thus, the areas of physically interesting behavior. This can be seen in the upper plot. From $\Delta I^N / I^N$ in the lower plot, it becomes however apparent that these are unfortunately the areas with the largest violation in particle conservation. However, within the given parameter regime, the violation remains small enough to trust the calculations and reliably observe the physical behavior. In general, $\Delta I^N > 0$ only occurs for $V > \omega_0$, where phonon-processes are energetically possible. The violation increases with increasing ε_2, where we also observe the previously mentioned current conservation at particle-hole symmetry $\varepsilon_2 = 0$. We note, that this is a case-to-case study and has to be applied independently to different models when treated with FRG.

Conclusion

In this chapter, we studied a combination of the IRLM and the SAHM using FRG in first-order truncation on the Keldysh contour. The model thus combines the effects of Coulomb repulsion between fermions and of a fermion-phonon coupling. We found effects of both interactions in the particle current. This includes a power-law decay at large bias voltages due to the Coulomb interaction and shoulder-like features at $V = 2\omega_0$ induced by the coupling to the phonon mode. When both interactions are present simultaneously and for weak interactions, the features simply superimpose without generating new ones. A similar behavior is seen in the differential transport coefficients, where the interactions do not seem to influnce each other. Moreover, the effects of the Coulomb interaction can be fully captured by renormalizing the low-energy scale, $\tilde{\Gamma} \to T_{\mathrm{K}}$, when expressing all parameters in terms of T_{K}. Thus, in the first-order truncation scheme within FRG, the two interactions behave almost independently, and the well-known interaction effects, such as the aforementioned features in the particle current, are straightforwardly superimposed.

We also commented on the violation of particle current conservation arising from employing the approximate truncated FRG method. Due to the frequency-dependent effective interaction induced by the fermion-phonon coupling, this phenomenon occurs already in first-order truncation. We showed that the violation scales as expected, being second-order in the interaction, i.e., proportional to λ^4. This provides an internal consistency check for the reliability and the numerical implementation of the FRG in first-order truncation. Finally, we demonstrated that even though particle current conservation violation occurs in the parameter regime where interesting nonequilibrium many-body physics can be observed, there exist parameter regimes where the effect is negligible, and the key features remain observable. In particular, the violation vanishes completely at particle-hole symmetry.

Part V.

Conclusion

Finally, we conclude our findings, while simultaneously motivating future studies.

13. Summary and Outlook

In the present thesis, we discussed a low-dimensional impurity system coupled to two non-interacting leads in equilibrium and non-equilibrium setups. We coupled this fermionic system to a single-mode bosonic resonator in two distinct ways: via Peierls coupling, modeling the coupling to a light cavity, and via capacitive coupling, modeling the coupling to phonons or, in circuit quantum electrodynamics, the coupling to an *LC* oscillator. We primarily focused on how the mean occupation of the quantum dot and the fermionic transport through the impurity region change due to interaction with the resonator. To this end, the main method used was perturbation theory in the lowest order of the interaction strength, based on the Matsubara and Keldysh Green function formalism. We compared the results with results from the Lindblad master equation and exact diagonalization in various parameter regimes and setups. Further, we also applied the functional renormalization group method, which is known to treat the effective energy scales arising due to Coulomb interaction and phonon-electron coupling correctly.

13.1. Coupling matter to quantum light in cavity quantum electrodynamics

First, we studied light-matter coupling for a linear chain of quantum dots. We focused on extending the existing theoretical framework for light-matter coupling, with particular emphasis on impurity systems.

Peierls substitution for impurity systems in Coulomb gauge

To begin with, we considered the coupling of light and matter. We analyzed the Peierls substitution approach in the Coulomb gauge and extended it for impurity systems, where the vector potential violates the dipole approximation in parts of the system's space. This approximation is central in the known derivation of the Peierls phase for infinite systems. The violation of the dipole approximation led to additional boundary terms, which could be addressed by adapting the Peierls phase at the boundaries of the impurity. The analysis was conducted using the one-orbital approximation in the electronic system.

For future studies, this approach should be applied to multi-orbital systems, where the light-matter coupling leads to additional interdot interaction terms. Similarly, we only discussed the coupling to one cavity mode, and future research should consider multiple resonance frequencies. As shown in [86], the light-matter coupling is very sensitive to the truncation of the Hilbert space. This especially holds in the Coulomb gauge, where the light-matter coupling enters in a highly non-linear way through the Peierls phase, entangling the light and matter degrees of freedom. Thus, it is important to include the larger Hilbert space in the calculations and study how this affects the boundary terms in the impurity system.

Expansion of the exponential in the Peierls substitution

We also discussed the truncation of the expansion of the exponential function of the Peierls substitution in orders of the vector potential. We found, in agreement with the literature, that at least the second-order term must be considered to obtain physical behavior consistent with theoretical studies in which the full exponential function is kept. The applied perturbation theory in first-order in the effective fermion-fermion interaction arising from the fermion-boson coupling is in second-order in the coupling strength to the resonator and, therefore, of the same order as the second-order neglected in the exponential expansion term. We introduced a scheme to include the second-order expansion via a non-self-consistent mean-field approach, which renormalizes the fermionic interdot hopping, resonator frequency, and coupling between the two systems. This approach showed good agreement with exact diagonalization results in which the full Peierls phase was kept when analyzing dot occupation in closed systems. We also showed that considering only the linear term of the Peierls substitution leads to vastly different behavior when considering the linear conductance. Thus we showed the general necessity to include this term.

Using the developed method, we studied two fermionic transport phenomena: (i) the interference effects in the linear conductance arising due to the effective long-range interaction induced by the cavity and (ii) the energy transfer between the fermionic and bosonic system and how the boson-assisted tunneling leads to peak-like structures of increased fermionic current. This phenomenon is driven by global population inversion.

In open systems in the infinite-bias limit, we found that Lindblad and perturbation theory results were well comparable in the small coupling regime. However, in first-order perturbation theory higher-order processes, which are taken into account by the Lindblad master equation, are neglected. This includes, among others the change in the resonator mode due to the coupling to the quantum dot system being fed back to the fermionic system. Thus, the resonator is seen as always effectively empty in the zero temperature limit, which corresponds to a cavity with large dissipation. On the other hand, we considered an infinitely narrow cavity mode, which corresponds to zero dissipation. Therefore, we there is no straightforward limit for the dissipation where the two methods agree.

It would be interesting to apply the developed mean-field method to study also different transport phenomena or different configurations of the impurity. This could include more complex quantum dot systems, e.g. including more intricate spatial structures via long-range hopping terms, similar to what was done in the present thesis for the capacitive coupling. Relative spatial distance of the quantum dots would also influence the Peierls phase, leading to different coupling strengths g_{ij} for different hopping terms. Another pathway could be to include not only a voltage bias to induce a non-equilibrium situation but also consider a temperature gradient between the two leads. By, e.g. studying the differential transport coefficients, this would provide further insight into the influence the cavity has on the fermionic transport properties. It could lead to interesting effects, such as the enhancement of the thermo-electric efficiency as found in [99, 219] for a electron-phonon coupling.

For future studies, it is also essential to investigate how to include Coulomb interaction when considering light-matter coupling. This should be done in the different gauges, and it is important to investigate whether a multi-orbital approach is necessary for accurate results. A similar discussion was already started by [85] for an infinite lattice, but it should also be adapted to the impurity system. It would be interesting if the results found in this thesis, as the transport properties, are robust against Coulomb interaction and in what way these two effects influence each other.

Light-matter coupling in the Dipole gauge for the impurity model

Additionally, we discussed the gauge invariance of the Peierls substitution and applied the Power-Zienau-Woolley transformation to change from Coulomb gauge to dipole gauge, where the one-orbital approximation is known to provide more accurate results. We derived an expression for the light-matter coupling in the impurity system with the vector potential being non-vanishing only on a finite sublattice. The dipole gauge in continuum formulation and tight-binding approximation for one orbital per lattice site were employed. The light-matter coupling in the Dipole gauge for the impurity model not only leads to the polarization shift of the bosonic degrees of freedom but also introduces boundary terms containing exponential functions that include the vector potential.

It would be interesting to apply the expressions derived for the coupling in an exemplary toy model and compare it to the results obtained in the Coulomb gauge as a proof of concept that these two approaches provide the same physical behavior and indeed the gauge invariance holds in the approximations under considerations. This could for example be conducted with the perturbative approach, considered in the majority of the present thesis. However, with this method, the exponential in the boundary terms in the dipole gauge and the exponential in the Peierls phase in the Coulomb gauge cannot be included exactly. Thus, one either has to consider how to include both exponentials in a consistent manner or employ different methods, such as the Lindblad master equation.

13.2. Coupling matter to vibrations and circuit quantum electrodynamics

Also for the capacitive coupling, we studied the effect of the presence of the resonator on the fermionic transport properties. In particular, we also showed how interference dips occur in the linear conductance due to the effective long-range interaction. Even though these interference effects were found for both couplings, they appeared in different energy regimes.

Boson-assisted transport in artificial molecules

We discussed how the energy transfer between a fermionic system in non-equilibrium and a resonator, leads to boson-assisted tunneling processes. For the capacitive coupling, we focused on a triple quantum dot setup, where next-nearest neighbor hopping in the fermionic system could lead to interference effects seen as dips in the particle current, even without interactions present. We analyzed two setups where global and local population inversion of the dot system resulted in energy transfer into the resonator, which simultaneously caused peaks in the particle current. This setup extends the idea of using quantum dots as analog simulators of molecules, which have a more complex internal structure compared to linear chains of quantum dots. Examples of this include hydrocarbon molecules. Our analysis provided a set of checkpoints an experimental triple quantum dot system must fulfill. Afterward, it may be used to simulate molecules in other energy regimes that are challenging to treat analytically.

In the future, it would be interesting to observe the experimental realization of these artificial molecules. This should be of value for example to study the relevance of phonon-coupling in chemistry as well as in biology. For example, it is suggested that the high efficiency in energy transport in photosynthetic processes can be explained by the phononic excitations of organic molecules [236, 237]. The underlying process is based on the Föster resonance energy transfer, mentioned in Sect. 1.2, where the coupling of vibrational degrees of freedom can lead to the delocalization and, therefore, stabilizes the energy transfer over larger distances. Artificial molecules could provide a feasible platform to study this effect. Also, the aforementioned Jahn-Teller effect [35] in hydrocarbon molecules could be studied in an analog simulator.

Thermo-electric transport in the interacting resonant level model with electron-phonon coupling

Finally, we discussed the interplay of nearest-neighbor Coulomb interaction and the capacitive coupling to a phonon mode using a first-order truncation scheme in the functional renormalization group method. For the phonon mode coupling in the anti-adiabatic regime, we demonstrated that the features in the particle current and differential transport coefficients are a superposition of effects due to the isolated interactions. In the differential transport coefficients (κ_e, G, S), the Coulomb interaction is fully described by the renormalization of the effective general energy scale of the renormalized lead-dot tunneling T_{K}. This behavior was found both in the finite-bias and zero-voltage cases. The low-energy scale is influenced by both interactions.

For future research, it would be valuable to explore whether these effects also superimpose in a straightforward way when considering higher-order truncation schemes in the functional renormalization group, where higher-order terms in the interaction, including mixing terms of the order $\mathcal{O}\left[\lambda^2 U\right]$, are fully accounted for.

Appendix

A. Effective interaction vertex

When the bosonic fields only occur quadratic in the highest order, they can be integrated out of the Gaussian integral of the action in Equ. (3.76) to obtain an effective fermion-fermion interaction vertex. We consider the general form of the Hamiltonian

$$H = H_{\mathrm{f}} + \omega_0 \left(a^\dagger a + \frac{1}{2} \right) + a^\dagger n + n^\dagger a, \tag{A.1}$$

where n is an arbitrary one-particle operator of the form $n = \sum_{i,j} A_{i,j} c_i^\dagger c_j$ with fermionic $\{c_i^{(\dagger)}\}$ and H_{f} contains only fermionic fields. The fermion-boson interaction is therefore of the same form introduced in Equ. (2.21). We will demonstrate, the calculation in the Matsubara formalism, while the calculation on the Keldysh contour works similarly. The calculation is taken from my master's thesis [231]. The partition function Equ. (3.76) in the functional integral formulation, introduced in Sect. 3.6, takes the form

$$\frac{Z}{Z_0} = \frac{1}{Z_0^f} \int \mathcal{D}(\bar{\psi}, \psi) \frac{1}{Z_0^f} \int \mathcal{D}(\phi^*, \phi) \, \exp\left[S_{\mathrm{f}}(\bar{\psi}, \psi) - \phi^*(\partial_t + \omega_0)\phi - \phi^* n\,(\bar{p}si, \psi) - \bar{n}\,(\bar{p}si, \psi)\,\phi \right], \tag{A.2}$$

with the complex bosonic fields ϕ and the fermionic Grassmann fields ψ. The bosonic contributions take a Gaussian form and can therefore analytically be integrated out while simultaneously introducing the bosonic propagator $D(\tau - \tau') = G_{\mathrm{b}}^0(\tau - \tau') - G_{\mathrm{b}}^0(\tau' - \tau)$

$$\frac{Z}{Z_0} = \frac{1}{Z_0^f} \int \mathcal{D}(\bar{\psi}, \psi) \exp\left[S_{\mathrm{f}}(\bar{\psi}, \psi) - S_{\mathrm{fb}}(\bar{\psi}, \psi) \right]. \tag{A.3}$$

with

$$\begin{aligned} S_{\mathrm{fb}}(\bar{\psi}, \psi) &= \int_0^\beta \mathrm{d}\tau \int_0^\beta \mathrm{d}\tau' \, \bar{n}(\tau) \frac{D(\tau - \tau')}{2} n(\tau') \\ &= \frac{1}{\beta^2} \sum_{\substack{n',n \\ m',m}} \int_0^\beta \mathrm{d}\tau \int_0^\beta \mathrm{d}\tau' \, \bar{n}\left(\bar{\psi}(\mathrm{i}\,\omega_{n'}), \psi(\mathrm{i}\,\omega_n) \right) \frac{D(\tau - \tau')}{2} n\left(\bar{\psi}(\mathrm{i}\,\omega_{m'}), \psi(\mathrm{i}\,\omega_m) \right) e^{\mathrm{i}(\omega_{n'} - \omega_n)\tau} e^{\mathrm{i}(\omega_{m'} - \omega_m)\tau}. \end{aligned} \tag{A.4}$$

In the last line, a transformation to frequency space, cf. Equ. (3.79), was conducted for the case of n being a one-particle operator. The exact calculation of the integral can be found in [118], which then leads to the effective antisymmetrized interaction

$$\begin{aligned} \bar{v}_{i_{1'}, i_{2'} | i_1, i_2}(\mathrm{i}\,\omega_{1'}, \mathrm{i}\,\omega_{2'} | \,\mathrm{i}\,\omega_1, \mathrm{i}\,\omega_2) = \frac{1}{\beta} \delta(\omega_{1'} + \omega_{2'} - \omega_1 - \omega_2) \\ \left[D(\mathrm{i}\,\omega_{1'} - \mathrm{i}\,\omega_1)\, A^*_{i_1 i_{1'}} A_{i_{2'} i_2} - D(\mathrm{i}\,\omega_{1'} - \mathrm{i}\,\omega_2)\, A^*_{i_2 i_{1'}} A_{i_{2'} i_1} \right]. \end{aligned} \tag{A.5}$$

in the Matsubara formalism.

On the Keldysh contour, the time integral can be evaluated more straightforward [231], leading to the effective interaction vertex

$$\begin{aligned} \bar{v}^{\nu_{1'}, \nu_{2'} | \nu_1, \nu_2}_{i_{1'}, i_{2'} | i_1, i_2}(\omega_{1'}, \omega_{2'} | \omega_1, \omega_2) = \operatorname{sign}(\nu_{1'}) \operatorname{sign}(\nu_{2'}) \delta(\omega_{1'} + \omega_{2'} - \omega_1 - \omega_2) \\ \left[\delta_{\nu_{1'}, \nu_1} \delta_{\nu_{2'}, \nu_2} D^{\nu_{1'} \nu_{2'}}(\omega_{1'} - \omega_1) A^*_{i_1 i_{1'}} A_{i_{2'} i_2} - \delta_{\nu_{1'}, \nu_2} \delta_{\nu_{2'}, \nu_1} D^{\nu_{1'} \nu_{2'}}(\omega_{1'} - \omega_2) A^*_{i_2 i_{1'}} A_{i_{2'} i_1} \right] \end{aligned} \tag{A.6}$$

B. Currents from the Lindblad master equation

We take a closer look at the particle current Eu. (6.38) and energy current Equ. (6.40) calculated within the Lindblad master equation formalism for our specific quantum dot system. To this end, the Liouvillian of the system is plugged in, and the steady state ρ_{ss} is considered. This calculation can also be found in the appendix of [221].

B.1. Particle current through the fermionic system

First, we discuss the particle current $I_j^N = \mathrm{Tr}\left[n_j \mathcal{L} \rho_{\mathrm{ss}}\right]$. The quantum dot Hamiltonian without the leads and bosonic bath ($\Gamma = 0, \kappa = 0$) conserves the particle number and the coherent contribution

$$-\mathrm{i}\,\mathrm{Tr}\left(n_i\left[H, \rho_{\mathrm{ss}}\right]\right) = -\mathrm{i}\,\mathrm{Tr}\left(\left[n_i, H\right]\rho_{\mathrm{ss}}\right) = 0 \tag{B.1}$$

vanishes. The dissipative contributions can be brought in the form

$$\sum_\alpha \gamma_\alpha \mathrm{Tr}\left(n_i L_\alpha \rho_{\mathrm{ss}} L_\alpha^\dagger - \frac{1}{2} n_i L_\alpha^\dagger L_\alpha \rho_{\mathrm{ss}} - \frac{1}{2} n_i \rho_{\mathrm{ss}} L_\alpha^\dagger L_\alpha\right) = \sum_j \gamma_j \left(\langle L_\alpha^\dagger n_i L_\alpha\rangle - \frac{1}{2}\langle n_i L_\alpha^\dagger L_\alpha\rangle - \frac{1}{2}\langle L_\alpha^\dagger L_\alpha n_i\rangle\right). \tag{B.2}$$

Where we used the cyclic property of the trace and that bosonic and fermionic operators commute. For the current through the first dot $i = 1$ from the left lead, $L_\alpha = c_L^\dagger$ gives the only non-vanishing contribution

$$\langle c_1 n_1 c_1^\dagger\rangle - \frac{1}{2}\langle n_1 c_1 c_1^\dagger\rangle - \frac{1}{2}\langle c_1 c_1^\dagger n_1\rangle = 1 - \langle n_1\rangle. \tag{B.3}$$

For $i = M$, only $L_\alpha = c_M$ contributes:

$$\langle c_M^\dagger n_M c_M\rangle - \frac{1}{2}\langle n_M c_M^\dagger c_M\rangle - \frac{1}{2}\langle c_M^\dagger c_M n_M\rangle = -\langle n_M\rangle. \tag{B.4}$$

This then provides the current given in Equ. (6.39):

$$I_L^N = 2\Gamma\left(1 - \langle c_1^\dagger c_1\rangle\right), \qquad I_R^N = -2\Gamma\langle c_M^\dagger c_M\rangle. \tag{B.5}$$

B.2. Energy current into the bosonic system

The energy current into the resonantor $I_{\mathrm{b}}^E = \mathrm{Tr}\left[H_{\mathrm{b}} \mathcal{L} \rho\right]$, cf. Equ (6.40), depends strongly on the coupling between the fermionic and bosonic systems. We consider the general form in Equ. (2.21). The calculation is analog to the particle current and leads to three non-vanishing contributions. The first one stems from the fermion-boson coupling with

$$\begin{aligned} \mathrm{Tr}\left(a^\dagger a\left[H, \rho_{\mathrm{ss}}\right]\right) &= \mathrm{Tr}\left(a^\dagger a\left[a^\dagger \sum_{i,j} A_{i,j} c_i^\dagger c_j + a \sum_{i,j} A_{i,j}^* c_j^\dagger c_i, \rho_{\mathrm{ss}}\right]_-\right) \\ &= \sum_{i,j}\left[A_{ij}\langle c_i^\dagger c_j a^\dagger\left[a, a^\dagger\right]_-\rangle + A_{ij}^*\langle c_j^\dagger c_i a\left[a^\dagger, a\right]_-\rangle\right] = \sum_{i,j}\left[A_{ij}\langle c_i^\dagger c_j a^\dagger\rangle + A_{ij}^*\langle c_j^\dagger c_i a\rangle\right]. \end{aligned} \tag{B.6}$$

The other originates from the dissipative jump operators $L_\alpha = a$, where

$$\mathrm{Tr}\left(a^\dagger a a \rho_\mathrm{ss} a^\dagger - \frac{1}{2} a^\dagger a a^\dagger a \rho_\mathrm{ss} - \frac{1}{2} \rho_\mathrm{ss} a^\dagger a a^\dagger a\right) = \langle a^\dagger a^\dagger a a\rangle - \frac{1}{2}\langle a^\dagger a a^\dagger a\rangle - \frac{1}{2}\langle a^\dagger a a^\dagger a\rangle = -\langle a^\dagger a\rangle. \quad \text{(B.7)}$$

and analogously $L_\alpha = a^\dagger$, where

$$\mathrm{Tr}\left(a^\dagger a a^\dagger \rho_\mathrm{ss} a - \frac{1}{2} a^\dagger a a a^\dagger \rho_\mathrm{ss} - \frac{1}{2} \rho_\mathrm{ss} a^\dagger a a a^\dagger\right) = 1 + \langle a^\dagger a\rangle. \quad \text{(B.8)}$$

Thus, the energy current reads

$$I_\mathrm{b}^E = -\,\mathrm{i}\,\omega_0 \sum_{i,j} \left[A_{ij}\langle c_i^\dagger c_j a^\dagger\rangle + A_{ij}^*\langle c_j^\dagger c_i a\rangle\right] - 2\kappa(1 + n_\mathrm{b}(\omega_0))\omega_0 \left\langle a^\dagger a\right\rangle + 2\kappa n_\mathrm{b}(\omega_0)\omega_0 \left(1 + \left\langle a^\dagger a\right\rangle\right). \quad \text{(B.9)}$$

For small temperatures with $n_\mathrm{b}(\omega_0 > 0) \to 0$, the last term is neglible.

C. Spectral decomposition for the quantum regression theorem

As stated in the main text in Sect. 6.2.3, a similar decomposition for the Green functions to the Lehmann representation in an open quantum system can be found by using the QRT Equ. (6.33) within the master equation formalism. This is shown in the following for the retarded and lesser component of the Green function.

Using QRT Equ. (6.33), the retarded Green function Equ. (3.23) in steady state with the density ρ_{ss} is given by

$$\begin{aligned} G^{\mathrm{R}}_{xy}(t) &= -\mathrm{i}\,\theta(t)\left[\langle d_x(t)d^\dagger_y(0)\rangle - \zeta \underbrace{\langle d^\dagger_y(0)d_x(t)\rangle}_{\mathrm{Tr}\left[d_y(0)\rho_{\mathrm{ss}}(-t)d^\dagger_x(-t)\right]}\right] = -\mathrm{i}\,\theta(t)\,\mathrm{Tr}\left[d_x e^{\mathcal{L}t} d^\dagger_y \rho_{\mathrm{ss}} - \zeta d_x e^{\mathcal{L}t}\rho_{\mathrm{ss}} d^\dagger_y\right] \\ &= -\mathrm{i}\,\theta(t)\sum_\alpha \left\{e^{\lambda_\alpha t}\,\mathrm{Tr}\left[d_x r_\alpha\right]\mathrm{Tr}\left[l^\dagger_\alpha d^\dagger_y \rho_{\mathrm{ss}}\right] - \zeta e^{\lambda_\alpha t}\,\mathrm{Tr}\left[d_x r_\alpha\right]\mathrm{Tr}\left[l^\dagger_\alpha \rho_{\mathrm{ss}} d^\dagger_y\right]\right\}, \end{aligned} \tag{C.1}$$

where d_x can be bosonic or fermionic operators with arbitrary quantum numbers x and respectively, the commutator or anticommutator is applied, with $\zeta = 1$ for bosonic operators and $\zeta = -1$ for fermionic ones. In the last line, the spectral decomposition of the Liouville superoperator Equ. (6.21) was used. Transforming into frequency space, this leads to

$$\begin{aligned} G^{\mathrm{R}}_{xy}(\omega) &= -\mathrm{i}\int_{-\infty}^{\infty} \mathrm{d}\,t\, e^{\mathrm{i}\,\omega t}\theta(t)\sum_\alpha \left\{e^{\lambda_\alpha t}\,\mathrm{Tr}\left[d_x r_\alpha\right]\mathrm{Tr}\left[l^\dagger_\alpha d^\dagger_y \rho_{\mathrm{ss}}\right] - \zeta e^{\lambda_\alpha t}\,\mathrm{Tr}\left[d_x r_\alpha\right]\mathrm{Tr}\left[l^\dagger_\alpha \rho_{\mathrm{ss}} d^\dagger_y\right]\right\} \\ &= -\mathrm{i}\sum_\alpha \underbrace{\int_0^\infty \mathrm{d}\,t\, e^{\mathrm{i}\,\omega t + \lambda_\alpha t}}_{\frac{-1}{\mathrm{i}\,\omega + \lambda_\alpha}} \left\{\mathrm{Tr}\left[d_x r_\alpha\right]\mathrm{Tr}\left[l^\dagger_\alpha d^\dagger_y \rho_{\mathrm{ss}}\right] - \zeta\,\mathrm{Tr}\left[d_x r_\alpha\right]\mathrm{Tr}\left[l^\dagger_\alpha \rho_{\mathrm{ss}} d^\dagger_y\right]\right\} \\ &= \sum_\alpha \frac{\mathrm{Tr}\left[d_x r_\alpha\right]\mathrm{Tr}\left[l^\dagger_\alpha \left[d^\dagger_y, \rho_{\mathrm{ss}}\right]_{-\zeta}\right]}{\omega - \mathrm{i}\,\lambda_\alpha}. \end{aligned} \tag{C.2}$$

The convergence of the integral is ensured by the fact that $\mathrm{Re}\lambda_\alpha \leq 0$ for all α [238].

In a similar manner, the steady-state lesser Green function in Equ. (3.7) can be decomposed. To apply the QRT Equ. (6.33), which only holds for $t \geq 0$, the time integral can be rewritten

$$\begin{aligned} G_{xy}(\omega) &= -\zeta\mathrm{i}\int_0^\infty \left[e^{\mathrm{i}\,\omega t}\langle d^\dagger_y(0)d_x(t)\rangle\right] - \zeta\mathrm{i}\underbrace{\int_{-\infty}^0 \left[e^{\mathrm{i}\,\omega t}\langle d^\dagger_y(0)d_x(t)\rangle\right]}_{\int_0^\infty\left[e^{-\mathrm{i}\,\omega t}\langle d^\dagger_y(t)d_x(0)\rangle\right]} \\ &= -\zeta\mathrm{i}\int_0^\infty \mathrm{d}\,t\left\{e^{\mathrm{i}\,\omega t}\,\mathrm{Tr}\left[d_x e^{\mathcal{L}t}\rho_{\mathrm{ss}} d^\dagger_y\right] + e^{-\mathrm{i}\,\omega t}\,\mathrm{Tr}\left[d^\dagger_y e^{\mathcal{L}t} d_x \rho_{\mathrm{ss}}\right]\right\}. \end{aligned} \tag{C.3}$$

The remaining calculations are analog to the above derivation of G^{R}_{xy} and lead to

$$G^{<}_{xy}(\omega) = \zeta \sum_{\alpha} \left(\frac{\mathrm{Tr}\left[d_x r_\alpha\right] \mathrm{Tr}\left[l_\alpha^\dagger \rho_{\mathrm{ss}} d_y^\dagger\right]}{\omega - \mathrm{i}\,\lambda_\alpha} - \frac{\mathrm{Tr}\left[d_y^\dagger r_\alpha\right] \mathrm{Tr}\left[l_\alpha^\dagger d_x \rho_{\mathrm{ss}}\right]}{\omega + \mathrm{i}\,\lambda_\alpha} \right). \tag{C.4}$$

D. Regularized PZW transformation

As stated in Sect. 7.4.1, we use the Baker-Campbell-Hausdorff formular to study transformations of the form:

$$e^{-X}Oe^{X} = O - [X,O]_- + \frac{1}{2!}\left[X,[X,O]_-\right]_- - \frac{1}{3!}\left[X,\left[X,[X,O]_-\right]_-\right]_- + \dots \quad , \tag{D.1}$$

for arbitrary operators X, O. Therefore, we have to calculate the commutators to evaluate the transformation. Additionally, we use the identities [239]

$$[A,BC]_- = [A,B]_-\,C + B\,[A,C]_- = [A,BC]_+\,C - B\,[A,C]_+ \,. \tag{D.2}$$

Together with the usual (anti-) commutation relations for (fermionic) bosonic operators, this allows us to evaluate the PWZ transformation

$$e^{-\mathrm{i}\,S}He^{\mathrm{i}\,S}, \qquad \text{with } S = q\int \mathrm{d}\,x\theta(x)\psi\,\dagger\,(x)\psi(x). \tag{D.3}$$

For the fermionic part H_f, we have to evaluate the commutator of the fermionic field operators

$$\left[\psi^\dagger(x')\psi(x), \psi^\dagger(x)\psi(x)\right]_- = \delta(x-x')\left\{\psi^\dagger(x)\psi(x') - \psi^\dagger(x')\psi(x)\right\} = 0, \tag{D.4}$$

which leads to Equ. (7.47)

$$e^{-\mathrm{i}\,S}\int \mathrm{d}\,xV(x)\psi^\dagger(x)\psi(x)\,e^{\mathrm{i}\,S} = \int \mathrm{d}\,xV(x)\psi^\dagger(x)\psi(x). \tag{D.5}$$

For the bososnic part H_b, we study how the canonical bosonic operators q and π Equ. (7.45) transform. The coordinate operator q commutes with the generator S and therefore $e^{-\mathrm{i}\,S}q\,e^{\mathrm{i}\,S} = q$. The momentum operator π however results in a finite commutator

$$[S,\pi]_- = \int \mathrm{d}\,x\theta(x)\psi^\dagger(x)\psi(x), \tag{D.6}$$

It only contains the fermionic operators and therefore all higher-order commutators vanish. The bosonic part of the Hamiltonian thus takes the form Equ. (7.48)

$$\frac{1}{2}e^{-\mathrm{i}\,S}\left\{\omega_0^2\pi^2 + q^2\right\}e^{\mathrm{i}\,S} = \frac{1}{2}\left\{\left(\pi + \int \mathrm{d}\,x\theta(x)\psi^\dagger(x)\psi(x)\right)^2 + \omega_0^2 q^2\right\}. \tag{D.7}$$

For the mixed part H_fb, the commutators do not vanish at a certain order and we obtain an infinite sum, providing an exponential function. For the following calculations, we define the differential operator $D_x := [\mathrm{i}\,\partial_x + A(x)]^2$. We consider first the single commutator, where is important to keep in mind which operators the derivation acts

$$\left[\psi^\dagger(x')\psi(x'), \psi^\dagger(x)D_x\psi(x)\right]_- = \delta(x-x')\psi^\dagger(x')D_x\psi(x) - \psi^\dagger(x)\psi(x')D_x\delta(x-x'), \tag{D.8}$$

and therefore

$$[\mathrm{i}\,S, H_{\mathrm{bf}}]_- = \frac{i}{2m}\int \mathrm{d}\,x \left\{ q\theta(x)\psi^\dagger(x)D_x\psi(x) - \int \mathrm{d}\,x'\; q\theta(x')\psi^\dagger(x)\psi(x')D_x\delta(x-x')\right\}. \tag{D.9}$$

By continuing analogously for the higher-order terms, a structure can be identified, leading to the form

$$\begin{aligned}\underbrace{[\mathrm{i}\,S, \dots [\mathrm{i}\,S, H_{\mathrm{bf}}]_- \dots]_-}_{n\text{ times}} &= \frac{\mathrm{i}^n}{2m}\int \mathrm{d}\,x\; (q\theta(x))^n\, \psi^\dagger(x)D_x\psi(x) \\ &+ \frac{\mathrm{i}^n}{2m}\int \mathrm{d}\,x \int \mathrm{d}\,x'\; \left\{(q\theta(x) - q\theta(x'))^n - (q\theta(x))^n\right\}\psi^\dagger(x)\psi(x')D_x\delta(x-x').\end{aligned} \tag{D.10}$$

With the help of mathematical induction, this expression can be shown to hold true for all $n \geq 0$, which we do not show here directly but is easy to reproduce. Summing up all terms and using the series representation of the exponential function, the mixed part of the Hamiltonian is transformed to Equ. (7.50)

$$\begin{aligned} e^{-\mathrm{i}\,S}\int \mathrm{d}\,x\psi^\dagger(x)\frac{D_x}{2m}\psi(x)\,e^{\mathrm{i}\,S} &= \frac{1}{2m}\int \mathrm{d}\,x e^{-\mathrm{i}\,\theta(x)}\psi^\dagger(x)D_x\psi(x) \\ &+ \frac{1}{2m}\int \mathrm{d}\,x\int \mathrm{d}\,x'\; e^{-\mathrm{i}(\theta(x)-\theta(x'))}\psi^\dagger(x)\psi(x)D_x\delta(x-x') \\ &- \frac{1}{2m}\int \mathrm{d}\,x\int \mathrm{d}\,x'\; e^{-\mathrm{i}\,\theta(x)}\psi^\dagger(x)\psi(x')D_x\delta(x-x').\end{aligned} \tag{D.11}$$

E. Linear conductance of the non-interacting triple-dot system

In Sect. 8.3 we discussed the linear conductance through a triple-dot system of the general type described in Sect. 2.1 for $M = 3$ while detuning all quantum dots simultaneously $\varepsilon_1 = \varepsilon_2 = \varepsilon_3 = \varepsilon$. Here, we aim for a better understanding of how the structure of the conductance as a function detuning ε is related to the (effective) eigenenergies of the system. To this end, we neglect all interactions ($A_{ij} = 0, U = 0$) and only consider the coupling to the leads in the effective spectrum.

The effective one-particle Hamiltonian H^0_{eff} only includes the lead contributions, cf. Sect. 3.5.4, and takes the form

$$H^0_{\text{eff}} = \left[-G_0(\mathrm{i}\,0^+)\right]^{-1} = \begin{pmatrix} \varepsilon - \mathrm{i}\,\Gamma & t & 0 \\ t & \varepsilon & t \\ 0 & t & \varepsilon - \mathrm{i}\,\Gamma \end{pmatrix}. \tag{E.1}$$

The energy spectrum is then given by $E^0_{\text{eff},0} = \varepsilon - \mathrm{i}\,\Gamma$ and $E^0_{\text{eff},\pm} = \varepsilon - \mathrm{i}\,\Gamma/2 \pm \sqrt{2t^2 - \Gamma^2/4}$. The transmission coefficient of the linear conductance Equ. (3.73) is given by

$$T_{13}(0) = \Gamma^2 \left| \frac{1}{\varepsilon(\Gamma + \mathrm{i}\,\varepsilon) - 2\,\mathrm{i}\,t^2} \frac{\mathrm{i}\,t^2}{-\varepsilon + \mathrm{i}\,\Gamma} \right|^2 = \Gamma^2 \underbrace{\frac{1}{\varepsilon^2\Gamma^2 + (\varepsilon^2 - 2t^2)^2}}_{(1)} \underbrace{\frac{t^4}{\varepsilon^2 + \Gamma^2}}_{(2)} \tag{E.2}$$

(1) has maxima at $\varepsilon = \pm\sqrt{2t^2 - \Gamma^2/2}$ and (2) at $\varepsilon = 0$. Thus, the peaks of the conductance do not directly lay on the energy spectra of the effective Hamiltonian $E^0_{\text{eff},\epsilon}$.

To understand this difference, we note that there is a difference to the model of energy levels $E_{\pm,0}$, which are coupled in parallel to the reservoirs with the Hamiltonian

$$H^0 = \begin{pmatrix} E_- & 0 & 0 \\ 0 & E_0 & 0 \\ 0 & 0 & E_+ \end{pmatrix} \tag{E.3}$$

and the coupling matrices to the left or right lead [137]

$$\Gamma_L = \Gamma_R = \begin{pmatrix} \Gamma & 0 & 0 \\ 0 & \Gamma & 0 \\ 0 & 0 & \Gamma \end{pmatrix}. \tag{E.4}$$

For the parallel model, the transmission takes the form

$$T_{13}(0) = \mathrm{Tr}\left[\Gamma_L G^R \Gamma_R G^A\right] = \mathrm{Tr}\begin{pmatrix} \frac{\Gamma^2}{|-E_- + \mathrm{i}\,\Gamma|^2} & 0 & 0 \\ 0 & \frac{\Gamma^2}{|-E_0 + \mathrm{i}\,\Gamma|^2} & 0 \\ 0 & 0 & \frac{\Gamma^2}{|-E_+ + \mathrm{i}\,\Gamma|^2} \end{pmatrix}, \tag{E.5}$$

giving peaks of the conductance at every energy of the spectrum. On the other hand, when we consider our linear system and change into the diagonal basis of H^0_{eff}, we also have to transform $\mathit{\Gamma}_{L/R}$ giving rise to non-diagonal elements. This is easily seen in $T_{13}(0) = \operatorname{Tr}\left[\mathit{\Gamma}_L G^R \mathit{\Gamma}_R G^A\right] = \operatorname{Tr} \mathit{\Gamma}_L U U^\dagger G^R U U^\dagger \mathit{\Gamma}_R U U^\dagger G^A U U^\dagger$, where $U, U^\dagger$ diagonalizes $U^\dagger G^R U = \tilde{G}^R$. The coupling matrizes are then given by $\tilde{\mathit{\Gamma}}_{L,ij} = U^\dagger_{i1} \mathit{\Gamma} U_{1j}$ and $\tilde{\mathit{\Gamma}}_{R,ij} = U^\dagger_{i3} \mathit{\Gamma} U_{3j}$. This couples then the different energy levels

$$T_{13}(0) = \sum_{i,j} \tilde{\mathit{\Gamma}}_{L,ij} \tilde{G}^R_{jj} \tilde{\mathit{\Gamma}}_{R,ji} \tilde{G}^A_{ii} \tag{E.6}$$

in the diagonal basis.

F. Logarithmic divergence in perturbation theory and functional renormalization group

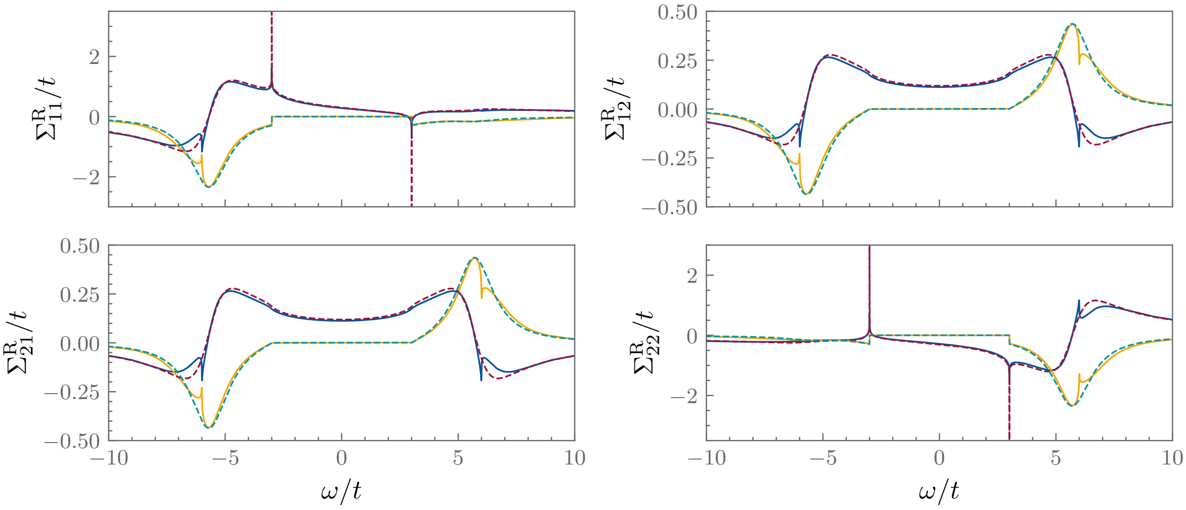

Figure F.1.: The real (blue, red) and imaginary (yellow, green) part of the perturbative self-energy as a function of frequency ω in equilibrium $V = 0$ and in the zero-temperature limit $T_L = T_R = T_{\mathrm{b}} = 0$. The results are for $\Gamma/t = 1$ and close to resonant detuning $\varepsilon_1 = -\varepsilon_2 = 2.5t$ for $\omega_0/t = 3$ and for the coupling $\lambda/t \approx 1.56\,\mathrm{i}$, so that $|\lambda|^2/\omega_0\Gamma = 0.9^2$. Dashed lines are calculated in first-order perturbation theory and solid lines with FRG in first-order truncation.

As described in Sect. 5, it is known that perturbation theory can suffer from logarithmic divergences at low energy scales. For some systems, FRG can cure these divergencies by resumming the logarithms to power-laws. This was also discussed in Sect. 5. As we will show, the perturbative treatment of the Peierls substitution in the first-order expansion of the phase, Equ. (7.20), and the capacitive coupling, Equ. (2.20) also exhibits this unphysical behavior at frequencies close to the mode frequency of the cavity. We will study the logarithmic divergence which occurs in the self-energy components calculated using first-order perturbation theory. We compare the scaling with the results from FRG in first-order truncation to see if this method indeed cures the divergencies of the system under consideration. To this end, we utilize log-linear and log-log derivative to identify logarithmic- or power-law scaling.

For this analysis, we will utilize the double quantum dot ($M = 2$) coupled via the Peierls coupling or the capacitive coupling to the resonator. In both cases, we detune the quantum dot system asymmetrically $\varepsilon_1 = -\varepsilon_2 = \varepsilon/2$ and close to resonant with the resonator.

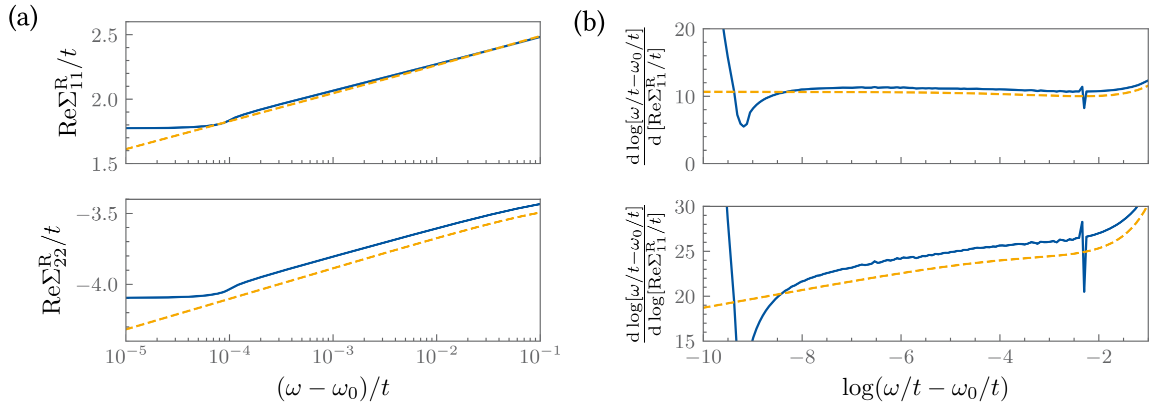

Figure F.2.: The real part of the 1,1 and 2,2 component of the retarded self-energy for frequencies ω close to the cavity frequency ω_0 for the same parameters as in Fig. F.1. The yellow dashed lines indicate the results from perturbation theory and the blue solid lines from FRG. (a) the self-energy on a log-linear scale. (b) the log-linear (top) and log-log (bottom) derivative of the self-energy 1,1 component.

F.1. Peierls coupling

First, we consider the light-matter coupling via the Peierls substitution and define $\lambda := \mathrm{i}\,gt$. As discussed in Sect. 5, the FRG approach in first-order truncation takes into account all terms in first order in the interaction and, thus, is exact in $\mathcal{O}(g^2)$, but also includes higher-order terms due to the feedback of the self-energy into the FRG flow. Further, the MF renormalized variables t, ω_0 and λ are only exact in $\mathcal{O}(g^2)$ and neglect higher-order terms. Therefore, the introduction of the MF variables into the FRG flow would lead to an uncontrolled generation of higher-order terms. Thus, instead of utilize the MF approach (cf. Sect. 7.3.3) to include the second-order terms in the vector potential of the exponential function in the Peierls substitution, we omit the second-order terms arising from the exponential expansion discussed in Sect. 7.3 and focus solely on the linear term for both methods.

First, we demonstrate the logarithmic divergence occurring in the perturbative treatment. To this end, we consider a double quantum dot with $M = 2$ where the cavity only renormalizes the hopping between the two dots. With respect to the discussion for the finite system in Sect. 7.1.2, this means that the cavity is applied exclusively between the two dots. The real and imaginary parts of the retarded self-energies are shown in Fig. F.1, where the results from first-order perturbation theory are represented by dotted lines. For $\omega \to \omega_0$, we observe a divergence in the real part of the diagonal components of the retarded self-energy. This divergence originates from the Fock term in Equ. (4.9), more specifically from the Cauchy principal value integral over the Keldysh Green function.

In Fig. F.2, we confirm that the divergence of the perturbative results is indeed logarithmic around ω_0. In Fig. F.2(a), the real part of the diagonal self-energy components obtained from perturbation theory as a function of frequency close to ω_0 is shown as dashed lines. Note the logarithmic scaling of the x-axis, which causes the logarithmic behavior to appear linear. In Fig. F.2(b), we present the log-linear and log-log derivatives of the real part of the 1,1 component, as defined in the figure's y-labels. The derivative is obtained numerically. The log-linear derivative gives a constant value for a logarithmic dependence, $\mathrm{Re}\,\Sigma^{\mathrm{R}}_{11} \sim \log(\omega-\omega_0)$. This constant behavior is clearly visible in the perturbative result. The log-log derivative, on the other hand, identifies power laws, $\mathrm{Re}\,\Sigma^{\mathrm{R}}_{11} \sim (\omega-\omega_0)^{\alpha}$, with an appearing constant value representing the exponent α. No power law behavior is observed.

In general, this divergence can be cut off by other energy scales, such as a finite temperature. This also implies that numerical inaccuracies, such as those arising from a discrete frequency grid, can prevent the divergence from fully developing. Therefore, in contrast to the rest of this thesis, the perturbation theory is implemented here without using the Riemann sum to treat the integrals on the right-hand side of Equs. (4.8), (4.9) and (4.10), as described in Sect. 4.3. Instead, the bare Green functions are evaluated using `integrate.quad` from `scipy` [152]. This method treats the Cauchy integral more accurately without requiring an increase in the precision of the frequency grid. However, the evaluation of perturbation theory for one component is approximately 10 times slower, and vector operations cannot be used in the integral, further decreasing the efficiency of the calculations. This approach provides a highly accurate but inefficient method for calculations where high precision is required for a limited number of data points.

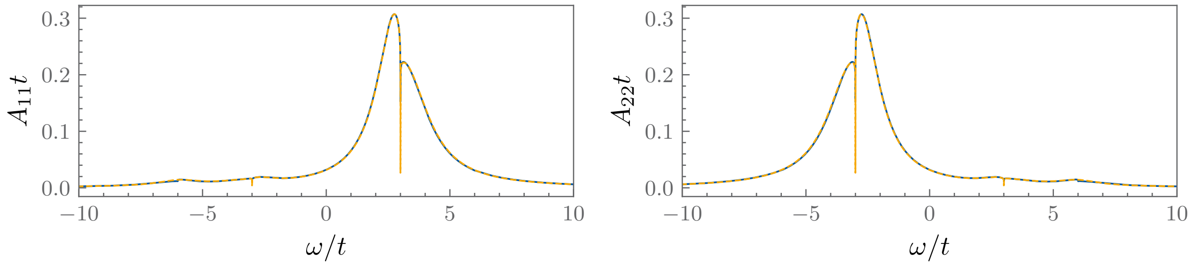

Figure F.3.: Spectral function as a function of frequency for the same parameters as in Fig. F.1. Dashed, yellow lines are calculated in first-order perturbation theory, and solid lines with FRG in first-order truncation.

In Sect. 5, we have discussed that in the renormalization group approach, a resummation of diagrams occurs during the flow. In some cases [13, 33, 97, 240], this is known to resum logarithmic terms leading to power-laws instead and therefore be able to cure the logarithmic divergence occurring in perturbation theory. Thus, we hope that FRG is able to cure the logarithmic divergence in the perturbative treatment of the Peierls coupling as well. The retarded self-energy terms calculated with FRG are also shown in Fig. F.1. The FRG results are in general equal to the perturbation theory ones in the first order in the interaction, meaning in λ^2. However, deviations arise due to the higher-order corrections. So, we observe a kink at the second side band $\omega = 2\omega_0$, due to feedback effects. Most importantly, however, no divergence can be observed for the self-energies calculated with FRG. At this point, it is however not clear, if the divergence is cut due to the FRG-treatment or due to numerical inaccuracies, discussed above. The calculations are, in contrast with the perturbation theory, conducted using the finite grid and Rieman-sums. This has been done, due to the numerical inefficiency of the `integrate.quad`-routine.

Therefore, the retarded self-energy is studied more carefully in Fig. F.2 for frequencies close to ω_0, where the FRG-results are shown as solid lines. In Fig. F.2(a), the real part of the retarded self-energy components 1,1 and 2,2 are compared to the perturbative results close to ω_0 on a log-linear scale. For larger distances $\omega - \omega_0$, the behavior of the two methods seems to agree quite well. Note, that for smaller distances, $\omega - \omega_0 < 10^{-4}$, the decrease of the self-energies seems to be cut off for the FRG calculations. This results from the finite resolution of the frequency grid, as described above, which is around this order of magnitude. To investigate, if the decrease follows a logarithmic- or power-law, the log-linear and log-log derivative are shown in Fig. F.2(b). It becomes quite clear, that also FRG follows a logarithmic behavior, exactly as first-order perturbation theory. The peaked structure around $\log(\omega/t - \omega_0/t) \approx -2.2$ is caused by numerics and is due to fluctuations in the grid. They can be neglected. Therefore, we see that despite our hope, FRG does not cure the logarithmic divergence present in perturbation theory but exhibits the same behavior.

The divergent behavior of the self-energies can also directly affect physical observables. For the Peierls coupling, this is, e.g., the case for the spectral function, where divergencies in the self-energy lead to zeros. The spectral function calculated with perturbation theory as well as with FRG is shown in Fig. F.3. It is important to note, that the sharp features do not greatly affect integrated variables, such as the occupation and currents introduced in Sect. 3.5. We can therefore trust perturbation theory to reproduce the correct physical behavior of these quantities.

F.2. Capacitive coupling

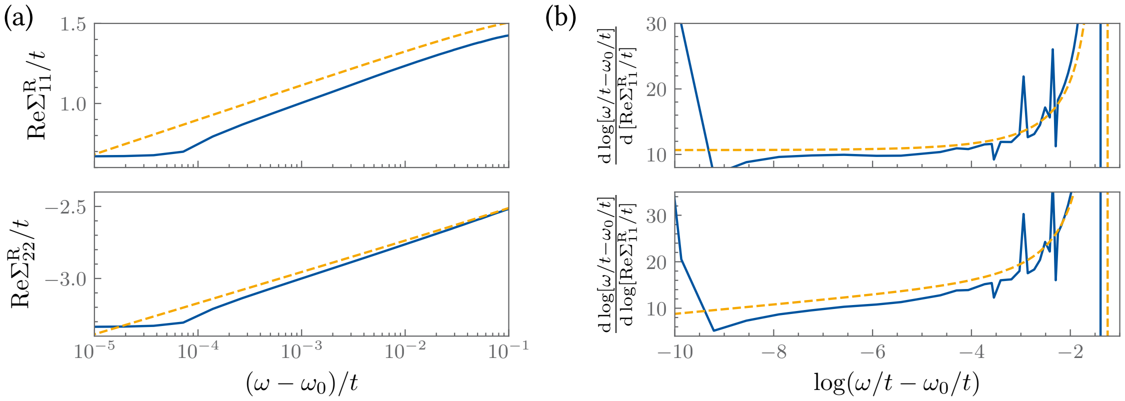

Figure F.4.: The real part of the retarded self-energy 1,1 and 2,2 components as a function of frequency around the divergence point ω_0 in equilibrium $V = 0$ and in the zero-temperature limit $T_L = T_R = T_\mathrm{b} = 0$. For $\Gamma/t = 1$ and close to resonant detuning $\varepsilon_1 = -\varepsilon_2 = 2.5$ for $\omega_0/t = 3$ and with the coupling strength $\lambda/t \approx 1.56$, so that $|\lambda|^2/\omega_0\Gamma = 0.9^2$. Dashed lines are calculated in first-order perturbation theory and solid lines with FRG in first-order truncation. (a) the 1,1 and 2,2 components of the retarded self-energy with logarithmic scaled x-axis. (b) the log-linear and log-log derivative of the 1,1 components of the retarded self-energy.

Now, we couple the quantum dot system with the resonator via capacitive coupling and conduct the same analysis as in the preceding section. The self-energies, as well as the spectral energy function, similar to Fig. F.1 and F.3 for the Peierls coupling, are shown in Figs. F.5 and F.6 respectively when considering a capacitive coupling instead.

Here, we comment only on the divergence of the diagonal retarded self-energy components in Fig. F.4(a), along with their logarithmic and double-logarithmic derivatives in Fig. F.4(b). Those are calculated within first-order perturbation theory, where the occurrence of the logarithmic divergence is known, and compared them with the results from FRG in first-order truncation. As noted in Sect. 9.4, the logarithmic dependence manifests as a constant in the log-derivative, while power-law behavior appears as a constant in the log-log derivative. The self-energy calculated with FRG exhibits the same scaling behavior as the one calculated with perturbation theory. Thus, it is evident in Fig. F.4 that the FRG approach does not resolve the logarithmic divergence in perturbation theory, similar to the behavior observed for the Peierls substitution system in Sect. 9.4. Additionally, we found the same logarithmic divergence when extending the analysis deeper into the anti-adiabatic limit for larger ω_0. Thus, the outcome for both couplings remains the same.

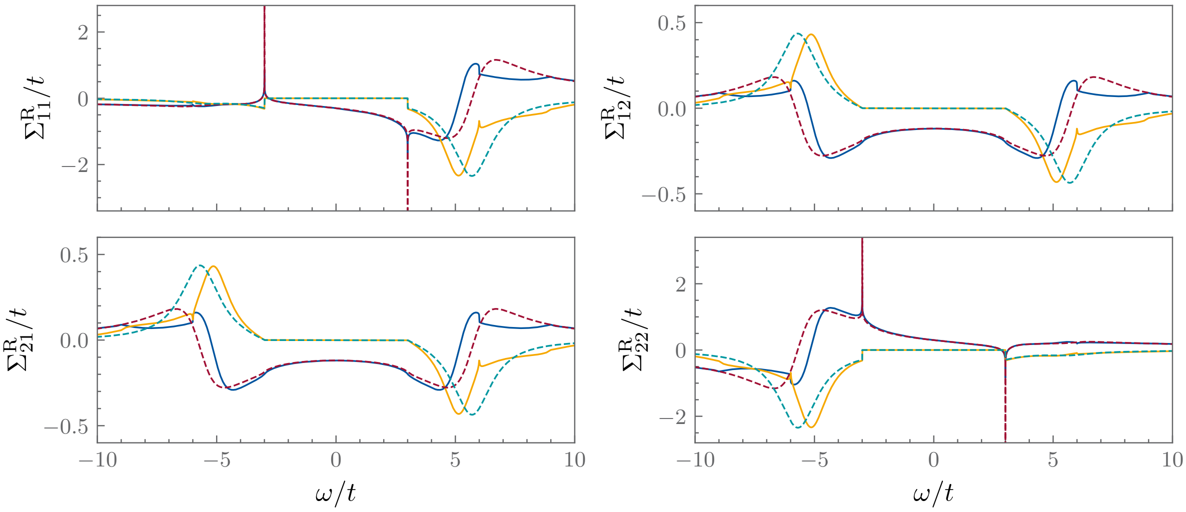

Figure F.5.: The real (blue, red) and imaginary part (yellow, green) of the retarded self-energy components as a function of frequency in equilibrium $V = 0$ and in the zero-temperature limit $T_L = T_R = T_\mathrm{b} = 0$. We consider, $\Gamma/t = 1$, $\varepsilon_1 = -\varepsilon_2 = 2.5t$ close to resonant detuning, $\omega_0/t = 3$ and for the coupling $\lambda/t \approx 1.56$, so that $|\lambda|^2/\omega_0\Gamma = 0.9^2$. Dashed lines are calculated in first-order perturbation theory and solid lines with FRG in first-order truncation.

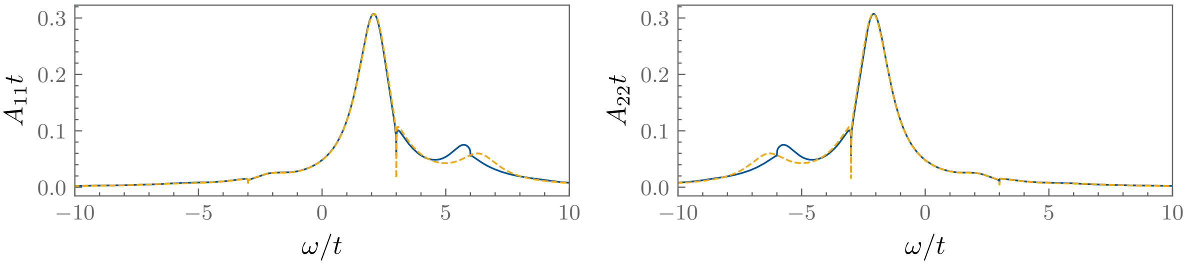

Figure F.6.: The components of the spectral function as a function of frequency for the same parameters as in Fig. F.4. Dashed, yellow lines are calculated in first-order perturbation theory, and solid lines with FRG in first-order truncation.

G. Energy transfer - results from the Lindblad master equation

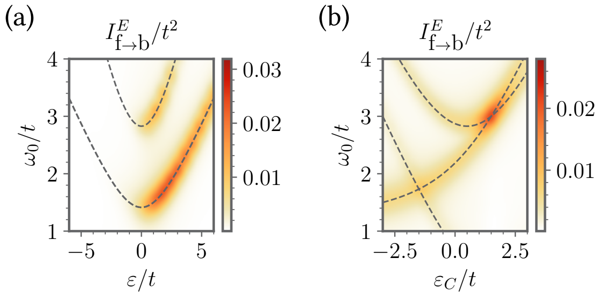

Figure G.1.: Energy transfer from the fermionic to the bosonic system calculated with the Lindblad master equation. Same parameters as in Figs. 11.7. (a) for the linear configuration and (b) for the triangular one.

H. Renormalization of linear transport coefficients

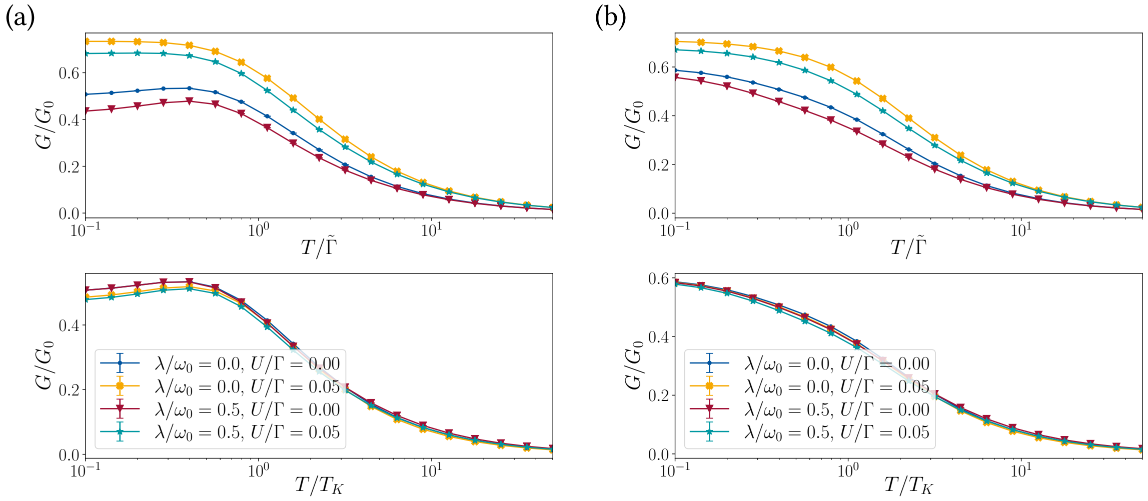

Figure H.1.: Conductance G/G_0 as a function of temperature T, with G_0 being the conductance quantum. Parameters are set and renormalized as in Fig. 12.3. For (a) in the linear regime ($V \to 0$, $T_L \to T_R = T$) and in (b) in the non-linear regime for finite V and $|T_L - T_R|$. In the upper plots, the energy scales are renormalized by $\tilde{\Gamma}$ and in the lower ones with T_K.

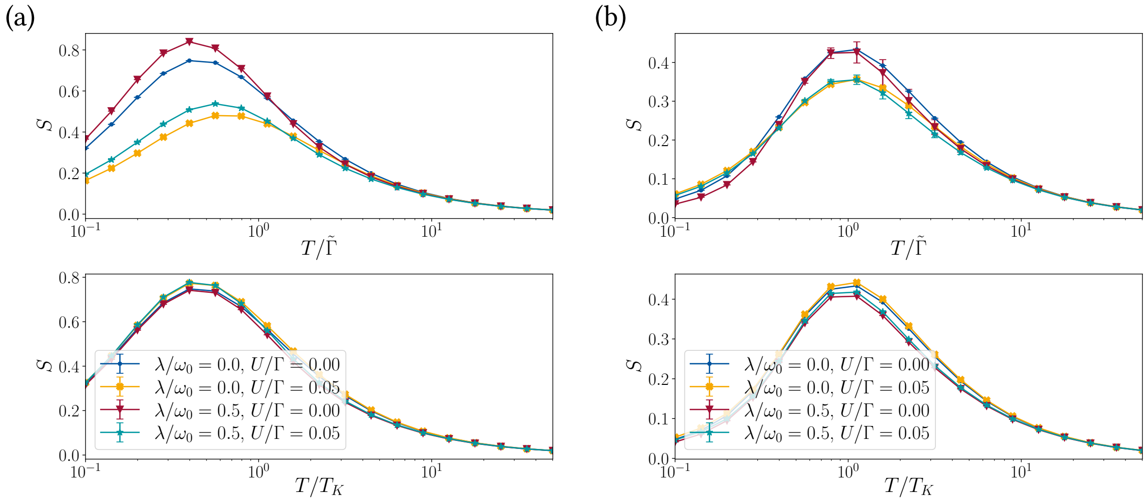

Figure H.2.: Same as in Fig. H.1 with the Seebeck coefficient S as a function of the temperature T.

Publications

[221] C. Hermansen, M. Caltapanides, V. Meden, and J. Paaske, “Simulating electron-vibron energy transfer with quantum dots and resonators”, Phys. Rev. B **110**, 205424 (2024).

[231] M. Caltapanides, D. M. Kennes, and V. Meden, “Finite-bias transport through the interacting resonant level model coupled to a phonon mode: a functional renormalization group study”, Phys. Rev. B **104**, 085125 (2021).

Bibliography

[1] W. Cao, H. Bu, M. Vinet, M. Cao, S. Takagi, S. Hwang, T. Ghani, and K. Banerjee, “The future transistors”, Nature **620**, 501–515 (2023).

[2] Y. Liu, X. Duan, H.-J. Shin, S. Park, Y. Huang, and X. Duan, “Promises and prospects of two-dimensional transistors”, Nature **591**, 43–53 (2021).

[3] T. Ayral, P. Besserve, D. Lacroix, and E. A. Ruiz Guzman, “Quantum computing with and for many-body physics”, The European Physical Journal A **59**, 227 (2023).

[4] K. Head-Marsden, J. Flick, C. J. Ciccarino, and P. Narang, “Quantum information and algorithms for correlated quantum matter”, Chemical Reviews **121**, 3061–3120 (2021).

[5] L. Amico, D. Anderson, M. Boshier, J.-P. Brantut, L.-C. Kwek, A. Minguzzi, and W. von Klitzing, “Colloquium: atomtronic circuits: from many-body physics to quantum technologies”, Rev. Mod. Phys. **94**, 041001 (2022).

[6] D. A. Vajner, L. Rickert, T. Gao, K. Kaymazlar, and T. Heindel, “Quantum communication using semiconductor quantum dots”, Advanced Quantum Technologies **5**, 2100116 (2022).

[7] A. Haleem, M. Javaid, R. P. Singh, S. Rab, and R. Suman, “Applications of nanotechnology in medical field: a brief review”, Global Health Journal **7**, 70–77 (2023).

[8] S. E. McNeil, “Nanotechnology for the biologist”, Journal of Leukocyte Biology **78**, 585–594 (2005).

[9] D. S. Chemla and J. Shah, “Many-body and correlation effects in semiconductors”, Nature **411**, 549–557 (2001).

[10] E. Morosan, D. Natelson, A. H. Nevidomskyy, and Q. Si, “Strongly correlated materials”, Advanced Materials **24**, 4896–4923 (2012).

[11] E. Dagotto, “Complexity in strongly correlated electronic systems”, Science **309**, 257–262 (2005).

[12] B. Bertini, F. Heidrich-Meisner, C. Karrasch, T. Prosen, R. Steinigeweg, and M. Žnidari č, “Finite-temperature transport in one-dimensional quantum lattice models”, Rev. Mod. Phys. **93**, 025003 (2021).

[13] C. Karrasch, M. Pletyukhov, L. Borda, and V. Meden, “Functional renormalization group study of the interacting resonant level model in and out of equilibrium”, Phys. Rev. B **81**, 125122 (2010).

[14] D. M. Kennes, D. Schuricht, and V. Meden, “Efficiency and power of a thermoelectric quantum dot device”, Europhysics Letters **102**, 57003 (2013).

[15] S. Andergassen, V. Meden, H. Schoeller, J. Splettstoesser, and M. R. Wegewijs, “Charge transport through single molecules, quantum dots and quantum wires”, Nanotechnology **21**, 272001 (2010).

[16] V. Meden and F. Marquardt, “Correlation-induced resonances in transport through coupled quantum dots”, Phys. Rev. Lett. **96**, 146801 (2006).

[17] J. Wu and Z. Wang, *Quantum dot molecules*, Lecture Notes in Nanoscale Science and Technology, (Springer New York, 2013).

[18] F. Yoshihara, T. Fuse, S. Ashhab, K. Kakuyanagi, S. Saito, and K. Semba, “Superconducting qubit–oscillator circuit beyond the ultrastrong-coupling regime”, Nature Physics **13**, 44–47 (2017).

[19] T. Althuon, T. Cubaynes, A. Auer, C. Sürgers, and W. Wernsdorfer, “Nano-assembled open quantum dot nanotube devices”, Communications Materials **5**, 5 (2024).

[20] Y.-Y. Liu, J. Stehlik, C. Eichler, M. J. Gullans, J. M. Taylor, and J. R. Petta, “Semiconductor double quantum dot micromaser”, Science **347**, 285–287 (2015).

[21] R. Leturcq, C. Stampfer, K. Inderbitzin, L. Durrer, C. Hierold, E. Mariani, M. G. Schultz, F. von Oppen, and K. Ensslin, “Franck–condon blockade in suspended carbon nanotube quantum dots”, Nature Physics **5**, 327–331 (2009).

[22] S. Sapmaz, P. Jarillo-Herrero, Y. M. Blanter, C. Dekker, and H. S. J. van der Zant, “Tunneling in suspended carbon nanotubes assisted by longitudinal phonons”, Phys. Rev. Lett. **96**, 026801 (2006).

[23] A. C. Hewson, *The kondo problem to heavy fermions*, Cambridge Studies in Magnetism, (Cambridge University Press, 1993).

[24] M. Pletyukhov and H. Schoeller, “Nonequilibrium kondo model: crossover from weak to strong coupling”, Phys. Rev. Lett. **108**, 260601 (2012).

[25] A. Oguri, “Fermi liquid theory for the nonequilibrium kondo effect at low bias voltages”, Journal of the Physical Society of Japan **74**, 110–117 (2005).

[26] W. de Haas, J. de Boer, and G. van dën Berg, “The electrical resistance of gold, copper and lead at low temperatures”, Physica **1**, 1115–1124 (1934).

[27] J. Kondo, “Resistance Minimum in Dilute Magnetic Alloys”, Progress of Theoretical Physics **32**, 37–49 (1964).

[28] D. M. Kennes and V. Meden, “Interacting resonant-level model in nonequilibrium: finite-temperature effects”, Phys. Rev. B **87**, 075130 (2013).

[29] C. Karrasch, S. Andergassen, M. Pletyukhov, D. Schuricht, L. Borda, V. Meden, and H. Schoeller, “Non-equilibrium current and relaxation dynamics of a charge-fluctuating quantum dot”, Europhysics Letters **90**, 30003 (2010).

[30] B. Doyon, “New method for studying steady states in quantum impurity problems: the interacting resonant level model”, Phys. Rev. Lett. **99**, 076806 (2007).

[31] E. Perfetto, G. Stefanucci, and M. Cini, “Interacting resonant-level model with long-range interactions: fast screening and suppression of the zero-bias conductance”, Phys. Rev. B **85**, 165437 (2012).

[32] E. Boulat, H. Saleur, and P. Schmitteckert, “Twofold advance in the theoretical understanding of far-from-equilibrium properties of interacting nanostructures”, Phys. Rev. Lett. **101**, 140601 (2008).

[33] L. Borda, K. Vladár, and A. Zawadowski, “Theory of a resonant level coupled to several conduction-electron channels in equilibrium and out of equilibrium”, Phys. Rev. B **75**, 125107 (2007).

[34] D. Wanisch, “The Anderson-Holstein model with Coulomb interaction”, M.Sc. thesis (2019).

[35] J. P. Dehollain, U. Mukhopadhyay, V. P. Michal, Y. Wang, B. Wunsch, C. Reichl, W. Wegscheider, M. S. Rudner, E. Demler, and L. M. K. Vandersypen, "Nagaoka ferromagnetism observed in a quantum dot plaquette", Nature **579**, 528–533 (2020).

[36] T. Hensgens, T. Fujita, L. Janssen, X. Li, C. J. Van Diepen, C. Reichl, W. Wegscheider, S. Das Sarma, and L. M. K. Vandersypen, "Quantum simulation of a fermi–hubbard model using a semiconductor quantum dot array", Nature **548**, 70–73 (2017).

[37] C.-A. Wang, C. Déprez, H. Tidjani, W. I. L. Lawrie, N. W. Hendrickx, A. Sammak, G. Scappucci, and M. Veldhorst, "Probing resonating valence bonds on a programmable germanium quantum simulator", npj Quantum Information **9**, 58 (2023).

[38] P. Senn, "A simple quantum mechanical model that illustrates the jahn-teller effect", Journal of Chemical Education **69**, 819 (1992).

[39] A. Blais, A. L. Grimsmo, S. M. Girvin, and A. Wallraff, "Circuit quantum electrodynamics", Rev. Mod. Phys. **93**, 025005 (2021).

[40] C. Rye, R. Wise, V. Jurukovski, J. DeSaix, J. Choi, and Y. Avissar, *Biology*, (OpenStax, Houston, Texas, Oct. 2016).

[41] Y. Aharonov and D. Bohm, "Significance of electromagnetic potentials in the quantum theory", Phys. Rev. **115**, 485–491 (1959).

[42] F. Evers, R. Korytár, S. Tewari, and J. M. van Ruitenbeek, "Advances and challenges in single-molecule electron transport", Rev. Mod. Phys. **92**, 035001 (2020).

[43] C. M. Guédon, H. Valkenier, T. Markussen, K. S. Thygesen, J. C. Hummelen, and S. J. van der Molen, "Observation of quantum interference in molecular charge transport", Nature Nanotechnology **7**, 305–309 (2012).

[44] K. R. Parenti, R. Chesler, G. He, P. Bhattacharyya, B. Xiao, H. Huang, D. Malinowski, J. Zhang, X. Yin, A. Shukla, S. Mazumdar, M. Y. Sfeir, and L. M. Campos, "Quantum interference effects elucidate triplet-pair formation dynamics in intramolecular singlet-fission molecules", Nature Chemistry **15**, 339–346 (2023).

[45] C.-C. Chen, Y.-c. Chang, and D. M. T. Kuo, "Quantum interference and electron correlation in charge transport through triangular quantum dot molecules", Phys. Chem. Chem. Phys. **17**, 6606–6611 (2015).

[46] C.-Y. Hsieh, Y.-P. Shim, M. Korkusinski, and P. Hawrylak, "Physics of lateral triple quantum-dot molecules with controlled electron numbers", Reports on Progress in Physics **75**, 114501 (2012).

[47] S. Sangtarash, H. Sadeghi, and C. J. Lambert, "Exploring quantum interference in heteroatom-substituted graphene-like molecules", Nanoscale **8**, 13199–13205 (2016).

[48] Z.-T. Jiang and Q.-f. Sun, "Quantum transport through circularly coupled triple quantum dots", Journal of Physics: Condensed Matter **19**, 156213 (2007).

[49] X. Yang and Y. Liu, "Multiple-path quantum interference effects in a double-aharonov-bohm interferometer", Nanoscale research letters **5**, 1228–35 (2010).

[50] G. Rajput, "Interference effects in coupled triple quantum dot systems", Materials Today: Proceedings (2023).

[51] J. Bloch, A. Cavalleri, V. Galitski, M. Hafezi, and A. Rubio, "Strongly correlated electron–photon systems", Nature **606**, 41–48 (2022).

[52] F. Schlawin, D. M. Kennes, and M. A. Sentef, “Cavity quantum materials”, Applied Physics Reviews **9**, 011312 (2022).

[53] A. de la Torre, D. M. Kennes, M. Claassen, S. Gerber, J. W. McIver, and M. A. Sentef, “Colloquium: nonthermal pathways to ultrafast control in quantum materials”, Rev. Mod. Phys. **93**, 041002 (2021).

[54] F. J. Garcia-Vidal, C. Ciuti, and T. W. Ebbesen, “Manipulating matter by strong coupling to vacuum fields”, Science **373**, eabd0336 (2021).

[55] A. Frisk Kockum, A. Miranowicz, S. De Liberato, S. Savasta, and F. Nori, “Ultrastrong coupling between light and matter”, Nature Reviews Physics **1**, 19–40 (2019).

[56] K. D. Greve, D. Press, P. L. McMahon, and Y. Yamamoto, “Ultrafast optical control of individual quantum dot spin qubits”, Reports on Progress in Physics **76**, 092501 (2013).

[57] D. M. Kennes, E. Y. Wilner, D. R. Reichman, and A. J. Millis, “Transient superconductivity from electronic squeezing of optically pumped phonons”, Nature Physics **13**, 479–483 (2017).

[58] D. Fausti, R. I. Tobey, N. Dean, S. Kaiser, A. Dienst, M. C. Hoffmann, S. Pyon, T. Takayama, H. Takagi, and A. Cavalleri, “Light-induced superconductivity in a stripe-ordered cuprate”, Science **331**, 189–191 (2011).

[59] M. Budden, T. Gebert, M. Buzzi, G. Jotzu, E. Wang, T. Matsuyama, G. Meier, Y. Laplace, D. Pontiroli, M. Riccò, F. Schlawin, D. Jaksch, and A. Cavalleri, “Evidence for metastable photo-induced superconductivity in k3c60”, Nature Physics **17**, 611–618 (2021).

[60] M. Mitrano, A. Cantaluppi, D. Nicoletti, S. Kaiser, A. Perucchi, S. Lupi, P. Di Pietro, D. Pontiroli, M. Riccò, S. R. Clark, D. Jaksch, and A. Cavalleri, “Possible light-induced superconductivity in k3c60 at high temperature”, Nature **530**, 461–464 (2016).

[61] Y. Murakami, N. Tsuji, M. Eckstein, and P. Werner, “Nonequilibrium steady states and transient dynamics of conventional superconductors under phonon driving”, Phys. Rev. B **96**, 045125 (2017).

[62] L. D’Alessio and M. Rigol, “Long-time behavior of isolated periodically driven interacting lattice systems”, Phys. Rev. X **4**, 041048 (2014).

[63] S. Haroche and J. Raimond, *Exploring the quantum: atoms, cavities, and photons*, (Oxford University Press, Oxford, England, 2006).

[64] W. E. Lamb and R. C. Retherford, “Fine structure of the hydrogen atom by a microwave method”, Phys. Rev. **72**, 241–243 (1947).

[65] G. J. Maclay, “History and some aspects of the lamb shift”, Physics **2**, 105–149 (2020).

[66] H. B. G. Casimir, “On the attraction between two perfectly conducting plates”, Indag. Math. **10**, 261–263 (1948).

[67] E. M. Purcell, “Proceedings of the american physical society”, Phys. Rev. **69**, 674–674 (1946).

[68] J. D. van der Waals, “Over de continuïteit van den gas- en vloeistoftoestand (on the continuity of the gaseous and liquid states)”, Doctoral dissertation, PhD thesis, (University of Leiden, Leiden, Netherlands, 1873).

[69] S. Haroche, M. Brune, and J. M. Raimond, “From cavity to circuit quantum electrodynamics”, Nature Physics **16**, 243–246 (2020).

[70] M. Ruggenthaler, D. Sidler, and A. Rubio, “Understanding polaritonic chemistry from ab initio quantum electrodynamics”, Chemical Reviews **123**, 11191–11229 (2023).

[71] P. Meystre, *Quantum optics: taming the quantum*, Graduate Texts in Physics, (Springer International Publishing, 2021).

[72] D. Hagenmüller, J. Schachenmayer, S. Schütz, C. Genes, and G. Pupillo, “Cavity-enhanced transport of charge”, Phys. Rev. Lett. **119**, 223601 (2017).

[73] I. V. Dinu, V. Moldoveanu, and P. Gartner, “Many-body effects in transport through a quantum-dot cavity system”, Phys. Rev. B **97**, 195442 (2018).

[74] G. Arwas and C. Ciuti, “Quantum electron transport controlled by cavity vacuum fields”, Phys. Rev. B **107**, 045425 (2023).

[75] E. Orgiu, J. George, J. A. Hutchison, E. Devaux, J. F. Dayen, B. Doudin, F. Stellacci, C. Genet, J. Schachenmayer, C. Genes, G. Pupillo, P. Samorì, and T. W. Ebbesen, “Conductivity in organic semiconductors hybridized with the vacuum field”, Nature Materials **14**, 1123–1129 (2015).

[76] G. Jarc, S. Y. Mathengattil, A. Montanaro, F. Giusti, E. M. Rigoni, R. Sergo, F. Fassioli, S. Winnerl, S. Dal Zilio, D. Mihailovic, P. Prelovšek, M. Eckstein, and D. Fausti, “Cavity-mediated thermal control of metal-to-insulator transition in 1t-tas2”, Nature **622**, 487–492 (2023).

[77] R. H. Dicke, “Coherence in spontaneous radiation processes”, Phys. Rev. **93**, 99–110 (1954).

[78] M. Roses and E. Dalla Torre, “Dicke model”, PLOS ONE **15**, e0235197 (2020).

[79] P. Kirton, M. M. Roses, J. Keeling, and E. G. Dalla Torre, “Introduction to the dicke model: from equilibrium to nonequilibrium, and vice versa”, Advanced Quantum Technologies **2**, 1800043 (2019).

[80] E. Jaynes and F. Cummings, “Comparison of quantum and semiclassical radiation theories with application to the beam maser”, Proceedings of the IEEE **51**, 89–109 (1963).

[81] J. M. Luttinger, “The effect of a magnetic field on electrons in a periodic potential”, Phys. Rev. **84**, 814–817 (1951).

[82] O. Dmytruk, M. Trif, C. Mora, and P. Simon, “Out-of-equilibrium quantum dot coupled to a microwave cavity”, Phys. Rev. B **93**, 075425 (2016).

[83] J. Li, D. Golez, G. Mazza, A. J. Millis, A. Georges, and M. Eckstein, “Electromagnetic coupling in tight-binding models for strongly correlated light and matter”, Phys. Rev. B **101**, 205140 (2020).

[84] C. J. Eckhardt, G. Passetti, M. Othman, C. Karrasch, F. Cavaliere, M. A. Sentef, and D. M. Kennes, “Quantum floquet engineering with an exactly solvable tight-binding chain in a cavity”, Communications Physics **5**, 122 (2022).

[85] O. Dmytruk and M. Schiró, “Gauge fixing for strongly correlated electrons coupled to quantum light”, Phys. Rev. B **103**, 075131 (2021).

[86] M. A. Sentef, J. Li, F. Künzel, and M. Eckstein, “Quantum to classical crossover of floquet engineering in correlated quantum systems”, Phys. Rev. Res. **2**, 033033 (2020).

[87] D. A. Ryndyk, “Introduction”, in *Theory of quantum transport at nanoscale: an introduction* (Springer International Publishing, Cham, 2016), pp. 1–14.

[88] K. Hepp and E. H. Lieb, “On the superradiant phase transition for molecules in a quantized radiation field: the dicke maser model”, Annals of Physics **76**, 360–404 (1973).

[89] N. Tonchev, J. Brankov, and V. Zagrebnov, “Overview of the superradiant phase transition: the dicke model”, Journal of optoelectronics and advanced materials **11**, 1142–1149 (2009).

[90] J. Koch, F. von Oppen, and A. V. Andreev, “Theory of the franck-condon blockade regime”, Phys. Rev. B **74**, 205438 (2006).

[91] T. Frederiksen, M. Paulsson, M. Brandbyge, and A.-P. Jauho, “Inelastic transport theory from first principles: methodology and application to nanoscale devices”, Phys. Rev. B **75**, 205413 (2007).

[92] A. Khedri, “Thermoelectric transport through vibrating molecular quantum dots”, Doctoral dissertation, PhD thesis, (RWTH Aachen University, Aachen, 2018).

[93] H. Park, J. Park, A. K. L. Lim, E. H. Anderson, A. P. Alivisatos, and P. L. McEuen, “Nanomechanical oscillations in a single-c60 transistor”, Nature **407**, 57–60 (2000).

[94] M. Galperin, M. A. Ratner, and A. Nitzan, “Molecular transport junctions: vibrational effects”, Journal of Physics: Condensed Matter **19**, 103201 (2007).

[95] I. Díez-Pérez, J. Hihath, Y. Lee, L. Yu, L. Adamska, M. A. Kozhushner, I. I. Oleynik, and N. Tao, “Rectification and stability of a single molecular diode with controlled orientation”, Nature Chemistry **1**, 635–641 (2009).

[96] A. Jovchev and F. B. Anders, “Influence of vibrational modes on quantum transport through a nanodevice”, Phys. Rev. B **87**, 195112 (2013).

[97] A. Khedri, T. A. Costi, and V. Meden, “Exponential and power-law renormalization in phonon-assisted tunneling”, Phys. Rev. B **96**, 195155 (2017).

[98] R. Hützen, S. Weiss, M. Thorwart, and R. Egger, “Iterative summation of path integrals for nonequilibrium molecular quantum transport”, Phys. Rev. B **85**, 121408 (2012).

[99] A. Khedri, T. A. Costi, and V. Meden, “Nonequilibrium thermoelectric transport through vibrating molecular quantum dots”, Phys. Rev. B **98**, 195138 (2018).

[100] M. A. Laakso, D. M. Kennes, S. G. Jakobs, and V. Meden, “Functional renormalization group study of the anderson–holstein model”, New Journal of Physics **16**, 023007 (2014).

[101] S. Braig and K. Flensberg, “Vibrational sidebands and dissipative tunneling in molecular transistors”, Phys. Rev. B **68**, 205324 (2003).

[102] L. Childress, A. S. Sørensen, and M. D. Lukin, “Mesoscopic cavity quantum electrodynamics with quantum dots”, Phys. Rev. A **69**, 042302 (2004).

[103] T. Hönigl-Decrinis, I. Antonov, R. Shaikhaidarov, K. H. Kim, V. N. Antonov, and O. V. Astafiev, “Capacitive coupling of coherent quantum phase slip qubits to a resonator”, New Journal of Physics **25**, 113020 (2023).

[104] J. Clarke, A. N. Cleland, M. H. Devoret, D. Esteve, and J. M. Martinis, “Quantum mechanics of a macroscopic variable: the phase difference of a josephson junction”, Science **239**, 992–997 (1988).

[105] A. Wallraff, D. I. Schuster, A. Blais, L. Frunzio, R.-. S. Huang, J. Majer, S. Kumar, S. M. Girvin, and R. J. Schoelkopf, “Strong coupling of a single photon to a superconducting qubit using circuit quantum electrodynamics”, Nature **431**, 162–167 (2004).

[106] S.-S. Gu, Y.-Q. Xu, R. Wu, S.-L. Jiang, S.-K. Ye, T. Lin, B.-C. Wang, H.-O. Li, G. Cao, and G.-P. Guo, "Gain of a high-impedance cavity coupled to strongly driven semiconductor quantum dots", Phys. Rev. Appl. **19**, 054020 (2023).

[107] B. Njegic and M. S. Gordon, "Exploring the effect of anharmonicity of molecular vibrations on thermodynamic properties", The Journal of Chemical Physics **125**, 224102 (2006).

[108] C. Sandorfy, R. Buchet, and G. Lachenal, "Principles of molecular vibrations for near-infrared spectroscopy", in *Near-infrared spectroscopy in food science and technology* (John Wiley and Sons, Ltd, 2006) Chap. 2, pp. 11–46.

[109] N. W. Ashcroft and N. D. Mermin, *Solid State Physics*, (Holt-Saunders, 1976).

[110] S. H. Simon, *The Oxford solid state basics*, (Oxford Univ. Press, Oxford, UK, 2013).

[111] R. T. Scalettar, "An introduction to the hubbard hamiltonian", unpublished.

[112] U. Busch and K. A. Penson, "Tight-binding electrons on open chains: density distribution and correlations", Phys. Rev. B **36**, 9271–9274 (1987).

[113] Y. Liu, Y. Zheng, W. Gao, and T. Lü, "Electronic transport through a quantum dot chain with strong dot-lead coupling", Physics Letters A **365**, 495–500 (2007).

[114] Z.-M. Bai, Y.-R. Wang, and M.-L. Ge, "Electric current and conductance in a chain of quantum dots", Journal of Physics A: Mathematical and General **34**, 1595 (2001).

[115] Y. Asai and H. Fukuyama, "Theory of length-dependent conductance in one-dimensional chains", Phys. Rev. B **72**, 085431 (2005).

[116] M.-H. Cha and J. Hwang, "Quantum transport in a chain of quantum dots with inhomogeneous size distribution and manifestation of 1D anderson localization", Scientific Reports **10**, 16701 (2020).

[117] U. Weiss, *Quantum dissipative systems*, Series in modern condensed matter physics, (World Scientific, 2008).

[118] M. Caltapanides, "Non-equilibrium transport through interacting and vibrating quantum dots", M.Sc. thesis, 2020.

[119] J. W. Negele and H. Orland, *Quantum many-particle systems*, (Westview Press, Nov. 1998).

[120] S. G. Jakobs, M. Pletyukhov, and H. Schoeller, "Properties of multi-particle green's and vertex functions within keldysh formalism", Journal of Physics A: Mathematical and Theoretical **43**, 103001 (2010).

[121] J. Rammer, *Quantum field theory of non-equilibrium states*, (Cambridge University Press, 2007).

[122] A. Kamenev, *Field theory of non-equilibrium systems*, (Cambridge University Press, 2011).

[123] G. Stefanucci and R. van Leeuwen, *Nonequilibrium many-body theory of quantum systems: a modern introduction*, (Cambridge University Press, 2013).

[124] S. G. Jakobs, "Functional renormalization group studies of quantum transport through mesoscopic systems", Doctoral dissertation, PhD thesis, (RWTH Aachen University, 2010).

[125] D. M. Kennes and V. Meden, "Quench dynamics of correlated quantum dots", Phys. Rev. B **85**, 245101 (2012).

[126] L. V. Keldysh, "Diagram technique for nonequilibrium processes", Soviet Physics—JETP **20**, 1018–1026 (1965).

[127] C. Karrasch, “The functional renormalization group for zero-dimensional quantum systems in and out of equilibrium”, Doctoral dissertation, PhD thesis, (RWTH Aachen University, 2010).

[128] H. Bruus and K. Flensberg, *Many-body quantum field theory in condensed matter physics: an introduction*, English, (Oxford University Press, United Kingdom, 2003).

[129] J. Taylor, *Scattering theory: quantum theory on nonrelativistic collisions*, (Wiley, 1972).

[130] S. G. Jakobs, *Functional renormalization group studies of quantum transport through mesoscopic systems*, tech. rep., Lecture notes (2009).

[131] Y. Meir and N. S. Wingreen, “Landauer formula for the current through an interacting electron region”, Phys. Rev. Lett. **68**, 2512–2515 (1992).

[132] A. Hernández, V. M. Apel, F. A. Pinheiro, and C. H. Lewenkopf, “Quantum electronic transport: Linear and nonlinear conductance from the Keldysh approach”, Phys. A Stat. Mech. its Appl. **385**, 148–160 (2007).

[133] D. M. Kennes, “Dynamics in low-dimensional correlated quantum systems”, Doctoral dissertation, PhD thesis, (RWTH Aachen University, 2014).

[134] L. Onsager, “Reciprocal relations in irreversible processes. i.”, Phys. Rev. **37**, 405–426 (1931).

[135] B. K. Agarwalla, J.-H. Jiang, and D. Segal, *Thermoelectricity in molecular junctions with harmonic and anharmonic modes*, arXiv:1506.03102, 2015.

[136] A. Oguri, “Transmission probability for interacting electrons connected to reservoirs”, Journal of the Physical Society of Japan **70**, 2666–2681 (2001).

[137] S. Datta, *Electronic transport in mesoscopic systems*, Cambridge Studies in Semiconductor Physics and Microelectronic Engineering, (Cambridge University Press, 1995).

[138] W. Metzner, M. Salmhofer, C. Honerkamp, V. Meden, and K. Schönhammer, “Functional renormalization group approach to correlated fermion systems”, Rev. Mod. Phys. **84**, 299–352 (2012).

[139] P. Kopietz, L. Bartosch, and F. Schütz, *Introduction to the functional renormalization group*, (Springer, 2010).

[140] B. K. Agarwalla, M. Kulkarni, S. Mukamel, and D. Segal, “Tunable photonic cavity coupled to a voltage-biased double quantum dot system: diagrammatic nonequilibrium green’s function approach”, Phys. Rev. B **94**, 035434 (2016).

[141] A. Cottet, Z. Leghtas, and T. Kontos, “Theory of interactions between cavity photons induced by a mesoscopic circuit”, Phys. Rev. B **102**, 155105 (2020).

[142] D. Svintsov, G. Alymov, and L. Martin-Moreno, “Modification of one-dimensional electron localization induced by coupling to an electromagnetic cavity”, arXiv:2211.13075 (2022).

[143] J. Bak and D. Newman, *Complex analysis*, Undergraduate Texts in Mathematics, (Springer New York, 1999).

[144] T. Frederiksen, “Inelastic electron transport in nanosystems”, M.Sc. thesis, (Department of Micro and Nanotechnology, Technical University of Denmark, 2022).

[145] J. Diekmann and S. G. Jakobs, “Parquet approximation and one-loop renormalization group: equivalence on the leading-logarithmic level”, Phys. Rev. B **103**, 155156 (2021).

[146] J. Sólyom, “The fermi gas model of one-dimensional conductors”, Advances in Physics **28**, 201–303 (1979).

[147] J. Diekmann and S. G. Jakobs, “Leading-logarithmic approximation by one-loop renormalization group within matsubara formalism”, Phys. Rev. B **109**, 115134 (2024).

[148] R. Hedden, V. Meden, T. Pruschke, and K. Schönhammer, “A functional renormalization group approach to zero-dimensional interacting systems”, Journal of Physics: Condensed Matter **16**, 5279 (2004).

[149] S. G. Jakobs, M. Pletyukhov, and H. Schoeller, “Nonequilibrium functional renormalization group with frequency-dependent vertex function: a study of the single-impurity anderson model”, Phys. Rev. B **81**, 195109 (2010).

[150] C. Klöckner, D. M. Kennes, and C. Karrasch, “Second-order functional renormalization group approach to quantum wires out of equilibrium”, Phys. Rev. B **102**, 235113 (2020).

[151] T. R. Morris, “The exact renormalization group and approximate solutions”, International Journal of Modern Physics A **09**, 2411–2449 (1994).

[152] P. Virtanen, R. Gommers, T. E. Oliphant, M. Haberland, T. Reddy, D. Cournapeau, E. Burovski, P. Peterson, W. Weckesser, J. Bright, S. J. van der Walt, M. Brett, J. Wilson, K. J. Millman, N. Mayorov, A. R. J. Nelson, E. Jones, R. Kern, E. Larson, C. J. Carey, İ. Polat, Y. Feng, E. W. Moore, J. VanderPlas, D. Laxalde, J. Perktold, R. Cimrman, I. Henriksen, E. A. Quintero, C. R. Harris, A. M. Archibald, A. H. Ribeiro, F. Pedregosa, P. van Mulbregt, and SciPy 1.0 Contributors, “SciPy 1.0: Fundamental Algorithms for Scientific Computing in Python”, Nature Methods **17**, 261–272 (2020).

[153] A. Weiße and H. Fehske, “Exact diagonalization techniques”, in , Vol. 739 (Dec. 2007), pp. 529–544.

[154] J. M. Zhang and R. X. Dong, “Exact diagonalization: the bose–hubbard model as an example”, European Journal of Physics **31**, 591–602 (2010).

[155] P.-Q. Jin, M. Marthaler, J. H. Cole, A. Shnirman, and G. Schön, “Lasing and transport in a quantum-dot resonator circuit”, Phys. Rev. B **84**, 035322 (2011).

[156] B. K. Agarwalla, M. Kulkarni, and D. Segal, “Photon statistics of a double quantum dot micromaser: quantum treatment”, Phys. Rev. B **100**, 035412 (2019).

[157] M. Galperin, M. A. Ratner, and A. Nitzan, “Inelastic electron tunneling spectroscopy in molecular junctions: peaks and dips”, The Journal of Chemical Physics **121**, PubMed-not-MEDLINE, 11965–11979 (2004).

[158] D. Manzano and E. Kyoseva, “An atomic symmetry-controlled thermal switch”, Scientific Reports **6**, 31161 (2016).

[159] B. Kraus, H. P. Büchler, S. Diehl, A. Kantian, A. Micheli, and P. Zoller, “Preparation of entangled states by quantum markov processes”, Phys. Rev. A **78**, 042307 (2008).

[160] M. A. Nielsen and I. L. Chuang, *Quantum computation and quantum information: 10th anniversary edition*, (Cambridge University Press, 2010).

[161] J. Liouville, “Note sur la théorie de la variation des constantes arbitraires”, Journal de Mathématiques Pures et Appliquées, Serie 1 **3**, 342–349 (1838).

[162] D. Manzano, “A short introduction to the Lindblad master equation”, AIP Advances **10**, 025106 (2020).

[163] H.-P. Breuer and F. Petruccione, *The Theory of Open Quantum Systems*, (Oxford University Press, Jan. 2002).

[164] D. Walls and G. Milburn, *Quantum optics*, (Springer Berlin Heidelberg, 2008).

[165] A. Redfield, “The theory of relaxation processes”, in *Advances in magnetic resonance*, Vol. 1, edited by J. S. Waugh, Advances in Magnetic and Optical Resonance (Academic Press, 1965), pp. 1–32.

[166] J. Johansson, P. Nation, and F. Nori, “Qutip: an open-source python framework for the dynamics of open quantum systems”, Computer Physics Communications **183**, 1760–1772 (2012).

[167] J. Johansson, P. Nation, and F. Nori, “Qutip 2: a python framework for the dynamics of open quantum systems”, Computer Physics Communications **184**, 1234–1240 (2013).

[168] G. Kir šanskas, M. Franckié, and A. Wacker, “Phenomenological position and energy resolving lindblad approach to quantum kinetics”, Phys. Rev. B **97**, 035432 (2018).

[169] F. Thompson and A. Kamenev, “Field theory of many-body lindbladian dynamics”, Annals of Physics **455**, 169385 (2023).

[170] A. Kamenev, *Field Theory of Non-Equilibrium Systems*, (Cambridge University Press, Cambridge, England, UK, Jan. 2023).

[171] L. M. Sieberer, M. Buchhold, and S. Diehl, “Keldysh field theory for driven open quantum systems”, Reports on Progress in Physics **79**, 096001 (2016).

[172] M. Lax, “Formal theory of quantum fluctuations from a driven state”, Phys. Rev. **129**, 2342–2348 (1963).

[173] Q.-W. Wang, “Exact dynamical correlations of nonlocal operators in quadratic open Fermion systems: a characteristic function approach”, SciPost Phys. Core **5**, 027 (2022).

[174] F. Schwarz, M. Goldstein, A. Dorda, E. Arrigoni, A. Weichselbaum, and J. von Delft, “Lindblad-driven discretized leads for nonequilibrium steady-state transport in quantum impurity models: recovering the continuum limit”, Phys. Rev. B **94**, 155142 (2016).

[175] A. A. Dzhioev and D. S. Kosov, “Super-fermion representation of quantum kinetic equations for the electron transport problem”, The Journal of Chemical Physics **134**, 044121 (2011).

[176] O. Scarlatella, A. A. Clerk, and M. Schiro, “Spectral functions and negative density of states of a driven-dissipative nonlinear quantum resonator”, New Journal of Physics **21**, 043040 (2019).

[177] Y. Ashida, A. ç. İmamo ğlu, and E. Demler, “Cavity quantum electrodynamics at arbitrary light-matter coupling strengths”, Phys. Rev. Lett. **126**, 153603 (2021).

[178] J. Román-Roche and D. Zueco, “Effective theory for matter in non-perturbative cavity QED”, SciPost Phys. Lect. Notes, 50 (2022).

[179] R. Peierls, “Zur theorie des diamagnetismus von leitungselektronen”, Zeitschrift für Physik **80**, 763–791 (1933).

[180] M. Kiffner, J. R. Coulthard, F. Schlawin, A. Ardavan, and D. Jaksch, “Manipulating quantum materials with quantum light”, Phys. Rev. B **99**, 085116 (2019).

[181] V. K. Kozin, D. Miserev, D. Loss, and J. Klinovaja, “Quantum phase transitions and cat states in cavity-coupled quantum dots”, Phys. Rev. Res. **6**, 033188 (2024).

[182] D. De Bernardis, T. Jaako, and P. Rabl, “Cavity quantum electrodynamics in the nonperturbative regime”, Phys. Rev. A **97**, 043820 (2018).

[183] A. Stokes and A. Nazir, “Gauge ambiguities imply jaynes-cummings physics remains valid in ultrastrong coupling qed”, Nature Communications **10**, 499 (2019).

[184] N. Marzari, A. A. Mostofi, J. R. Yates, I. Souza, and D. Vanderbilt, “Maximally localized wannier functions: theory and applications”, Rev. Mod. Phys. **84**, 1419–1475 (2012).

[185] T. M. Gunawardana, A. M. Turner, and R. Barnett, “Optimally localized single-band wannier functions for two-dimensional chern insulators”, Phys. Rev. Res. **6**, 023046 (2024).

[186] K. Rza żewski, K. Wódkiewicz, and W. Żakowicz, “Phase transitions, two-level atoms, and the A^2 term”, Phys. Rev. Lett. **35**, 432–434 (1975).

[187] C. J. Eckhardt, “Cavitronics in low-dimensional systems”, Doctoral dissertation, PhD thesis, (RWTH Aachen University, Aachen, 2024).

[188] O. Di Stefano, A. Settineri, V. Macrı, L. Garziano, R. Stassi, S. Savasta, and F. Nori, “Resolution of gauge ambiguities in ultrastrong-coupling cavity quantum electrodynamics”, Nature Physics **15**, 803–808 (2019).

[189] A. M. Stewart, “Vector potential of the coulomb gauge”, European Journal of Physics **24**, 519 (2003).

[190] F. P. M. Méndez-Córdoba, J. J. Mendoza-Arenas, F. J. Gómez-Ruiz, F. J. Rodríguez, C. Tejedor, and L. Quiroga, “Rényi entropy singularities as signatures of topological criticality in coupled photon-fermion systems”, Phys. Rev. Res. **2**, 043264 (2020).

[191] M. Trif and Y. Tserkovnyak, “Resonantly tunable majorana polariton in a microwave cavity”, Phys. Rev. Lett. **109**, 257002 (2012).

[192] P. Rao and F. Piazza, “Non-fermi-liquid behavior from cavity electromagnetic vacuum fluctuations at the superradiant transition”, Phys. Rev. Lett. **130**, 083603 (2023).

[193] I. Amelio, L. Korosec, I. Carusotto, and G. Mazza, “Optical dressing of the electronic response of two-dimensional semiconductors in quantum and classical descriptions of cavity electrodynamics”, Phys. Rev. B **104**, 235120 (2021).

[194] Z. Zhiqiang, C. H. Lee, R. Kumar, K. J. Arnold, S. J. Masson, A. S. Parkins, and M. D. Barrett, “Nonequilibrium phase transition in a spin-1 dicke model”, Optica **4**, 424–429 (2017).

[195] K. Baumann, C. Guerlin, F. Brennecke, and T. Esslinger, “Dicke quantum phase transition with a superfluid gas in an optical cavity”, Nature **464**, 1301–1306 (2010).

[196] A. Kara Slimane, P. Reck, and G. Fleury, “Simulating time-dependent thermoelectric transport in quantum systems”, Phys. Rev. B **101**, 235413 (2020).

[197] P. Wissgott, J. Kune š, A. Toschi, and K. Held, “Dipole matrix element approach versus peierls approximation for optical conductivity”, Phys. Rev. B **85**, 205133 (2012).

[198] A. Vukics, T. Grießer, and P. Domokos, “Elimination of the A-square problem from cavity qed”, Phys. Rev. Lett. **112**, 073601 (2014).

[199] E. A. Power, S. Zienau, and H. S. W. Massey, “Coulomb gauge in non-relativistic quantum electro-dynamics and the shape of spectral lines”, Philosophical Transactions of the Royal Society of London. Series A, Mathematical and Physical Sciences **251**, 427–454 (1959).

[200] R. G. Woolley and C. A. Coulson, “Molecular quantum electrodynamics”, Proceedings of the Royal Society of London. A. Mathematical and Physical Sciences **321**, 557–572 (1971).

[201] E. Vlasiuk, V. K. Kozin, J. Klinovaja, D. Loss, I. V. Iorsh, and I. V. Tokatly, “Cavity-induced charge transfer in periodic systems: length-gauge formalism”, Phys. Rev. B **108**, 085410 (2023).

[202] A. Abedi, E. Khosravi, and I. V. Tokatly, “Shedding light on correlated electron–photon states using the exact factorization”, The European Physical Journal B **91**, 194 (2018).

[203] I. V. Tokatly, “Conserving approximations in cavity quantum electrodynamics: implications for density functional theory of electron-photon systems”, Phys. Rev. B **98**, 235123 (2018).

[204] D. L. Andrews, G. A. Jones, A. Salam, and R. G. Woolley, “Perspective: quantum hamiltonians for optical interactions”, The Journal of Chemical Physics **148**, 040901 (2018).

[205] B. C. Hall, “The baker—campbell—hausdorff formula”, in *Lie groups, lie algebras, and representations: an elementary introduction* (Springer New York, New York, NY, 2003), pp. 63–90.

[206] I. N. Levine, *Quantum chemistry*, Seventh edition., (PHI Learning Private Limited, Delhi, 2014).

[207] F. Schwabl, *Advanced quantum mechanics (QM II)*, (1997).

[208] A. E. Miroshnichenko, S. Flach, and Y. S. Kivshar, “Fano resonances in nanoscale structures”, Rev. Mod. Phys. **82**, 2257–2298 (2010).

[209] M. Mendoza and P. A. Schulz, “Imaging and switching of fano resonances in open quantum cavities”, Phys. Rev. B **71**, 245303 (2005).

[210] M. Yamaguchi, A. Lyasota, and T. Yuge, “Theory of fano effect in cavity quantum electrodynamics”, Phys. Rev. Res. **3**, 013037 (2021).

[211] U. Fano, “Effects of configuration interaction on intensities and phase shifts”, Phys. Rev. **124**, 1866–1878 (1961).

[212] A. Ueda and M. Eto, “Resonant tunneling and fano resonance in quantum dots with electron-phonon interaction”, Phys. Rev. B **73**, 235353 (2006).

[213] H. Aikawa, K. Kobayashi, A. Sano, S. Katsumoto, and Y. Iye, “Interference effect in multilevel transport through a quantum dot”, Journal of the Physical Society of Japan **73**, 3235–3238 (2004).

[214] M. I. Lepsa, “Resonant tunneling in quantum structures”, Peter Grünberg Institute (PGI-9), JARA-Fundamentals for Information Technology, Research Center Jülich, 52425.

[215] W. R. Inc., *Mathematica, Version 14.1*, Champaign, IL, 2024.

[216] H. Schoeller, “Transport theory of interacting quantum dots”, in *Mesoscopic electron transport*, Vol. E 345, edited by L. Sohn, NATO ASI Series (Dordrecht, Institut für Theoretische Festkörperphysik, Universität Karlsruhe, 76128 Karlsruhe, Germany, 1997), pp. 291–330.

[217] N. C. van der Vaart, S. F. Godijn, Y. V. Nazarov, C. J. P. M. Harmans, J. E. Mooij, L. W. Molenkamp, and C. T. Foxon, “Resonant tunneling through two discrete energy states”, Phys. Rev. Lett. **74**, 4702–4705 (1995).

[218] B. W. Shore and P. L. Knight, “The jaynes-cummings model”, Journal of Modern Optics **40**, 1195–1238 (1993).

[219] A. Khedri, V. Meden, and T. A. Costi, “Influence of phonon-assisted tunneling on the linear thermoelectric transport through molecular quantum dots”, Phys. Rev. B **96**, 195156 (2017).

[220] E. Eidelstein, D. Goberman, and A. Schiller, “Crossover from adiabatic to antiadiabatic phonon-assisted tunneling in single-molecule transistors”, Phys. Rev. B **87**, 075319 (2013).

[222] K. G. L. Pedersen, M. Strange, M. Leijnse, P. Hedegård, G. C. Solomon, and J. Paaske, “Quantum interference in off-resonant transport through single molecules”, Phys. Rev. B **90**, 125413 (2014).

[223] Z. Chen, I. M. Grace, S. L. Woltering, L. Chen, A. Gee, J. Baugh, G. A. D. Briggs, L. Bogani, J. A. Mol, C. J. Lambert, H. L. Anderson, and J. O. Thomas, “Quantum interference enhances the performance of single-molecule transistors”, Nature Nanotechnology **19**, 986–992 (2024).

[224] H.-G. Duan, P. Nalbach, R. J. D. Miller, and M. Thorwart, “Intramolecular vibrations enhance the quantum efficiency of excitonic energy transfer”, Photosynthesis Research **144**, 137–145 (2020).

[225] O. Svelto, *Principles of lasers*, trans. by D. Hanna, 4th, (Springer, 1998).

[226] C. Xu and M. G. Vavilov, “Full counting statistics of photons emitted by a double quantum dot”, Phys. Rev. B **88**, 195307 (2013).

[227] A. A. Vyshnevyy, “Gain-dependent Purcell enhancement, breakdown of Einstein’s relations, and superradiance in nanolasers”, Phys. Rev. B **105**, 085116 (2022).

[228] K. Ohno, “Some remarks on the pariser-parr-pople method”, Theoretica chimica acta **2**, 219–227 (1964).

[229] T. Y. Ahmed, N. R. Abdullah, and V. Gudmundsson, “Controlling thermoelectric, heat, and energy currents through a quantum dot in sequential and cotunneling coulomb-blockade regimes”, Physica B: Condensed Matter **628**, 413607 (2022).

[230] M. A. Sierra and D. Sánchez, “Nonlinear heat conduction in coulomb-blockaded quantum dots”, Materials Today: Proceedings **2**, 12th European Conference on Thermoelectrics, 483–490 (2015).

[232] A. Mitra, I. Aleiner, and A. J. Millis, “Phonon effects in molecular transistors: quantal and classical treatment”, Phys. Rev. B **69**, 245302 (2004).

[233] T. Koch, J. Loos, A. Alvermann, and H. Fehske, “Nonequilibrium transport through molecular junctions in the quantum regime”, Phys. Rev. B **84**, 125131 (2011).

[234] C. Karrasch, T. Hecht, A. Weichselbaum, J. von Delft, Y. Oreg, and V. Meden, “Phase lapses in transmission through interacting two-level quantum dots”, New Journal of Physics **9**, 123 (2007).

[235] P. Murphy, S. Mukerjee, and J. Moore, “Optimal thermoelectric figure of merit of a molecular junction”, Phys. Rev. B **78**, 161406 (2008).

[236] V. I. Novoderezhkin, E. Romero, and R. van Grondelle, “How exciton-vibrational coherences control charge separation in the photosystem ii reaction center”, Phys. Chem. Chem. Phys. **17**, 30828–30841 (2015).

[237] A. G. Dijkstra, C. Wang, J. Cao, and G. R. Fleming, “Coherent exciton dynamics in the presence of underdamped vibrations”, The Journal of Physical Chemistry Letters **6**, 627–632 (2015).

[238] S. Lange and C. Timm, “Random-matrix theory for the Lindblad master equation”, Chaos: An Interdisciplinary Journal of Nonlinear Science **31**, 023101 (2021).

[239] H. Schoeller, “Quantum theory of condensed matter i”, unpublished.

[240] V. Meden, “Correlation effects on electronic transport through dots and wires”, in *Advances in solid state physics* (Springer Berlin Heidelberg, Berlin, Heidelberg, 2008), pp. 183–195.

Acronyms

cavity QED	cavity quantum electrodymanics
circuit QED	circuit quantum electrodymanics
ED	exact diagonalization
FRG	functional renormalization group
IRLM	interacting resonant level model
MF	mean-field
PHS	particle hole symmetry
PZW	Power-Zienau-Wooley
QRT	quantum regression theorem
SAHM	spinless Anderson-Holstein model

Acknowledgments

First and foremost, I would like to express my sincere gratitude to Volker Meden for his guidance and support throughout my PhD journey. I am especially grateful to him for offering me the opportunity to continue exploring the fascinating field of correlated electron systems following my Master's thesis under his supervision. His meticulous attention to detail and thorough approach have greatly influenced my work and contributed significantly to my growth, both academically and personally, during these years.

I also extend my deepest thanks to Dante M. Kennes, my second supervisor, for his insightful perspectives across various research fields and his support throughout my doctoral studies. I am particularly thankful for his introduction to the field of cavity QED.

My sincere appreciation also goes to Jens Paaske, who hosted my stay at the Niels Bohr Institute in Copenhagen, which I very much enjoyed. I am grateful for the many fruitful discussions with him and Cecilie Hermansen, and for the pleasant collaboration.

During my years at the Institute for Theory of Statistical Physics at RWTH Aachen University, I had the privilege of meeting and working alongside many remarkable colleagues and friends. I thank Valentin Bruch, Matthew Bunney, Nils Çaçi, Fabian Engelhardt, Ammon Fischer, Francesco Grandi, Lukas Grunwald, Jan Herre, Javed Lindner, Florian Kischel, Claudia Merger, Takuya Okugawa, Giacomo Passetti, Jonas Profe, Adrien Reingruber, Anna Stollenwerk, Alexander Sushchyev, Clara Weber, Lukas Weber, Feng Xiong, and Lefan Zhang. I would like to particularly acknowledge Lukas Grunwald and Francesco Grandi, with whom I shared an office and who were always open to engaging discussions and who motivated new ideas. Special thanks are also due to Christian Eckhardt, Hanno Jacobs and Maria Spethmann for their stimulating conversations and fresh perspectives on both physics and life at the institute. I am especially grateful to many of my colleagues who took the time to review parts of this thesis and provide valuable feedback. In particular, I thank Clara Weber and Ammon Fischer for their insights and support during our 'Schreibbüro'-sessions.

I would also like to acknowledge the financial support provided by the DFG via RTG 1995, as well as the computing resources generously made available by RWTH Aachen University and the Forschungszentrum Jülich. Their support has been instrumental to the successful completion of this work.

I would like to thank Jonathan Conrad, Federica Demattè, Hannah Erpenbeck, Maria Häser, Franca auf der Heiden, Pia Kielbock, Claudia Merger, Rebecca Rodrigo, and Pascal Rogalla, who accompanied me during my Bachelor's and Master's studies. I would not have reached this point without their camaraderie and insights. I would especially like to mention Pascal Rogalla and Melanie Glusa for their invaluable support during my PhD; Thank you.

My deepest thanks go to my family and my partner for their unconditional love and support. I am profoundly grateful to my parents, Anke and Stefan Caltapanides, who have encouraged and supported me in more ways I can count for the past 30 years and who first sparked my curiosity in science. I also thank my brother, Timon Caltapanides, whose serenity and sincerity are qualities I greatly admire and strive to embody. My heartfelt thanks to my grandmother, Christel Caltapanides, for her unwavering presence in my life. Finally, I wish to thank Daniel Felder for sharing these past years with me. Your support throughout my Bachelor's and Master's studies, and doctoral research, along with the personal growth you have inspired in me, has meant the world. Thank you for always believing in me and motivating me to reach my potential.

EIDESSTATTLICHE ERKLÄRUNG

Ich, Mara Caltapanides, erkläre hiermit, dass diese Dissertation und die darin dargelegten Inhalte die eigenen sind und selbstständig, als Ergebnis der eigenen originären Forschung, generiert wurden.

Hiermit erkläre ich an Eides statt

1. Diese Arbeit wurde vollständig oder größtenteils in der Phase als Doktorand dieser Fakultät und Universität angefertigt;
2. Sofern irgendein Bestandteil dieser Dissertation zuvor für einen akademischen Abschluss oder eine andere Qualifikation an dieser oder einer anderen Institution verwendet wurde, wurde dies klar angezeigt;
3. Wenn immer andere eigene oder Veröffentlichungen Dritter herangezogen wurden, wurden diese klar benannt;
4. Wenn aus anderen eigenen oder Veröffentlichungen Dritter zitiert wurde, wurde stets die Quelle hierfür angegeben. Diese Dissertation ist vollständig meine eigene Arbeit, mit der Ausnahme solcher Zitate;
5. Alle wesentlichen Quellen von Unterstützung wurden benannt;
6. Wenn immer ein Teil dieser Dissertation auf der Zusammenarbeit mit anderen basiert, wurde von mir klar gekennzeichnet, was von anderen und was von mir selbst erarbeitet wurde;
7. Teile dieser Arbeit wurden zuvor veröffentlicht, und zwar in
    - **M. Caltapanides**, D. M. Kennes, and V. Meden, ”Finite-bias transport through the interacting resonant level model coupled to a phonon mode: a functional renormalization group study”, *Phys. Rev. B*, 104, 085125 (2021).
    - C. Hermansen, **M. Caltapanides**, V. Meden, and J. Paaske, ”Simulating electron-vibron energy transfer with quantum dots and resonators”, *Phys. Rev. B*, 110, 205424 (2024).

Aachen, 16. Januar 2025
Mara Caltapanides